ISSN 2959-0663 (Print)
ISSN 2959-0671 (Online)
ISSN-L 2959-0663

EURASIAN JOURNAL OF CHEMISTRY

2026. Vol. 31 No. 2(122)

ISSN 2959-0663 (Print)
ISSN 2959-0671 (Online)
ISSN-L 2959-0663

EURASIAN JOURNAL OF CHEMISTRY

2026

Volume 31, No. 2 (122)

Founded in 1996

Published 4 times a year

Karaganda
2026

Publisher: **NLC "Karaganda National Research University named after academician Ye.A. Buketov"**
Postal address: 28 University St., Karaganda 100024, Kazakhstan
E-mail: chemistry.vestnik.ksu.kz@gmail.com; ipustolaikina@gmail.com
Tel./fax: +7(7212) 34-19-40.
Web-site: https://ejc.buketov.edu.kz

Eurasian Journal of Chemistry. — 2026. — Vol. 31, No. 2(122). — 124 p.
ISSN 2959-0663 (Print). ISSN 2959-0671 (Online). ISSN-L 2959-0663

Proprietary: NLC "Karaganda National Research University named after academician Ye.A. Buketov".

Registered by the Ministry of Culture and Information of the Republic of Kazakhstan. Re-registration certificate No. KZ02VPY00134144 dated 14.11.2025.

Signed in print 30.06.2026. Format 60×84 1/8. Offset paper. Volume 15,5 p.sh. Circulation 200 copies. Price upon request. Order № 75.

Printed in the Publishing house of NLC "Karaganda National Research University named after academician Ye.A. Buketov".
28 University St., Karaganda 100024, Kazakhstan. Tel.: +7(7212) 35-63-16. E-mail: printed@karnu-buketov.edu.kz

CONTENTS

ORGANIC CHEMISTRY

PHYSICAL AND ANALYTICAL CHEMISTRY

INORGANIC CHEMISTRY

CHEMICAL TECHNOLOGY

How to Cite: Anwar, B., Febriani, L.I., Dara, F., & Yuliani, G. (2026). Biopolymer-Based Pectin/PVP/CNC Nanocomposites as Sustainable Matrices for Solid Polymer Electrolyte Systems. *Eurasian Journal of Chemistry, 31, 2(122), 4–15.* https://doi.org/10.31489/2959-0663/2-26-4

ORGANIC CHEMISTRY

Article

Received: 9 January 2026 | Revised: 27 April 2026 |
Accepted: 12 May 2026 | Published online: 19 May 2026

UDC 544.42+519.242.7

https://doi.org/10.31489/2959-0663/2-26-4

Budiman Anwar[1, 2*], Lidya I. Febriani[1], Fitri Dara[3], Galuh Yuliani[1, 2]

[1]*Chemistry Programs, Universitas Pendidikan Indonesia, Bandung, Indonesia;*
[2]*ChemTransform for Sustainability Research Group, Universitas Pendidikan Indonesia, Bandung, Indonesia;*
[3]*National Research and Innovation Agency (BRIN), Bandung, Indonesia*
*(*Corresponding author's e-mail: budimananwar@upi.edu)*

Biopolymer-Based Pectin/PVP/CNC Nanocomposites as Sustainable Matrices for Solid Polymer Electrolyte Systems

Biopolymer-based solid polymer electrolytes (SPEs) are attractive as sustainable alternatives to petroleum-derived systems; however, balancing mechanical integrity and chain mobility remains challenging. In this study, cellulose nanocrystals (CNCs) were incorporated into an optimized pectin/poly(vinyl pyrrolidone) (PVP) polyblend to elucidate their role as functional nanofillers in biopolymer-based SPE matrix design. CNCs were introduced into the pectin/PVP (7:1, w/w) matrix at loadings of 2, 4, and 6 wt% via solution casting. FTIR and SEM analyses suggest good compatibility and homogeneous dispersion of CNCs through hydrogen-bond-mediated interactions. Mechanical testing shows that CNC incorporation does not function as conventional reinforcement; instead, low to intermediate CNC contents reduce stiffness and strength while enhancing ductility, indicating increased segmental mobility. DSC analysis reveals CNC-induced modulation of Tg-related enthalpy relaxation without inducing crystallinity. SEM observations further confirm a continuous polymer matrix with CNC-induced interfacial heterogeneity and no macroscopic phase separation. These findings demonstrate that CNCs function as mobility-regulating nanofillers, enabling controlled tuning of thermal–mechanical behavior, and highlight pectin/PVP/CNC nanocomposites as promising sustainable matrices for future solid polymer electrolyte systems.

Keywords: biopolymers, nanocomposite, pectin, poly(vinyl pyrrolidone), cellulose nanocrystals, solid polymer electrolyte, polyblend, sustainable polymer matrices

Introduction

The rapid growth of electrochemical energy storage technologies has intensified the demand for safe, flexible, and sustainable electrolyte materials. Among various candidates, solid polymer electrolytes (SPEs) have attracted considerable attention owing to their improved safety, mechanical integrity, and processability compared to liquid electrolytes [1]. Conventional SPE matrices are predominantly based on petroleum-derived polymers such as poly(ethylene oxide) (PEO) [2], poly(vinylidene fluoride) (PVDF) and its copolymers [3], poly(methyl methacrylate) (PMMA) [4], and poly(vinyl alcohol) (PVA) [5], which have demonstrated promising ion-transport capabilities when combined with lithium salts and suitable plasticizers. However, concerns regarding environmental sustainability, resource depletion, and end-of-life disposal have motivated the exploration of biopolymer-based alternatives.

Biopolymers derived from renewable resources, including polysaccharides and their derivatives, offer inherent advantages such as biodegradability, low toxicity, and abundant functional groups capable of coordinating ionic species [6–8]. Among these materials, pectin, a naturally occurring anionic polysaccharide, has emerged as a promising host polymer due to its film-forming ability, hydrophilicity, and rich hydroxyl

and carboxyl functionalities. Nevertheless, pristine pectin films often suffer from limited mechanical strength and thermal stability, restricting their direct application as SPE matrices. To overcome these limitations, polymer blending, particularly with poly(vinyl pyrrolidone) (PVP), has been demonstrated as an effective strategy to enhance mechanical performance and compatibility through hydrogen bonding interactions [9].

Beyond polymer blending, the incorporation of nanoscale fillers has proven to be a powerful approach for tailoring the structure–property relationships of SPE matrices. In particular, cellulose nanocrystals (CNCs) have attracted increasing interest as sustainable nanofillers due to their high aspect ratio, superior mechanical stiffness, large specific surface area, and abundance of surface hydroxyl groups. Previous studies have shown that CNCs can enhance mechanical integrity, modify polymer chain mobility, and influence dielectric properties, all of which are critical parameters governing ion transport in polymer electrolytes. In addition, CNCs may act as physical crosslinking points and facilitate the formation of continuous ion-conduction pathways through polymer–filler interactions [10, 11].

Despite growing interest in CNC-containing SPE systems, most reported studies focus on synthetic polymer matrices, while biopolymer-based CNC-reinforced matrices remain relatively underexplored. In particular, systematic investigations addressing how CNC incorporation influences the mechanical, thermal, and physicochemical properties of pectin/PVP matrices—as prerequisites for SPE applications—are still scarce. Understanding these effects is essential for establishing design principles for sustainable SPE platforms that balance mechanical robustness, thermal stability, and ion-hosting capability.

Therefore, in this work, CNCs were incorporated into an optimized pectin/PVP polyblend to elucidate their role as functional nanofillers in biopolymer-based SPE matrices. Rather than focusing on ionic conductivity at this stage, this study emphasizes the structure–property relationships induced by CNC incorporation, including mechanical behavior, thermal transitions, hydrophilicity, and microstructural homogeneity, which collectively determine the suitability of the material as a solid polymer electrolyte matrix.

Experimental

Materials. Pectin extracted from citrus peel, poly(vinyl pyrrolidone) (PVP, average molecular weight 40 kDa), and glycerol were purchased from Sigma-Aldrich (Merck, Germany) and used as received. Bacterial cellulose (BC), in the form of *nata de coco* sheets, was obtained from a local commercial source and used as the precursor for cellulose nanocrystal (CNC) isolation.

Isolation of CNC. BC pellicles were dried at 70 °C for 7 h, ground into powder, and sieved to obtain a homogeneous particle size distribution. CNCs were isolated from BC via sulfuric acid hydrolysis under optimized conditions reported previously [12, 13]. Briefly, BC powder was hydrolyzed using 50 wt% sulfuric acid at a solid-to-liquid ratio of 1:50 (m/v) at 45 °C for 45 min under continuous stirring. The reaction was quenched by dilution with cold distilled water (1:10, v/v), followed by centrifugation at 4000 rpm for 10 min. The collected suspension was dialyzed against distilled water until pH ≈ 6, sonicated for 20 min at 75 % amplitude, and freeze-dried to obtain CNC powder.

Preparation of Pectin/PVP Polyblend Films. Pectin/PVP polyblend films were prepared by the solution casting method with minor modifications from reported procedures [9]. PVP and pectin were dissolved separately in distilled water, combined under stirring, and plasticized with glycerol (0.5 mL). The total polymer concentration was kept constant, while pectin/PVP weight ratios were varied at 8:0, 7:1, 6:2, and 5:3 (w/w). The resulting solutions were degassed, cast onto plastic Petri dishes, and dried at ambient conditions to obtain free-standing films.

Preparation of Pectin/PVP/CNC Nanocomposite Films. Pectin/PVP/CNC nanocomposite films were prepared by incorporating CNCs (2, 4, and 6 wt% relative to total polymer weight) into the optimized pectin/PVP matrix using solution casting. CNCs were dispersed in distilled water, stirred overnight, and ultrasonicated prior to addition into the polymer blend. The resulting ternary mixtures were homogenized, degassed, cast, and dried under ambient conditions to obtain free-standing nanocomposite films for characterization.

Fourier Transform Infrared (FTIR) Spectroscopy. FTIR spectroscopy was employed to investigate the chemical structure, intermolecular interactions, and crystallinity of BC, CNC, and polymer films. FTIR spectra of BC and CNC powders were recorded using a Bruker Alpha II FTIR spectrometer. The samples were prepared in the form of KBr pellets and analyzed over the wavenumber range of 4000–500 cm^{-1} to evaluate changes in chemical composition induced by the acid hydrolysis process.

FTIR spectra of pectin, PVP, pectin/PVP polyblend films, and pectin/PVP/CNC nanocomposite films at the optimum composition were recorded using a Shimadzu 8400 FTIR spectrometer in the frequency range

of 4000–400 cm^{-1}. FTIR analysis of the film samples was performed to identify functional groups, assess changes in chemical composition, and elucidate intermolecular interactions through hydrogen bonding within the polymer matrix.

X-ray Diffraction (XRD). XRD measurements of BC and CNC powders were carried out using a diffractometer equipped with Cu Kα radiation (λ = 0.154 nm). Diffraction patterns were recorded over a 2θ range of 2–90° with a step size of 0.02°, operating at a generator voltage of 45 kV and a tube current of 40 mA. XRD analysis was employed to determine the crystallinity index (CI) and crystallite size (*L*) of the samples. The CI was calculated using the Segal method [14] according to Eq. (1):

$$\mathrm{CI}(\%) = \frac{I_{200} - I_{am}}{I_{200}} \times 100, \quad (1)$$

where I_{200} is the maximum intensity of the crystalline peak at 2θ ≈ 22.5°, and I_{am} is the intensity of the amorphous region at 2θ ≈ 18°. The crystallite size was estimated using the Scherrer equation (Eq. (2)) [13]:

$$\mathrm{D} = \frac{K\lambda}{\beta \cos\theta}, \quad (2)$$

where *K* is the Scherrer constant (0.94), λ is the X-ray wavelength, β is the full width at half maximum (FWHM) of the diffraction peak in radians, and θ is the Bragg angle.

Transmission Electron Microscopy (TEM). Transmission electron microscopy (TEM) was used to examine the morphology and particle size of the isolated CNCs. A drop of CNC aqueous suspension was deposited onto a carbon-coated copper grid and allowed to dry at ambient conditions prior to observation using a Hitachi HT7700 TEM. Particle dimensions were statistically determined by measuring approximately 200 individual CNC particles using the ImageJ software.

Particle Size Analysis (PSA). The particle size distribution of CNCs dispersed in distilled water was determined using a particle size analyser based on dynamic light scattering (DLS). Prior to measurement, the CNC suspension was ultrasonicated for 5 min to ensure uniform dispersion. Measurements were conducted at 25.1 °C using a refractive index of 1.30.

Scanning Electron Microscopy (SEM). The surface morphology of pectin, pectin/PVP polyblend, and pectin/PVP/CNC nanocomposite films were examined using an EVO MA 10 scanning electron microscope. Film samples were cut into specimens with dimensions of 2×2 cm^2 and observed at an accelerating voltage of 15 kV with magnifications of up to ×2000.

Tensile Test. The mechanical properties of the films, including tensile strength, elongation at break, and Young's modulus, were evaluated using a Textechno Favigraph I-PI-067 tensile testing instrument. Tensile tests were performed at a crosshead speed of 6.0 mm min^{-1} under dry conditions at room temperature. Prior to testing, all films were cut into rectangular specimens with a width of 3 mm and a gauge length of 50 mm.

Differential scanning calorimetry (DSC). The glass transition temperature (T_g) and enthalpy relaxation change (ΔH_{relax}) of the films were investigated by DSC using a NETZSCH DSC 214 Polyma instrument under a nitrogen atmosphere. Film specimens were hermetically sealed in aluminum DSC pans and heated from 25 to 250 °C at a heating rate of 10 °C min^{-1}.

Results and Discussion

The successful formation of cellulose nanocrystals (CNCs) from bacterial cellulose (BC) was confirmed through a combination of FTIR, XRD, TEM, and particle size analysis (PSA). These complementary techniques collectively verify that the acid hydrolysis process effectively transformed bulk cellulose into nanoscale crystalline domains.

FTIR spectra of bacterial cellulose (BC) and cellulose nanocrystals (CNC) exhibit the characteristic absorption bands of cellulose, including the broad O–H stretching vibration in the range of 3300–3400 cm^{-1}, C–H stretching near 2900 cm^{-1}, and C–O–C stretching vibrations between 1000 and 1150 cm^{-1} (Fig. 1). The preservation of these characteristic bands after sulfuric acid hydrolysis indicates that the fundamental chemical structure of cellulose remains intact and that no significant chemical modification of the cellulose backbone occurs during CNC isolation [13].

Compared to BC, CNC shows a noticeable reduction in the intensity and breadth of the O–H stretching band, which can be attributed to the preferential removal of disordered cellulose domains containing loosely hydrogen-bonded hydroxyl groups. A decrease in the intensity of the CH_2 bending vibration at approximate-

ly 1430 cm^{-1} is also observed for CNC. Rather than being interpreted as a direct indicator of crystallinity, this change reflects a reduction in flexible and amorphous chain segments resulting from the selective dissolution of amorphous regions during acid hydrolysis [15].

No new absorption bands appear in the CNC spectrum, confirming that sulfuric acid hydrolysis selectively removes amorphous cellulose without altering the intrinsic cellulose framework. FTIR analysis provides qualitative evidence for the elimination of disordered domains while preserving the cellulose backbone, thereby supporting the successful formation of cellulose nanocrystals. Quantitative assessment of crystallinity is therefore more appropriately derived from X-ray diffraction analysis, as discussed in the subsequent paragraphs.

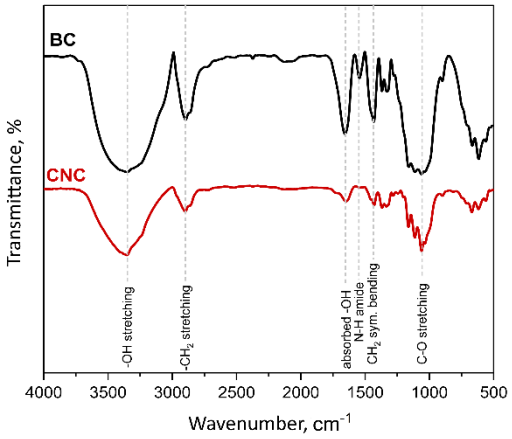

Figure 1. FTIR Spectra of BC and CNC

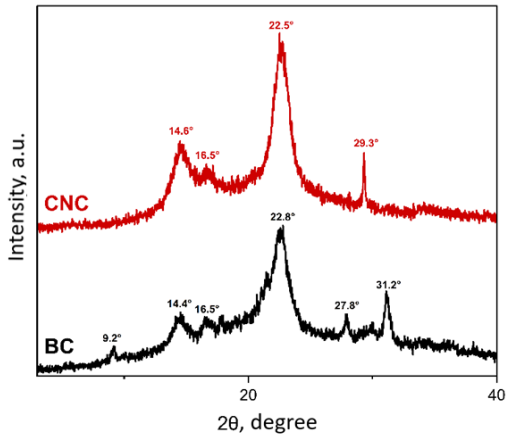

Figure 2. X-ray diffractogram of BC and CNC

XRD patterns of BC and CNC exhibit characteristic reflections of cellulose I, with diffraction peaks appearing at $2\theta \approx 14–17°$ and a dominant peak at $2\theta \approx 22–23°$, corresponding to the $(1\bar{1}0)$, (110), and (200) crystallographic planes (Fig. 2). The preservation of these diffraction features after sulfuric acid hydrolysis confirms that the native cellulose I crystalline structure remains unchanged during CNC isolation. Compared to BC, the diffraction pattern of CNC displays sharper and more intense crystalline reflections, particularly for the (200) plane, indicating a higher degree of structural ordering. This observation is consistent with the preferential removal of amorphous cellulose domains during acid hydrolysis, resulting in the enrichment of crystalline regions within the CNC structure [13, 16].

In addition to changes in crystallinity, the crystallite size, estimated using the Scherrer equation, shows an apparent increase after hydrolysis. The increase in crystallite size suggests that acid hydrolysis effectively removes disordered regions surrounding the crystalline domains, leading to more well-defined and coherent crystalline segments [17, 18]. The calculated values of crystallinity index (Eq. 1) and crystallite size (Eq. 2) for both BC and CNC are summarized in Table 1.

Importantly, no additional diffraction peaks or phase transformations were observed after hydrolysis, confirming that the acid treatment selectively removes disordered regions without altering the intrinsic crystalline form of cellulose. These XRD results provide quantitative evidence supporting the FTIR findings, demonstrating that sulfuric acid hydrolysis effectively converts bacterial cellulose into cellulose nanocrystals with higher crystallinity while maintaining the cellulose I crystal structure.

Table 1

Crystallinity index (CI) and crystallite size (*L*) of BC and CNC

Sample	CI, %	L_{200}, nm
BC	62	4.93
CNC	80	5.48

The morphology and size characteristics of the isolated CNCs were analyzed using TEM and PSA to provide complementary information on their physical dimensions. TEM images (Fig. 3*a*) show that the CNCs exhibit a rod-like (needle-shaped) morphology, which is typical for nanocrystalline cellulose obtained

via sulfuric acid hydrolysis. The nanocrystals appear well separated, indicating effective removal of the amorphous regions of bacterial cellulose and the release of individual crystalline domains.

Quantitative analysis based on TEM images (Figs. 3*b* and 3*c*) reveals that the CNCs possess an average length of 714 ± 12 nm and an average diameter of 31 ± 0.2 nm, resulting in a high aspect ratio (L/D) of ~ 23. Such a high aspect ratio is a defining characteristic of cellulose nanocrystals and is indicative of their rigid, anisotropic nature. These dimensions confirm that the hydrolysis process successfully produced nanocrystals rather than nanofibrillated or microcrystalline cellulose.

The particle size distribution obtained from PSA measurements (Fig. 3*d*) shows an average particle diameter of 80 ± 22 nm, which is larger than the diameter determined by TEM. This difference is expected, as PSA based on dynamic light scattering measures the hydrodynamic diameter of particles in suspension, which is influenced by solvation layers, particle orientation, and possible interparticle interactions. In contrast, TEM provides direct measurements of the physical dimensions of individual nanocrystals in the dry state.

While TEM analysis shows a Gaussian distribution (Fig. 3*c*) corresponding to the actual geometric dimensions of CNCs, the DLS-derived number distribution exhibits a positively skewed profile (Fig. 3*d*). This difference arises from the hydrodynamic nature of DLS measurements and the anisotropic morphology of CNCs, and therefore a Gaussian distribution is not necessarily expected for DLS data.

The combined TEM and PSA results consistently confirm the formation of well-defined cellulose nanocrystals with nanoscale dimensions and high aspect ratio, validating the effectiveness of sulfuric acid hydrolysis in converting bacterial cellulose into CNCs.

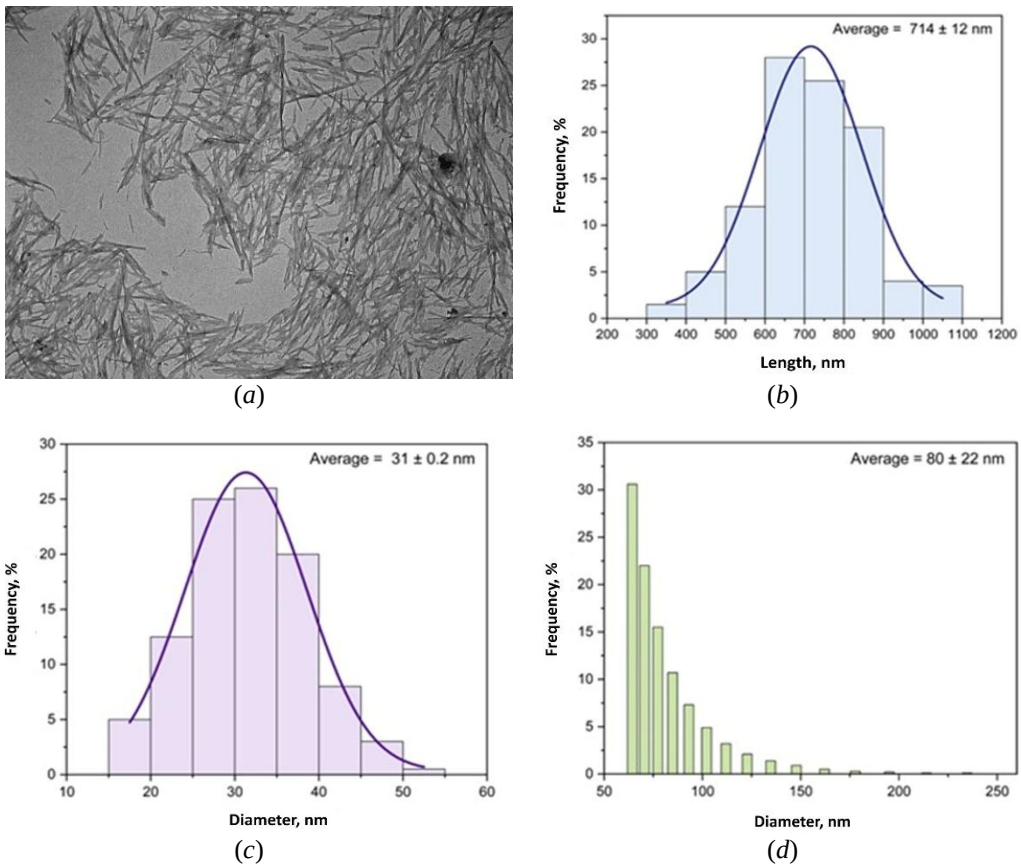

Figure 3. (*a*) TEM image of CNCs, (*b*) length and (*c*) diameter distribution of CNCs based on TEM, (*d*) diameter distribution of CNCs obtained from PSA

The mechanical properties of pectin/PVP polyblend films with different compositions were systematically evaluated to identify an optimal matrix for subsequent CNC incorporation. As summarized in Table 2, the mechanical response of the films shows a noticeable dependence on the PVP content, reflecting the balance between intermolecular interactions and plasticization effects. Neat pectin films (8:0) exhibit moderate tensile strength but limited flexibility, indicative of a relatively stiff and brittle polysaccharide network.

The incorporation of a small amount of PVP (7:1, w/w) leads to an observable improvement in overall mechanical performance, characterized by simultaneous enhancement of tensile strength and elongation at break. This synergistic behavior can be attributed to strong intermolecular hydrogen bonding between the hydroxyl groups of pectin and the carbonyl groups of PVP, which promotes good miscibility and efficient stress transfer while preserving sufficient chain mobility. Similar structure–property relationships have been reported for polysaccharide/PVP blends, where optimal PVP content maximizes mechanical performance through hydrogen-bond-driven miscibility without excessive plasticization [19].

Table 2

Mechanical properties of pectin and pectin/PVP blend films

Pektin/PVP composition, w/w	Film thickness, μm	Tensile strength, Mpa	Elongation at break, %	Young's modulus, MPa
8:0	101 ± 4	27.9 ± 4.3	13.4 ± 2.3	222.4 ± 96.0
7:1	93 ± 4	30.5 ± 5.7	17.5 ± 2.8	1702.4 ± 93.1
6:2	106 ± 6	27.1 ± 6.4	15.2 ± 1.6	194.4 ± 67.4
5:3	100 ± 2	28.6 ± 5.7	12.9 ± 2.7	112.1 ± 45.8

At higher PVP contents (6:2 and 5:3), the mechanical properties deteriorate, as evidenced by reduced tensile strength, elongation at break, and modulus. In this system, the plasticization effect is primarily attributed to PVP (40 kDa), which enhances chain mobility by disrupting pectin–pectin interactions. However, at higher PVP contents, excessive incorporation leads to over-plasticization, where the disruption of cohesive pectin–pectin interactions becomes dominant [20, 21]. This results in reduced intermolecular cohesion and weakened mechanical integrity, indicating a balance between plasticization and structural weakening of the polymer network [22]. Consequently, the pectin/PVP composition of 7:1 (w/w) provides the most balanced combination of strength and flexibility and was therefore selected as the optimum matrix for CNC incorporation. Figure 4 displays a photograph of pectin, pectin/PVP, and pectin/PVP/CNC films.

(*a*) (*b*) (*c*)

Figure 4. Photograph of (*a*) pectin, (*b*) pectin/PVP (7:1), and (*c*) pectin/PVP/CNC 6 % films

The effect of CNC incorporation on the mechanical properties of the optimized pectin/PVP (7:1, w/w) matrix was evaluated at CNC loadings of 2, 4, and 6 wt% (Tab. 3). The neat pectin/PVP film (0 % CNC) exhibits a relatively high tensile strength and Young's modulus with moderate elongation at break, indicating a mechanically robust polyblend network.

Table 3

Mechanical properties of pectin/PVP/CNC films

CNC composition, %	Film thickness, μm	Tensile strength, Mpa	Elongation at break, %	Young's modulus, MPa
0	93 ± 4	30.5 ± 5.7	17.5 ± 2.8	1702.4 ± 93.1
2	105 ± 14	10.2 ± 0.3	17.7 ± 5.9	117.6 ± 61.8
4	117 ± 2	9.2 ± 1.8	24.5 ± 6.2	59.4 ± 15.4
6	108 ± 4	13.8 ± 2.5	15.0 ± 3.4	123.0 ± 51.0

Upon CNC addition, a pronounced reduction in tensile strength and modulus is observed, particularly at 2–4 wt% CNC. At 2 wt% CNC, tensile strength decreases to 10.2 ± 0.3 MPa and modulus to 117.6 ± 61.8 MPa, while elongation remains comparable to the CNC-free film. At 4 wt% CNC, the film

shows the highest ductility with elongation increasing to 24.5 ± 6.2 %, accompanied by the lowest modulus (59.4 ± 15.4 MPa) and reduced tensile strength (9.2 ± 1.8 MPa). This trend suggests that, within this loading range, CNC incorporation does not act as a conventional reinforcing filler; instead, it likely disrupts the cohesive pectin–PVP network and introduces interfacial regions that facilitate chain mobility, resulting in a more compliant and extensible film [23].

Interestingly, at 6 wt% CNC, the tensile strength partially recovers to 13.8 ± 2.5 MPa and the modulus increases to 123.0 ± 51.0 MPa, while elongation decreases to 15.0 ± 3.4 %. The partial recovery at higher CNC loading may indicate the onset of a more effective filler contribution, potentially due to increased filler–matrix contacts and the formation of a percolated rigid phase that restricts deformation. Nevertheless, the overall decrease in strength and stiffness compared to the neat polyblend implies that CNC dispersion state and interfacial compatibility dominate the mechanical response of the nanocomposites.

FTIR spectroscopy was employed to elucidate the intermolecular interactions within the pectin/PVP matrix and to examine the effect of CNC incorporation on the chemical environment of the polymer films (Fig. 4). The spectrum of neat pectin (Fig. 5*a*) exhibits a broad O–H stretching band centered at ~3406 cm^{-1}, characteristic of extensive hydrogen bonding in polysaccharide networks. The absorption near 2924 cm^{-1} corresponds to C–H stretching, while the band at ~1626 cm^{-1} is associated with asymmetric stretching of carboxylate groups. The strong absorption in the range of 1000–1150 cm^{-1} originates from C–O–C and C–O stretching vibrations of the polysaccharide backbone [24].

Pure PVP (Fig. 5*b*) shows a distinct absorption band at ~1659 cm^{-1}, attributed to the C=O stretching of the pyrrolidone ring (amide I), along with C–H stretching around 2955 cm^{-1} and characteristic bands in the 1280–1300 cm^{-1} region corresponding to C–N stretching. These features confirm the presence of carbonyl groups capable of acting as strong hydrogen-bond acceptors [25].

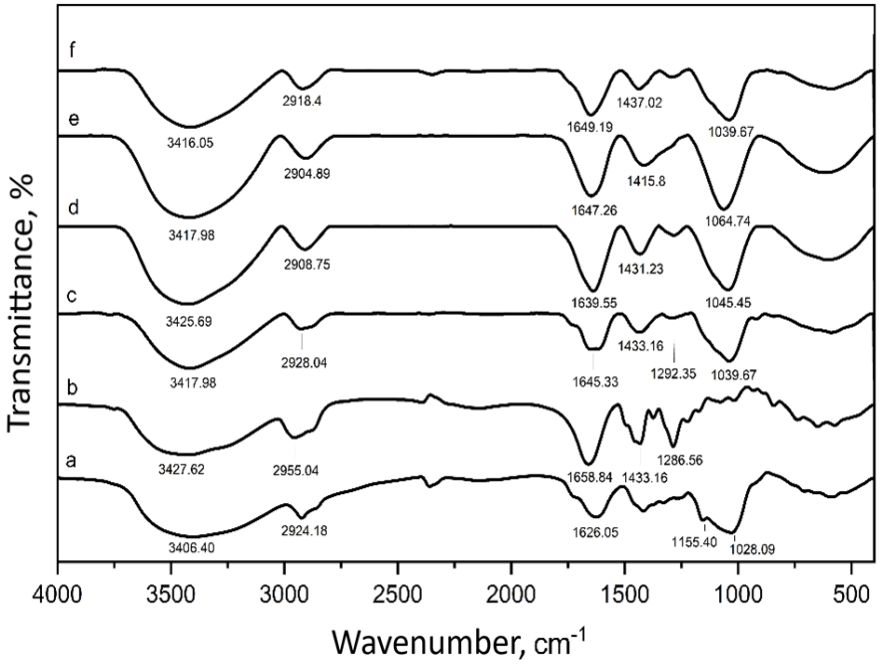

Figure 5. FTIR spectra of (*a*) pectin, (*b*) PVP, (*c*) pectin/PVP, (*d*) pectin/PVP/CNC 2 %, (*e*) pectin/PVP/CNC 4 %, and (*f*) pectin/PVP/CNC 6 %

Upon blending pectin with PVP (Fig. 5*c*), noticeable spectral changes are observed in the O–H stretching region. The broad O–H band of neat pectin centered at ~3406 cm^{-1} (Fig. 4*a*) shifts to a higher wavenumber (~3418 cm^{-1}) in the pectin/PVP film and becomes narrower and sharper. This blue shift and band narrowing suggest a more uniform hydrogen-bonding environment and a redistribution of hydroxyl interactions, consistent with reduced heterogeneity of the polysaccharide hydrogen-bond network upon PVP incorporation [26]. In parallel, the carbonyl stretching band of PVP around ~1659 cm^{-1} (Fig. 4*b*) shifts to ~1645 cm^{-1} in the polyblend (Fig. 4*c*), indicating specific interactions between the PVP carbonyl groups and pectin hydroxyl/carboxyl functionalities. Together, these spectral changes support good polymer–polymer

compatibility mediated by hydrogen bonding, which is consistent with the improved mechanical balance observed for the pectin/PVP (7:1) matrix.

Following CNC incorporation into the pectin/PVP matrix (Fig. 5*d-f*), further systematic changes are observed in the O–H stretching region. Compared to the pectin/PVP film, the O–H band remains centered in the range of ~3416–3418 cm^{-1} but becomes slightly broader with increasing CNC content, reflecting the introduction of additional hydroxyl groups from the CNC surface into the hydrogen-bonding network. Unlike the pectin/PVP blend, where the O–H band is relatively narrow and sharp, the presence of CNC reintroduces a degree of heterogeneity in hydrogen bonding due to polymer–CNC and CNC–CNC interactions [26].

In addition, subtle variations are detected in the CH_2 bending region (~1430–1440 cm^{-1}) and the C–O stretching bands around 1039–1065 cm^{-1} upon CNC addition. These changes indicate physical interactions between CNC and the polymer matrix rather than the formation of new covalent bonds. The absence of new absorption bands across all CNC loadings confirms that CNC functions as a physically interacting nanofiller, primarily through hydrogen bonding.

The evolution of the hydrogen-bond-related bands provides a molecular-level explanation for the mechanical behavior of the nanocomposite films. At low to intermediate CNC loadings, the redistribution and partial heterogenization of hydrogen bonds weaken the original pectin–PVP cohesive network, resulting in reduced tensile strength and modulus but enhanced ductility. At higher CNC content, the increased density of polymer–CNC interactions contributes to partial restriction of chain mobility, which is consistent with the observed recovery in mechanical stiffness. The FTIR results corroborate that hydrogen-bond-mediated interactions govern the balance between mechanical compliance and rigidity in the pectin/PVP/CNC nanocomposites.

The DSC thermograms of pectin, pectin/PVP, and pectin/PVP/CNC films (Fig. 6) exhibit two distinct thermal events. The dominant thermal transition is a broad endothermic peak observed in the range of ~70–100 °C, which is assigned to enthalpy relaxation (ΔH_{relax}) related to the glass transition region, strongly influenced by the release of bound water and the rearrangement of hydrogen-bonded polymer chains. A secondary endothermic event observed at higher temperatures (~210–240 °C) is associated with further molecular relaxation or the onset of structural rearrangement prior to thermal degradation, rather than crystalline melting.

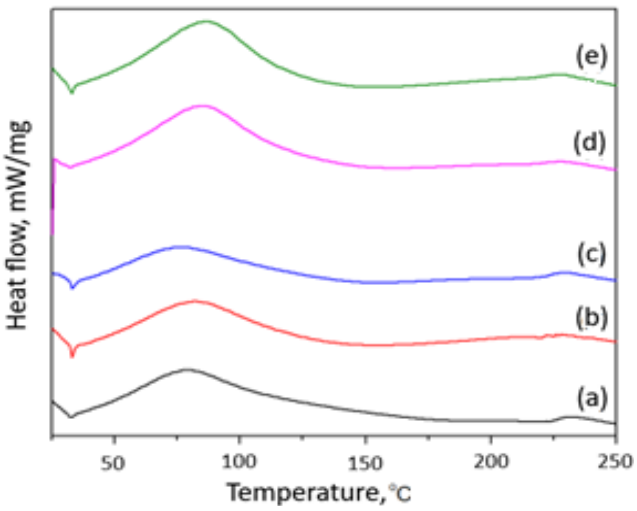

Figure 6. Thermogram DSC of (*a*) pectin, (*b*) pectin/PVP, (*c*) pectin/PVP/CNC 2 %, (*d*) pectin/PVP/CNC 4 %, and (*e*) pectin/PVP/CNC 6 % films

Quantitative DSC parameters derived from the thermograms (Fig. 6) are summarized in Table 4, including the apparent glass transition temperature (T_g) and ΔH_{relax}. It should be noted that, in hydrophilic biopolymer systems, the reported T_g values correspond to the temperature region of enthalpy relaxation rather than a classical baseline step change, due to the strong influence of bound water and hydrogen-bond rearrangement [27, 28].

Neat pectin exhibits a T_g-related relaxation at 78.9 °C with a relatively high ΔH_{relax} of 308.3 J g^{-1}, indicating a rigid polysaccharide network with limited segmental mobility and a high degree of internal stress

stored during film formation. Upon blending with PVP, the T_g shifts to a higher temperature (82.5 °C), while ΔH_{relax} decreases substantially to 225.5 J g^{-1}. This reduction in relaxation enthalpy suggests a more homogeneous and dynamically equilibrated polymer network, consistent with hydrogen-bond-driven miscibility between pectin and PVP and the improved mechanical balance observed for the polyblend.

Table 4

Thermal properties of pectin, pectin/PVP, and pectin/PVP/CNC

Data	Pectin	Pectin/PVP	Pectin/PVP/CNC 2 %	Pectin/PVP/CNC 4 %	Pectin/PVP/CNC 6 %
T_g, °C	78.9	82.5	76.3	84.4	86.5
ΔH_{relax}, J/g	308.3	225.5	188.4	324.9	318.8

The incorporation of CNC further modulates the thermal relaxation behavior. At 2 wt% CNC, the T_g decreases to 76.3 °C, accompanied by a pronounced reduction in ΔH_{relax} (188.4 J g^{-1}). This combination indicates enhanced chain mobility and reduced structural constraints, which can be attributed to the disruption of the pectin/PVP hydrogen-bond network by polymer–CNC interfacial interactions. Such behavior is consistent with the increased ductility observed in mechanical testing at low CNC loading.

At higher CNC contents (4 and 6 wt%), T_g shifts progressively to higher temperatures (84.4 and 86.5 °C, respectively), while ΔH_{relax} increases to 324.9 and 318.8 J g^{-1}. The increase in T_g reflects partial restriction of polymer chain motion due to the higher density of polymer–CNC interactions, whereas the elevated ΔH_{relax} indicates the development of a more heterogeneous hydrogen-bonding network with increased stored relaxation energy. This trend correlates with the partial recovery of mechanical stiffness at higher CNC loading [29].

Scanning electron microscopy was employed to examine the surface morphology of neat pectin, pectin/PVP polyblend, and pectin/PVP/CNC nanocomposite films (Fig. 7). The SEM micrograph of neat pectin shows a relatively rough and heterogeneous surface, characterized by irregular features and micro-scale undulations. This morphology reflects the rigid and highly hydrogen-bonded polysaccharide network of pectin, which is consistent with its limited ductility and higher brittleness observed in mechanical testing.

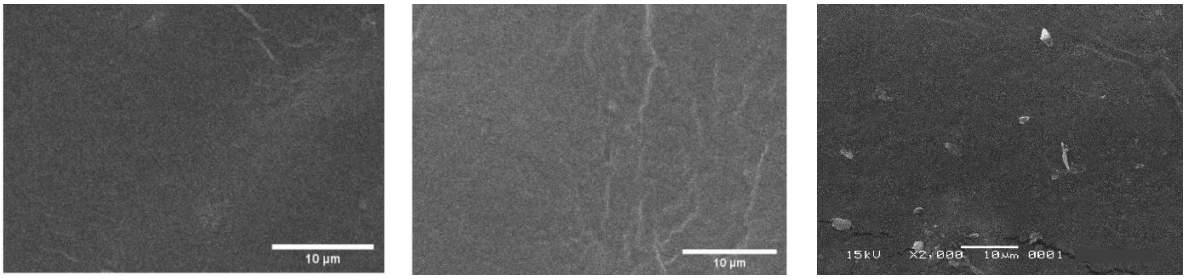

(*a*) (*b*) (*c*)

Figure 7. SEM image of (*a*) pectin, (*b*) pectin/PVP, (*c*) pectin/PVP/CNC films

In contrast, the pectin/PVP (7:1) polyblend film exhibits a smoother and more homogeneous surface morphology with no visible phase separation. The absence of distinct domains or cracks indicates good miscibility between pectin and PVP, which can be attributed to strong intermolecular hydrogen bonding between the hydroxyl groups of pectin and the carbonyl groups of PVP. This homogeneous morphology corroborates the FTIR evidence of polymer–polymer interactions and explains the improved mechanical balance of strength and flexibility in the polyblend film.

Upon incorporation of CNC into the pectin/PVP matrix, the surface morphology shows noticeable changes. The pectin/PVP/CNC nanocomposite films display a slightly roughened surface compared to the polyblend, with fine granular features uniformly distributed across the surface. No large CNC agglomerates or phase-separated regions are observed, indicating a reasonably good dispersion of CNC within the polymer matrix. The increased surface roughness is attributed to the presence of CNC and polymer–CNC interfacial regions, which disrupt the smooth polymer surface while maintaining overall film integrity.

The evolution of surface morphology with CNC incorporation is consistent with the observed mechanical and thermal behavior. The introduction of CNC-induced interfacial heterogeneity contributes to enhanced

ductility at lower CNC loadings and partial recovery of stiffness at higher CNC content, as well as to the modulation of segmental mobility evidenced by DSC analysis. From the perspective of solid polymer electrolyte matrices, the absence of macroscopic defects and the presence of a continuous polymer phase are essential for maintaining electrode–electrolyte contact and mechanical stability during operation.

The combined FTIR, DSC, SEM, and mechanical analyses reveal a coherent structure–property mechanism governing the behavior of the pectin/PVP/CNC nanocomposites. FTIR results demonstrate that the system is dominated by hydrogen-bond-mediated interactions, where blending pectin with PVP reorganizes the original polysaccharide network into a more homogeneous matrix, while CNC incorporation introduces additional hydroxyl-rich interfacial domains without forming new covalent bonds. These molecular interactions directly influence chain dynamics, as evidenced by DSC, where the T_g-related enthalpy relaxation and its evolution with CNC content reflect a tunable balance between segmental mobility and structural constraint. SEM observations further confirm that this balance is achieved through good matrix continuity and uniform CNC dispersion, with no macroscopic phase separation or agglomeration that could compromise mechanical integrity. Consequently, the mechanical response of the films transitions from a rigid and brittle behavior (neat pectin) to an optimized combination of strength and ductility (pectin/PVP), followed by a CNC-modulated response in which low filler loading enhances compliance while higher loading restores stiffness.

The confirmed formation of cellulose nanocrystals with well-defined morphology and nanoscale dimensions provides a robust nanofiller platform for tailoring the structure and properties of pectin/PVP matrices. The combined results from FTIR, DSC, SEM, and mechanical analysis consistently demonstrate that CNC incorporation modulates hydrogen-bond interactions, segmental mobility, and microstructural homogeneity in a composition-dependent manner. At intermediate CNC loadings, enhanced chain mobility contributes to improved ductility, while higher CNC contents partially restore stiffness and mechanical integrity without inducing crystallinity. This tunable balance between flexibility and structural stability highlights the ability of CNC to regulate the intermolecular network of the polymer matrix. These findings establish a clear structure–property relationship and indicate that the pectin/PVP/CNC system represents a promising platform for further development of functional biopolymer-based materials, including future exploration in solid polymer electrolyte systems.

Conclusions

This study demonstrates that pectin/PVP/CNC nanocomposites constitute a tunable biopolymer platform whose structural interactions and thermal–mechanical responses can be systematically tailored through controlled CNC incorporation. The results show that hydrogen-bond-mediated interactions govern the organization of the polymer network, enabling modulation of segmental mobility, relaxation behavior, and mechanical integrity without inducing crystallinity or phase separation. The optimized balance between compliance and stiffness, together with preserved amorphous character and thermal stability, highlights the suitability of the pectin/PVP/CNC system as a sustainable matrix for solid polymer electrolytes. These findings provide a mechanistic basis for the rational design of bio-based electrolyte matrices and open pathways for further optimization through salt incorporation and electrochemical performance evaluation. Future work will focus on lithium salt incorporation to evaluate the electrochemical window, ionic conductivity, and cycling stability of the pectin/PVP/CNC-based solid polymer electrolytes.

Funding

This work was supported by the Directorate of Research and Community Service Universitas Pendidikan Indonesia through the Strengthening Research Groups Scheme 2025 (Contract Number: 443/UN40/PT.01.02/2025). The authors have no competing interests to declare that are relevant to the content of this article.

Data Availability

The data that support the findings of this study are available from the corresponding authors upon reasonable request.

*Author Information**

**The authors' names are presented in the following order: First Name, Middle Name and Last Name*

Budiman Anwar (*corresponding author*) — Doctor of Material Chemistry, Head of ChemTransform for Sustainability Research Group, Associate Professor at Chemistry Programs, Universitas Pendidikan Indonesia, Jl. Dr. Setiabudhi No. 229, Bandung, Indonesia; e-mail: budimananwar@upi.edu; https://orcid.org/0000-0001-8085-9568

Lidya Intan Febriani — Bachelor of Chemistry, Junior Researcher, Chemistry Programs, Universitas Pendidikan Indonesia, Jl. Dr. Setiabudhi No. 229, Bandung, Indonesia; e-mail: lidiainfeb@gmail.com

Fitri Dara — Doctor of Chemistry, Senior Researcher, National Research and Innovation Agency (BRIN), Prof. Dr. Samaun Samadikun Science and Technology Area (KST), Jl. Sangkuriang, Bandung, Indonesia; e-mail: fitr002@brin.go.id; https://orcid.org/0000-0003-2678-4248

Galuh Yuliani — Doctor of Chemistry, Senior Lecturer, Chemistry Programs Universitas Pendidikan Indonesia, Jl. Dr. Setiabudhi No. 229, Bandung, Indonesia; e-mail: galuh@upi.edu; https://orcid.org/0000-0003-4291-6618

Author Contributions

The manuscript was written through contributions of all authors. All authors have given approval to the final version of the manuscript. CRediT: **Budiman Anwar** conceptualization, data curation, funding acquisition, resources, supervision, validation, writing-original draft, writing-review & editing; **Lidya Intan Febriani** investigation, formal analysis, visualization; **Fitri Dara** data curation, formal analysis, resources; **Galuh Yuliani** data curation, formal analysis, funding acquisition, writing-review & editing.

Acknowledgments

The authors would like to express their sincere appreciation to the Directorate of Research and Community Service Universitas Pendidikan Indonesia for the financial support.

Conflicts of Interest

The authors declare no conflict of interest.

References

1 Ma, C., Cui, W., Liu, X., Ding, Y., & Wang, Y. (2022). In situ preparation of gel polymer electrolyte for lithium batteries: Progress and perspectives. *InfoMat*, *4*(2), e12232. https://doi.org/10.1002/inf2.12232

2 Song, Y., Su, M., Xiang, H., Kang, J., Yu, W., Peng, Z., Wang H., Cheng B., Deng, N., & Kang, W. (2025). PEO-based solid-state polymer electrolytes for wide-temperature solid-state lithium metal batteries. *Nano-Micro Small*, *21*(3), 2408045. https://doi.org/10.1002/smll.202408045

3 Khan, K.H., Haleem, A., Arwish, S., Shah, A., & Hussain, H. (2025) PVDF-based solid polymer electrolytes for lithium-ion batteries: strategies in composites, blends, dielectric engineering, and machine learning approaches. *RSC Advanced*, *15*, 20629-20656. https://doi.org/10.1039/d5ra02951a

4 Chen, T., Zhao, F., Wang, L., Ma, S., Shi, G., Liu, Q., Liu, Y., & Han, G. (2025). High-performance PMMA based solvent-free solid transparent polymer electrolyte modified by succinonitrile for electrochromic devices. *Solar Energy Materials and Solar Cells*, *285*, 113538. https://doi.org/10.1016/j.solmat.2025.113538

5 Dennis, J.O., Shukur, M.F., Aldaghri, O.A., Ibnaouf, K.H., Adam, A.A., Usman, F., Hassan, Y.M., Alsadig, A., Danbature, W.L., & Abdulkadir, B.A. (2023). A Review of current trends on poly(vinyl alcohol) (PVA)-based solid polymer electrolytes. *Molecules*, *28*(4), 1781. https://doi.org/10.3390/molecules28041781

6 Kumar, L.S., Selvin, P.C., & Selvasekarapandian, S. (2021). Impact of lithium triflate ($LiCF_3SO_3$) salt on tamarind seed polysaccharide-based natural solid polymer electrolyte for application in electrochemical device. *Polymer Bulletin*, *78*, 1797–1819. https://doi.org/10.1007/s00289-020-03185-5

7 Rani, M.S., Rudhziah, S., Ahmad, A., & Mohamed, N.S. (2014). Biopolymer electrolyte based on derivatives of cellulose from kenaf bast fiber. *Polymers 6*(9), 23712385. https://doi.org/10.3390/polym6092371

8 Adlin, H.P., Ajith, K., Infanta, D.M., Lakshmi, D., & Christopher, S.P. (2022). Chitosan-based biopolymer electrolyte reinforced with V_2O_5 filler for magnesium batteries: an inclusive investigation. *Journal of Materials Science: Materials in Electronics 33*(7), 3925–3937. https://doi.org/10.1007/s10854-021-07587-7

9 Nešić, A., Ružić, J., Gordić, M., Ostojić, S., Micić, D., & Onjia, A. (2017). Pectin-polyvinylpyrrolidone films: A sustainable approach to the development of biobased packaging materials. *Composites Part B: Engineering 110*, 56-61. https://doi.org/10.1016/j.compositesb.2016.11.016

10 Ilyas, R.A., Sapuan, S.M., Sanyang, M.L., Ishak, M.R., & Zainudin, E.S. (2018). Nanocrystalline cellulose as reinforcement for polymeric matrix nanocomposites and its potential applications: A review. *Current Analytical Chemistry*, *14*(3), 203–225. https://doi.org/10.2174/1573411013666171003155624

11 Xu, X., Liu, F., Jiang, L., Zhu, J.Y., Haagenson, D., & Wiesenborn, D.P. (2013). Cellulose nanocrystals vs. cellulose nanofibrils: A comparative study on their microstructures and effects as polymer reinforcing agents. *ACS Applied Materials & Interfaces*, *5*(8), 2999–3009. https://doi.org/10.1021/am302624t

12 Anwar, B., Bundjali, B., & Arcana, I.M. (2015). Isolation of cellulose nanocrystals from bacterial cellulose produced from pineapple peel waste juice as culture medium. *Procedia Chemistry*, *16*, 279–284. https://doi.org/10.1016/j.proche.2015.12.051

13 Anwar, B., Bundjali, B., Sunarya, Y., & Arcana, I.M. (2021). Properties of bacterial cellulose and its nanocrystalline obtained from pineapple peel waste juice. *Fibers and Polymers, 22*, 1228–1236. https://doi.org/10.1007/s12221-021-0765-8

14 Segal, L., Creely, J.J., Martin, Jr. A.E., & Conrad, C.M. (1959). An empirical method for estimating the degree of crystallinity of native cellulose using the X-ray diffractometer. *Textile Research Journal*, *29*, 786–794. https://doi.org/10.1177/004051755902901003

15 Nelson, M.L. & O'Connor, R.T. (1964). Relation of certain infrared bands to cellulose crystallinity and crystal lattice type. Part II. A new infrared ratio for estimation of crystallinity in celluloses I and II. *Journal of Applied Polymer Science*, *8*(3), 1325–1341. https://doi.org/10.1002/app.1964.070080323

16 Thakur, M., Sharma, A., Ahlawat, V., Bhattacharya, M., & Goswami, S. (2020). Process optimization for the production of cellulose nanocrystals from rice straw derived α-cellulose. *Materials Science for Energy Technologies*, *3*, 328–34. https://doi.org/10.1016/j.mset.2019.12.005

17 Newman, R.H. (1999). Estimation of the lateral dimensions of cellulose crystallites using ^{13}C NMR signal strengths. *Solid State Nuclear Magnetic Resonance, 15*(1), 21–29. https://doi.org/10.1016/S0926-2040(99)00043-0

18 French, A.D. & Cintron, M.S. (2013). Cellulose polymorphy, crystallite size, and the Segal Crystallinity Index. *Cellulose, 20*, 583–588. https://doi.org/10.1007/s10570-012-9833-y

19 Lewandowska, K. & Szulc, M. (2021). Characterisation of hyaluronic acid blends modified by poly(*N*-vinylpyrrolidone). *Molecules, 26*(17), 5233 https://doi.org/10.3390/molecules26175233

20 Hazrati, K.Z., Sapuan, S.M., Zuhri, M.Y.M., & Jumaidin, R. (2021). Effect of plasticizers on physical, thermal, and tensile properties of thermoplastic films based on *Dioscorea hispida* starch. *International Journal of Biological Macromolecules*, *185*, 219–228. https://doi.org/10.1016/j.ijbiomac.2021.06.099

21 Sanyang, M.L., Sapuan, S.M., Jawaid, M., Ishak, M.R., & Sahari, J. (2015). Effect of plasticizer type and concentration on tensile, thermal and barrier properties of biodegradable films based on sugar palm (*Arenga pinnata*) starch. *Polymers, 7*(6), 1106–1124; https://doi.org/10.3390/polym7061106

22 Garavito, J., Castellanos-González, S., Peña-Venegas, C.P., & Castellanos, D.A. (2026). Development and characterization of reinforced flexible packaging based on amazonian cassava starch through flat sheet extrusion. *Polymer*, *18*(6), 675, 1–24. https://doi.org/10.3390/polym18060675

23 Shi, S., Wang, Y., Zhang, Y. et al. (2023). Plasticizer role of cellulose nanocrystals in the biodegradable polymer blend with ductile polymer as continuous phase. *Cellulose, 30*, 10139–10156. https://doi.org/10.1007/s10570-023-05501-4

24 Ding, C., Zhang, M., & Li, G. (2015). Preparation and characterization of collagen/hydroxypropyl methylcellulose (HPMC) blend film. *Carbohydrate Polymers*, *119*, 194. http://dx.doi.org/10.1016/j.carbpol.2014.11.057

25 Voronova, M., Rubleva, N., Kochkina, N., Afineevskii, A., Zakharov, A., & Surov, O. (2018). Preparation and characterization of polyvinylpyrrolidone/cellulose nanocrystals composites. *Nanomaterials, 8*(12), 1011. https://doi.org/10.3390/nano8121011

26 Yu, Y., Tyrikos-Ergas, T., Zhu, Y., et al. (2019). Systematic hydrogen-bond manipulations to establish polysaccharide structure–property correlations. *Angewandte Chemie, 58*(37), 13127–13132. https://doi.org/10.1002/anie.201906577

27 Kawai, K., Sogabe, T., Nakagawa, H., Yamada, T., & Koseki, S. (2024). Effect of water activity on the mechanical glass transition and dynamical transition of bacteria-solute systems. *Journal of Food Engineering 375*, 112066. https://doi.org/10.1016/j.jfoodeng.2024.112066

28 Anwar, B., Nurhashiva, C., Arwa, R., & Yuliani, G. (2023). Physicochemical properties of bioplastic based on hydroxyethylcellulose and polyvinylpyrrolidone blend. *Journal of the Serbian Chemical Society*, *89*, 215–30. https://doi.org/10.2298/jsc231023103a

29 Sydykov, B., Oldenhof, H., Sieme, H., & Wolkers, W.F. (2017). Hydrogen bonding interactions and enthalpy relaxation in sugar/protein glasses. *Journal of Pharmaceutical Sciences, 106*(3), 761–769. https://doi.org/10.1016/j.xphs.2016.11.003

How to Cite: Alibrahimi, A.A., & Abdul-Hassan, W.S. (2026). Design and Synthesis of Novel Molecular Switches Functionalized with a Viologen Unit Based on Copper(II) Bis(ethyl 4-chloroacetoacetate) Complex. *Eurasian Journal of Chemistry*, *31*, *2(122)*, *16–40.* https://doi.org/10.31489/2959-0663/2-26-1

Article

Received: 3 November 2025 | Revised: 20 April 2026 | Accepted: 12 May 2026 | Published online: 22 May 2026

UDC 544.42+519.242.7

https://doi.org/10.31489/2959-0663/2-26-1

Ahmed A. Alibrahimi*, Wathiq S. Abdul-Hassan

Department of Chemistry, College of Science, University of Thi-Qar, Nassiria, Iraq
*(*Corresponding author's e-mail: ahmedoudah501@gmail.com)*

Design and Synthesis of Novel Molecular Switches Functionalized with a Viologen Unit Based on Copper(II) Bis(ethyl 4-chloroacetoacetate) Complex

Viologen-based molecular switches have attracted significant attention due to their reversible redox properties and promising applications in electronic and sensing devices. This study focuses on the design and development of novel chemically and electrochemically responsive molecular switches constructed through non-covalent π–dimerization of viologen radicals within copper(II) β-diketone complexes in solution. Initially, the bidentate O_2 donor ligand ethyl 4-chloroacetoacetate were coordinated to copper(II) to afford the base complexes CuECl, respectively. Subsequent axial coordination of CuECl with the neutral ligand 4,4′-bipyridine (bpy) led to the corresponding functionalized viologen system: $CuEV^{+}\cdot Cl^{-}$. Moreover, S_N2 nucleophilic substitution reactions of CuECl with bpy, afforded the additional complex $CuEV^{+}\cdot Cl^{-}$. A total of eleven complexes were successfully synthesized and comprehensively characterized using FT-IR, LC-mass spectrometry, TGA, DTA, DSC, XRD, EDS, and UV–visible absorption spectroscopy, along with electrochemical and reduction studies. Finally, chemical and electrochemical reduction of the viologen unit in, $CuEV^{+}\cdot Cl^{-}$ produced intra and intermolecular π-dimers of the resulting viologen radicals. Additionally, interactions of CuECl with bpy was examined in DMF solution, and the absorption spectra of these mixtures were compared with those of the corresponding adduct complexes.

Keywords: molecular switches, viologen, dimerization, copper(II) complexes, 4,4′-bipyridine, ethyl 4-chloroacetoacetate, β-diketone, bidentate ligand

Introduction

The magnetic behavior of π-radical systems is inherently governed by their aggregation state. In the paramagnetic regime, these radicals predominantly exist as discrete π-mers bearing unpaired electrons, which results in a measurable magnetic moment. In contrast, strong intermolecular interactions promote π-dimerization, leading to complete spin pairing and consequently, the loss of paramagnetism. This reversible paramagnetic–diamagnetic transition, extensively documented in viologen and tetrathiafulvalene derivatives, is a hallmark of radical π-systems and constitutes a key topic in contemporary supramolecular and materials chemistry [1, 2].

Viologens are a family of organic salts derived from 4,4′-bipyridyl with the general formula $(C_5H_4NR)_2^{n+}$. They are best known for their intensely colored blue derivatives and their facile, reversible redox behavior. Upon one-electron reduction, viologens are converted into highly colored radical monocations, typically exhibiting violet hues, and can undergo multiple reversible color changes upon successive reduction and oxidation cycles. The term "viologen" was first introduced by Michaelis in 1933 after observing the emergence of a violet coloration resulting from the one-electron reduction of 1,1′-dimethyl or 4,4′-bipyridinium salt (DMV^{2+}), leading to the generation of a radical cation dimer [3, 4].

A molecular switch is defined as a molecule capable of reversibly interconverting between at least two (or more) stable states under the influence of external stimuli such as thermal, chemical, electrical, or optical inputs. In this context, viologen radical cations display intense coloration and high molar absorptivity, attributed to intramolecular charge transfer between the +1 and neutral nitrogen centers. In aqueous media, for instance, the blue methyl viologen radical cation can shift to a purple color at higher concentrations. Upon heating, the purple solutions revert to blue, and this color change is fully reversible. Such dimerization of viologen radicals in water is widely recognized [5–7].

The present study was designed with two primary objectives. First, to synthesize and characterize the copper(II) complex of (CuECl) and its corresponding bipyridine terminal to investigate the formation of the viologen-based complex $CuEV^{+}\cdot Cl^{-}$, obtained by combining CuECl with a propylene-spacer viologen (V^{+}).

Second, particular attention was given to monitoring the redox-induced π-dimerization of the $CuEV^{+}\cdot Cl^{-}$ complex by chemical and electrochemical reduction.

Experimental

Instruments

FT-IR spectra of the metal complexes were recorded on KBr pellets using a SHIMADZU FT-IR Affinity analytical apparatus (Japan) over the range 150–4000 cm^{-1}. UV–Visible absorption spectra were obtained in 1 cm quartz cuvettes using a PG Instruments T90+ spectrophotometer (UK) in the wavelength range of 200–900 nm. Thermal stability of the complexes was investigated by thermogravimetric analysis (TGA) using an SDT Q600 V20.9 thermal analyzer (TA Instruments, USA). Powder X-ray diffraction (XRD) patterns were collected on a PANalytical diffractometer (Netherlands) with Cu Kα radiation (λ ≈ 1.5406 Å). Molecular ions were analyzed using an Agilent 5973 Network LC–mass spectrometer (USA) operating in electron ionization (EI) mode at 70 eV. Electrochemical properties were examined by cyclic voltammetry (CV) using a PARSTAT 4000 electrochemical workstation (Princeton Applied Research, USA) under an argon atmosphere at room temperature.

Chemical Reagents

All chemical reagents and solvents were of analytical grade and used as received without further purification. The following compounds were purchased from Energy Chemical (China): ethyl 4-chloroacetoacetate (98 %); Hyper Chem (China): 4,4'-bipyridine (98 %) and Zn powder (99.9 %); Inter-chimiques (France): methyl iodide (99.9 %); Thomas Baker (India): copper(II) acetate monohydrate (99 %) and acetone (99 %); Alpha Chemika (India): methanol (99.7 %) and dichloromethane (99.8 %); Loba Chemie (Belgium): ethanol (99.8 %), acetonitrile (99.5 %), N,N-dimethylformamide (99.8 %), and hydrochloric acid (37 %); Scharlau (Spain): ethyl acetate (99.9 %); Romil (UK): benzene (99.7 %) and hexane (99 %); and Merck (Germany): dimethyl sulfoxide (DMSO, 99 %).

Methods of Synthesis

Synthesis of CuECl Complex

A solution of ethyl 4-chloroacetoacetate (2 mL, 14.8004 mmol, 2 eq) dissolved in MeOH (1 mL) was added dropwise over 10 min with stirring to a solution of copper(II) acetate monohydrate (1.344 g, 7.4 mmol, 1 eq) dissolved in a 1:1 methanol–water mixture (10 mL). The reaction mixture was stirred for 1 h, then heated at 60 °C for 2 h. The progress of the reaction was monitored by TLC (ethyl acetate : hexane, 7:3). The resulting precipitate was collected by filtration, washed with a 1:1 H_2O–MeOH mixture, and dried under vacuum to afford CuECl as a green solid (Scheme 1). Green solid, yield: 81 % (2.3 g), M.P.: 170–172 °C, soluble in H_2O, MeOH, EtOH, MeCN, acetone, DCM, C_6H_6, EtOAc, DMF and DMSO. FT-IR (KBr disc, cm^{-1}): 2983 (aliphatic C–H), 1600, 1530 (C=C coupled with C=O and C=N), 1414, 1360, 1310 (aromatic and olefinic C–H bending), 1360, 1310 (aliphatic C–H bending), 1181, 1138 (C–O), 791, 767 (C–C stretching), 668 (C–Cl bending), 577 (Cu–O).

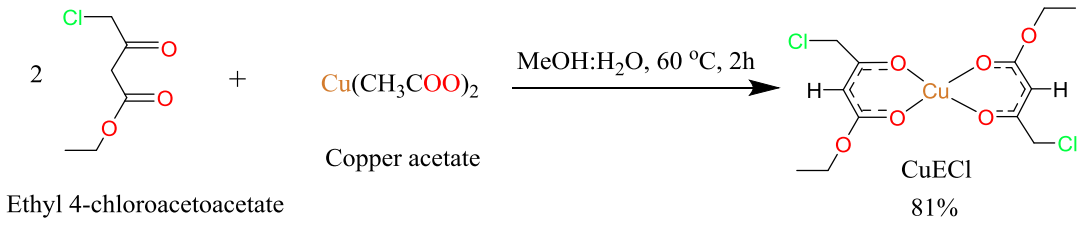

Scheme 1. Synthesis of bis(ethyl 4-chloroacetoacetate)copper(II)

Synthesis of $CuEV^{+}\cdot Cl^{-}$ Complex

A solution of bpy (0.5 g, 3.2012 mmol, 2 eq) dissolved in DMF (1 mL) was added gradually with stirring over 1 min to a hot solution of CuECl (0.6260 g, 1.600 mmol, 1 eq) dissolved in DMF (2.5 mL). The reaction mixture was heated at 60 °C for 80 min under an argon atmosphere. The progress of the reaction was monitored by TLC (MeCN : H_2O : saturated KNO_3, 10:1:1). The resulting precipitate was collected by filtration and dried under vacuum to afford $CuEV^{+}\cdot Cl^{-}$ as a grey solid (Scheme 2). Grey solid, yield: 69 %

(0.73 g), M.P.: 156–158 °C, sparingly soluble in H_2O, MeOH, EtOH, MeCN, DMF and DMSO. FT-IR (KBr disc, cm^{-1}): 3068, 3047 (aromatic C–H and C=C–H stretching), 2979, 2955, 2900 (aliphatic C–H), 1654, 1610, 1551 (C=C coupled with C=O and C=N), 1472, 1419 (aromatic and olefinic C–H bending), 1364 (aliphatic C–H bending), 1270, 1216 (C–N), 1175 (C–O), 759 (C–C stretching), 642 (C–Cl bending), 575 (Cu–O).

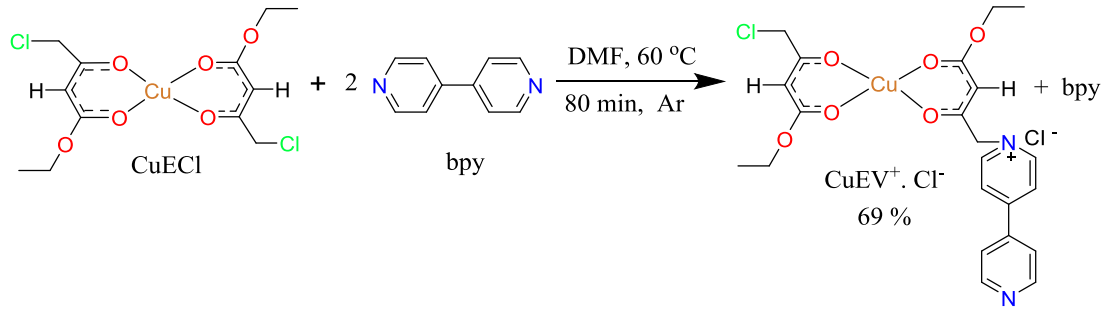

Scheme 2. Synthesis of $CuEV^{+}\cdot Cl^{-}$ complex

Results and Discussion

FTIR Spectra of Copper Complexes

FTIR spectra of the complexes CuECl and $CuEV^{+}\cdot Cl^{-}$ were recorded and are presented in Figures S1 and S2; the corresponding FT-IR spectral data are listed in Table 1.

Table 1

Important FT-IR data of Cu(II) complexes

CuECl	$CuEV^{+}\cdot Cl^{-}$	Assignment
–	3068, 3047	C–H of both stretch aromatic and C=C–H
2983	2979, 2955, 2900	Aliphatic C–H
1600, 1530	1610, 1654, 1551	C=C coupled with C=O and C=N
1414, 1360, 1310	1472, 1419	Aromatic and olefinic C–H bending
1360, 1310	1364	Aliphatic C–H bending
–	1270, 1216	C–N
1181, 1138	1175	C–O
791, 767	759	Stretching C–C
668	642	Bending C–Cl
577	575	Cu–O

Aromatic and olefinic C–H stretching vibrations are observed in the 3100–3000 cm^{-1} region. Specifically, the FT-IR spectrum of CuECl exhibits a band at 3098 cm^{-1}, while the terminally bound species $CuEV^{+}\cdot Cl^{-}$ shows a characteristic peak at 3068 cm^{-1}. These features are diagnostic of the retention of the aromatic and olefinic C–H environments upon coordination [8].

Aliphatic C–H stretching is observed in <3000 cm^{-1} region. Bands at 2983 cm^{-1} for CuECl correspond to ν(C–H) of aliphatic methylene groups. Terminal species give bands at 2979, 2955 and 2900 cm^{-1} ($CuEV^{+}\cdot Cl^{-}$), these confirm the presence of alkyl substituents on the viologen or bipyridine units [9].

C=O and C=C stretching of the β-diketonate core is observed in the 1710 and 1500 cm^{-1} regions. The base complexes show characteristic β-diketonate bands at 1600 and 1530 cm^{-1} (CuECl). Terminally bound species show 1654, 1610 and 1551 cm^{-1} ($CuEV^{+}\cdot Cl^{-}$). These absorptions are attributed to the overlapping ν(C=O) and ν(C=C) stretches of the β-diketone backbone conjugated with coordinated nitrogen donors [10].

Aromatic and olefinic C–H bending is observed in the 1500–1300 cm^{-1} region. Bends at 1414 cm^{-1} (CuECl), terminal species exhibit 1472–1419 cm^{-1} ($CuEV^{+}\cdot Cl^{-}$). These bands confirm the retention of the aromatic character in the coordinated ligands [11].

New bands observed at 1270 and 1216 cm^{-1} for $CuEV^{+}\cdot Cl^{-}$, which are absent in the precursor and CuECl spectra, are assigned to C–N stretching vibrations. The emergence of these bands confirms the for-

mation of a new complex characterized by the expected adduct structure and terminal linkage [10]. Bending vibrations were observed at 1181, 1138 cm^{-1} for CuECl, while the terminal linkage compounds with viologen appear bands at 1175, 1090 and 1050 cm^{-1} for $CuEV^{+}\cdot Cl^{-}$, these bands are assigned to vibrational modes involving bending coupled with stretching within the C–O group [10].

The bands observed at approximately 650 and 430 cm^{-1} are assigned to C–Cl stretching and metal–ligand vibrations, respectively. Characteristic bands were identified at 668 cm^{-1} (CuECl), 642 cm^{-1} ($CuEV^{+}\cdot Cl^{-}$), 674 and 656 cm^{-1} ($CuEC_1V_2^{2+}\cdot Cl^{-}\cdot I^{-}$). Lower-frequency peaks at 577 cm^{-1} (CuECl) is assigned to ν(Cu–O). These confirm direct coordination of both β-diketonate oxygen and bipyridine/viologen nitrogen donors to the copper(II) center [8, 9].

LC-Mass Spectrometry of Cu(II) Complexes

The LC-mass spectra of CuECl and $CuEV^{+}\cdot Cl^{-}$ are depicted in Figures S3 and S4. The LC-mass spectrum of CuECl complex exhibited a molecular ion peak at *m/z* = 391.1. Other important peaks occurred at *m/z* = 617.83 due to the dimer losing one ligand unit [2M-L]. Isotope peaks of the molecular ions due to ^{37}Cl, $[2M\text{-}L^{+}]$ and $[M^{+}Cu^{+1}]^{+}$ confirm the presence of chlorine atoms. Other importent peaks are shown in the suggested mechanism at *m/z* = 291.1, 263.1, 217, 181.91, 148.9, 115.15, 90.9 and 69 due to $[M^{\bullet+}\text{-}C_{11}H_{16}CuO_5^{+}]$, $[C_9H_{12}CuO_5^{+}]$, $[M^{\bullet+}\text{-}C_8H_{10}CuO_3^{+}]$, $[M^{\bullet+}\text{-}C_4H_4ClCuO_2^{+}]$, $[M^{\bullet+}\text{-}C_4H_5CuO_2^{+}]$, $[M^{\bullet+}\text{-}C_6H_{11}O_2^{+}]$, $[M^{\bullet+}\text{-}C_4H_7Cl^{+}]$ and $[M^{\bullet+}\text{-}C_4H_5O^{+}]$ respectively. The intensive peak (base peak) at *m/z* = 617.83, 682.49 and 709.26 are attributed $[C_{18}H_{24}Cl_3Cu_2O_9^{+}]$, $[C_{23}H_{32}Cl_2Cu_2O_{11}^{+}]$ and $[C_{19}H_{20}Cl_4Cu_2O_{12}^{+}]$ respectively [12–14].

The LC-mass spectrum of $CuEV^{+}\cdot Cl^{-}$ is depicted in Figure S4. The LC-mass spectrum of $CuEV^{+}\cdot Cl^{-}$ complex showed a peak at *m/z* = 665.38 corresponds to molecular ion $[M]^{+}$. The peak at *m/z* = 1019.84 is attributed to loss of 2 chlorine atoms and 3H from the dimer of the molecular ion $[2M\text{-}2Cl\text{-}3H]^{+}$. The peak of *m/z* = 156.95 confirm the removal of the bpy from the $CuEV^{+}\cdot Cl^{-}$ complex. Other important peaks are note at *m/z* = 464.3, 352, 311.15, 283.15, 270.20, 197.95, 270.20, 311.15, 318, 393,407.97, 462.96, 476.99, 556.53, 561, 726.16, 806.83 and 902.59 [12–14].

X-Ray Diffraction of Copper Complexes

The Powder X-ray diffraction (XRD) patterns of the Cu(II) complexes are presented in Figures S5 and S6, with the corresponding diffraction data summarized in Tables 2 and 3. The average crystallite sizes were calculated using the Scherrer-Debye equation (Eq. 1), based on the full width at half maximum (FWHM) of the high-intensity diffraction peaks:

$$D = \frac{K\lambda}{\beta}\cdot\frac{1}{\cos\theta}, \quad (1)$$

where *D* is the average crystal size, K is the Scheerer's constant (the shape factor with a typical value of 0.94), λ is the wavelength of the X-ray source (0.15405 nm, 1.5405 Å for Cu Kα radiation), β is the full width at the half maximum (FWHM) of the diffraction peak in radians, θ is the Bragg diffraction angle [15–17].

The calculation of avenge crystallite size using the Scherrer model involves calculating the crystallite sizes (*D*) for individual peaks and then computing their mean values. Table 2 contain the mean crystallite dimensions calculated using the Scherrer equation [18].

Table 2

Average crystallite size (*D*) values of the synthesized complexes calculated using the Scherrer equation

Average crystal size, nm	
CuECl	$CuEV^{+}\cdot Cl^{-}$
34.29781605	21.89748354

Although the Scherrer equation provides a straightforward method by considering solely the contribution of physical broadening and neglecting instrumental effects, the Williamson–Hall model overcomes this limitation by simultaneously incorporating both crystallite size and lattice strain contributions. Thus, this model provides a more comprehensive analysis of peak broadening [19]:

$$\beta = \beta_1 + \beta_2, \quad (2)$$

where β is the total broadening, β_1 is the broadening due to the full width at half maximum FWHM of crystallite size (Scherrer equation), β_2 is the broadening due to strain.

$$\varepsilon = \frac{\beta}{4\tan\theta} = \frac{\beta_2 \cos\theta}{4\sin\theta}. \quad (3)$$

Substituting equations 2 and 3, yields equation 4:

$$\beta = \beta_1 + \beta_2 = \frac{K\lambda}{D\cos\theta} + 4\varepsilon\frac{\sin\theta}{\cos\theta}. \quad (4)$$

After arranging the Equation 4, yields equation 5:

$$\beta\cos\theta = K\lambda/D + 4\varepsilon\sin\theta. \quad (5)$$

According to Equation (5), a plot of β cos θ (Y-axis) versus 4 sin θ (X-axis) yields a linear relationship. In this plot, the slope corresponds to the micro strain (ε), while the intercept represents Kλ/*D*, where K is the shape factor, λ is the X-ray wavelength, and *D* is the crystallite size [20, 21].

The resulting linear plots are illustrated in Figures 1 and 2.

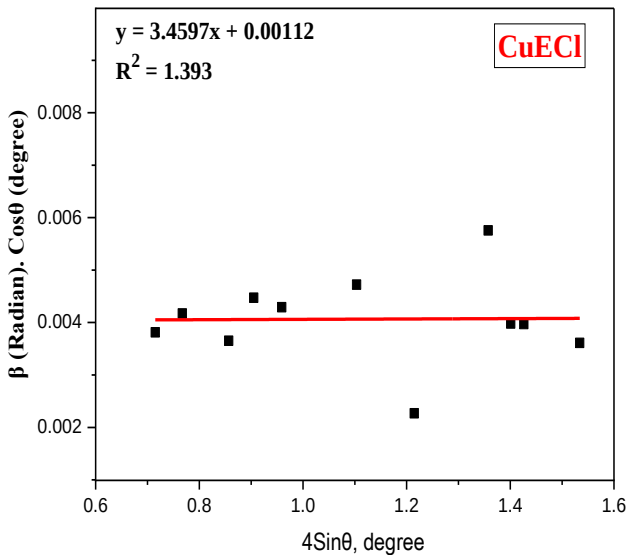

Figure 1. UDM plot of CuECl complex

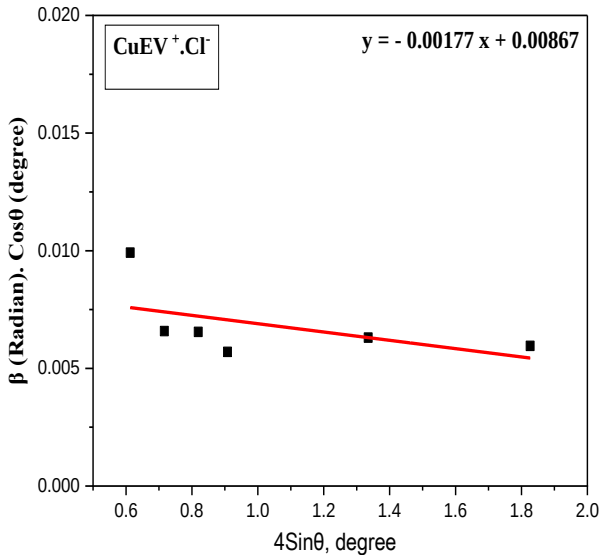

Figure 2 UDM plot of $CuEV^{+}\cdot Cl^{-}$ complex

The variations in the number and intensity of diffraction peaks, as well as the calculated crystallite sizes (*D*), provide clear evidence for the successful formation of CuECl and $CuEV^{+}\cdot Cl^{-}$ from their respective precursors. These observations also confirm the synthesis of additional copper complexes derived from CuECl. The X-ray diffraction patterns were recorded over the 10°–80° 2θ range, with the most prominent reflections appearing at 24.741° and 24.791° for CuECl, and at 23.543° for $CuEV^{+}\cdot Cl^{-}$. It is noted the complex incorporating viologen-functionalized ligand: $CuEV^{+}\cdot Cl^{-}$ keep middle crystallinity among the last three complexes and the other rest complexes .The complex CuECl showed the highest *d*-spacing.

Table 3 presents the average crystallite sizes (D) of the synthesized complexes, calculated using the Williamson–Hall module. In fact, dramatic differences are noted in both *d*-spacing and lattice strain values. As mentioned before, Scherrer model estimates *d*-spacing considering only crystallite size. But, Williamson–Hall model considers both size and lattice strain. In other words, the Scherrer model considers peak broadening that is due to crystallite size only. This model assumes the material is strain free and gives crystallite size but not strain or d-spacing changes due to strain. While, Williamson–Hall method separates peak broadening into two sources: crystallite size and lattice strain (Ɛ). Now, let us consider *d*-spacing values obtained from both models.

Firstly, the complex CuECl and showed *d*-spacing values obtained from W–H model higher than those obtained from Scherrer model. This trend indicates positive lattice strain which stretches the lattice planes of these complexes. There is distortion for the lattice and this induces tensile strain. This tensile strain causes

peak shifting to lower angles which results in increased *d*-spacing (via Bragg's law = $n\lambda = 2d \sin\theta$). Here, because W-H model account for this referred strain which shows expanded lattice planes (higher *d*). While, Scherrer und estimates the spacing since it ignores strain then lower *d*-spacing are obtained by Scherrer model [18, 19].

Table 3

Average crystallite size (*D*) values of the synthesized complexes calculated using the Williamson–Hall model

CuECl		$CuEV^{+}\cdot Cl^{-}$	
Slope = strain, ε	Crystal size *D* = Kλ/Intercept	Slope = strain, ε	Crystal size *D* = Kλ/Intercept
3.4597	58.8906774	–0.00177	16.70207612

Secondly, the complexes and $CuEV^{+}\cdot Cl^{-}$ showed W-H *d*-spacing values lower than those obtained by Scherrer model. This trend indicates that these complexes have compressive strain. This compressive strain squeezes the lattice of these complexes and reduces *d*-spacing where the peak shift to higher 2θ angles. W-H model includes this contraction in its calculation, hence lower d-spacing is noted than Scherrer *d*-spacing.

The variation in *d*-spacing between W-H and Scherrer across the prepared copper complexes reflects differences in internal strain which depend on: Ligand type (ECl, bpy, or ECl functionalized by the last three ligands). Also, this strain depends on crystal packing, symmetry, solvent inclusion or loss, defects, dislocations or coordination geometry. The expanded lattice due to tensile strain in the complex CuECl (observation of *d* (W-H) > *d* (Scherrer)) compared to the lattice contracted due to compressive strain (observation of *d* (W-H) < *d* (Sherrer)) is attributed to the presence of chloride substitution in CuECl. The chloride atom induce disorder or packing issues which increases the strain. The two Cl groups introduce larger atomic radii and distortions, causing expansion [20, 21].

The $CuEV^{+}\cdot Cl^{-}$ complex (compared to its precursor (CuECl) has compressive strain as it is clear from its negative lattice strain and W-H. *d*-spacing < Sherrer *d*-spacing. The reason of this opposite trend compared to its precursor might be the absence of Cl group which enhances the electrostatic interactions thus reducing *d*-spacing value [20, 21].

The above discussion of XRD patterns, both W-H *d*-spacing and Scheller *d*-spacing values and lattice strain values confirms the formation and the structures of the complexe CuECl. Also, it supports undoubtedly the axial coordination of the bpy and positive ligands and formation the adduct complexes. Additionally, the complexes having their ligands functionalized by viologen showed structural differences compared with either its precursor CuECl or the other adduct complexes.

Thermogravimetric Analyses of Copper Complexes

The thermal behavior of complexes CuECl and $CuEV^{+}\cdot Cl^{-}$ was investigated by thermogravimetric analysis (TGA), differential thermal analysis (DTA), and differential scanning calorimetry (DSC) up to 800 °C. The measurements were conducted at a heating rate of 10 °C/min under an argon atmosphere [22]. The TGA, DTA, and DSC curves are shown in Figures 3–7.

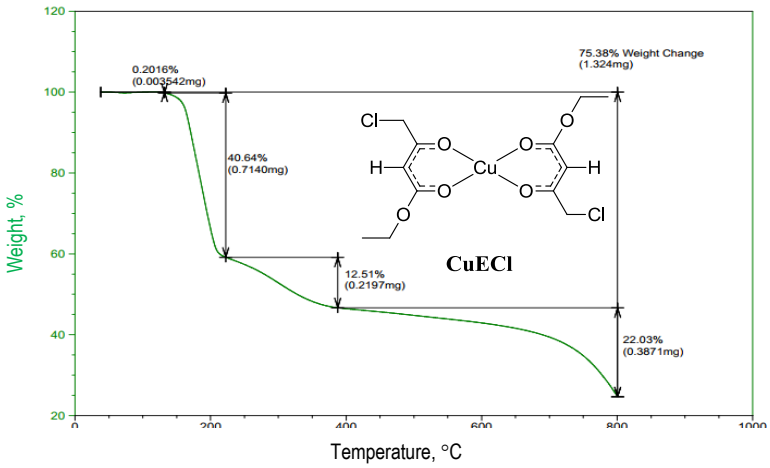

Figure 3. TGA curve of CuECl complex

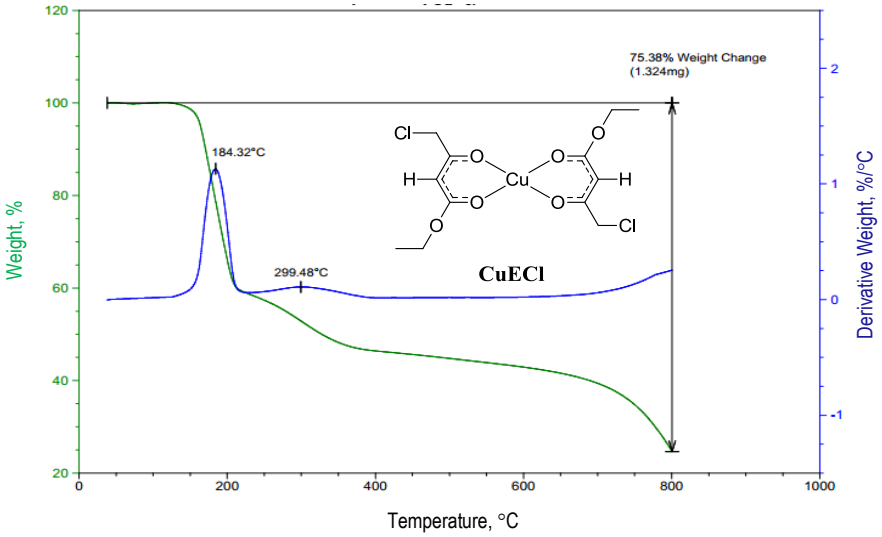

Figure 4. TGA/DTG curve of CuECl complex

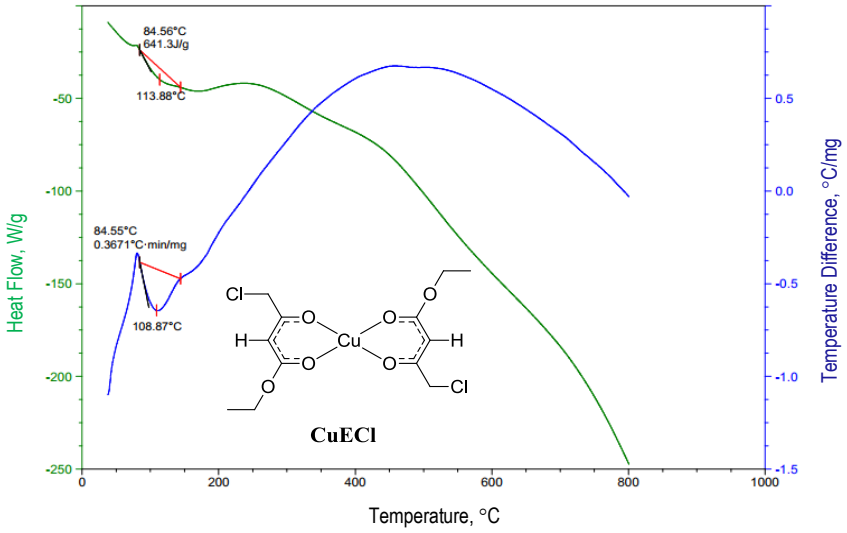

Figure 5. DSC / TGA curves of CuECl complex

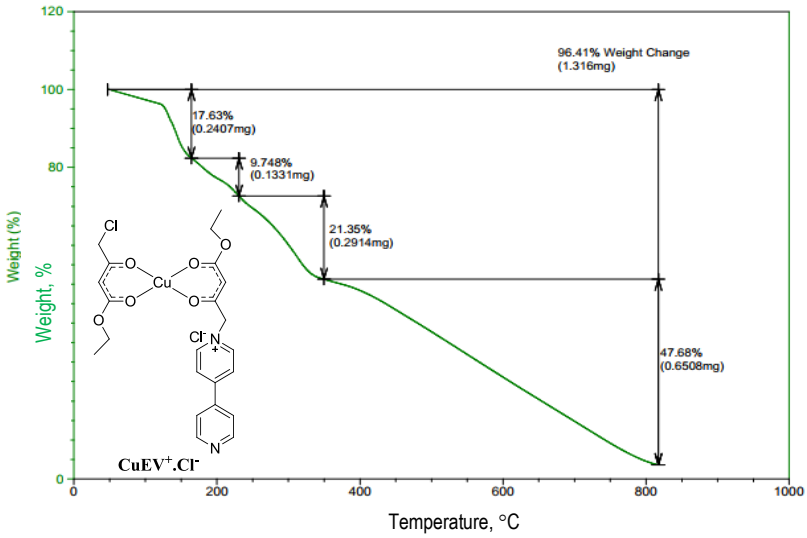

Figure 6. TGA curve of $CuEV^{+}{\cdot}Cl^{-}$ complex

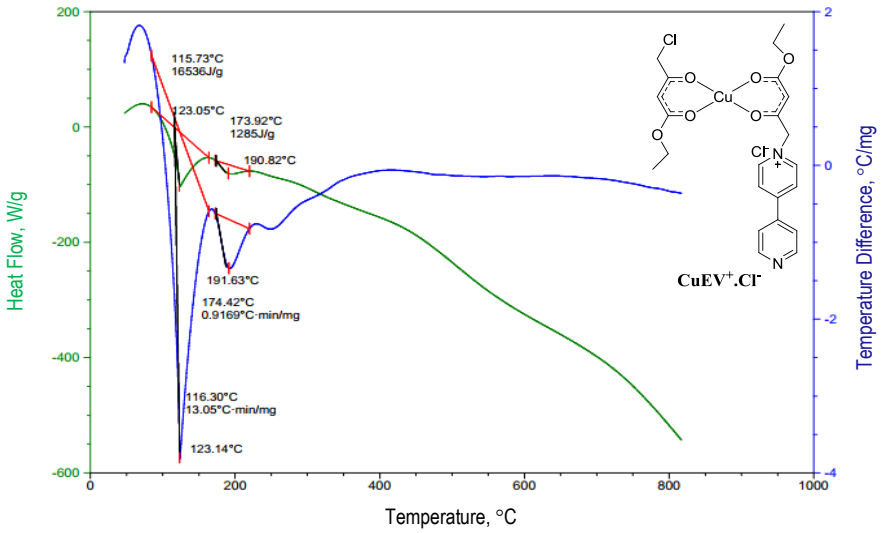

Figure 7. DSC / TGA curve of $CuEV^{+}\cdot Cl^{-}$ complex

The thermal decomposition patterns occur in four steps (for CuECl, and $CuEV^{+}\cdot Cl^{-}$). The kinetic (K_1, $t_{1/2}$ and E_a) and thermodynamic parameters (ΔH, ΔS and ΔG) of each decomposition phase are calculated for copper complexes as explained in the next item [23–26].

Calculation of Kinetic and Thermodynamic Functions of Decomposition Reaction

All thermal decomposition stages were assumed to follow first-order kinetics for the calculation of kinetic parameters. The rate constant for each decomposition stage was determined using the first-order kinetic equation:

$$\frac{dx}{dt} = k_1 \cdot (1-x), \tag{6}$$

where

$$x = \frac{w_i - w_t}{w_i - w_f}, \tag{7}$$

w_i is the initial weight of each TG phase, w_t is a weight of sample at particular time during TG phase, w_f is the final weight at the end of TG phase, t is the time.

Equation 8 can be written as:

$$\ln(1-x) = -k_1 t. \tag{8}$$

Plotting of ln(1–x) (as y-axis) against time (min) (as x-axis) give liner relationship which confirm that TG phase are first order reaction. Slope of each line gives the value of the first order rate constant (k) for particular phase, see Figures 8 and 9. Half-life time ($t_{1/2}$) is determined using Equation 9:

$$t_{1/2} = \frac{0.693}{K_1}. \tag{9}$$

Values of k and $t_{1/2}$ are given in Tables 4 and 5 [27].

Table 4

Kinetic and thermodynamic parameters for the thermal decomposition stages of CuECl

Phase	Temperature, K	K, min^{-1}	$t_{1/2}$, min	E_a, J/mole	ΔH, J/mole	ΔS, J/mole·K	ΔG, J/mole
1	437.77	0.0047	147.44	222226.5	218586.8	–97666.74	120920
2	497.79	0.25198	2.75	94205.43	90066.65	–45141.9	135208.5
3	700.46	0.05468	12.67	7799.395	1975.56	–209924	211899.8
4	1073.74	0.02884	24.029	4800.012	4127.38	–342892	338764.4

Table 5

Kinetic and thermodynamic parameters for the thermal decomposition stages of $CuEV^{+}\cdot Cl^{-}$

Phase	Temperature, K	K, min^{-1}	$t_{1/2}$, min	E_a, J/mole	ΔH, J/mole	ΔS, J/mole. K	ΔG, J/mole
1	440.07	0.0771	8.988	29876.19	26217.34	–105925	132142.37
2	507.27	0.0355	19.52	13102.26	8884.694	–144096	152980.73
3	628.08	0.0685	10.12	17715.61	12493.6	–174537	187030.31
4	1090.32	0.0848	8.17	22618.72	13553.5	–310750	324303.28

The kinetic parameters were evaluated by applying a modified version of the Coats–Redfern method, as expressed in Equation (10):

$$\ln\left[-\ln(1-x)\right] = \ln\frac{ART^2}{\beta E_a} - \frac{E_a}{RT}, \tag{10}$$

where A is the pre-exponential factor, β is the heating rate (20 °C min^{-1}), R is the universal gas constant (8.3143 J mol^{-1} K^{-1}), E_a is the activation energy, T is the absolute temperature expressed in Kelvin.

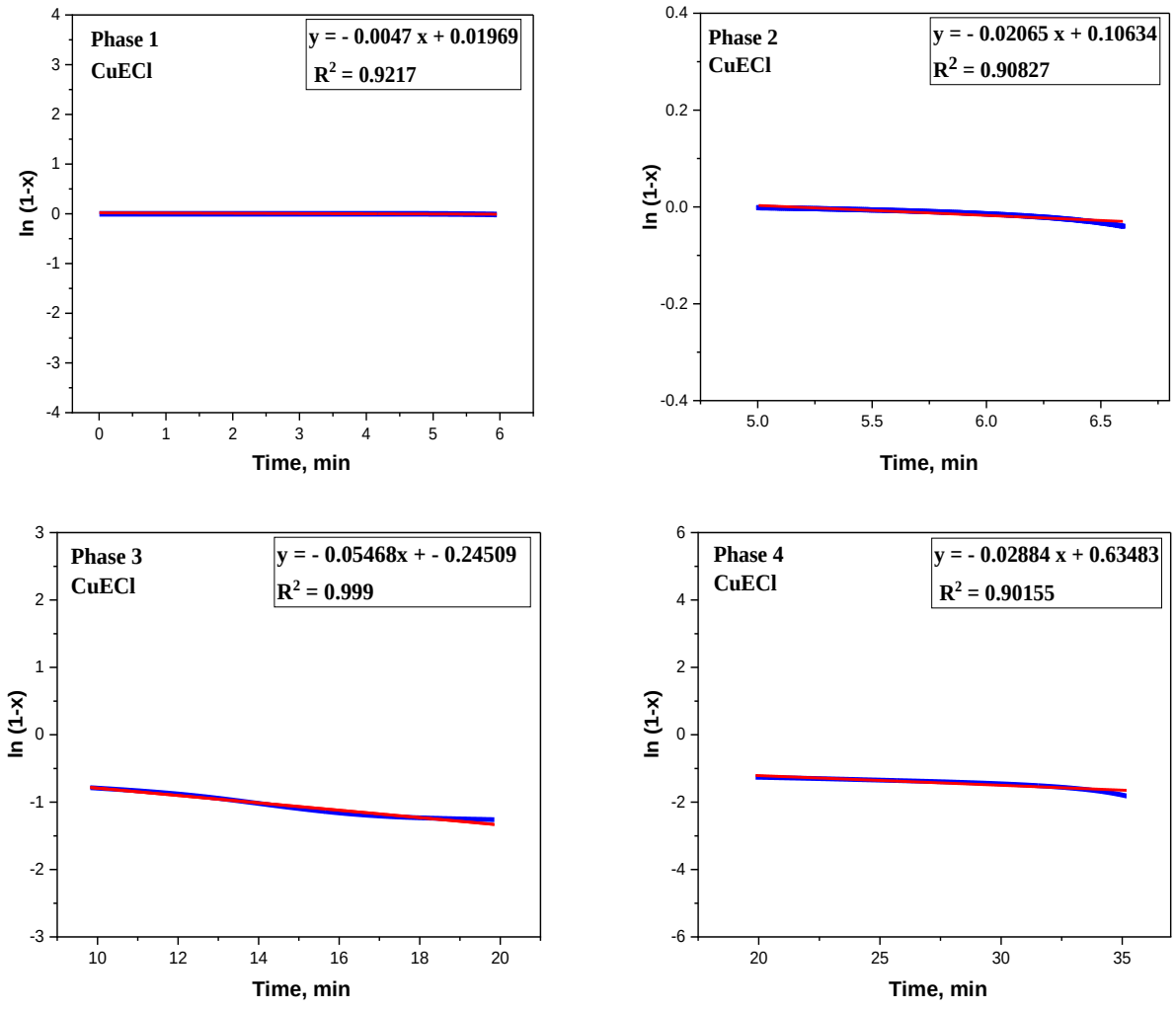

Figure 8. Plots of ln(1–x) versus time for the four decomposition stages of the CuECl complex

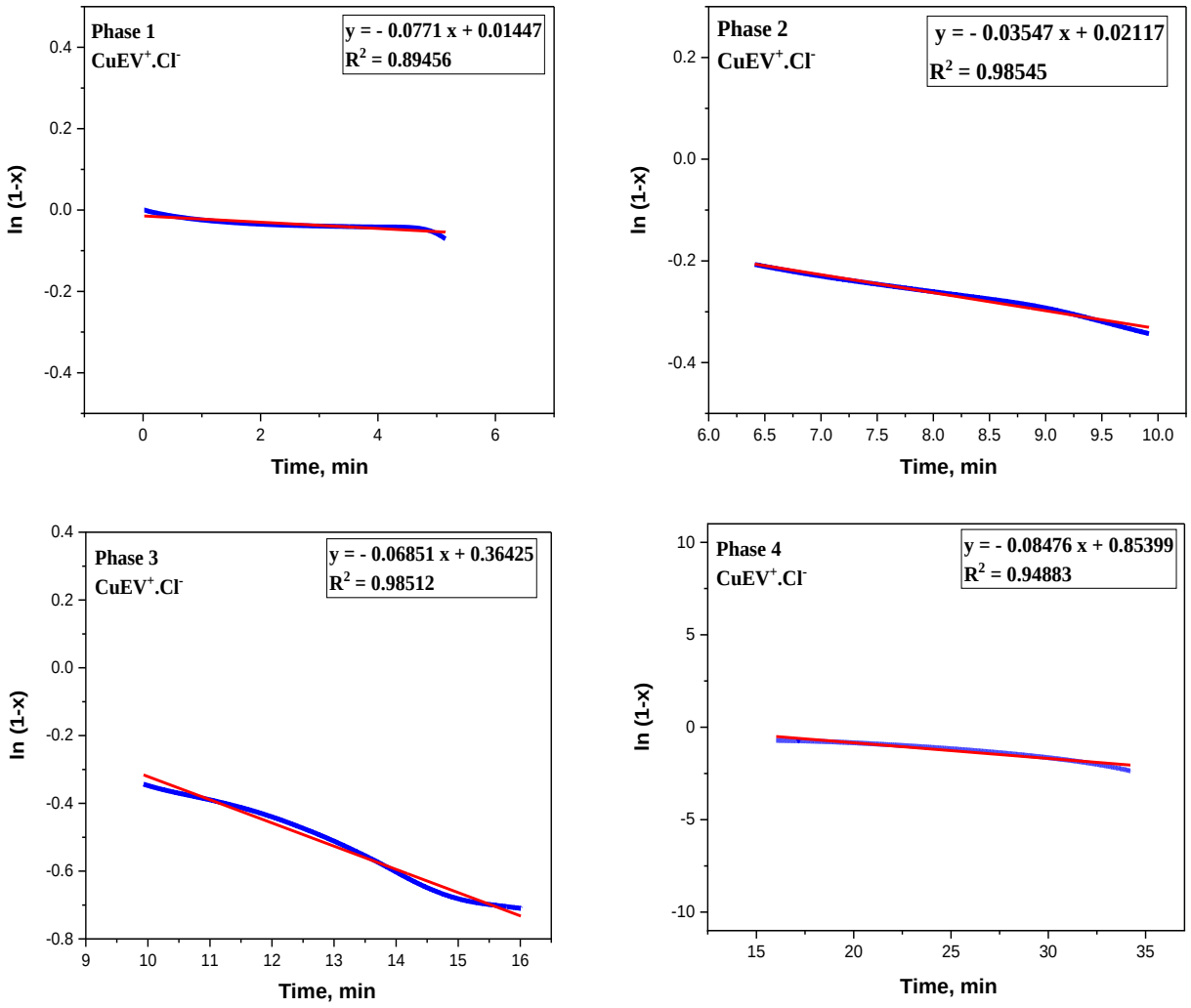

Figure 9. Plots of ln(1–*x*) versus time for the four decomposition stages of the $CuEV^{+}\cdot Cl^{-}$ complex

By plotting ln[–ln(1–*x*)] as *y*-axis versus 1000/*T* as *x*-axis for each phase Figures 10 and 11, linear relationship was obtained. The activation energy (E_a) and the pre-exponential factor (A) were calculated from the slope and intercept of the linear plots, respectively, according to the following equations [27]:

$$E_a = |\text{slope}| * R$$

$$A = \beta \cdot E_a \cdot \exp\frac{\text{intercept}}{RT^2}.$$

The thermodynamic parameters, including enthalpy (ΔH^*), entropy (ΔS^*), and Gibbs free energy (ΔG^*), were calculated using the following equations:

$$\Delta H^* = E_a - RT;$$

$$\Delta S^* = R\ln\left(\frac{Ah}{KT}\right);$$

$$\Delta G^* = \Delta H - T\Delta S,$$

where K is the Boltzmann constant.

The calculated values for E_a, ΔS^*, ΔH^* and ΔG^* are summarized in Tables 4-5 [27].

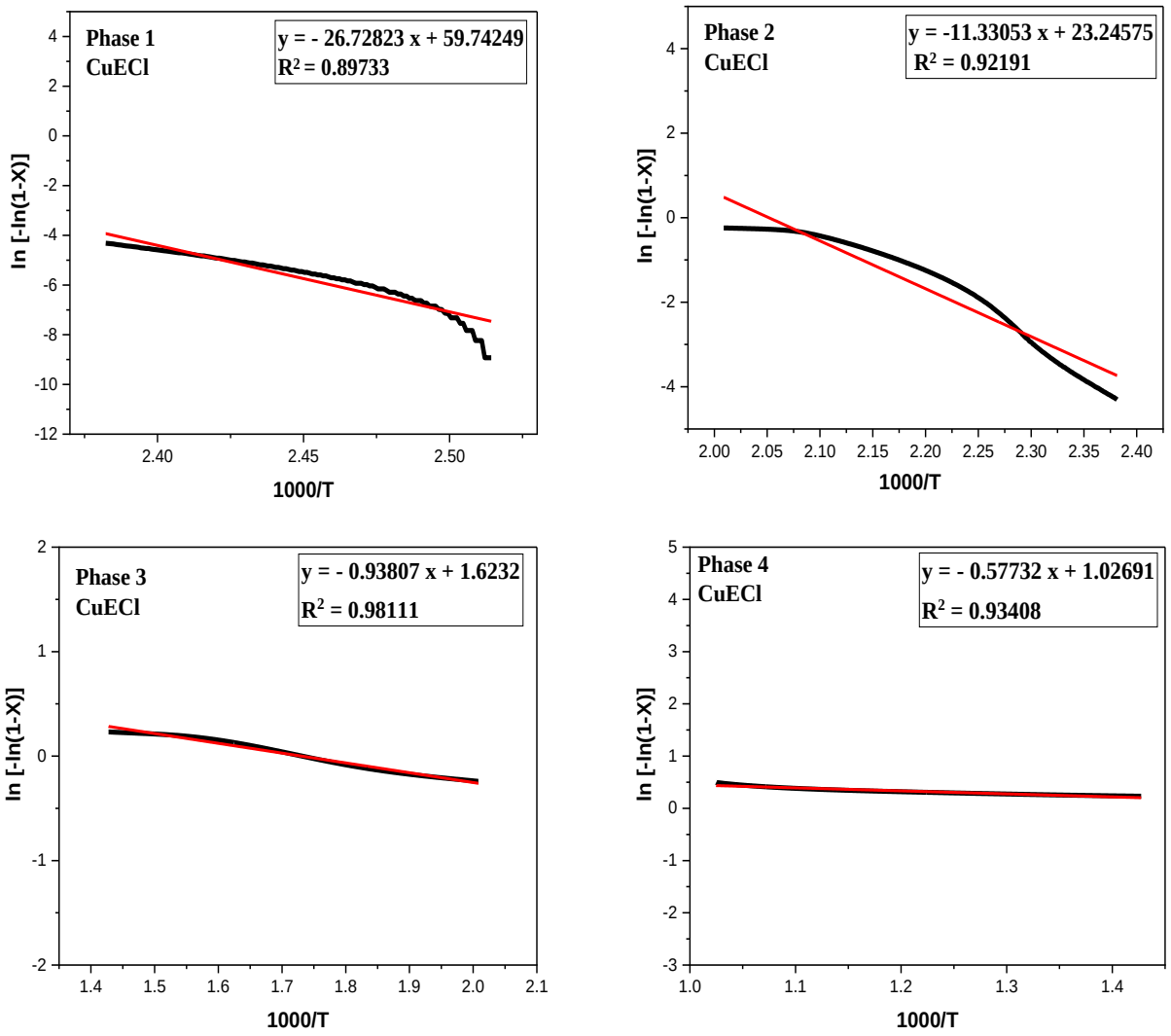

Figure 10. Plots of ln[–ln(1–*x*)] versus 1000/*T* for the four decomposition stages of the CuECl complex

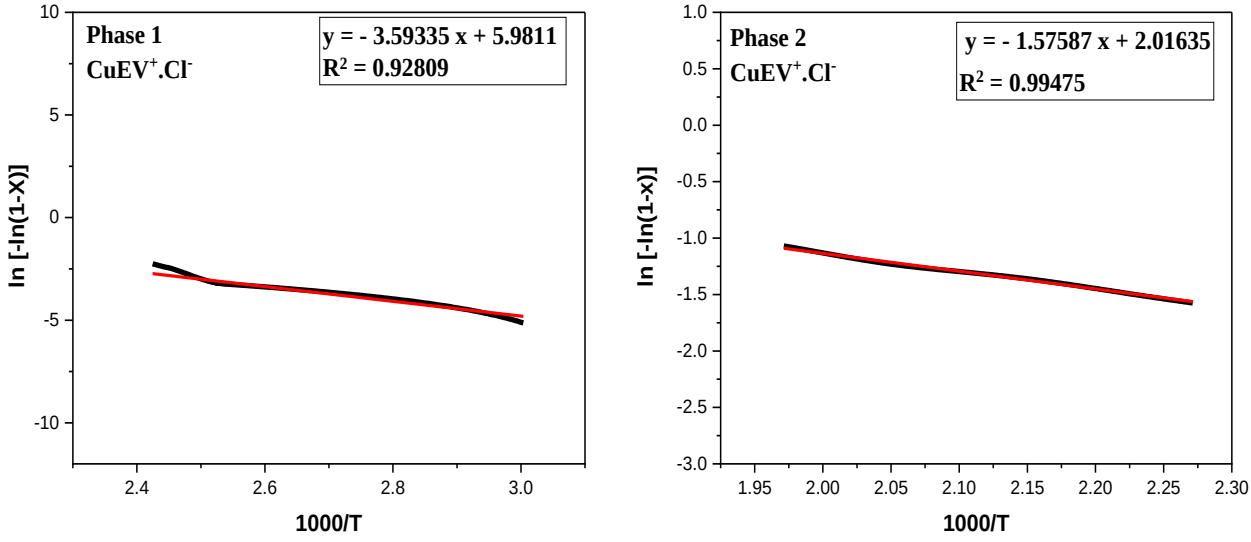

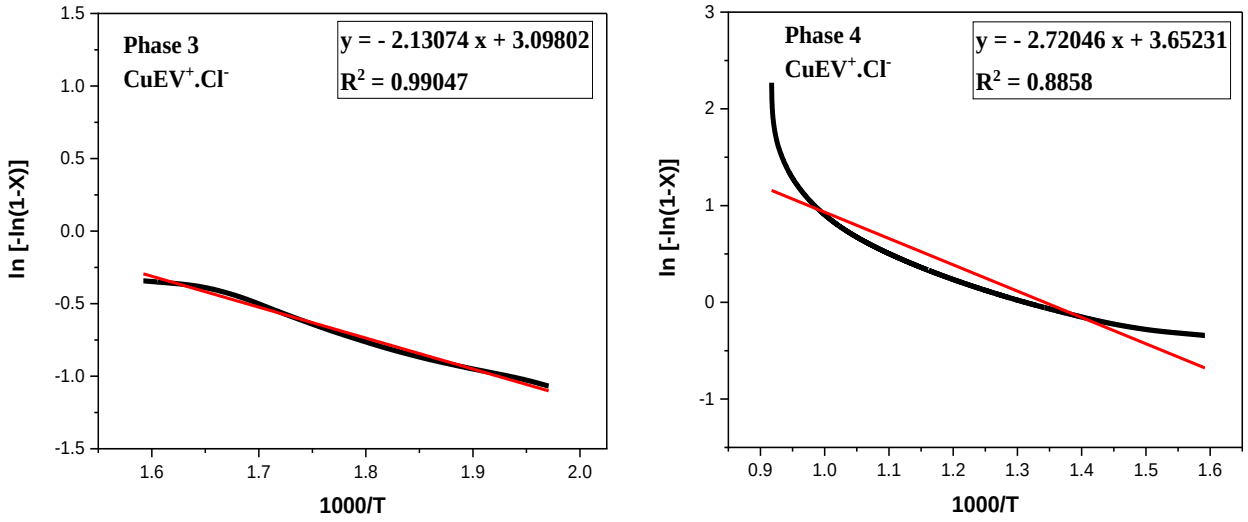

Figure 11. Plots of ln[–ln(1–*x*)] versus 1000/*T* for the four decomposition stages of the $CuEV^{+}\cdot Cl^{-}$ complex

According to the guidelines of the International Confederation for Thermal Analysis and Calorimetry (ICTAC), an increase in activation energy (E_a) among a set of compounds reflects an enhancement in their thermal stability, whereas lower E_a values correspond to reduced stability. Consequently, based on the calculated E_a values ($\times 10^3$ J·mol^{-1}) presented in Tables 4 and 5, the thermal stability of the compounds follows the sequence: $CuEV^{+}\cdot Cl^{-}$ (83312.78) < CuECl (329031.337). For the complex of the ligand functionalized with viologen, their thermal stabilities increases in the sequence: $CuEV^{+}\cdot Cl^{-}$. The thermal stability of CuECl is nearly 2.6 times higher. The thermodynamic analysis for each decomposition stage indicates that all processes are non-spontaneous and endothermic, accompanied by increases in disorder, as reflected by the negative ΔS values [23–26].

Energy Dispersive X-Ray Spectroscopy of Copper (II) Complexes (EDX)

Energy-dispersive X-ray (EDX) spectra for the copper(II) complexes are presented in Figures 12 and 13, with the corresponding scanning electron microscopy (SEM) images shown in Figures 14 and 15.

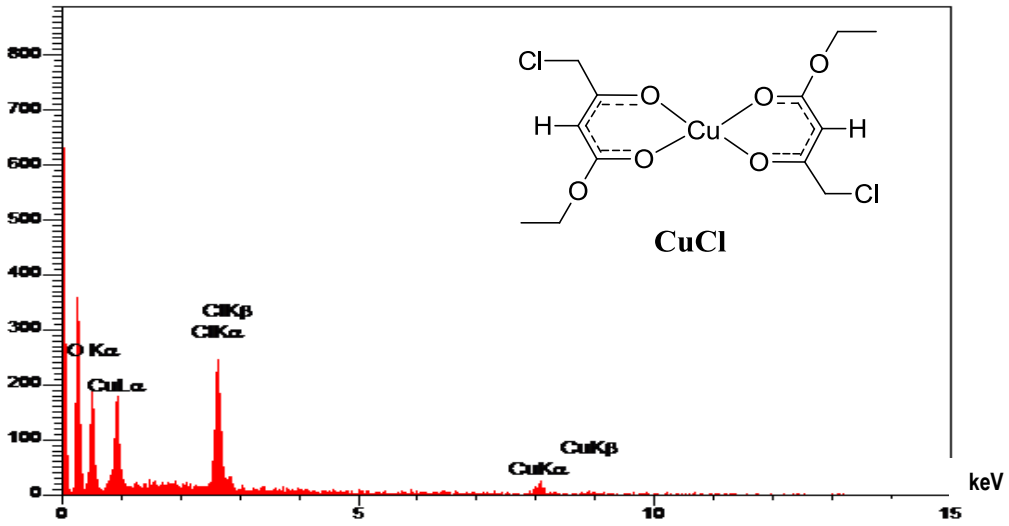

Figure 12. Energy-Dispersive X-ray (EDX) spectrum of the CuECl complex

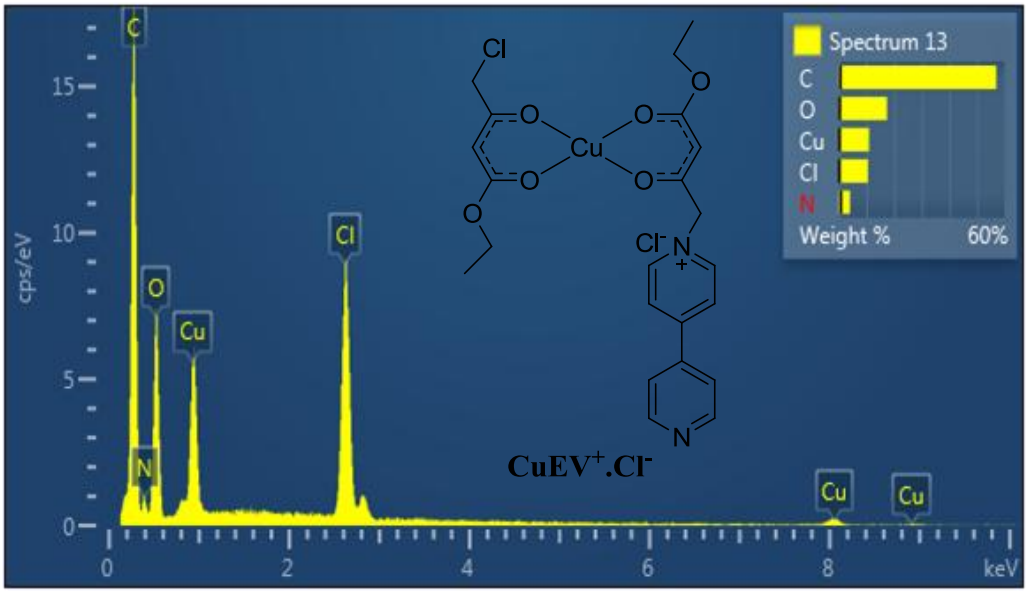

Figure 13. Energy-Dispersive X-ray (EDX) spectrum of the $CuEV^{+}\cdot Cl^{-}$ complex

The expected elements (C, O, N, Cu, I, Cl, F, Br and P) peaks are noted in the EDS spectra, which confirms and agrees with their presence in the prepared complexes. The elemental percentages that appeared in the quantitative results of this spectroscopy did not fully agree with the theoretical values of the prepared complexes. It was strangely noted that the EDS Cu% agrees only with the theoretical Cu% of CuE, and both EDS Cu% and O% showed agreement with those the theoretical of $CuEV^{+}\cdot Cl^{-}$, while other elements did not agreed in same those complexes. Undoubtedly, if one EDS or C, H, N, S and O analysis of a certain compound then the other EDS or C, H, N, S and O elements % should be agreed too. Otherwise, we should expect technical errors in the quantitative analysis of some or all the elements. Additionally, the received quantitative results of the standards are empty. For these two reasons, the quantitative results obtained from this spectroscopy should be excluded and only the qualitative results should be considered. Au and other signals observed in the EDS spectra are attributed to the coating (e.g., gold coating) and not to the sample itself [28].

Hydrogen is absent because EDS analysis can not detect it. Dramatic and typical differences are note in the SEM images among the Copper (II) complexes are depicted in Figures 20 and 21 respectively. The complex CuECl have shorter, thicker and more irregular in length and width crystals. Some CuECl crystals are stacked or clustered which indicates interrupted or altered growth. While, CuECI crystals appear rougher and more granular and this likely due to Cl substitution that disrupt regular packing as concluded before from XRD spectroscopy. The size of CuECI are shorter and broader suggesting lower crystallinity or altered nucleation rate. In term of distribution, the CuE is more aligned and compact showing better organization, while CuECl is more. Scattered oriented with possible agglomeration. Therefore, the Chlorine substitution in CuECl effects on crystal growth making it as shorter and thicker crystals. The morphology of CuECl is less regular and it has rougher surfaces. CuECl packing is less ordered. All this reflects how small ligand change, like the halogenation by chlorine can significantly Impact solid-state material properties like solubility electronic behavior. In addition to Chlorine substitution as result for mentioned difference above, the solvent effect or reaction conditions (e.g., fast precipitation, low temperature) [29, 30].

A detailed comparison of the surface morphologies for the CuECl and $CuEV^{+}\cdot Cl^{-}$ complexes, as observed in the SEM images (Figs. 14 and 15), is provided below. The CuECl complex displays well-defined, elongated rod- or needle-like crystals indicating high crystallinity and uniform growth along preferred directions. This is likely due to strong packing of small symmetric ligands. In contrast, $CuEV^{+}\cdot Cl^{-}$ shows irregular, blocky and aggregated particles with less-defined edges. This reflects disruption of crystal packing due to the bulkier viologen moiety. The CuECl crystals appear smooth and clean suggesting an orderly homogenous surface, the surface of an $CuEV^{+}\cdot Cl^{-}$ is rougher and more porous, possibly due to incorporation of viologen into the ligand that disrupting tight molecular packing. The crystals of CuECl are long and thin (often exceeding 10–20 μm) with relatively narrow widths. While, the $CuEV^{+}\cdot Cl^{-}$ particles are shorter and thicker with less uniform size distribution. Some particles form small fragments and others form large agglomerates. In term of distribution CuECl has highly ordered and dispersed arrangements with minimal aggregation.

Therefore, the transition from CuECl to $CuEV^{+}\cdot Cl^{-}$ results in: loss of needle-like crystal morphology, more irregular and less crystalline texture, increased surface roughness and size heterogeneity and aggregation. These differences show how introducing bulky or charged group like viologen significantly alters the molecular self-assembly and morphology at the microstructural level. The following discussion deals with a comparison between the SEM image of $CuEV^{+}\cdot Cl^{-}$. $CuEV^{+}\cdot Cl^{-}$ has irregular and blocky particles. The structure appears disordered and amorphous compared to well-crystallized materials. In term of surface texture, $CuEV^{+}\cdot Cl^{-}$ is rough and porous.

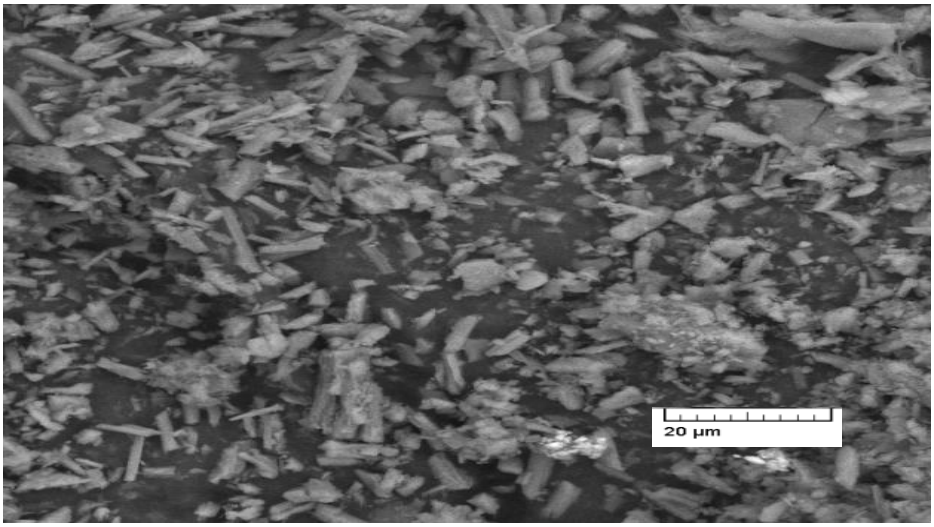

Figure 14. SEM image of CuECl complex

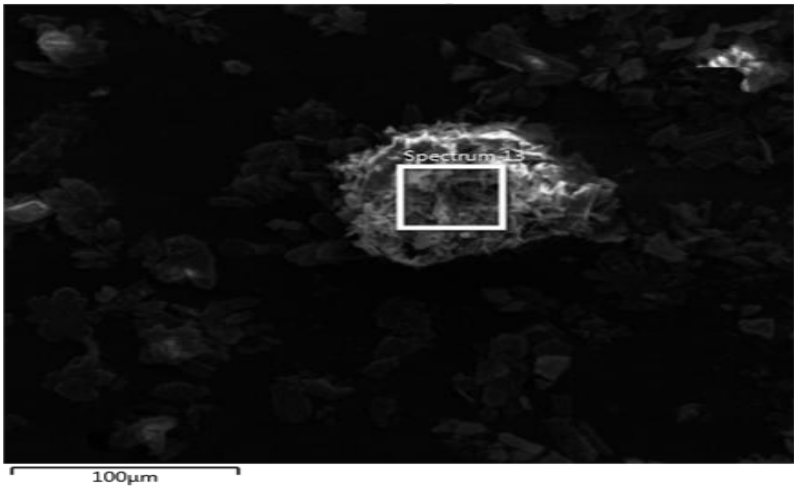

Figure 15 SEM image of $CuEV^{+}\cdot Cl^{-}$ complex

The $CuEV^{+}\cdot Cl^{-}$ has brand particle size distribution. Some particles are large aggregates and some are fine particles. The $CuEV^{+}\cdot Cl^{-}$ particles are unevenly dispersed with some regions of clustering [29, 30].

UV–Vis Characterization of Cu(II) Coordination Compounds

Show electronic absorption spectrum of CuECl in different solvents are C_6H_6, EtOAc, DCM, acetone, EtOH, MeOH, ACN, DMF, DMSO and D.W with three concentrations representative in Figures 16–26 with Absorbance & wavelength (nm) along with that of copper (II) acetate two solvent ethanol and DMF.

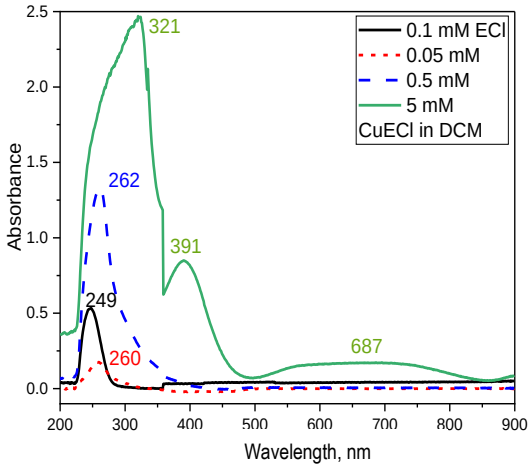

Figure 16. UV-Vis absorption spectra of ethyl acetoacetate (0.1 mM, black), copper acetate (5 mM, purple), CuECl (0.05 mM, red, (0.5 mM, blue and 5 mM, green) in EtOH

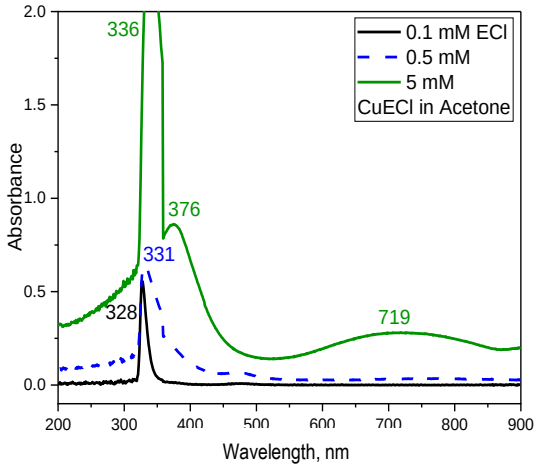

Figure 17. UV-Vis absorption spectra of ethyl 4-chloroacetoacetate (0.1 mM, black), copper acetate (5 mM, purple), CuECl (0.05 mM, red, 0.5 mM, blue and 5 mM, green) in DMF

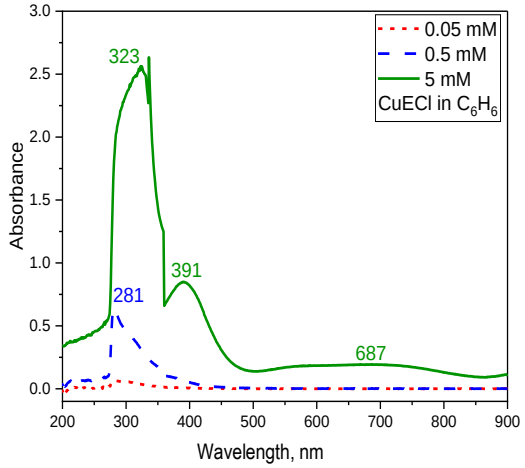

Figure 18. UV-Vis absorption spectra of CuECl (0.05 mM, red, 0.5 mM, blue and 5 mM, green) in C_6H_6

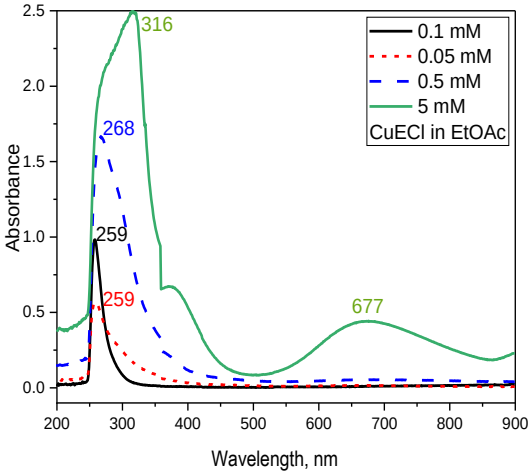

Figure 19. UV-Vis absorption spectra of ethyl 4-chloroacetoacetat (0.1 mM, black), CuECl (0.05 mM, red, 0.5 mM, blue and 0.05 mM, green) in EtOAc

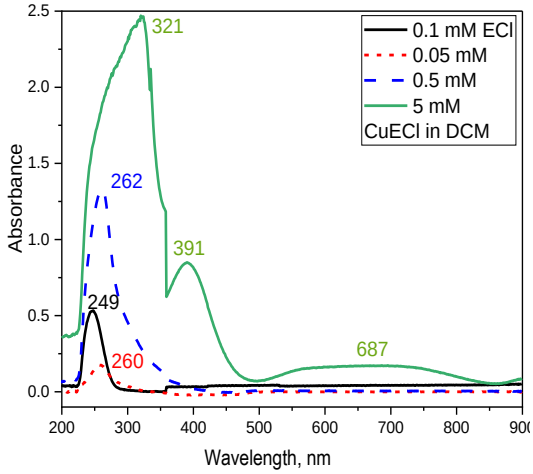

Figure 20. UV-Vis absorption spectra of ethyl 4-chloroacetoacetat (0.1 mM, black), CuECl (0.05 mM, red, 0.5 mM, blue and 5 mM, green) in DCM

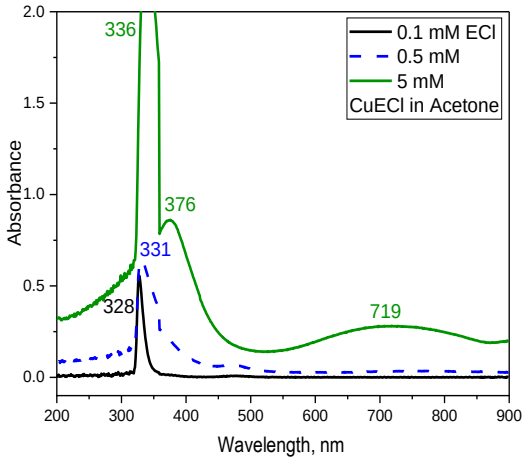

Figure 21. UV-Vis absorption spectra of ethyl 4-chloroacetoacetat (0.1 mM, black), CuECl (0.5 mM, blue and 5 mM, green) in Acetone

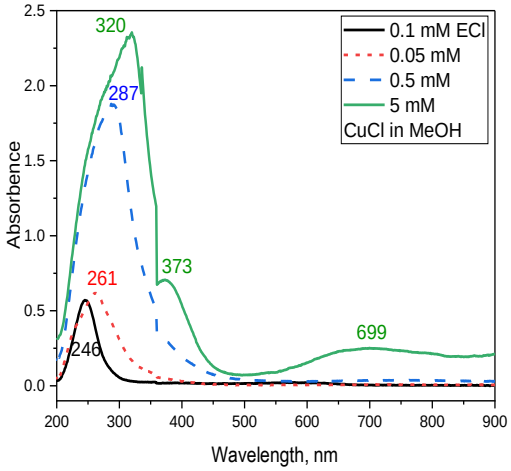

Figure 22. UV-Vis absorption spectra of ethyl 4-chloroacetoacetat (0.1 mM, black), CuECl (0.05 mM, red, 0.5 mM, blue and 5 mM, green) in MeOH

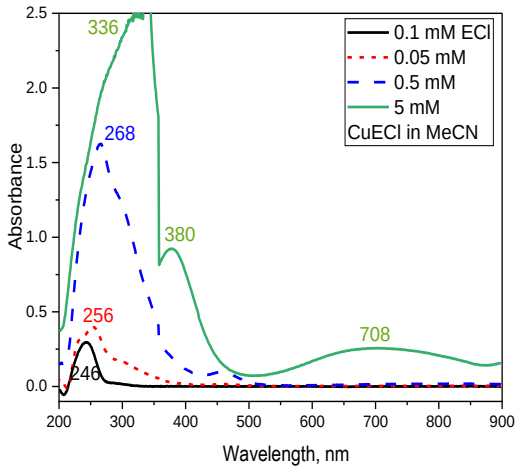

Figure 23. UV-Vis absorption spectra of ethyl 4-chloroacetoacetat (0.1 mM, black), CuECl (0.05 mM, red, 0.5 mM, blue and 5 mM, green) in MeCN

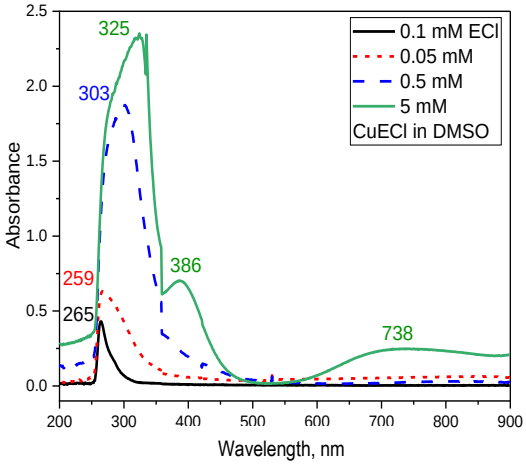

Figure 24. UV-Vis absorption spectra of ethyl 4-chloroacetoacetat (0.1 mM, black), CuECl (0.05 mM, red, 0.5 mM, blue and 5 mM, green) in DMSO

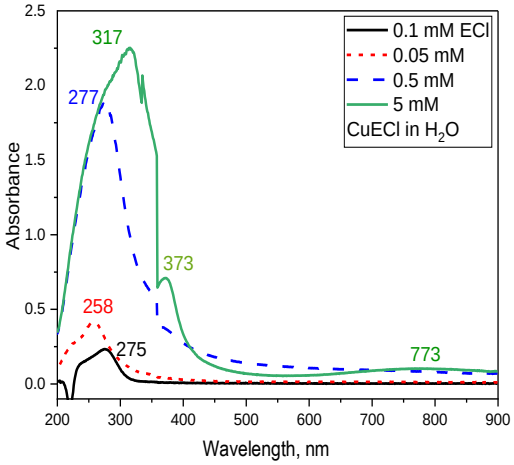

Figure 25. UV-Vis absorption spectra of ethyl 4-chloroacetoacetat (0.1 mM, black), CuECl (0.05 mM, red, 0.5 mM, blue and 5 mM, green) in H_2O

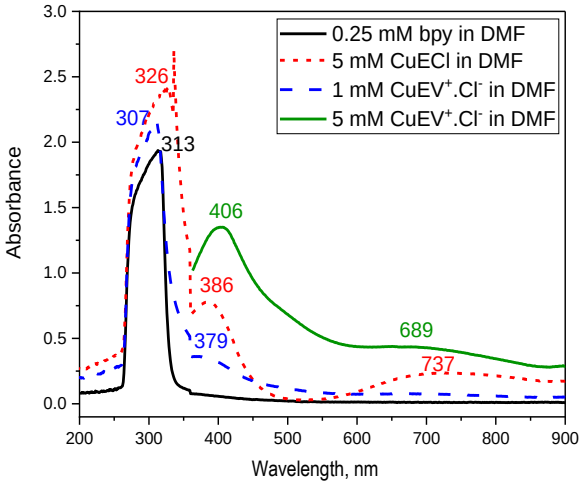

Figure 26. UV-Vis absorption spectra of bpy (0.25 mM, black), CuECl (5 mM, red), $CuEV^{+}.Cl^{-}$ (1 mM, blue and 5 mM, green) in DMF

The *d-d* electronic transition bands for CuECl and copper(II) acetate were detected at wavelengths of 697 nm and 700 nm in ethanol, and at 737 nm and 704 nm in DMF, respectively. Compared to copper(II) acetate, the CuECl bands exhibit hypsochromic shifts of 3 nm in ethanol and 33 nm in DMF, indicating the formation of a coordination complex between the Cu^{2+} center and the ECl ligand. Furthermore, the UV absorption band of CuECl in ethanol appears at 257 nm, which is blue-shifted relative to copper(II) acetate (300 nm), suggesting more energetic electronic transitions within the complex. The ligand ECl displays multiple absorption bands in the same solvents at 249, 328, 259, 246, 250, 246, 271, 265, and 275 nm, respectively, reflecting its inherent electronic transitions [31].

These UV absorptions of ECl is oscillatory with increasing of solvent polarity [31]. With respect to polarity, the non-bonding (*n*) orbital exhibits greater polarity than the π* orbital, which itself is more polar than the π orbital. In solvents of higher polarity, both the π and π* orbitals experience stabilization, albeit to differing degrees. Because the π* orbital is more polar than the π-orbital, so in a more polar solvent, the magnitude of stabilizing of π* orbital of the highest energy will be greater than the magnitude of stabilizing of π orbited of the at lower energy levels, the stabilization of the π* orbital in a more polar solvent is greater than that of the π orbital. Consequently, the energy gap (ΔE) between the π and π* orbitals decreases as solvent polarity increases [32]. As a result, the maximum absorption wavelength (λ_max) in a more polar solvent becomes larger than that in a less polar solvent (since $\Delta E \propto 1/\lambda\_max$). This leads to a bathochromic (red) shift of the π-π* absorption band in polar media [33].

It is valuable to examine the influence of solvent polarity on the λ_max of the n–π* transition. In highly polar solvents, both the non-bonding (*n*) and antibonding (π*) orbitals undergo stabilization, albeit to varying degrees. Due to the higher polarity of the *n* orbital relative to the π* orbital, its stabilization is more pronounced in polar media. Consequently, the energy of the *n* orbital decreases to a greater degree than that of the π* orbital. This results in an enlarged energy gap between the *n* and π* orbitals relative to that in less polar solvents. This results in a hypochromic (blue) shift of the *n*-π* transition, i.e., the λ_{max} of this transition decreases as solvent polarity increases. Conversely, the more intense π-π* transition exhibits a bathochromic (red) shift with increasing solvent polarity. Thus, as solvent polarity rises, the π-π* and *n*-π* transitions approach each other in wavelength. For the ECl ligand, intra-molecular hydrogen bonding within the solution further stabilizes resonance structures, lowering the energy of the π-π* transition. Simultaneously, hydrogen bonding weakens the *n*-π* transition, contributing to its blue shift. The combined effect of orbital polarity differences, solvent stabilization, Hydrogen bonding causes the *n*-π* and π-π* transitions to converge, effectively causing the high-intensity π-π* band to overlap with the lower-intensity *n*-π* band in the ECl ligand [31].

The UV absorptions of the weaker ligand ECl (249 nm, 328 nm, 259 nm, 246 mm, 250 nm, 246 nm, 271 nm, 265 nm and 275 nm) are red shifted [31]. This reflects the energetically easier transitions for the ligand ECl. These easier UV transition could be related to the longer extended conjugation system in the ligand ECl due to the existence of Cl atom. Except for ECl in H_2O, both the complex of CuECl showed red shifted UV transitions compared with those of the ligand of ECl respectively. The easier UV transition of the complexes could be related that upon complexation with Cu^{2+} ion. The established structure of the free ligand ECl adopts a more planar geometry upon coordination in the CuECl complex [34]. This increased planarity facilitates greater electron delocalization (resonance) within the complex, relative to the free ligand, leading to bathochromic (red) shifts in the UV absorption spectra of the complexes. In general, the shifts in wavelength positions and variations in absorption intensities of the UV bands observed for the copper complexes relative to their ligands provide clear evidence for the coordination of Copper(II) ions induces a greater planarity in the resulting complexes relative to the corresponding free ligands [35–38].

The visible absorption bands occur as a result of electronic transitions between split d-electron energy levels. In the visible region of the spectrum, of CuECl showed two bands, sharp band of higher energy and the second is broad with lower energy in different solvents attributed to the intra-atomic *d-d* transitions of the copper(II) ion in the complex [37].

This band can be assigned to the electronic transition *dxz, dyz-dxy* [32]. Two weak-defined bands appeared of CuECl as one broad band due to dz^2-*dxy* transitions respectively. This broad band occurred at 687, 687, 719, 677, 708, 697, 656, 737, 738 and 773 nm in benzene, EtOAc, Acetone, MeCN, DCM, EtOH, MeOH, DMF, DMSO and H_2O respectively. In same solvents, (except H_2O). These three single electron *d-d* transitions are consonant with square planar CuECl complexe (Cu^{2+} with a d^9 configuration). The square planer Cu^{2+} d^9 configuration has four-fold splitting with decreasing energy in the following order: $dxz, dyz < dz^2 < d^2x^2 — y^2 < dxy$ [32–37].

The reaction of CuECl that have positive axial ligands (very weak ligands). These uncommon complexes are very sparingly soluble complexes showed very exceptional behavior in DMF media. The axial coordinated viologen within these complexes are reduced at dissolving only in DMF at air atmosphere [38, 39].

The S_N2 nucleophilic substitution of the complexes CuECl, with each of bpy, affords the complexe $CuEV^{+}\cdot Cl^{-}$. In these exceptional complexes, the complexed β-ketoester ligand has been modified to positive ligand within the complexes structures. The Ultraviolet-Vis absorption spectrum of these complexes are recorded in DMF media and presented in Figures 16–26. The purple color of $CuEV^{+}\cdot Cl^{-}$ solution in DMF refers undoubtedly to the generation of a π-dimeric association involving two $V^{\bullet}$ radicals within two complexes. Also, the peaks occurred at 406 nm and 689 nm are juxtapose to the formation of non-dimer viologen radical ($V^{\bullet}$) consequently there is an equilibrium among non-dimerized viologen radical $V^{\bullet}$ and dimerized viologen radicals stand $(C_1V)_2$ within $CuEV^{+}\cdot Cl^{-}$ structures [37–39] (Scheme 3).

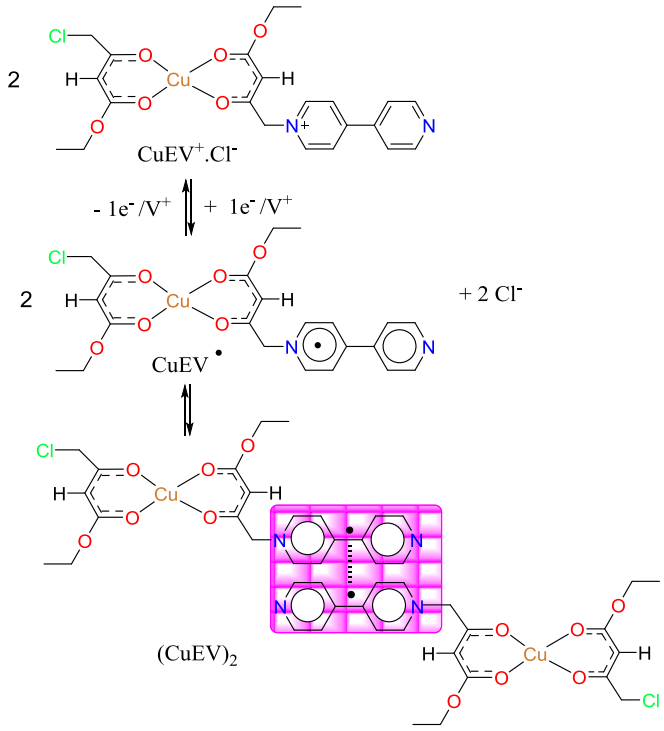

Scheme 3. Inter-molecular dimerized viologen radicals of $CuEV^{+}\cdot Cl^{-}$ in DMF

Formation of Molecular Switches: Reduction of Viologen Units within the Complexes

The UV-Visible absorption spectra were obtained after reducing the mixtures using solvation in Zn powder, with concentrations of 0.5 mM for $CuEV^{+}\cdot Cl^{-}$. In these cases the viologen formed complexes terminal linkage with CuECl. Additionally, reduction was carried out using activated zinc powder. The absorption spectra were recorded over a range of 190–900 nm and are presented in Figures 27 and 28.

The viologen-terminated copper(II) complex, $CuEV^{+}\cdot Cl^{-}$, was reduced using activated Zn powder and monitored via UV-Vis absorption spectroscopy. To accurately track the spectral changes associated with the reduction of the viologen units (both in the free ligand and when coordinated to the Cu(II) center), two reference blanks were employed: the pure DMF solvent and the non-reduced complex solution.

In Cu(II)-viologen complex of $CuEV^{+}\cdot Cl^{-}$, viologen radical cations are formed as a consequence of the reduction ($V^{\bullet+}$), which dimerize into $[V^{\bullet+}]_2$ dimers through strong π-π stacking interactions. The spectral shift from 550–600 nm to 700–800 nm, along with the distinct appearance of peaks near 800 nm in all compounds, indicates the successful reduction and the subsequent formation of dimers. This observed dimer formation is consistent with the mechanism proposed in Scheme 4. The presence of Cu(II) can modulate the stability and redox properties of the dimer, differentiating the behavior of coordinated vs. free viologen radicals [40–43].

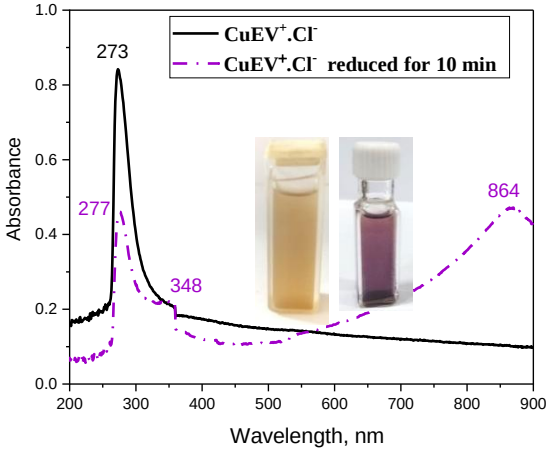

Figure 27. UV-Vis absorption spectra of $CuEV^{+}\cdot Cl^{-}$ (0.5 mM, Black) and reduced $CuEV^{+}\cdot Cl^{-}$ (0.5 mM, Purple) in DMF. Reference blank: $CuEV^{+}\cdot Cl^{-}$ (0.5 mM)

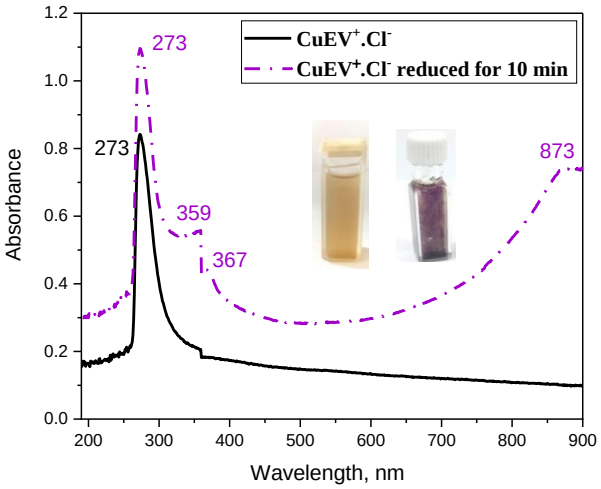

Figure 28. UV-Vis absorption spectrum of $CuEV^{+}\cdot Cl^{-}$ (0.5 mM, Black) and reduced $CuEV^{+}\cdot Cl^{-}$ (0.5 mM, Purple) in DMF. Reference blank: DMF

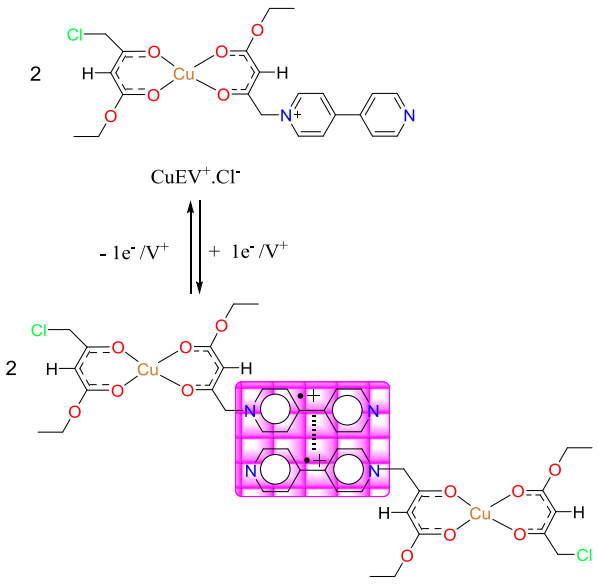

Scheme 4. Inter-molecular dimerized viologen radicals of $CuEV^{+}\cdot Cl^{-}$ in DMF

Electrochemical Studies of Molecular Switches

The electrochemical behavior of the ECl ligand, its corresponding copper(II) coordination complexes, bpy adducts, and the viologen-terminated species ($CuEV^{+}\cdot Cl^{-}$) was systematically examined in DMF containing 0.1 M TBAP as the supporting electrolyte by means of cyclic voltammetry (CV). All reported potentials are referenced to a silver pseudo-reference electrode. To minimize oxidative degradation of the electrogenerated species, all voltammetric measurements were performed at ambient laboratory temperature under an inert argon atmosphere. A conventional three-electrode setup was employed, consisting of a glassy carbon disk as the working electrode and a platinum wire as the counter electrode. Additional experimental conditions for each voltammogram are provided in the experimental section or indicated in the figure captions.

The cyclic voltammograms (CVs) of the complex CuECl are depicted in Figures 29 and 30 respectively. These CVs will be compared with the CVs of their precursor: $Cu(OAc)_2$ and ECl that are presented in Figures 31–33 respectively. An irreversible reduction process of the free ECl ligand was observed at –2.025 V respectively at f 0.3 V/s. The irreversible oxidation of Cu^{2+} ion in $Cu(OAc)_2$ is noted at 845.666 mv rt 0.3 V/s, see Figure 32.

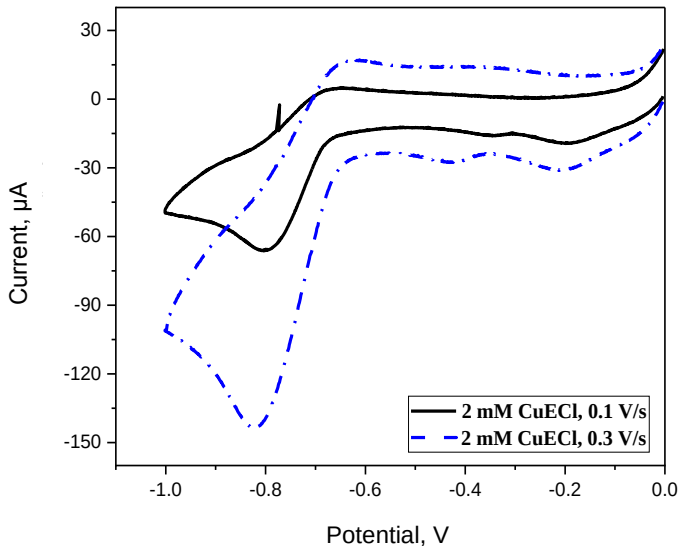

Figure 29. Cyclic voltammograms (CVs) of 2 mM CuECl in DMF (0.1M TBAP) at scan rates of 0.1 V/s (black) and 0.3 V/s (blue dashed). WE: (3 mm) VC. RE: Ag

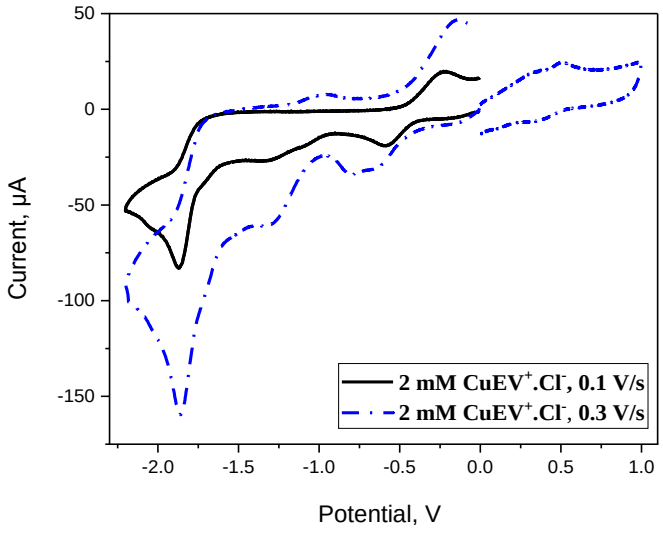

Figure 30. Cyclic voltammograms (CVs) of 2 mM $CuEV^{+}\cdot Cl^{-}$ in DMF (0.1M TBAP) at scan rates of 0.1 V/s (black) and 0.3 V/s (blue dashed). WE: (3 mm) VC. RE: Ag

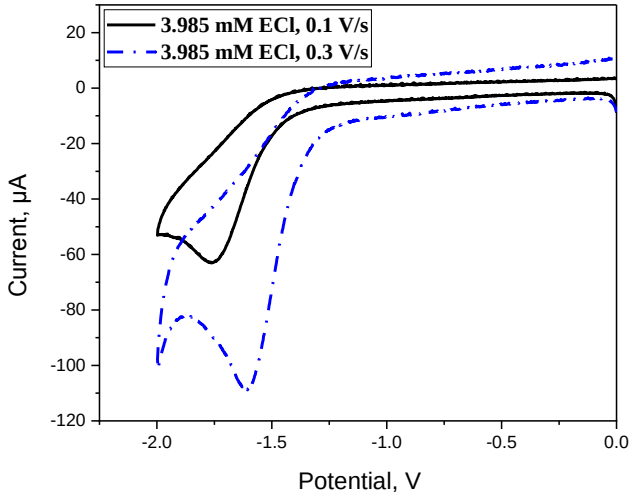

Figure 31. Cyclic voltammograms (CVs) of 3.985 mM ECl in DMF (0.1M TBAP) at scan rates of 0.1 V/s (black) and 0.3 V/s (blue dashed). WE: (3 mm) VC. RE: Ag

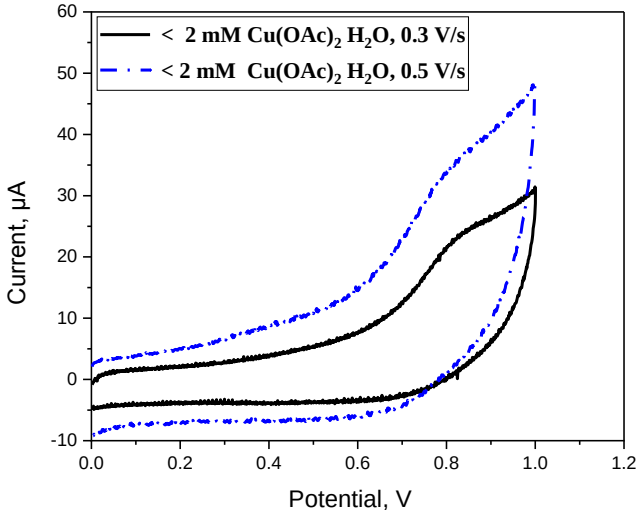

Figure 32. Cyclic voltammograms (CVs) of less than 2 mM $Cu(OAC)_2$ in DMF (0.1M TBAP) at scan rates of 0.1 V/s (black) and 0.3 V/s (blue dashed). WE: (3 mm) VC. RE: Ag

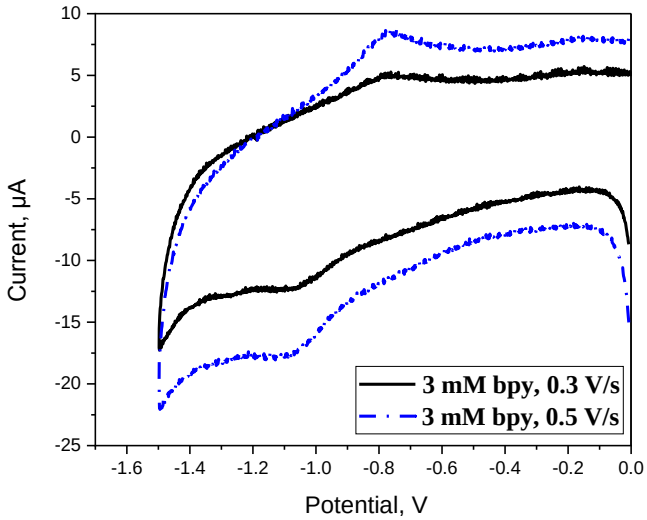

Figure 33. Cyclic voltammograms (CVs) of 3 mM bpy in DMF (0.1M TBAP) at scan rates of 0.3 V/s (black) and 0.5 V/s (blue dashed). WE: (3 mm) VC. RE: Ag

The reduction of Cu^{2+} ion in the complexe CuECl occured at –346.348 mv respectively. The of CuECl (–4571.19 mv) is consistent with the more electron deficiency of Cu^{2+} ion in the complex CuECl. The reduction of the coordinated ECl in the complex CuECl respectively is noted at –804.26 mv. Here, the coordinated ECl suffers more electron deficiency than the coordinated E which in turns lends to easier reduction for the coordinated ECl. Both the reduction of the coordinated ECl is anodically shifted compared with the reduction of the free ECl. These shifts reflect the decrease of the electron densities of the ligands after complexations.

The nucleophilic substitution (S_N2) of the complex CuECl with each of bpy afford the complexe bearing the viologen units within their ligands: $CuEV^{+}\cdot Cl^{-}$. The CVs of these novel complexes are presented in Figures 29-30. The reductions of viologen unit in $CuEV^{+}\cdot Cl^{-}$ are anodically shifted to be at –646.536 mv and –813.768 mv. The observed shifts are clearly ascribed to the formation of intermolecular π-dimers between viologen radicals ($V^{\bullet}\ldots V^{\bullet}$) from two $CuEV^{+}\cdot Cl^{-}$ complexes. The reduction at –1326 mv could be assigned to the formation of ($V^{\bullet}$) followed by the formation of π-dimer with different conformation. The reduction of the coordinated ECl happened at –1878 mv easier than the free ECl ligand. The oxidation process happened at –918.278 mv could be related to the oxidation of the previous reduced species that have been absorbed on the electrode while, the reduction of the coordinated Cu^{2+} ion $Cu^{2+} + 1e^{-} \rightarrow Cu^{+}$ is not seen well, its oxidation process is not at –77.903 mv.

The reduction noted at –1528 mv is assigned to the coordinated ECl. The reduction of the coordinated Cu^{2+} ion to Cu^{+} is noted at –472.941 mv and the oxidation of the resulted Cu^{+} species happened at –269.134 mv [44–46].

Our electrochemical results, supported the formation of the complexes and showed well the electronic properties of the coordinated Cu(II) ion, ligands and viologen units.

Conclusions

In this study, two complementary design strategies were successfully established for the incorporation of viologen redox units into copper(II) β-diketone frameworks, enabling systematic modulation of structural and electrochemical properties. The first strategy involved axial coordination of the viologen moiety to preformed Cu(II) β-diketone complexes, whereas the second relied on the structural integration of the viologen (or bpy) unit within the β-diketone ligand prior to complexation. These approaches provide a controlled platform for tuning structure–property relationships in copper-based redox-active systems. The formation of CuECl and $CuEV^{+}\cdot Cl^{-}$ was confirmed by mass spectrometry, elemental analysis, and spectroscopic techniques, while XRD and SEM analyses revealed well-defined nanocrystalline domains whose morphology and crystallite size depend strongly on ligand functionalization. Crystallite sizes calculated using Scherrer and Williamson–Hall models, together with lattice strain analysis, demonstrated that viologen incorporation significantly influences microstructural parameters. Thermal studies further showed enhanced stability for CuECl relative to $CuEV^{+}\cdot Cl^{-}$, with all decomposition stages being endothermic and entropy-driven, reflecting the robustness of the coordination framework.

The electronic absorption spectra of the CuECl complex were recorded at three different concentrations (0.05 mM, 0.5 mM, and 5 mM) in various solvents to examine solvent effects on electronic transitions, electronic absorption studies confirmed the preservation of ligand-centered π-π* and *n*-π* transitions upon coordination, in addition to characteristic *d-d* bands consistent with square-planar Cu(II) geometry.

Notably, the intense violet coloration of $CuEV^{+}\cdot Cl^{-}$ in DMF and the absorption bands at 406 and 689 nm provide clear spectroscopic evidence for reversible equilibrium between monomeric viologen radicals and π-dimer species. Cyclic voltammetry further demonstrated that both coordination modes preserve the redox activity of the viologen unit, enabling controlled switching between radical and π-dimer states under chemical and electrochemical stimuli.

Overall, the present work establishes a versatile synthetic and structural framework for integrating viologen-based molecular switches into copper(II) β-diketone systems. The demonstrated correlation between coordination mode, crystallinity, thermal stability, and redox-switching behavior offers valuable design principles for the development of responsive inorganic–organic hybrid materials and copper-based molecular electronic platforms.

Supporting Information

The Supporting Information is available free at https://ejc.buketov.edu.kz/ejc/article/view/548/399

*Author Information**

**The authors' names are presented in the following order: First Name, Middle Name and Last Name*

Ahmed Abd alridha Alibrahimi (*corresponding author*) — Assistant Professor, Department of Chemistry, College of Science, University of Thi-Qar, 64001, Nassiria, Iraq; e-mail: ahmedoudah501@gmail.com; https://orcid.org/0000-0002-3271-9015

Wathiq Sattar Abdul-Hassan — Professor, Department of Chemistry, College of Science, University of Thi-Qar, 64001, Nassiria, Iraq; e-mail: Wathiq.a_chem@sci.utq.edu.iq; https://orcid.org/0000-0003-1297-3822

Author Contributions

The manuscript was written through contributions of all authors. All authors have given approval to the final version of the manuscript. CRediT: **Ahmed Abd alridha Alibrahimi** conceptualization, data curation, formal analysis, investigation, methodology, validation, visualization, writing-review & editing; **Wathiq Sattar Abdul-Hassan** conceptualization, data curation, formal analysis, funding acquisition, resources, supervision, validation, writing-original draft, writing-review & editing.

Acknowledgments

Both authors extend their thanks and appreciation to: *Department of Chemistry, College of Science, University of Thi-Qar*, and all those who helped us in this research.

Conflicts of Interest

The authors declare no conflict of interest.

References

1 Lee, C.K., Gangadharappa, C., Fahrenbach, A.C., & Kim, D.J. (2024). Harnessing Radicals: Advances in Self-Assembly and Molecular Machinery. *Advanced Materials*, *36*(42), 2408271. https://doi.org/10.1002/adma.202408271

2 Zhang, D.W., Tian, J., Chen, L., Zhang, L., & Li, Z.T. (2015). Dimerization of Conjugated Radical Cations: An Emerging Non-Covalent Interaction for Self-Assembly. *Chemistry–An Asian Journal*, *10*(1), 56–68 https://doi.org/10.1002/asia.201402805

3 Carrington, M.E., Sokołowski, K., Jónsson, E., Zhao, E.W., Graf, A.M., Temprano, I., & Scherman, O.A. (2023). Associative pyridinium electrolytes for air-tolerant redox flow batteries. *Nature*, *623*(7989), 949–95. https://doi.org/10.1038/s41586-023-06664-7

4 Liu, L., Yao, Y., Wang, Z., & Lu, Y.C. (2021). Viologen radical stabilization by molecular spectators for aqueous organic redox flow batteries. *Nano Energy*, *84*, 105897. https://doi.org/10.1016/j.nanoen.2021.105897

5 Zhou, C., Tian, J., Wang, J. L., Zhang, D. W., Zhao, X., Liu, Y., & Li, Z.T. (2014). A three-dimensional cross-linking supramolecular polymer stabilized by the cooperative dimerization of the viologen radical cation. *Polymer Chemistry*, *5*(2), 341–345. https://doi.org/10.1039/C3PY01006F

6 Dalvand, P., Nono, K.N., Shetty, D., Benyettou, F., Asfari, Z., Platas-Iglesias, C., & Elhabiri, M. (2021). Viologen–cucurbituril host/guest chemistry–redox control of dimerization versus inclusion. *RSC advances*, *11*(47), 29543–29554. https://doi.org/10.1039/D1RA05488K

7 Imabayashi, S.I., Kitamura, N., Tokuda, K., & Tazuke, S. (1987). Intramolecular Association of Viologen Dimer and Trimer Radical Cations. An Electrochemical and Spectroscopic Study. *Chemistry Letters*, *16*(5), 915–918. https://doi.org/10.1246/cl.1987.915

8 Malik, M., Świtlicka, A., Bieńko, A., Komarnicka, U.K., Bieńko, D.C., Kozieł, S., ... & Machura, B. (2022). Copper (II) complexes with 2-ethylpyridine and related hydroxyl pyridine derivatives: structural, spectroscopic, magnetic and anticancer in vitro studies. *RSC advances*, *12*(42), 27648–27665. https://doi.org/10.1039/D2RA05133H

9 Rostas, A.M., Badea, M., Ruta, L.L., Farcasanu, I.C., Maxim, C., Chifiriuc, M. C., & Olar, R. (2020). Copper (II) complexes with mixed heterocycle ligands as promising antibacterial and antitumor species. *Molecules*, *25*(17), 3777. https://doi.org/10.3390/molecules25173777

10 El-Sayed, D.S., Tawfik, E.M., Elhusseiny, A.F., & El-Dissouky, A. (2023). A perception into binary and ternary copper (II) complexes: synthesis, characterization, DFT modeling, antimicrobial activity, protein binding screen, and amino acid interaction. *BMC chemistry*, *17*(1), 55. https://doi.org/10.1186/s13065-023-00962-x

11 Sebastian, S., Sylvestre, S., Sundaraganesan, N., Karthikeyan, B., & Silvan, S. (2022). Conformational analysis, molecular structure, spectroscopic, NBO, reactivity descriptors, wavefunction and molecular docking investigations of 5,6-dimethoxy-1-indanone: A potential anti Alzheimer's agent. *Heliyon*, *8*(1). https://doi.org/10.1016/j.heliyon.2022.e08821

12 Holtzclaw, H.F., Lintvedt, R.L., Baumgarten, H.E., Parker, R.G., Bursey, M.M., & Rogerson, P.F. (1969). Mass spectra of metal chelates. I. Substituent effects on ionization potentials and fragmentation patterns of some 1-methyl-3-alkyl-1, 3-dione-copper (II) chelates. *Journal of the American Chemical Society*, *91*(14), 3774–3778. https://doi.org/10.1021/ja01042a014

13 Turgambaeva, A.E., Bykov, A.F., & Igumenov, I.K. (1995). Investigation of the thermal decomposition of bis(acetylacetonato)copper(II) vapour by a mass spectrometric method. *Thermochimica acta*, *256*(2), 443–456. https://doi.org/10.1016/0040-6031(95)91302-Y

14 Jinan, A. Azouz, & Wathiq, S. Abdul-Hassan. (2025). Synthesis, characterization, and redox-responsive novel molecular switching behavior of copper(II)–Viologen adduct complexes. *Applied Chemical Engineering*. https://doi.org/10.59429/ace.v8i3.5751

15 Neelakantan, P. (1964, June). Raman spectrum of ethyl chloroacetate. In *Proceedings of the Indian Academy of Sciences-Section A*, *59*(6), 385–389. New Delhi: Springer India. https://doi.org/10.1007/BF03049210

16 Köse, D.A. (2007). Synthesis and characterization of bis(nicotinamide)-m-hydroxybenzoate complexes of Co (II), Ni (II), Cu (II), and Zn (II). *Russian Journal of Inorganic Chemistry*, *52*(9), 1384–1390. https://doi.org/10.1134/S0036023607090124

17 Holtzclaw, H.F., Lintvedt, R.L., Baumgarten, H.E., Parker, R.G., Bursey, M.M., & Rogerson, P.F. (1969). Mass spectra of metal chelates. I. Substituent effects on ionization potentials and fragmentation patterns of some 1-methyl-3-alkyl-1, 3-dione-copper (II) chelates. *Journal of the American Chemical Society*, *91*(14), 3774–3778. https://doi.org/10.1021/ja01042a014

18 Turgambaeva, A.E., Bykov, A.F., & Igumenov, I.K. (1995). Investigation of the thermal decomposition of bis(acetylacetonato)copper(II) vapour by a mass spectrometric method. *Thermochimica acta*, *256*(2), 443–456. https://doi.org/10.1016/0040-6031(95)91302-Y

19 Azhar H. Gatea, & Wathiq S. Abdul-Hassan. (2023). Ligand Adducts of Bis(acetylacetonato) Copper(II), Bis(3-chloroacetylacetonato) Copper(II) with 4,4'-bipyridine, and Propylene Spacered Bis-viologen. *Journal of Medicinal and Chemical Sciences*, *6*(2), 280–303. http://doi:10.26655/JMCHEMSCI.2023.2.10

20 Waseda, Y., Matsubara, E., & Shinoda, K. (2011). *X-ray diffraction crystallography: introduction, examples and solved problems*. Springer Science & Business Media. http://doi:10.1007/978-3-642-166355-8

21 Prabhu, Y.T., Rao, K.V., Kumar, V.S.S., & Kumari, B.S. (2014). X-ray analysis by Williamson-Hall and size-strain plot methods of ZnO nanoparticles with fuel variation. *World Journal of Nano Science and Engineering*, *2014*. http://dx.doi.org/10.4236/wjnse.2014.41004

22 Lalancette, R.A., Syzdek, D., Grebowicz, J., Arslan, E., & Bernal, I. (2019). The thermal decomposition and analyses of metal tris-acetylacetonates: Free radical formation from Al, Cr, Mn, Fe and Co complexes. *Journal of Thermal Analysis and Calorimetry*, *135*(6), 3463–3470. https://doi.org/10.1007/s10973-018-7598-8

23 Sheikh, J., Juneja, H., Ingle, V., Ali, P., & Hadda, T.B. (2013). Synthesis and in vitro biology of Co (II), Ni (II), Cu (II) and Zinc (II) complexes of functionalized beta-diketone bearing energy buried potential antibacterial and antiviral O, O pharmacophore sites. *Journal of Saudi Chemical Society*, *17*(3), 269–276. https://doi.org/10.1016/j.jscs.2011.04.004

24 Jassema, I.A., Abdul-Hassana, W.S., Flafela, I.A., & Jghebilb, H.O. (2023). Axial ligation for copper (II) complexes of bis(acetylacetonato)ethylenediimine and bis(3-chloroacetylacetonato)ethylenediimine. *Journal of Medicinal and Pharmaceutical Chemical Research*, 5, 173–203 https://doi.org/10.22034/ecc.2023.363684.1533

25 Lalancette, R.A., Syzdek, D., Grebowicz, J., Arslan, E., & Bernal, I. (2019). The thermal decomposition and analyses of metal tris-acetylacetonates: Free radical formation from Al, Cr, Mn, Fe and Co complexes. *Journal of Thermal Analysis and Calorimetry*, *135*(6), 3463–3470. https://doi.org/10.1007/s10973-018-7598-8

26 Chrissafis, K., Lalia-Kantouri, M., & Aslanidis, P. (2011). Kinetic analysis of the thermal decomposition of copper (I) complexes with heterocyclic thiones. *Journal of thermal analysis and calorimetry*, *104*(3), 1045–1050. https://doi.org/10.1007/s10973-010-1164-3

27 Farrukh, M. A., Butt, K.M., Chong, K.K., & Chang, W.S. (2019). Photoluminescence emission behavior on the reduced band gap of Fe doping in CeO_2-SiO_2 nanocomposite and photophysical properties. *Journal of Saudi Chemical Society*, *23*(5), 561–575. https://doi.org/10.1016/j.jscs.2018.10.002

28 Vigato, P.A., Peruzzo, V., & Tamburini, S. (2009). The evolution of β-diketone or β-diketophenol ligands and related complexes. *Coordination Chemistry Reviews*, *253*(7-8), 1099–1201. https://doi.org/10.1016/j.ccr.2008.07.013

29 Papatriantafyllopoulou, C., Efthymiou, C.G., Raptopoulou, C.P., Vicente, R., Manessi-Zoupa, E., Psycharis, V., ... & Perlepes, S.P. (2007). Initial use of the di-2-pyridyl ketone/sulfate "blend" in 3d-metal cluster chemistry: Preparation, X-ray structures and physical studies of zinc (II) and nickel (II) cubanes. *Journal of molecular structure*, *829*(1–3), 176–188. https://doi.org/10.1016/j.molstruc.2006.06.022

30 Lindoy, L.F., Moody, W.E., & Taylor, D. (1977). Mass spectral and nuclear magnetic resonance (proton and carbon-13) study of metal complexes of quadridentate ligands derived from 1, 2-diaminoethane and substituted. beta-diketones; x-ray structure of N,N'-ethylenebis(5,5-dimethyl-4-oxohexan-2-iminato)nickel (II). *Inorganic Chemistry*, *16*(8), 1962–1968. https://doi.org/10.1021/ic50174a027

31 Martell, A.E., Belford, R.L., & Calvin, M. (1958). Influence of fluorine substitution on the properties of metal chelate compounds—II copper (II) chelates of tetradentate ligands. *Journal of Inorganic and Nuclear Chemistry*, *5*(3), 170–181. https://doi.org/10.1016/0022-1902(58)80127-X

32 Raman, N., Ravichandran, S., & Thangaraja, C. (2004). Copper (II), cobalt (II), nickel (II) and zinc (II) complexes of Schiff base derived from benzil-2,4-dinitrophenylhydrazone with aniline. *Journal of Chemical Sciences*, *116*(4), 215–219. https://doi.org/10.1007/BF02708270

33 Bünzli, J.C.G., & Piguet, C. (2005). Taking advantage of luminescent lanthanide ions. *Chemical Society Reviews*, *34*(12), 1048–1077. https://doi.org/10.1039/B406082M

34 Hassan, W.M., Zayed, E.M., Elkholy, A.K., Moustafa, H., & Mohamed, G.G. (2013). Spectroscopic and density functional theory investigation of novel Schiff base complexes. *Spectrochimica Acta Part A: Molecular and Biomolecular Spectroscopy*, *103*, 378–387. https://doi.org/10.1016/j.saa.2012.10.058

35 Vishwakarma, P.K., Mir, J.M., & Maurya, R.C. (2016). Pyrone-based Cu (II) complexes, their characterization, DFT based conformational drift from square planar to square pyramidal geometry and biological activities. *Journal of Chemical Sciences*, *128*(4), 511–522. https://doi.org/10.1007/s12039-016-1048-6

36 Faisal, A., & Maktoof, A. (2025). Analysis of Physical Properties and Evaluation of Heavy Element Concentrations in Euphrates River's Fish in Nasiriyah City. *University of Thi-Qar Journal of Science*, *12*(1), 233–237. https://doi.org/10.32792/utq/utjsci/v12i1.1380

37 Al-khafaji, N., Al-khafaji, B.Y., & Al-Omar, D.K. (2024). Assessment the Effects of Heavy Elements on Some Hematological Parameter in CKD Patients Undergoing Hemodialysis in Thi-Qar Province/Iraq. *University of Thi-Qar Journal of Science*, *11*(2), 54-58. https://doi.org/10.32792/utq/utjsci/v11i2.1192

38 Ding, C.C., Wu, S.Y., Xu, Y.Q., Wu, L.N., & Zhang, LJ. (2018). DFT studies for three Cu (II) coordination polymers: geometrical and electronic structures, g factors and UV–visible spectra. *Chemical Physics*, *508*, 20–25. https://doi.org/10.1016/j.chemphys.2018.04.016

39 Bamigboye, M., Mustapha, A., & Danjuma, F. (2024). Bioactivity Assessment of 8-Hydroxyquinoline and Monosodium Glutamate Mixed Ligand Copper Complex: Experimental and Computational. *University of Thi-Qar Journal of Science*, *11*(2), 175–184. https://doi.org/10.32792/utq/utjsci/v11i2.1302

40 Wasielewski, M.R. (1992). Photoinduced electron transfer in supramolecular systems for artificial photosynthesis. *Chemical reviews*, *92*(3), 435–461. https://doi.org/10.1021/cr00011a005

41 Abruña, H.D., Denisevich, P., Umana, M., Meyer, T.J., & Murray, R.W. (1981). Rectifying interfaces using two-layer films of electrochemically polymerized vinylpyridine and vinylbipyridine complexes of ruthenium and iron on electrodes. *Journal of the American Chemical Society*, *103*(1), 1–5. https://doi.org/10.1021/ja00391a001

42 Markel, F., Ferris, N.S., Gould, I.R., & Myers, A.B. (1992). Mode-specific vibrational reorganization energies accompanying photoinduced electron transfer in the hexamethylbenzene/tetracyanoethylene charge-transfer complex. *Journal of the American Chemical Society*, *114*(15), 6208–6219. https://doi.org/10.1021/ja00041a045

43 Chambron, J.C., Harriman, A., Heitz, V., & Sauvage, J.P. (1993). Ultrafast photoinduced electron transfer between porphyrinic subunits within a bis (porphyrin)-stoppered rotaxane. *Journal of the American Chemical Society*, *115*(14), 6109–6114. https://doi.org/10.1021/ja00067a028

44 Koomson, D.A., Nicholson, J.H., Brogan, A.P., & Aldous, L. (2024). Re-assessing viologens for modern bio-electrocatalysis. *Chemical Science*, *15*(24), 9325–9332. https://doi.org/10.1039/D4SC02431A

45 Nucera, A., Rizzuto, C., Pipita, M. M., Barba Castagnaro, I., Termine, R., Barberi, R. C., & Castriota, M. (2024). The Effects of Polymerization on the Performance of Viologen-Based Electrochromic Devices. *Gels*, *10*(11), 694. https://doi.org/10.3390/gels10110694

46 Monk, P.M., Turner, C., & Akhtar, S.P. (1999). Electrochemical behaviour of methyl viologen in a matrix of paper. *Electrochimica acta*, *44*(26), 4817–4826. https://doi.org/10.1016/S0013-4686(99)00225-X

How to Cite: Avazova, O.B., Pirniyazov, K.K., & Rashidova, S.Sh. (2026). Rheological Properties of the Polymeric Preparative Form of Chitosan Nanoascorbate from *Bombyx mori*. *Eurasian Journal of Chemistry, 31, 2(122), 41–54* https://doi.org/10.31489/2959-0663/2-26-11

Article

Received: 26 March 2026 | Revised: 22 May 2026 | Accepted: 2 June 2026 | Published online: 3 June 2026

UDC 547.9:541.64

https://doi.org/10.31489/2959-0663/2-26-11

Oynavod B. Avazova, Kudrat K. Pirniyazov*, Sayyora Sh. Rashidova

Institute of Polymer Chemistry and Physics, Academy of Sciences of the Republic of Uzbekistan, Tashkent, Uzbekistan
*(*Corresponding author's e-mail: qudratpirniyazov8875@gmail.com)*

Rheological Properties of the Polymeric Preparative Form of Chitosan Nanoascorbate from *Bombyx mori*

Chitosan nanoascorbate samples were synthesized by controlling the pH of the solution and the ratio of the initial components: ascorbic acid and chitosan derived from *Bombyx mori*. In this study, the rheological properties of polymeric preparative forms based on chitosan nanoascorbate and methylhydroxyethylcellulose systems at different concentrations were investigated. The chitosan nanoascorbate samples were obtained by regulating the ratio of Bombyx mori chitosan to ascorbic acid and adjusting the pH of the reaction medium during the synthesis process. In the initial 0.025 % chitosan nanoascorbate solution, the viscosity increased from 0.33 Pa·s to 4.14 Pa·s under shear, indicating possible hydrodynamic clustering and the formation of temporary aggregates between nanoparticles. In dilute systems containing 0.0125 % chitosan nanoascorbate and 0.1 % methylhydroxyethylcellulose, the viscosity increased from 3.1 Pa·s to 5.0 Pa·s, suggesting interactions between polymer chains and nanoparticles, although a fully developed spatial network was not formed. In the system with intermediate concentrations (0.025 % chitosan nanoascorbate : 0.2 % methylhydroxyethylcellulose), the viscosity varied from 6.2 Pa·s to 10.9 Pa·s and exhibited near-Newtonian flow behavior. In the system with the highest concentration (0.05 % chitosan nanoascorbate : 0.4 % methylhydroxyethylcellulose), the viscosity decreased from 45 Pa·s to 18 Pa·s, indicating pseudoplastic behavior and the partial disruption of the three-dimensional spatial network under shear. Frequency analysis and the Power-law model confirmed the viscosity and elastic properties of these two types of systems.

Keywords: chitosan nanoascorbate, *Bombyx mori*, polymeric preparative form, storage modulus, loss modulus, consistency coefficient, flow behavior index, dynamic viscosity, shear stress

1 Introduction

Polycationic and polyanionic polysaccharides found in marine algae, crustaceans, and insects are considered promising sources of biologically active compounds. Among these natural biopolymers, chitosan (CS) is of particular interest. CS is a non-toxic, biocompatible, and biodegradable polysaccharide that exhibits antimicrobial, antioxidant, and immunostimulating properties. In addition, CS can be used in medicine as a material that promotes rapid wound-healing and participates in tissue regeneration processes, as well as a carrier for biologically active compounds such as ascorbic acid (AA) [1–3]. In agriculture, CS and its derivatives are used as agents for combating plant and animal diseases and as growth stimulants [4]. It is well known that CS is insoluble in water due to strong intermolecular interactions and hydrogen bonding between macromolecules; however, it dissolves readily in dilute organic acids. Therefore, the preparation of water-soluble derivatives of CS significantly expands its applications in agriculture, biotechnology, and medicine [3, 5]. Among these derivatives, chitosan ascorbate (CSA)**,** a salt formed with ascorbic acid (AA)**,** and its nanostructured form, chitosan nanoascorbate (CSNA)**,** exhibit high biological activity. These materials have been reported to possess wound-healing, antimicrobial, and plant growth-stimulating properties [4, 6].

The synthesized CSA and CSNA samples are environmentally safe and exhibit antimicrobial activity against diseases occurring in plant and animal organisms [6, 7]. The investigation of the interaction mechanisms between CS and AA is currently one of the important scientific issues, since the interaction processes between CS and AA strongly depend on the pH of the medium and temperature. According to the literature data [8, 9], the formation of CSA compounds can proceed via three main mechanisms. In the first mechanism, covalent donor–acceptor complexes are formed. This interaction is based on the interaction between the enolic hydroxyl (OH) group located at the C3 carbon of AA and the amino (NH_2) groups of CS. The reaction proceeds in an aqueous medium at room temperature. In this case, the lactone ring of AA remains intact, while the amino groups of CS are in a protonated state [8].

In the literature, it has been reported that at pH 5–6.5 and a temperature of approximately 25 °C, the interaction between chitosan and ascorbic acid in aqueous solution over more than 6 hours may lead to the formation of a covalent imine (Schiff base) linkage [9, 10]. This can be explained by the fact that ascorbic acid, in the presence of dissolved oxygen in aqueous media, is partially oxidized to dehydroascorbic acid, which contains reactive carbonyl groups. It should be noted that ascorbic acid is unstable in aqueous solution, and its enolic form is readily susceptible to oxidation depending on the reaction conditions. Therefore, the interaction between amino groups of chitosan and carbonyl groups (including those formed via oxidation of ascorbic acid to dehydroascorbic acid) results in the formation of an imine (Schiff base) linkage between chitosan and ascorbic acid [10].

The third mechanism proceeds through the thermal opening of the lactone ring of AA. Under an inert nitrogen atmosphere at 60–70 °C and pH 6–7, the opening of the lactone ring of AA leads to the formation of carboxyl (COO^-) groups. These groups react with the amino groups of CS, resulting in the formation of covalent amide bonds. The formation of these bonds has been confirmed in the literature by NMR spectroscopy [11, 12].

In addition, chitosan nanoascorbate (CSNA) is commonly obtained by forming nanostructured complexes of CS with AA using the ionotropic gelation method in the presence of sodium tripolyphosphate (STPP). In this process, nanoparticles are formed due to electrostatic interactions between the protonated positively charged amino groups of CS and the negatively charged phosphate groups of STPP. The size of the nanoparticles mainly depends on the acid concentration and the degree of deacetylation (DD) of CS. CS with a higher DD contains a greater number of free amino groups, which increases the charge density and consequently the number of effective electrostatic cross-linking sites with STPP [13].

Although the biological properties of chitosan nanoderivatives have been widely studied, information in the literature on obtaining polymeric preparative forms of chitosan nanoderivatives based on AA and their application in sericulture remains limited [14]. Therefore, in the present study, a polymeric preparative form of CSNA was obtained in the presence of a methylhydroxyethylcellulose (MHEC) solution for potential application in sericulture. MHEC was selected because of its low toxicity, easy biodegradability in nature, and its ability to preserve the activity of CSNA**.** In addition, MHEC acts as an effective thickening agent for the formation of polymeric preparative formulations.

Currently, various polymer-based preparations are used to control diseases of the silkworm and to stimulate its growth and development. These preparations are mainly produced in powder, gel, and solution forms. In addition to their biochemical activity, it is also important to evaluate the resistance of these formulations to physical and mechanical effects during their application.

In addition, the spraying technology of preparations plays an important role in the effective application of pesticides, biopreparations, and plant protection agents in agriculture. During the spraying process, the physicochemical and rheological properties of the solution determine droplet formation, droplet size, adhesion to leaf surfaces, and dispersion behavior in the atmosphere. Therefore, in recent years, the investigation of the rheological properties of formulation systems has become an important research direction in agrochemistry and chemical sciences.

According to the literature, the rheological properties of spraying solutions significantly influence the atomization and dispersion mechanisms of droplets. In particular, an increase in solution viscosity leads to an increase in droplet diameter, which in turn reduces the efficiency of spraying [15].

At the same time, the addition of polymeric agents can modify the viscoelastic properties of the solutions, thereby improving the stability of droplets during the spraying process [16]. In spraying technology, the viscosity and surface tension of the solution are considered the main parameters. Studies have shown that solutions with low viscosity undergo atomization more easily and form smaller droplets. However, such droplets can disperse more readily in the atmosphere, which may reduce the efficiency of the applied preparation. Conversely, solutions with higher viscosity form larger droplets that exhibit better retention on plant surfaces [17].

In recent years, the use of polymer-based adjuvants has been considered one of the effective approaches for improving spraying technology. The long-chain structure of polymer molecules limits droplet breakup and enhances spray stability. This behavior is closely related to the non-Newtonian rheological properties of polymer solutions, in which the flow mechanism depends on the applied shear rate [18]. The pseudoplastic behavior of polymer solutions is associated with the alignment and deformation of macromolecular chains under shear flow, accompanied by a reduction in intermolecular interactions. As a result, an increase in shear rate leads to a decrease in apparent viscosity. This effect plays an important role in spraying systems, where reduced viscosity during pumping facilitates atomization [19]. In contrast, certain polymer and colloidal sys-

tems may exhibit dilatant behavior, where increasing shear rate intensifies particle interactions and leads to the formation of transient structures, resulting in increased viscosity.

In agrochemical formulations, solutions with optimized rheological properties ensure uniform spreading and retention on plant surfaces. Therefore, recent studies focus on key rheological parameters such as the consistency coefficient and flow behavior index. It has been demonstrated that controlling solution viscosity using polymer adjuvants improves droplet size distribution and enhances biological efficiency [19–21]. In addition, chitosan-based systems are widely studied due to their unique physicochemical properties, biocompatibility, and ability to form stable nano-sized structures [22–24]. Particularly, chitosan nanoparticles and their derivatives, including antioxidant-modified systems such as nanoascorbates, demonstrate enhanced stability and functional performance in solution [24, 25]. Furthermore, biomacromolecules derived from Bombyx mori, such as silk fibroin, are extensively used in the design of advanced polymeric systems due to their structural stability, biodegradability, and excellent mechanical properties [26, 27].

Thus, the rheological properties of spray solutions, including viscosity and non-Newtonian flow behavior, represent critical factors governing droplet formation and deposition efficiency on plant surfaces. Control of these parameters is essential for optimizing spraying performance and improving the effectiveness of agrochemical formulations. The main aim of this study was to obtain a polymeric preparative form of chitosan nanoascorbate (CSNA) derived from Bombyx mori and to investigate its rheological properties. Particular attention was given to evaluating the influence of component concentration on the flow behavior and structural characteristics of the system. Chitosan nanoascorbate (CSNA) represents a promising functional biopolymer system that combines antioxidant activity with tunable rheological properties, making it a potential candidate for the development of advanced spraying formulations with enhanced stability and performance.

2 Experimental

2.1 Synthesis of Chitosan Nanoascorbate Samples

In this study, CS derived from *Bombyx mori* (*B.M.*) silkworm pupae with a molecular weight of 140 kDa and a degree of deacetylation (DD) of 84 % was used. The molecular weight of chitosan was determined by viscometry using the Mark–Houwink equation based on intrinsic viscosity [1]. The intrinsic viscosity was obtained by extrapolation from the plot of reduced viscosity versus solution concentration. In addition, the molecular weight of chitosan nanoascorbate was determined using the dynamic light scattering (DLS) method. The DD of the initial CS samples was determined by conductometric titration in 0.1 N hydrochloric acid using a *Mettler Toledo* conductometer (USA). CS was obtained from *B.M.* silkworm pupae through deproteinization, demineralization, and subsequent deacetylation in a 50 % sodium hydroxide solution at 120 °C for 3 h. This process was carried out in the pilot-scale facility of the Institute of Polymer Chemistry and Physics of the Academy of Sciences of the Republic of Uzbekistan following the procedure described in the literature [1].

CSNA was synthesized in an aqueous medium by the ionotropic gelation method. During the process, a 0.5 % solution of STPP was used as a stabilizing agent based on electrostatic interactions. The synthesis was carried out by controlling the ratios of the initial components and the pH of the solution. To determine the amount of unreacted (free) ascorbic acid in the reaction system, the liquid phase was separated by centrifugation. The ascorbic acid (AA) content in CSNA was calculated based on the determination of free AA in the liquid phase by alkaline titration using phenolphthalein as an indicator. The degree of AA binding was calculated according to the ratio (M_{AA})exp./(M_{AA})calc. [24].

The obtained products were freeze-dried at −48 °C for 5–6 h using an "*Alpha Christ*" lyophilizer (Germany). The yield of the final products was evaluated as the ratio of the calculated mass to the experimentally obtained mass of the substance. The component ratios were calculated based on the molar concentrations of the initial substances. In all syntheses, a 0.05 M aqueous solution of ascorbic acid was used, while the concentration of chitosan was set at 0.2 M. The volume of the stabilizer (STPP) was determined based on its molar ratio relative to the other components. The pH of the reaction system was measured at the end of the synthesis at 25 °C using a *Bante-210* pH meter (China). Solutions of AA, the titrant, and STPP were prepared using an analytical procedure: the exact dry mass of the substances was weighed on an analytical balance, dissolved in distilled water, and stirred with a magnetic stirrer until complete dissolution.

2.2 Preparation of Solutions for Rheological Measurements

In the experiments, polymeric preparative forms based on CSNA and MHEC were prepared using their solutions in 2 % acetic acid at different concentrations. The studied systems included: No. 1 — 0.2 %

MHEC; No. 2 — 0.025 % CSNA; No. 3 — 0.0125 % CSNA and 0.1 % MHEC; No. 4 — 0.025 % CSNA and 0.2 % MHEC; and No. 5 — 0.05 % CSNA and 0.4 % MHEC. During the preparation of the solutions, accurately weighed amounts of the components were dissolved in 2 % acetic acid and stirred for 24 h using a magnetic stirrer until complete dissolution.

2.3 Rheological Measurement Method

The rheological properties of the samples were studied using an Anton Paar MCR 92 rotational rheometer (Austria). During shear flow of the solutions, macromolecular chains undergo deformation-induced orientation, and the samples exhibit non-Newtonian flow behavior over a wide concentration range. The rheological properties of CSNA samples were investigated using a cylindrical measuring system. The rheometer allows measurements to be performed in both rotational and oscillatory modes. To evaluate the structural characteristics and deformation behavior of the samples, the variation of shear stress (τ) was monitored during the increase and decrease of the shear rate (γ). Based on the obtained results, the rheological behavior of the solutions was analyzed.

Rheological measurements were performed using an Anton Paar MCR 92 rheometer under controlled temperature conditions (±0.1 °C). The instrument operates with a high level of precision, where the relative error in viscosity measurements does not exceed ±1 %, and the accuracy of shear stress determination is within ±0.5–1 %, according to the manufacturer's specifications.

These instrumental parameters ensure reliable and reproducible determination of viscoelastic properties. However, statistical error analysis (e.g., standard deviation) was not applied in this study, as replicate measurements for individual data points were not performed. Therefore, graphical data are presented as single experimental values with high instrumental accuracy rather than statistically averaged datasets.

2.4 Dynamic Light Scattering (DLS) Analysis

Particle size determination was carried out using dynamic light scattering (DLS) on a *BeNano 90* instrument (China). CSNA samples were dissolved in 2 % acetic acid at a concentration of 0.25 % and kept at room temperature (~25 °C) for approximately 24 h until complete dissolution was achieved. DLS measurements were not performed at a concentration of 0.025 % due to the inherent sensitivity limits of the DLS technique and the dependence of scattering intensity on particle size and concentration, which results in a low signal-to-noise ratio and unreliable measurements. Prior to measurement, the solutions were filtered through a microporous membrane filter (pore size 10–20 μm) to remove large particles and prevent clogging of the DLS cuvette. The filtered solution was transferred into a DLS cuvette (up to 1 ml), and measurements were performed to determine the average hydrodynamic diameter and particle size distribution. Each measurement was repeated 3–5 times to ensure statistical reliability. Based on the hydrodynamic diameter, the molecular weight (M) of the polymer was estimated using the following relationship:

$$Rh = k\,M^{\nu}, \tag{1}$$

where M is the molecular weight of the polymer (g/mol); k is the empirical coefficient specific to the polymer and solvent; ν is a scaling exponent dependent on the polymer chain conformation.

The values of k and ν were determined using standards of known molecular weight.

2.5 Atomic Force Microscopy (AFM) Analysis of CSNA

The morphology and particle size of CSNA were analyzed using atomic force microscopy (AFM) on an Agilent 5500 instrument (Agilent, USA). Silicon cantilevers with a spring constant of 9.5 $N \cdot m^{-1}$ and a resonant frequency of 145 kHz were used.

For sample preparation, diluted aqueous solutions of CSNA were deposited onto a clean glass substrate and allowed to dry under ambient conditions prior to analysis.

3 Results and Discussion

3.1 Results of DLS Analysis: Particle Size Distribution and Molecular Weight of CSNA, MHES, and Polymeric Preparative Forms

For this purpose, dynamic light scattering (DLS) measurements were performed using a BeNano 90 instrument. The molecular weight and particle size distribution of CSNA in solution were evaluated using samples synthesized at an initial component molar ratio of CS:AA:STPP = 4:1:0.25. The results showed that particles in the 0.025 % CSNA solution were distributed within the size range of 220–651 nm. The average hydrodynamic diameter was 567 nm, while the main peak in the DLS profile was observed at approximately 360 nm, indicating that particles with an average size of around 360 nm are predominant in the system.

Analysis of the particle size distribution revealed that approximately 50 % of the particles have a diameter of about 320 nm. It should be noted that in the present study, the term “nanoascorbate” is used not solely with respect to the geometric size of the particles, but rather to their nanostructured nature. The particle sizes in the range of 200–700 nm determined by DLS represent the hydrodynamic diameter of aggregates formed in solution. These aggregates consist of primary nanoscale domains formed as a result of ionotropic gelation and intermolecular interactions. Therefore, despite the overall particle size exceeding 100 nm, the system can be considered nanostructured in nature [28]. The obtained results are presented in Figure 1.

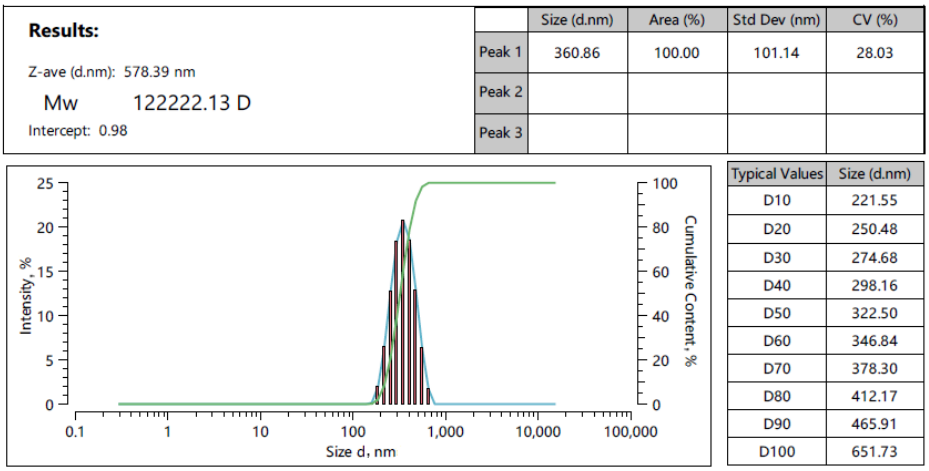

Figure 1. Results of DLS analysis: particle size distribution and molecular weight of a 0.25 % CSNA solution

MHEC was used as an auxiliary component in the preparation of the polymer preparative form of CSNA in order to regulate the viscosity of the solution. MHEC is a cellulose derivative that, unlike chitosan, does not contain amino groups and is mainly composed of hydroxyl (–OH), methoxy (–OCH_3), and hydroxyethyl (–OCH_2CH_2OH) ether groups. Therefore, MHEC is a neutral, non-ionic polymer that is soluble in water and some organic solvents. As a result, the DLS behavior of MHEC solutions differs significantly from that of chitosan solutions. MHEC does not interact chemically with acetic acid due to the absence of amino groups. Furthermore, since MHEC does not contain carboxyl groups typical of acidic compounds, it does not chemically interact with the amino groups of CSNA. However, in diluted solutions, acetic acid partially dissociates into ions, which may weaken and rearrange intermolecular hydrogen bonds between macromolecules, potentially leading to phase separation and the formation of two distinct phases. According to the DLS results, the particle size distribution of the 0.25 % MHEC solution prepared in 2 % acetic acid showed that the particle sizes were mainly in the range of 740–2672 nm (Fig. 2).

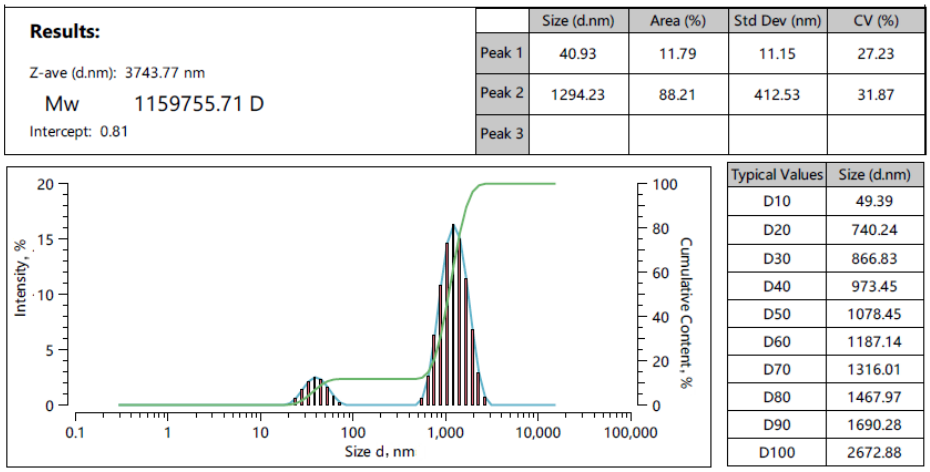

Figure 2. DLS results and particle size distribution of the 0.2 % MHEC solution

It can be concluded that, in the polymeric preparative form (PPF) of the CSNA solution, particles in the size range of 300–400 nm correspond to CSNA macromolecules, since such particles were not observed in the MHEC solution. In contrast, particles in the range of 700–2672 nm can be attributed to MHEC macromolecular structures. Analysis of the particle size distribution showed that less than 20 % of the particles fall within the 295–442 nm range, which can be associated with the presence of nanoscale CSNA structures within the polymeric preparative form. The obtained results are presented in Figure 3.

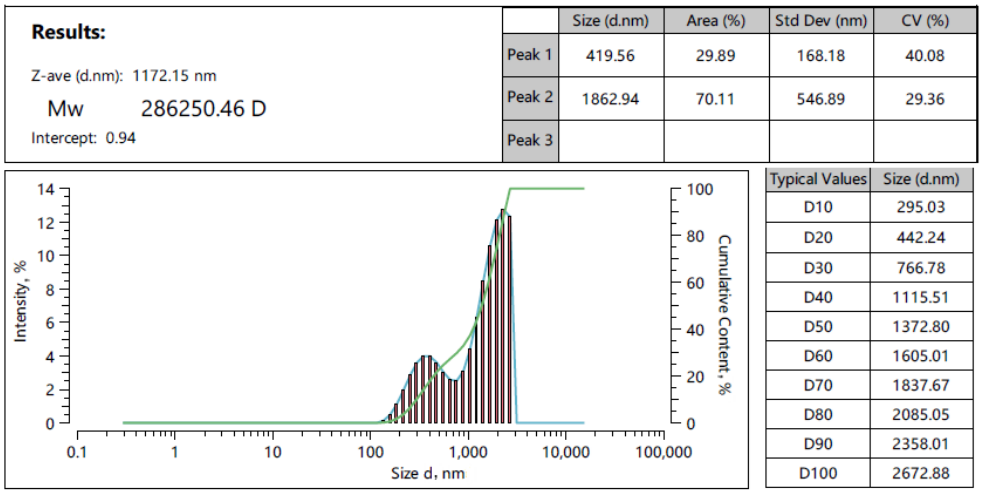

Figure 3. DLS results and particle size distribution of the CSNA PPF solution (CSNA 0.025 % and MHES 0.2 %)

3.2 Atomic Force Microscopy (AFM) Results

The obtained AFM results confirm the presence of particles with sizes ranging from 200 to 700 nm in the composition of chitosan nanoascorbate. The results are presented in Figure 4.

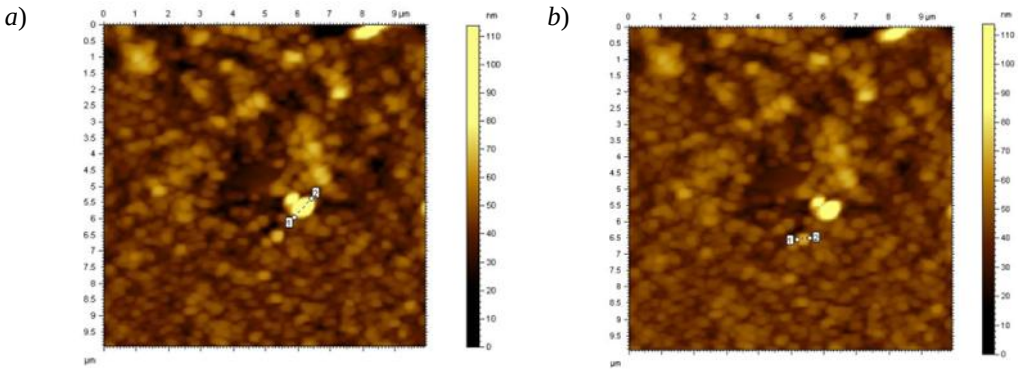

Figure 4. AFM images of CSNA obtained on a pilot-scale unit (CS:AA:STPP = 4:1:0.25): (*a*) particle size up to 709 nm; (*b*) particle size up to 200 nm

The AFM results are in good agreement with the particle sizes determined by DLS for the CSNA samples. In particular, according to the DLS analysis, the particle size of CSNA samples was found to be in the range of 220–651 nm, whereas AFM analysis showed a size range of 200–700 nm. Furthermore, due to the relatively large particle size and molecular weight of MHEC, the polymeric preparative form of CSNA and MHEC samples were not analyzed by AFM.

3.3 Rheological Properties of CSNA and Its Polymeric Preparative Formulation Solutions

The polymeric preparative formulation based on chitosan nanoascorbate (CSNA) is applied in solution form via spray application onto mulberry leaves and silkworms. During this process, viscosity (η) plays a crucial physicochemical role, as it directly influences droplet formation, dispersion behavior, surface adhesion, and ultimately the biological efficiency of the formulation. Therefore, the resistance of CSNA-based systems to mechanical deformation during spraying, as well as their viscosity characteristics, was investigated using rheological measurements.

In the rheological study, an amplitude sweep test was first performed to evaluate the response of the prepared solutions to increasing mechanical deformation. Based on the obtained results, the dependences of the storage modulus (G') and loss modulus (G'') on strain amplitude (γ, %) were plotted (Fig. 5).

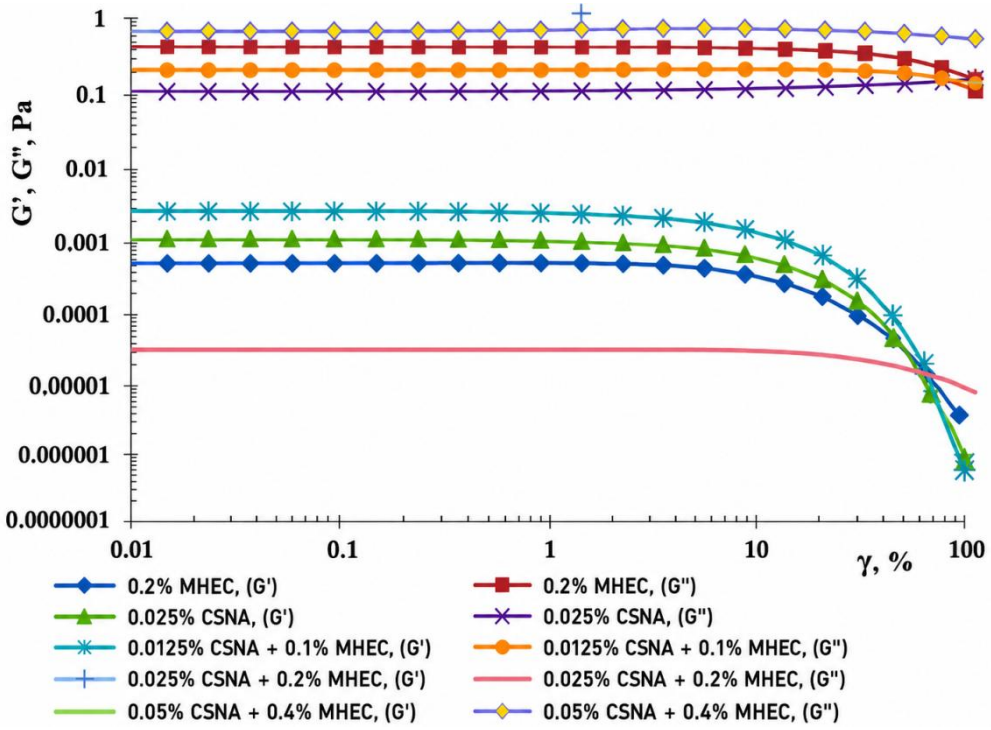

Figure 5. Dependence of storage (G') and loss (G'') moduli on shear strain amplitude (γ, %):
(*1*) 0.2 % MHEC; (*2*) 0.025 % CSNA; (*3*) 0.0125 % CSNA + 0.1 % MHEC; (*4*) 0.025 % CSNA + 0.2 % MHEC;
(*5*) 0.05 % CSNA + 0.4 % MHEC

As shown in Figure 5, all studied systems exhibit G″ values higher than G′ within the shear strain range up to approximately 10 %, indicating the predominance of viscous behavior in this region. This indicates that the samples exhibit a sol/viscoelastic liquid structure, in which the internal structure remains weakly developed in the initial state. The systems behave as viscoelastic fluids, demonstrating both elastic and viscous responses. This behavior suggests the presence of transient macromolecular network formation and significant intermolecular interactions.

With increasing strain amplitude (γ) in the range of 20–100 %, the value of G′ decreases sharply, while G″ decreases more gradually. Under these conditions, structural disruption occurs in the samples, leading to a transition from a more elastic state to a predominantly liquid-like behavior.

Sample No. 1 exhibits pronounced elastic behavior, where G′ decreases from approximately 7.6×10^{-4} to 7.13×10^{-7}, while G'' decreases from about 0.589 to 0.122. This indicates the presence of a highly interconnected elastic structure in the system. Samples No. 2 and No. 3 show semi-elastic behavior, with the initial values of G' and G'' being lower than those of sample No. 1. These systems are characterized by a moderately branched structure and relatively high chain mobility. Samples No. 4 and No. 5 behave as highly viscous systems with increased internal friction. In sample No. 5, the value of G'' is relatively high (around 0.613), indicating significant dissipative energy loss within the system. This suggests rapid molecular rearrangement processes. For all samples, the structural disruption region under deformation occurs within the strain amplitude range of approximately $\gamma \approx 6$–10 %. No intersection between G' and G'' was observed for any of the samples, indicating that the systems did not undergo a transition to a purely liquid state and retained their gel-like behavior.

As shown in Table 1, for samples No. 1–5, the dominance of G'' over G' ($G'' > G'$) was observed across the entire frequency range. In particular, for samples 1–3 at low frequencies ($\omega \approx 0.3$–1 rad/s), the values of G' were in the range of 10^{-7}–10^{-6} Pa, whereas G'' reached 10^{-2}–10^{-1} Pa. As a result, the loss tangent ($\tan\delta = G''/G'$) reached values up to approximately 20000. Although both G'' and G' increased proportionally, the G' values remained extremely low (10^{-7}–10^{-5} Pa).

Table 1

Frequency dependence of storage modulus (G') and loss modulus (G'') for samples No. 1–5

ω	No. 1		No. 2		No. 3		No. 4		No. 5	
(rad/s)	*G'*	*G"*	*G'*	*G"*	*G'*	*G"*	*G'*	*G"*	*G'*	*G"*
0.314	3.22E-07	0.006	4.86E-07	0.010	1.19E-07	0.002	0.000	0.004	0.010	0.022
0.521	5.58E-07	0.011	3.20E-07	0.006	5.45E-07	0.011	6.38E-07	0.013	0.005	0.032
0.866	1.93E-04	0.025	4.86E-07	0.010	4.57E-07	0.009	1.07E-06	0.021	0.004	0.048
1.440	1.32E-06	0.026	1.13E-06	0.023	1.24E-06	0.025	1.27E-06	0.025	0.005	0.078
2.380	2.52E-06	0.050	1.61E-06	0.032	1.13E-06	0.023	2.32E-06	0.046	0.013	0.131
3.960	4.01E-06	0.080	2.78E-06	0.056	5.90E-07	0.012	3.60E-06	0.072	0.015	0.214
6.570	6.93E-06	0.139	8.17E-06	0.163	4.53E-06	0.091	6.44E-06	0.129	0.002	0.342
10.900	1.27E-05	0.255	4.62E-06	0.092	8.52E-06	0.170	1.42E-05	0.284	2.85E-05	0.570
18.100	2.60E-05	0.519	1.13E-05	0.226	1.65E-05	0.330	2.94E-05	0.587	4.77E-05	0.954
30.000	5.84E-05	1.168	3.90E-05	0.780	3.27E-05	0.653	7.13E-05	1.427	8.64E-05	1.728
49.900	1.38E-04	2.761	9.63E-05	1.926	6.58E-05	1.316	1.80E-04	3.603	1.65E-04	3.299
82.800	3.38E-04	6.764	2.26E-04	4.525	1.30E-04	2.603	4.52E-04	9.049	3.76E-04	7.525
137.000	8.69E-04	17.380	6.33E-04	12.663	3.86E-04	7.715	1.19E-03	23.776	8.66E-04	17.321
228.000	3.15E-03	62.986	3.05E-03	61.080	2.12E-03	42.473	4.12E-03	82.355	3.20E-03	63.927
379.000	8.39E-03	167.870	5.06E-03	101.110	6.46E-03	129.200	9.86E-03	197.090	9.37E-03	187.370
628.000	6.87E-02	1374.100	6.00E-02	1200.100	6.54E-02	1309.000	6.01E-02	1202.700	5.86E-02	1171.500

Based on the data presented in Table 1, the corresponding graph is shown in Figure 6. Analysis of the graph indicates that samples 1–3 exhibit predominantly viscous behavior, with no formation of a three-dimensional network structure, and free relaxation of macromolecular chains is observed. With increasing frequency, the G'' values increase exponentially, indicating restricted molecular mobility under dynamic conditions. However, the very low values of G' confirm the instability of the network formation mechanism and indicate that the systems exist as viscous liquid dispersions. In these samples, the dominance of G'' results in pronounced flow behavior and relatively short relaxation times.

These solutions can be easily sprayed onto mulberry leaves without clogging the nozzle. However, a limitation of samples No. 1–3 is the very high tan δ values, indicating a predominantly liquid phase. As a result, after deposition on the leaf surface the solution may exhibit low adhesion and may partially flow off, leading to non-uniform coverage.

In contrast, for samples No. 4 and No. 5, at low frequencies (0.314–3.96 rad s^{-1}) the values of $G' \approx 0.009$–0.015 Pa and $G'' \approx 0.02$–0.21 Pa is relatively close, with tan $\delta \approx 2$–15.

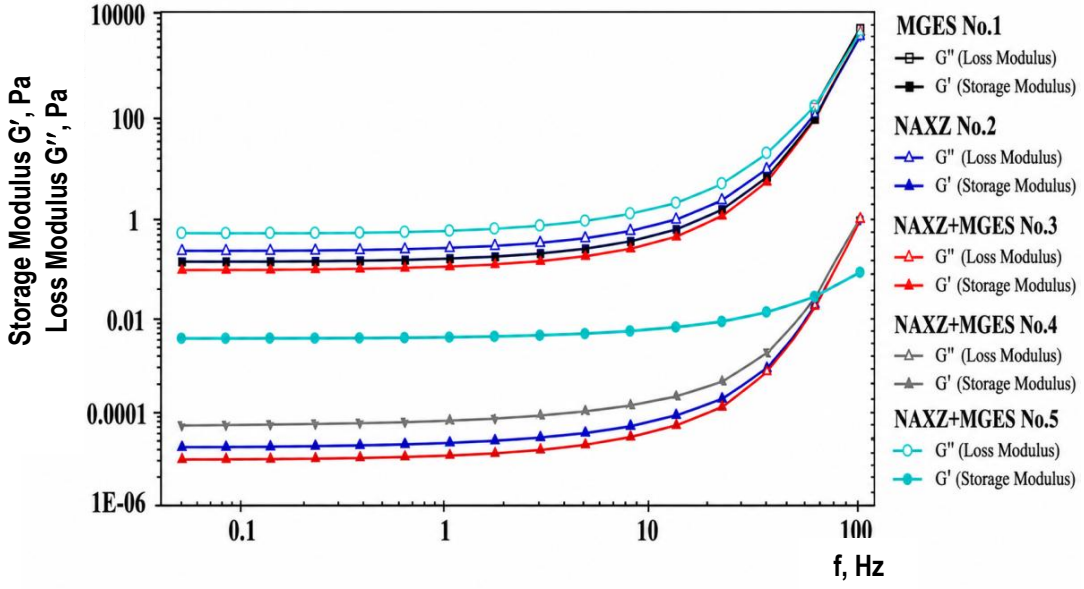

Figure 6. Dependence of the storage modulus (G') and loss modulus (G″) on frequency (f)

This indicates that the systems of samples No. 4-5 behave as viscoelastic liquids with the presence of partially developed intermolecular structures. At frequencies around 6–10 rad s^{-1}, a sharp decrease in G' (from 0.002022 to 2.85×10^{-5} Pa) and a significant increase in tan δ (up to ≈20000) were observed. This behavior can be attributed to the breakdown and destabilization of the network structure in these systems. The relaxation time is relatively short, approximately 1–3 s. Because samples No. 4–5 exhibit viscoelastic solution behavior, their spraying performance and adhesion to mulberry leaves are expected to be higher than those of samples No. 1–3. At higher frequencies, all samples (No. 1–5) show characteristics typical of flowing liquid systems.

Thus, the rheological frequency analysis shows that in the initial samples No. 1–3, the dominance of G'' and the very high values of tan δ confirm the predominantly viscous character of the system and the absence of a stable macromolecular network. In contrast, for samples No. 4-5, the noticeable values of G' at low frequencies indicate the formation of a temporary dynamic network structure. With increasing frequency, this network gradually breaks down and the system transitions to a dissipative regime. Such behavior is characteristic of biopolymer systems stabilized by electrostatic interactions and hydrogen bonding.

In addition, the changes in dynamic viscosity (η, mPa·s) and shear stress (τ, Pa) of MHEC, CSNA, and their mixed solutions with increasing shear rate (γ, s^{-1}) were investigated, and the results are presented in Table 2.

Table 2

Dependence of shear stress (τ) and viscosity (η) on shear rate (γ) for samples No. 1–5

γ, s^{-1}	No. 1		No. 2		No. 3		No. 4		No. 5	
	τ	η	τ	η	τ	η	τ	η	τ	η
0.100	0.001	5.730	–	–	0.000	3.167	–	–	0.005	45.740
0.171	0.001	6.591	–	–	0.000	2.506	–	–	0.008	45.416
0.291	0.002	7.167	–	–	0.001	2.250	0.002	6.257	0.013	45.031
0.497	0.004	7.541	–	–	0.001	2.176	0.003	6.257	0.022	44.577
0.849	0.007	7.784	0.000	0.340	0.002	2.197	0.005	6.257	0.037	44.042
1.450	0.012	7.945	0.001	0.421	0.003	2.275	0.009	6.257	0.063	43.408
2.470	0.020	8.054	0.001	0.502	0.003	2.393	0.015	6.257	0.106	42.656
4.230	0.034	8.134	0.003	0.599	0.006	2.537	0.026	6.257	0.177	41.773
7.210	0.059	8.197	0.005	0.714	0.011	2.705	0.045	6.257	0.294	40.731
12.300	0.102	8.249	0.010	0.851	0.020	2.891	0.077	6.257	0.487	39.506
21.000	0.175	8.294	0.021	1.014	0.036	3.097	0.132	6.257	0.801	38.068
35.800	0.299	8.336	0.043	1.209	0.065	3.320	0.224	6.257	1.306	36.388
61.300	0.514	8.376	0.088	1.442	0.119	3.561	0.383	6.258	2.108	34.441
104.000	0.878	8.415	0.179	1.719	0.218	3.821	0.654	6.261	3.364	32.196
179.000	1.510	8.454	0.365	2.049	0.399	4.102	1.120	6.278	5.292	29.642
305.000	2.588	8.492	0.746	2.446	0.731	4.405	1.936	6.352	8.168	26.808
519.000	4.430	8.530	1.517	2.915	1.343	4.727	3.475	6.697	12.361	23.767
887.000	7.599	8.568	3.086	3.476	2.455	5.077	7.527	8.477	18.378	20.703
1510.000	13.034	8.606	6.275	4.143	–	–	16.568	10.941	27.243	17.993

Based on the data presented in Table 2, the experimental rheological properties of the studied solutions (samples No. 1–5) were investigated under steady shear conditions in order to quantitatively evaluate their flow behavior. For all samples, an increase in the shear rate (γ) from 0.1 to 1510 s^{-1} resulted in a corresponding increase in the shear stress (τ). The relationship between shear stress (τ) and shear rate (γ) was analyzed using the Power-law model. The parameters of this model provide important information about the internal structure and flow characteristics of the solution systems.

$$\tau = K\,\gamma^{n}, \tag{1}$$

where K is the consistency coefficient and n are the flow behavior index.

The calculated n and K parameters for the investigated solutions are presented in Table 3.

The value of the flow behavior index (n) allows evaluation of the non-Newtonian behavior of the system: when $n < 1$, the fluid exhibits pseudoplastic behavior; when $n = 1$, Newtonian behavior is observed; and when $n > 1$, the system demonstrates dilatant rheological behavior [18, 19]. The consistency coefficient (K)

characterizes the overall viscosity level of the solution, and an increase in its value indicates stronger intermolecular interactions within the system.

Table 3

Power-law rheological parameters (flow behavior index n, consistency index *K*) and correlation coefficients (R^2) for different CSNA/MHEC systems

No.	Sample composition	*n*	*K*, Pa·s^n	R^2	Rheological behavior
1	0.2 % MHEC	1.04	6.3	0.999	Dilatant
2	0.025 % CSNA	1.32	0.28	0.997–0.999	Strongly dilatant
3	0.0125 % CSNA : 0.1 % MHEC	1.11	2.4	0.998	Moderately dilatant
4	0.025 % CSNA : 0.2 % MHEC	1.00	6.2	0.999	Near-Newtonian behavior
5	0.05 % CSNA : 0.4 % MHEC	0.90	36	0.995-0.998	Pseudoplastic behavior

The obtained rheological parameters demonstrate variation in flow behavior ranging from dilatant to pseudoplastic depending on system composition. As can be seen from Table 3, for sample No. 1 (0.2 % MHEC), the values of $n = 1.04$ and $K = 6.3$ Pa·s^n were determined. Since the n value is slightly greater than 1, the solution exhibits weakly dilatant behavior. This indicates that the internal resistance of the solution increases with increasing shear rate. Such behavior can be explained by the orientation of the chains under shear, the formation of temporary associations between macromolecules, and an increase in the hydrodynamic volume.

For sample No. 2 (0.025 % CSNA), the values $n \approx 1.32$ and $K \approx 0.28$ Pa·s^n were observed. The considerably higher *n* value indicates strongly dilatant rheological behavior. In this case, an increase in shear rate enhances intermolecular interactions and promotes the formation of temporary structures between macromolecules. However, the relatively low *K* value indicates that the overall viscosity of the solution is comparatively low. This can be attributed to the low polymer concentration and the weak intermolecular interactions between macromolecules. For sample No. 3 (0.0125 % CSNA : 0.1 % MHEC), the values $n \approx 1.11$ and $K \approx 2.4$ Pa·s^n were determined for the complex system. This sample exhibits moderately dilatant behavior, which may result from weak interactions between CSNA and MHEC macromolecules, leading to the formation of temporary aggregates. Under shear conditions, these aggregates undergo rearrangement, which determines the rheological behavior of the solution. For sample No. 4 (0.025 % CSNA : 0.2 % MHEC), the values $n \approx 1.00$ and $K \approx 6.2$ Pa·s^n were observed.

The solution of this sample exhibits near-Newtonian rheological behavior. This indicates that the macromolecular structure of the system is relatively stable, and variations in shear rate do not significantly affect the viscosity. Such behavior can be explained by the uniform distribution of polymer chains, the presence of dynamic equilibrium between macromolecules, and the partial stability of the structure. For sample No. 5 (0.05 % CSNA : 0.4 % MHEC), the values $n \approx 0.90$ and $K \approx 36$ Pa·s^n were determined. Since $n < 1$, the system exhibits pseudoplastic rheological behavior, which is the most typical rheological regime for polymer solutions. With increasing shear rate, macromolecules become oriented, the chains are stretched, and the structure is partially disrupted, resulting in a decrease in viscosity. The relatively high *K* value indicates a higher polymer concentration in the solution, leading to stronger intermolecular associations and enhanced macromolecular interactions.

In addition, the Power-law model analysis showed that with increasing concentration in CSNA–MHEC systems, the flow behavior index (*n*) decreases. In low-concentration samples, $n > 1$, indicating dilatant behavior, whereas in higher-concentration systems $n < 1$ and higher *K* values confirm the formation of a dynamic spatial network. This suggests that the system possesses a structured viscoelastic dispersed nature.

To evaluate the quality of the approximation of rheological data, the power-law model was applied. It was found that the coefficients of determination (R^2) for all studied systems are in the range of 0.995–0.999, indicating an excellent agreement between the model and the experimental data. The relationship between viscosity (η) and shear rate (γ) is presented in Figure 7.

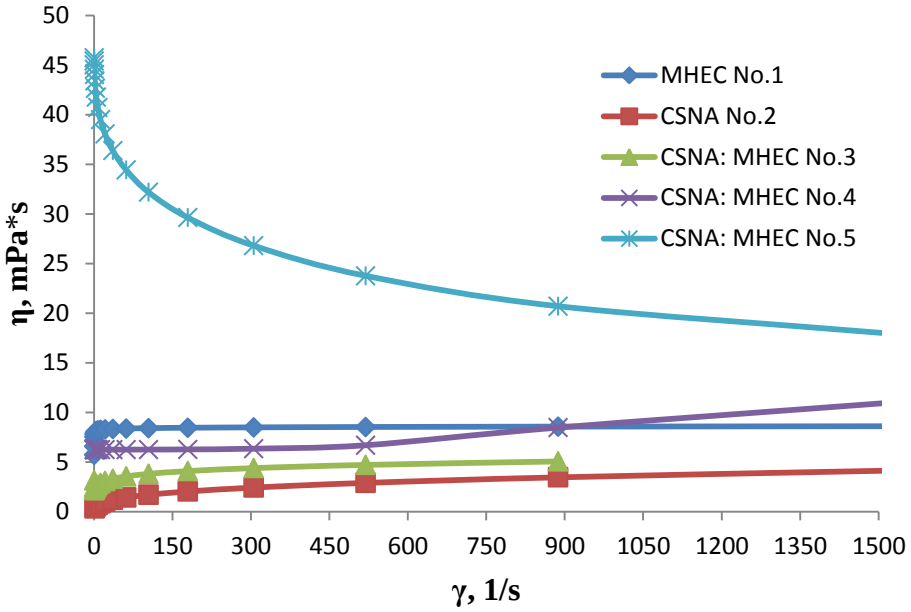

Figure 7. Dependence of viscosity (η) on shear rate (γ).

As can be seen from the graph, for sample No. 1 (0.2 % MHEC), when the shear rate increased from 0.1 to 1510 s^{-1}, the viscosity increased from 5.7 to 8.6 Pa·s. The increase in viscosity can be explained by the rearrangement of polymer chains in the direction of flow under shear and the increase in the number of entanglements, which leads to higher internal friction within the system.

A similar trend was observed for the 0.025 % CSNA solution (sample No. 2), where a gradual increase in viscosity under shear was detected (0.33 → 4.14 Pa·s). This behavior may be associated with hydrodynamic clustering of nanoparticles and the formation of temporary aggregates. Particle aggregation is governed not only by chemical attractive forces but also by hydrodynamic interactions arising from centrifugal forces under flow conditions. As a result, particles approach each other and form aggregates through weak intermolecular interactions.

For the low-concentration system (0.0125 % CSNA : 0.1 % MHEC, sample No. 3), a moderate increase in viscosity was observed (3.1 → 5.0 Pa·s). This behavior indicates the presence of certain interactions between the polymer chains and nanoparticles; however, a fully developed spatial network structure is not formed.

The medium-concentration system (0.025 % CSNA : 0.2 % MHEC, sample No. 4) exhibited near-Newtonian behavior, where the viscosity showed only a weak dependence on the shear rate (6.2 → 10.9 Pa·s). This can be explained by the rapid dynamic recovery of the solution structure. The highest concentration system (0.05 % CSNA : 0.4 % MHEC, sample No. 5) demonstrated pseudoplastic behavior. In this case, the viscosity decreased from 45 Pa·s to 18 Pa·s with increasing shear rate. This indicates the presence of a three-dimensional structure in the solution and its partial disruption under shear conditions.

The investigated solutions exhibited different rheological behaviors. In the case of MHEC and low-concentration CSNA samples, an increase in viscosity with increasing shear rate was observed. This behavior can be explained by hydrodynamic interactions between macromolecules and the strengthening of internal friction in the system due to molecular associations.

In contrast, in medium-concentration systems, the spatial network structure is not sufficiently developed; therefore, the resistance to flow changes only slightly, resulting in dilatant or near-Newtonian rheological behavior. Such rheological characteristics are favorable for the formation of stable dispersions in the spraying technologies used for agricultural preparations.

In high-concentration CSNA–MHEC solutions, pseudoplastic behavior was observed, indicating the formation of a temporary spatial network resulting from interactions between macromolecules and nanoparticles in the system. This structure is stabilized by hydrogen bonding, electrostatic interactions, and macromolecular associations. As a result, under increasing shear rate, the macromolecules become rearranged, leading to a decrease in viscosity and the manifestation of non-Newtonian rheological behavior.

Sample No. 4 (0.025 % CSNA : 0.2 % MHEC) exhibits near-Newtonian rheological behavior, where viscosity is almost independent of shear rate ($\eta \approx$ const). The macromolecular system remains stable, and temporary aggregates are continuously reformed. Due to the structural stability and uniform viscosity, nanoparticles are efficiently retained during the spraying process, and the solution can be easily applied.

In dilatant systems ($n > 1$), viscosity increases with shear rate due to the formation of transient associations, which complicates spraying. In contrast, pseudoplastic systems ($n < 1$) exhibit partial structural breakdown at high shear rates, requiring additional process control. Power-law model analysis ($n \approx 1$, $K \approx 6.2$ Pa·s^n) confirms that the solution possesses stable viscoelastic properties and ensures high efficiency during application.

4 Conclusions

The results of the study demonstrated that the rheological properties of CSNA–MHEC systems strongly depend on polymer concentration and composition. At low concentrations (0.0125–0.025 % CSNA), a gradual increase in viscosity under shear (0.33 → 5.0 Pa·s) was observed, indicating the formation of transient aggregates between macromolecules and nanoparticles. Systems with intermediate concentrations (0.025 % CSNA : 0.2 % MHEC) exhibited near-Newtonian behavior, confirming the presence of a dynamically reversible structure. In contrast, high-concentration systems (0.05 % CSNA : 0.4 % MHEC) showed pseudoplastic behavior and the formation of a three-dimensional network, accompanied by a partial decrease in viscosity and structural disruption under shear.

Power-law model analysis revealed that the flow behavior index (n) exceeds unity at low concentrations and decreases below unity at higher concentrations, while the increase in the consistency index (K) reflects stronger interactions between polymer chains and nanoparticles, as well as the formation of a dynamic spatial network. The high coefficients of determination (R^2 = 0.995–0.999) confirm the excellent agreement between the model and experimental data. Overall, the CSNA–MHEC systems exhibit stable viscoelastic and structured dispersed properties, which are of significant importance for the development of stable and structured polymer formulations in agriculture and pharmaceutical applications.

The results of DLS and AFM analyses confirmed the formation of nanoscale CSNA particles with sizes in the range of 200–700 nm. The DLS data revealed a dominant fraction of particles around 300–400 nm, corresponding to CSNA macromolecular structures, while larger particles (700–2672 nm) were attributed to MHEC. The good agreement between DLS and AFM results indicates the reliability of the obtained data. Overall, the polymeric preparative form represents a heterogeneous system consisting of CSNA nanoparticles and MHEC macromolecular structures.

*Author Information**

**The authors' names are presented in the following order: First Name, Middle Name and Last Name*

Oynavod Barotovna Avazova — Junior Researcher, Institute of Chemistry and Physics of Polymers of the Academy of Sciences of the Republic of Uzbekistan, 7B A. Kadyri St., 100128, Tashkent, Uzbekistan; e-mail: avazova1972@mail.ru, https://orcid.org/0000-0003-4552-6973

Kudrat Kadambayevich Pirniyazov (*corresponding author*) — Junior Researcher, Institute of Chemistry and Physics of Polymers of the Academy of Sciences of the Republic of Uzbekistan, 7B A. Kadyri St., 100128, Tashkent, Uzbekistan; e-mail: qudratpirniyazov8875@gmail.com, https://orcid.org/0009-0005-7014-7686

Sayyora Sharafovna Rashidova — Academician of the Academy of Sciences of the Republic of Uzbekistan, Doctor of Chemical Sciences, Professor, Head of the Laboratory "Synthesis of Advanced Polymers", Institute of Polymer Chemistry and Physics, Academy of Sciences of the Republic of Uzbekistan, 7B A. Kadyri St., 100128, Tashkent, Uzbekistan; e-mail: polymer@academy.uz, https://orcid.org/0000-0003-3104-6004

Author Contributions

The manuscript was written through contributions of all authors. All authors have given approval to the final version of the manuscript. CRediT: **Kudrat Kadambayevich Pirniyazov** conceptualization, data curation, investigation, methodology, validation, visualization, writing-review & editing; **Oynabod Boratovna Avazova** data curation, formal analysis, visualization; **Sayyora Sharafovna Rashidova** concep-

tualization, data curation, formal analysis, funding acquisition, resources, supervision, validation, writing-original draft, writing-review & editing.

Acknowledgments

The work was carried out at the expense of the Institute's budget (Institute of Polymer Chemistry and Physics, Academy of Sciences of the Republic of Uzbekistan, Tashkent, Uzbekistan).

Conflicts of Interest

The authors declare no conflict of interest.

References

1 Milusheva, R.Yu., & Rashidova, S.Sh. (2019). *Bombyx Mori* Chitosan Nanoparticles: Synthesis and Properties. *Open Journal of Organic Polymer Materials*, *09*(04), 63–73. https://doi.org/10.4236/ojopm.2019.94004

2 Pirniyazov, K.K., Milusheva, R.Yu., & Rashidova, S.Sh. (2023). Production and biological activity of chitosan nanoascorbate. *INEOS OPEN*, *6*(6), 156–162. https://doi.org/10.32931/io2326r

3 Pirniyazov, K.K., & Rashidova, S.Sh. (2020). Synthesis of Ascorbate and Chitosan Nanoascorbate and Their Biologically Active Properties. *Journal of Science and Innovative Development*, *3*(5), 47–62. https://doi.org/10.36522/2181-9637-2020-5-6

4 Pirniyazov, K.K., Tixonov, V.E., & Rashidova, S.Sh. (2021). Synthesis and properties of oligochitosan ascorbate from *Bombyx mori*. *Bulletin of the Karaganda University. Chemistry Series*, *1*(101), 91–98. https://doi.org/10.31489/2021Ch1/91-98

5 Wang, W., Meng, Q., Li, Q., Liu, J., Zhou, M., Jin, Z., & Zhao, K. (2020). Chitosan Derivatives and Their Application in Biomedicine. *International Journal of Molecular Sciences*, *21*(2), 487. https://doi.org/10.3390/ijms21020487

6 Pirniyazov, K.K., Asrakulova, D.I., & Rashidova, S.Sh. (2024). Synthesis and antimicrobial properties of chitosan nanoascorbate of *Bombyx mori*. *Moscow University Chemistry Bulletin*, *79*(5), 345–350. https://doi.org/10.3103/S002713142470038X

7 Tian, X.L., Tian, D.F., Wang, Z.Y., & Mo, F.K. (2009). Synthesis and evaluation of chitosan-vitamin C complex. *Indian J. Pharm Sci.*, *71*(4), 371–376. https://doi.org/10.4103/0250-474X.57284

8 Liping, L., Kexin, L., Huipu, D., Jia, L., & Jie, Z. (2020). Study on Preparation of a Chitosan/Vitamin C Complex and Its Properties in Cosmetics. *Natural Product Communications*, 15, 1–9. https://doi.org/10.1177/1934578X20946876

9 Hafsa, J., Charfeddine, B., Smach, M.A., Limem, K., Majdoub, H., & Sonia, R. (2014). Synthesis, characterization, antioxidant and antibacterial proprieties of chitosan ascorbate. *International Journal of Pharmaceutical and Chemical Sciences*, 4, 1072–1081. https://www.ijpcbs.com/articles/synthesis-characterization-antioxidant-and-antibacterial-proprieties-of-chitosan-ascorbate.pdf

10 Muzzarelli, R.A.A., Tanfani, F., & Emanuelli, M. (1984). Chelating Derivatives of Chitosan Obtained by Reaction with Ascorbic Acid. *Carbohydrate Polymers*, *4*(2), 137–151. https://doi.org/10.1016/0144-8617(84)90020-1

11 Zhuang, L., Zhi, X., Du, B., & Yuan, S. (2020). Preparation of Elastic and Antibacterial Chitosan–Citric Membranes with High Oxygen Barrier Ability by in Situ Cross-Linking. *ACS Omega*, 5, 1086–1097. https://doi.org/10.1021/acsomega.9b03206

12 Yalinca, Z., Yilmaz, E., Taneri, B., Bullici, F., & Tuzmen, S.J. (2013). Blood contact properties of ascorbyl chitosan. *Journal of Biomaterials Science, Polymer Edition*, 24, 1969–1987. https://doi.org/10.1080/09205063.2013.816929

13 Othman, N., Masarudin, M.J., Kuen, C.Y., Dasuan, N.A., Abdullah, L.C., Jamil, & S.N.A. Md. (2018). Synthesis and Optimization of Chitosan Nanoparticles Loaded with l-Ascorbic Acid and Thymoquinone. *Nanomaterials*, 8, 920. https://doi.org/10.3390/nano8110920

14 Soliman, A., & Gad, A. (2020). The Impact of Ascorbic Acid, Some Nanomaterials and Their Mixtures on Some Biological and Physiological Parameters of the Mulberry Silkworm *Bombyx mori L*. *Alexandria Science Exchange Journal*, 41, 393–398. https://doi.org/10.21608/asejaiqjsae.2020.119307

15 Ren, H., Liu, Y., Arshad, M., Dou, Z., & Han, X. (2024). Effect of formulations and adjuvants on the properties of acetamiprid solution and droplet deposition characteristics sprayed by UAV. *Frontiers in Plant Science*, 15, 1441193. https://doi.org/10.3389/fpls.2024.1441193

16 Basílio, S., Furtado, Júnior, M.R., Alvarenga, C.B., da Vitória, E.L., Costalonga Vargas, B., Privitera, S., Caruso, L., Cerruto, E., Manetto, G., & Caruso, L. (2024). Effect of adjuvants on physical–chemical properties, droplet size and drift reduction potential in agricultural spraying. *Agriculture*, 14(12), 2271. https://doi.org/10.3390/agriculture14122271

17 Hu, P., Zhang, R., Chen, L., Li, L., Tang, Q., Yan, W., & Yang, J. (2024). Effect of polymer adjuvant type and concentration on atomization characteristics of agricultural spray nozzles. *Agriculture*, 14(3), 404. https://doi.org/10.3390/agriculture14030404

18 Mewis, J., & Wagner, N.J. (2012). Colloidal suspension rheology. *Advances in Colloid and Interface Science*, 147–148, 214–227. https://doi.org/10.1016/j.cis.2008.09.005

19 Barnes, H.A. (1997). Thixotropy—a review. *Journal of Non-Newtonian Fluid Mechanics*, *70*(1–2), 1–33. https://doi.org/10.1016/S0377-0257(97)00004-9

20 Butler Ellis, M.C., & Tuck, C.R. (1999). How adjuvants influence spray formation with different hydraulic nozzles. *Crop Protection*, *18*(2), 101–109. https://doi.org/10.1016/S0261-2194(98)00098-5

21 Zhao, H., & Liu, H. (2019). Breakup Morphology and Mechanisms of Liquid Atomization. Environmental Impact of Aviation and Sustainable Solutions. *IntechOpen*, 1–19. https://doi.org/10.5772/intechopen.84998

22 Mun, R.P., Young, B.W., & Boger, D.V. (1999). Atomisation of dilute polymer solutions in agricultural sprays. *Journal of Non-Newtonian Fluid Mechanics, 83*(1–2), 163–178. https://doi.org/10.1016/S0377-0257(98)00130-7

23 Rinaudo, M. (2006). Chitin and chitosan: Properties and applications. *Progress in Polymer Science, 31*(7), 603–632. https://doi.org/10.1016/j.progpolymsci.2006.06.001

24 Pirniyazov, K.K., Nurgaliyev, I.N., & Rashidova, S.Sh. (2023). Reaction of the Formation of Chitosan Nanoascorbate *Bombyx Mori* and Computer Simulation of Its Structure. *Intelligent Biotechnologies of Natural and Synthetic Biologically Active Substances AIP Conference Proceedings*, 2931, 060002-1–060002-9. https://doi.org/10.1063/5.0182628

25 Kumar, M.N.V.R. (2000). A review of chitin and chitosan applications. *Reactive and Functional Polymers, 46*(1), 1–27. https://doi.org/10.1016/S1381-5148(00)00038-9

26 Fan, W., Yan, W., Xu, Z., & Ni, H. (2012). Formation mechanism of monodisperse, low molecular weight chitosan nanoparticles by ionic gelation technique. *Colloids and Surfaces B: Biointerfaces*, 90, 21–27. https://doi.org/10.1016/j.colsurfb.2011.09.042

27 Younes, I., & Rinaudo, M. (2015). Chitin and chitosan preparation from marine sources: Structure, properties and applications. *Marine Drugs*, 13(3), 1133–1174. https://doi.org/10.3390/md13031133

28 Desai, M.P., Labhasetwar, V., Amidon, G.L., & Levy, R.J. (1996). Gastrointestinal uptake of biodegradable microparticles: effect of particle size. *Pharmaceutical Research*, 13(12), 1838–1845. https://doi.org/10.1023/a:1016085108889

How to Cite: Ryabykh A.V., Maslova O.A., Beznosyuk S.A., Kravchuk R.I., Polyntsev A.S., Spodarev D.S. & Spodareva S.V. (2026). Functionalized C_{60} Fullerenes as Inorganic Redox Nanostructures: A Quantum Chemical Approach. *Eurasian Journal of Chemistry, 31, 2(122), 55–64*. https://doi.org/10.31489/2959-0663/2-26-2

PHYSICAL AND ANALYTICAL CHEMISTRY

Article

Received: 21 November 2025 | Revised: 20 April 2026 | Accepted: 4 May 2026 | Published online: 5 May 2026

UDC 544.18+546.26

https://doi.org/10.31489/2959-0663/2-26-2

Andrey V. Ryabykh*, Olga A. Maslova, Sergey A. Beznosyuk, Roman I. Kravchuk, Artem S. Polyntsev, Dmitriy S. Spodarev, Svetlana V. Spodareva

Altai State University, Barnaul, Russia
*(*Corresponding author's e-mail: ryabykh@chem.asu.ru)*

Functionalized C_{60} Fullerenes as Inorganic Redox Nanostructures: A Quantum Chemical Approach

A comprehensive quantum-chemical study of functionally modified C_{60} fullerenes ($C_{60}X_n$, n = 2, 4, 6) was performed using the hybrid PBE0 functional with dispersion correction (D4) and the SMD solvation model. Eighteen types of substituents with different electronic characteristics (X = $–CH_3$, $–C_2H_5$, $–C_3H_7$, –F, –Cl, –Br, –OH, $–OCH_3$, $–OC_2H_5$, –SH, $–SCH_3$, $–SC_2H_5$, $–NH_2$, $–NO_2$, –COOH, –COCl, $–CONH_2$, –CN) were attached to the fullerene structure to explore how their nature and number influence hydrophilicity, electronic structure, and antioxidant reactivity. The lipophilicity (log$P$), electronic chemical potential (μ), and reaction energy (ΔE) of superoxide ion deactivation were systematically analyzed. A correlation between μ and ΔE was revealed, showing that a decrease in μ enhances electron-accepting ability and antioxidant activity, although the relationship is modulated by the degree of substitution. The optimal balance between π-delocalization and electronic induction was found for tetra-substituted derivatives (n = 4). Electron-withdrawing groups ($–NO_2$, –CN, –COCl, –F, –Cl, –Br) significantly increased antioxidant efficiency, while alkyl and thioalkyl groups exhibited the opposite effect. The established relationships provide a quantitative framework for understanding redox behavior in carbon-based nanostructures and open prospects for the rational design of fullerene-derived antioxidants as inorganic molecular systems with tunable electronic properties.

Keywords: density functional theory, computer simulation, fullerenes, electronic chemical potential, antioxidant activity, structure-property relationship, inorganic nanomaterials, C_{60}

1 Introduction

Fullerenes are a special class of molecular carbon structures built from five- and six-membered cycles. The unique structural diversity and the resulting physico-chemical properties have made fullerenes and their functional derivatives the object of intensive research [1–15]. The study of fullerenes and their derivatives is of key importance for many modern technologies.

Due to their high antioxidant activity, they are used in biomedicine, where their potential as radioprotectors and anti-aging agents is being studied. Thus, due to the unsaturation of bonds between carbon atoms in fullerene molecules, their ability to exhibit antioxidant properties in relation to reactive oxygen species (ROS), for example, superoxide anion radicals O_2^-, is explained. However, fullerenes are lipophilic [2–6], nonpolar molecules, which complicates their transportation to the sites of ROS formation and accumulation.

To increase the solubility in water and reduce the logarithm of the distribution coefficient in the octanol-1 — water system (log$P$), which is 6.67 for fullerene C_{60} [2, 3], one can use ultrasonic dispersion of C_{60} dissolved in vegetable oil and polyvinyl alcohol [4].

Another, more effective method for increasing hydrophilicity involves chemical modification of the fullerene skeleton. To enhance hydrophilicity and solubility in an aqueous environment, fullerene molecules are modified with various polar and/or ionic groups (–OH, –COOH, –Cl, $–NH_2$, $–CH_2OCH_2–$, etc.) [2–8]. For example, in [5], synthesized C_{60}-aminocarboxylic acids were used to prevent apoptosis of rat PC12 cells induced by hydrogen peroxide. Greater viability was observed in cells treated with fullerene derivatives containing arginine and β-alanine residues. The latter derivative is recommended as a cell protector due to its greater solubility in both water and non-polar media. Similar results for C_{60} derivatives were confirmed amperometrically in [6]. In [7], C_{60} modified with proline and other functional groups (nitroalkyl, hydroxyalkyl, maleimide, carnosine) was studied. Proline provided hydrophilicity to the nanostructure, while other groups (including the fullerene backbone) provided biological activity: antiviral, antioxidant, and antitumor. It was noted that a derivative with carnosine, which is also an antioxidant, has an increased ability to interact with radicals. In the work [8], the influence of the lipophilicity of fullerene C_{60}, modified with amino acids with different contents of lyophilic and hydrophilic fragments, on the ability to inhibit lipid oxidation in an aqueous environment is studied using the chemiluminescence method. Rat brain homogenate was used as a lipid, *tert*-butyl hydroperoxide was the source of radicals, and the reaction was carried out in an aqueous medium in the presence of luminol. As a result, it was established that less hydrophilic derivatives, which can more easily penetrate the phospholipid and act as an ROS scavenger, have high inhibition efficiency. An increase in functional groups in fullerene molecules not only increases their solubility in water, but also reduces their antioxidant activity, which was demonstrated in the study of hydroxyfullerenes $C_{60}(OH)_n$, where $2 \le n \le 26$ [9], and others [2, 5, 7].

The antioxidant and lipophilic properties of fullerene molecules and their derivatives are also studied using quantum chemistry and computer modeling, complementing experiments. Quantum-chemical calculation methods have proven themselves to be effective theoretical methods for predicting properties. These calculations, based on density functional theory (DFT), have become a powerful tool for studying the reactivity of fullerenes. They have been used to study radical reactions [10] and the ozone addition process [11]. In [12–14], various quantum-chemical approaches to modeling the structure of fullerenes and estimating the energy of isomeric structures were considered and evaluated. It was shown that quantum-chemical modeling of such atomic-molecular systems has a high accuracy. In work [15], the DFT method was used to determine the energies of interaction of C_{60} with molecules of aminocarboxylic acids in the gas phase, and a hypothesis was put forward about the correlation of the thermodynamic functions of the formation of adducts of fullerenes with amino acids and the lipophilicity coefficient.

The accumulated experimental and theoretical information on the antioxidant properties of fullerenes and the effect of substituents on the lipophilicity of nanostructures based on them are one of the key points for the targeted design of nanomaterials, since the question remains to what extent it is advisable to reduce the hydrophobicity of fullerenes. There is also a question about the number of substituents on the fullerene backbone (more substituents means better solubility, but less activity as an ROS scavenger). Therefore, further study of the relationship between lipophilicity, antioxidant activity and electronic structure of fullerene derivatives is required. The purpose of this study is to perform quantum chemical modeling and compare a number of C_{60} fullerene derivatives modified with two, four, and six identical substituents of different electronic nature (X), both electron-donating and electron-acceptor (X = $–CH_3$, $–C_2H_5$, $–C_3H_7$, –F, –Cl, –Br, –OH, $–OCH_3$, $–OC_2H_5$, –SH, $–SCH_3$, $–SC_2H_5$, $–NH_2$, $–NO_2$, –COOH, –COCl, $–CONH_2$, –CN), to establish the relationships between the structure of molecules, their electronic structure, lipophilicity and antioxidant activity (the ability to accept an electron from a superoxide ion O_2^-, converting it into a safer triplet oxygen O_2).

2 Computational Details

2.1 Parameters of Quantum Chemical Computer Simulation

Among the variety of $C_{60}X_n$ isomers, one stable isomer of each series was selected [16]. The model of the C_{60} fullerene frame with the atom numbering used is shown in Figure 1. Functional groups were attached to the following C atoms: $C_{60}X_2$ (2, 15); $C_{60}X_4$ (6, 9, 12, 15); $C_{60}X_6$ (4, 6, 9, 12, 15, 58).

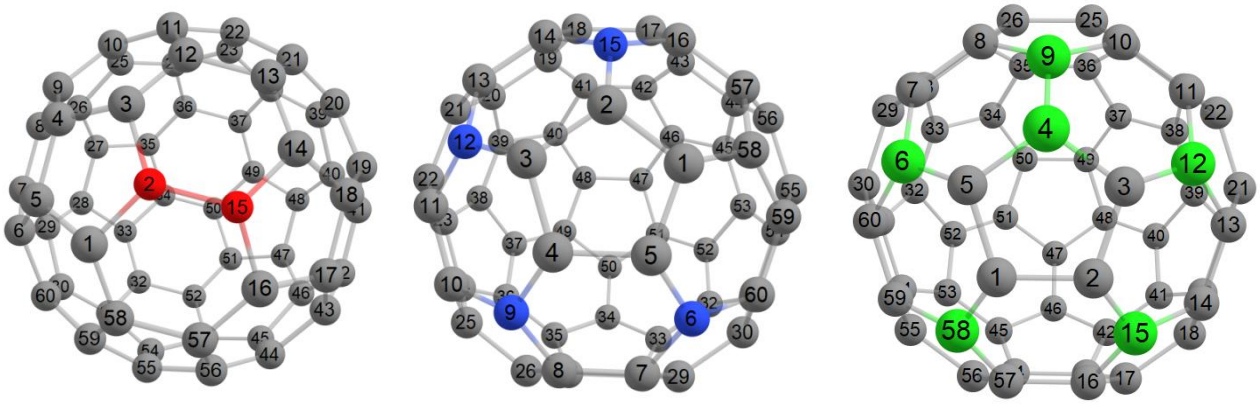

a *b* *c*

a — attachment of two X groups to red carbon atoms; *b* — attachment of four X groups to blue carbon atoms; *c* — attachment of six X groups to green carbon atoms

Figure 1. Designations of the positions of attachment of functional groups to the fullerene C_{60}

Computer modeling was performed in the ORCA 6.1 software package [17] using the hybrid density functional PBE0 as a calculation method [18]. It optimally combines an accurate account of the electronic structure of the π-system of the fullerene backbone and a reliable description of the energy of interaction with functional groups, including non-covalent interactions. To accurately describe the weak non-covalent interactions (for example, van der Waals forces) that can be significant in substituted fullerenes, especially with bulky alkyl chains, the D4 empirical dispersion correction scheme by Grimme and coworkers [19] was employed in conjunction with PBE0. This addition is critical for obtaining realistic structures and energies.

A dual-basis set strategy was adopted to ensure both efficiency and accuracy. The def2-SVP basis set [20] was used for geometry optimizations and frequency calculations. This basis offers a good compromise, providing reliable structural parameters for large molecules at a reasonable computational cost. For more accurate single-point energy calculations (essential for deriving electronic potentials and energies), the larger def2-TZVPD basis set was employed [20, 21]. This triple-zeta quality basis set, augmented with diffuse functions, is crucial for correctly describing electron affinities, ionization potentials, and anionic species (such as $C_{60}X_n^-$, O_2^-) involved in the antioxidant activity assessment [22].

2.2 The Octanol-Water Partition Coefficient (logP)

The octanol-water partition coefficient logP reflects the ability of a substance to be distributed between nonpolar (octanol) and polar (water) media (Equation 1):

$$P(C_{60}X_n) = \frac{[C_{60}X_n]_o}{[C_{60}X_n]_w} \quad (1)$$

The higher the log*P*, the more lipophilic the structure is. The lipophilicity coefficient was estimated using the chemical reaction isotherm equation (Equation 2) [23]:

$$\Delta G_{w\to o}(C_{60}X_n) = 2.303RT \log P(C_{60}X_n), \quad (2)$$

where $\Delta G_{w\to o}$ is the change in the Gibbs function of the transition process of a fullerene molecule from an aqueous medium to an octanol medium, J/mol; R is the universal gas constant, J/(mol·K); T is the temperature, K.

Here, the calculated lipophilicity coefficient of the modified fullerene was subtracted from the calculated lipophilicity coefficient of pure fullerene in order to be able to compare the lipophilicity and hydrophilicity of structures after modification and eliminate possible errors of the method and the basic set when comparing (Equation 3):

$$\Delta \log P(C_{60}X_n) = \log P(C_{60}X_n) - \log P(C_{60}) = \frac{\Delta G^0_{w\to o,298}(C_{60}) - \Delta G^0_{w\to o,298}(C_{60}X_n)}{2.303RT}. \quad (3)$$

The energies of molecules in an aqueous medium and an octanol medium were calculated using the continuous solvent model SMD [23]. The geometry of the molecules was optimized in each solvent (water and octanol) using the def2-SVP basis. To evaluate the Gibbs functions of the transition of molecules from

water to octanol ($\Delta G_{w\to o,298}{}^{0}$), the single-point energies ($FSP_{(\text{water})}$, $FSP_{(\text{octanol})}$) of these structures in water and in octanol were calculated, and thermal corrections were calculated taking into account the oscillation frequencies at T = 298.15 K and p = 1 atm ($\Delta E_{(\text{water})}$, $\Delta E_{(\text{octanol})}$,) for pure fullerene and its derivatives (Equation 4). The FSPs were calculated using the def2-TZVPD basis set, and the thermal corrections were calculated using the def2-SVP basis set:

$$\Delta G^{0}_{w\to o,298}(\text{Y}) = FSP_{(\text{octanol})}(\text{Y}) - FSP_{(\text{water})}(\text{Y}) + \Delta E_{(\text{octanol})}(\text{Y}) - \Delta E_{(\text{water})}(\text{Y}), \quad (4)$$

where Y is the C_{60} and $C_{60}X_n$.

It is important to note that the absolute calculated log$P$ value for unsubstituted C_{60} (9.06) overestimates the experimental value (6.67) [24]. According to the isotherm Equation 2, the error is 13.6 kJ/mol (0.14 eV), which is an acceptable error for calculating energies in continuous solvent models for large and voluminous, as well as highly hydrophobic molecular structures [25], such as pure unmodified fullerene. Therefore, to ensure the reliability of our structure-property analysis, we focus exclusively on the relative lipophilicity parameter, $\Delta\log P$. This relative scale effectively cancels out systematic errors in the solvation energy calculations for the common fullerene core, allowing for a robust comparison of the substituent effects.

Antioxidant Activity of Functionally Modified Fullerenes in Relation to Superoxide Ion

The antioxidant activity of modified $C_{60}X_n$ fullerenes (n = 2, 4, 6) was evaluated by the reaction of the fullerene structure with the superoxide ion, assuming the mechanism of electron transfer from the superoxide ion with its oxidation to molecular oxygen:

$$C_{60}X_n + O_2^- \rightarrow C_{60}X_n^- + O_2$$

The reaction energy ΔE was calculated according to Hess's law based on single point energies (Final Single Point Energy — *FSP*). Negative values of ΔE correspond to spontaneous reaction and high antioxidant activity

$$\Delta E = FSP(C_{60}X_n^-, opt) + FSP(O_2, opt) - FSP(C_{60}X_n, opt) - FSP(O_2^-, opt) \quad (5)$$

For the reaction energy ΔE, full geometry optimizations were performed for all species: neutral $C_{60}X_n$, O_2, radical anions $C_{60}X_n^-$, O_2^-. The optimizations were carried out at the PBE0-D4/def2-SVP/SMD(Water) level. FSP energies were then calculated with the def2-TZVPD basis set to obtain accurate energies.

For the structures in equation 5, the following values of charge (C) and spin multiplicity (M) were used: $C_{60}X_n$ (C = 0, M = 1); $C_{60}X_n^-$ (C = –1, M = 2); O_2^- (C = –1, M = 2); O_2 (C = 0, M = 3). All energies of the optimized neutral and anionic structures are listed in the Supplementary Materials (Table S1).

2.4 Electronic Chemical Potentials of Structures C60Xn

The electron chemical potential μ was chosen as a measure of the acceptor capacity of fullerene structures, which was calculated using the apparatus of the conceptual density functional theory (CDFT) [26]. The electronic chemical potential is a change in the energy of an atomic-molecular system (E) when an electron (N) is attached while the geometry of the structure remains constant (conservation of the nuclear potential V_n = const):

$$\mu = \left(\frac{\partial E}{\partial N}\right)_{Vn=const} \approx -\frac{I + A}{2} \quad (6)$$

In equation (6), I is the vertical ionization energy, and A is the vertical electron affinity of fullerene structures. They were calculated using equations (7) and (8), respectively:

$$I = FSP(C_{60}X_n^+) - FSP(C_{60}X_n), \quad (7)$$

$$A = FSP(C_{60}X_n) - FSP(C_{60}X_n^-). \quad (8)$$

The descriptor (μ) shows the ability of a structure to participate in donor-acceptor interactions and the ability to shift the electron density from another structure. When a system of interacting structures is formed, the electron density will predominantly flow to the structure with a more negative value of μ.

Cartesian coordinates and total energies for all structures are available in the Supplementary Materials (Table S2).

3 Results and Discussion

3.1 The Octanol-Water Partition Coefficient (logP)

log*P* is one of the key parameters in QSAR (Quantitative structure — activity relationship) and medicinal chemistry, as it reliably predicts the ability of a molecule to passively transport across biological membranes, its solubility, and overall bio-distribution *in vivo*. In this work, the relative hydrophobicity parameter (Δlog*P*), showing a change in hydrophobicity compared to unmodified C_{60} fullerene. This systematic approach allows for a detailed analysis of the effect of the nature and number of functional groups on the lipophilic properties of the fullerene framework. Figure 2 shows a heat map visualizing the effect of functional groups and the degree of substitution on the hydrophobicity of $C_{60}X_n$ fullerene derivatives relative to unmodified C_{60}.

Data analysis reveals several clear patterns:

1) The heat map shows a pronounced division of functional groups into two opposite clusters. Powerful hydrophobizers are located in the upper part: propyl- ($–C_3H_7$) and thioethyl- ($–SC_2H_5$) groups demonstrate the most significant increase in lipophilicity (Δlog*P* to +5.86 and +5.92 at $n = 6$, respectively). Hydrophilic groups are concentrated in the lower part, and the carboxyamide group ($–CONH_2$) exhibits the strongest hydrophilic effect (Δlog*P* up to –9.12 at $n = 6$);

2) A significant dependence is observed for most groups: an increase in the degree of substitution from $n = 2$ to $n = 6$ leads to an increase in the initial effect of the group. For most of the functional groups studied (for the simulated positions of groups on the fullerene framework), a distinct linear dependence of Δlog*P* on the degree of substitution *n* is observed. So, for the groups $–C_3H_7$, –F, –Cl, –SH, $–SCH_3$, $–SC_2H_5$, $–NH_2$, –COOH and $–CONH_2$, the correlation coefficient $R^2 > 0.99$. For the groups $–CH_3$, $–C_2H_5$, –Br, –OH, –COCl, –CN and $–NO_2$, the correlation coefficient $R^2 > 0.9$. For the groups $–OCH_3$ ($R^2 = 0.39$) and $–OC_2H_5$ ($R^2 = 0.22$), due to the peculiarities of their location on the fullerene framework, a strong nonlinear dependence is observed. The nonlinear behavior of certain groups is explained by a complex balance of steric, electronic, and solvation effects, which are not a simple sum of the contributions of individual substituents;

3) The ranking of groups by their effect on lipophilicity shows that the amide group ($–CONH_2$) is the most powerful hydrophilizer. Among hydrophobizers, groups with long hydrocarbon chains and thioalkyl substituents are most effective.

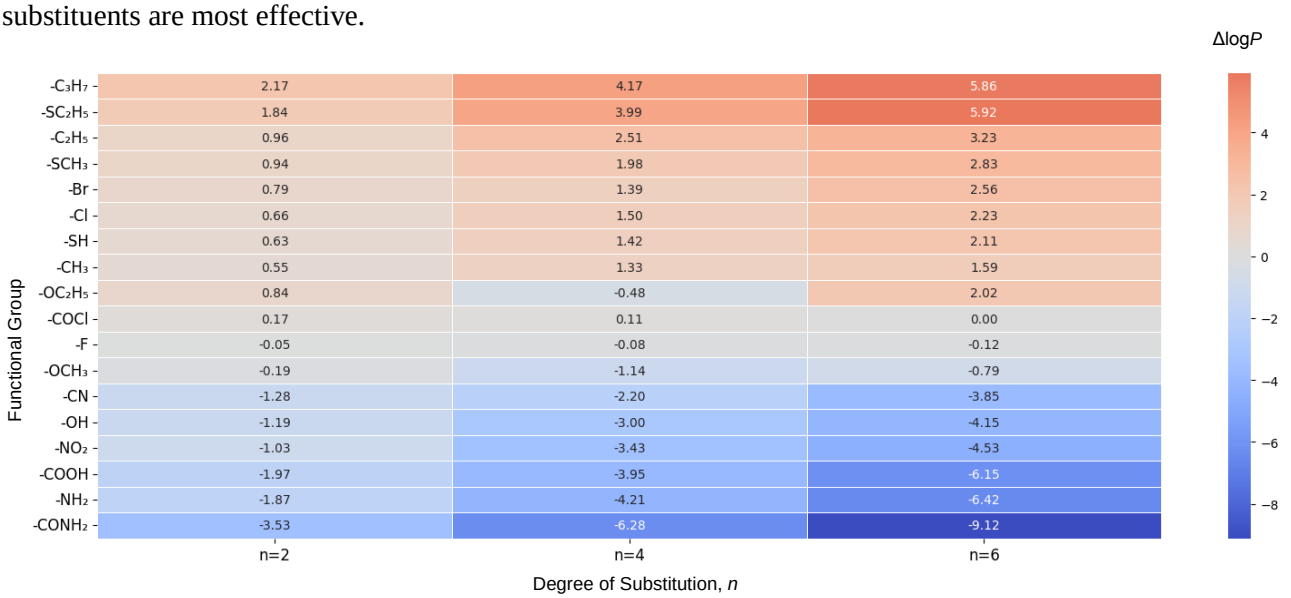

Figure 2. Heat map of the relative change in hydrophobicity (Δlog*P*) of functionally substituted $C_{60}X_n$ fullerenes calculated by quantum chemical methods relative to unmodified C_{60} fullerene (blue tones — more negative values of Δlog*P*, low hydrophobicity; red tones — more positive values of Δlog*P*, high hydrophobicity)

As can be seen from the analysis of the Δlog*P* dependence, the nature and number of functional substituents have a systematic effect on the hydrophobicity of the fullerene structure. Since hydrophobicity determines not only the solubility and transport of a molecule in biological media, but also the effectiveness of interaction with radical oxygen forms, it seems logical to compare these data with the electronic

characteristics and antioxidant activity of the obtained structures. In particular, it can be expected that an increase in hydrophilicity (a decrease in log*P*) due to the introduction of electron acceptor groups will be accompanied by a decrease in the electron chemical potential and an increase in the ability of the molecule to accept an electron from the superoxide ion. Thus, the transition from the analysis of ΔlogP to the assessment of antioxidant activity allows us to move from the macroscopic characteristics of solubility to the quantum chemical description of reactivity.

3.2 Antioxidant Activity of Functionally Modified Fullerenes in Relation to Superoxide Ion

The antioxidant activity of modified $C_{60}X_n$ fullerenes (n = 2, 4, 6) was evaluated by the equation 5. Figure 3 shows a heat map of the ΔE values for all 54 derivatives studied. In the case of calculating the reaction energy (5) for unmodified fullerene C_{60}, we obtained a value of ΔE = –35.2 kJ/mol. It is clearly seen that antioxidant activity depends non-linearly on both the nature of substituent X and the degree of functionalization n. For most compounds, a minimum of ΔE (the highest activity) is observed at n = 4, whereas at n = 2 and n = 6, the reaction becomes less advantageous. This effect is explained by the balance between the preservation of the delocalized π-system of the fullerene framework and the induction effect of substituents. It is important to note that in this study, the influence of the nature of the functional group on the properties of the fullerene structure was studied in the context of a single isomer in each series n = 2, 4, 6.

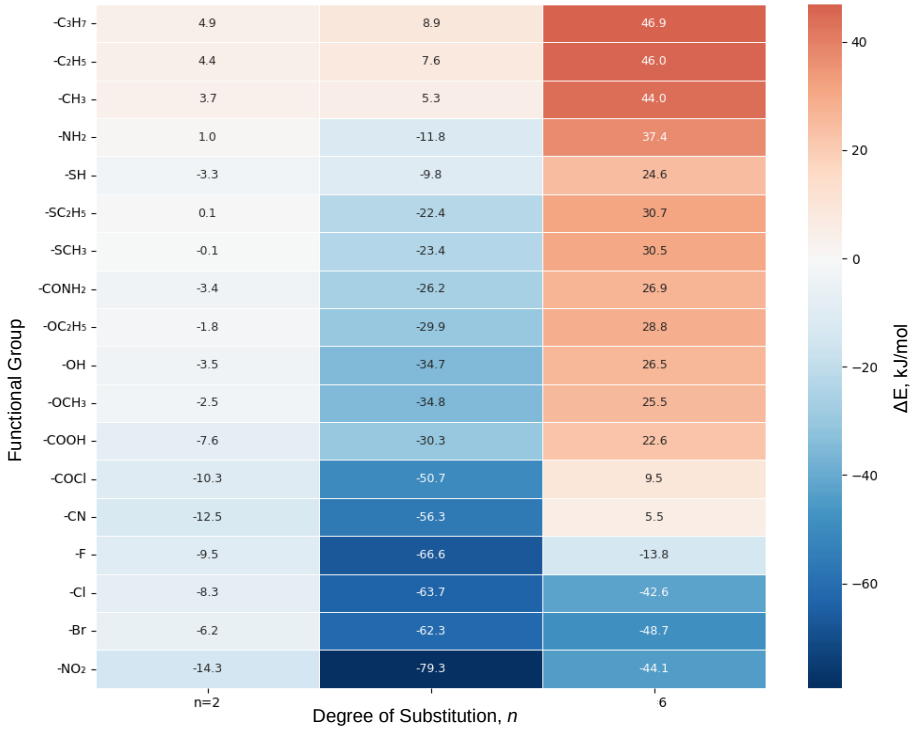

Figure 3. Heat map of reaction energy values ΔE (kJ/mol) for modified fullerenes $C_{60}X_n$ (n = 2, 4, 6) in reaction with the superoxide ion O_2^-. The color scale reflects the thermodynamic benefits of the process (blue tones — more negative values of ΔE, high antioxidant activity; red tones — more positive values of ΔE, low activity)

The maximum antioxidant activity is typical for compounds containing electron acceptor groups –F, –Cl, –Br, –NO_2, –CN and –COCl (ΔE from –40 to –80 kJ/mol at n = 4). These substituents lower the electron chemical potential of μ to –5.8÷–5.9 eV, which reflects their high ability to accept an electron. Electron-donating groups (alkyl, alkoxy, thioalkyl, and amino groups) exhibit the opposite effect: they increase the μ (up to –4.4 eV) and make the reaction less advantageous (ΔE > 0).

3.3 Electronic Chemical Potentials of Structures $C_{60}X_n$

The electronic chemical potential (μ) is one of the key parameters of the conceptual theory of the density functional, reflecting the general tendency of a molecule to receive or give electrons. More negative values of μ correspond to more pronounced electron-withdrawing properties and, consequently, a greater ten-

dency of the system to reduction. Table shows the calculated values of electronic chemical potentials μ for CDFT $C_{60}X_n$ structures according to equation 6.

The lowest values of μ are observed for structures containing electron acceptor groups –CN, $–NO_2$, –COCl, –F, –Cl, and –Br, which reflects the pronounced acceptor effect of these substituents on the π-electron system of the fullerene framework. The decrease in μ is especially noticeable during the transition from $n = 2$ to $n = 4$, which indicates an increase in the electron acceptor effect with an increase in the degree of functionalization. With a further increase in the number of substituents to $n = 6$, only a slight increase in μ is observed, which can be explained by the partial destabilization of the π-system due to oversaturation of the fullerene framework.

T a b l e

Values of electronic chemical potentials μ (eV) of $C_{60}X_n$ structures

Group X									
n	CN	NO_2	COCl	F	Cl	Br	OH	COOH	$CONH_2$
2	–5.45	–5.41	–5.28	–5.24	–5.20	–5.17	–5.09	–5.07	–5.06
4	–5.95	–5.90	–5.41	–5.32	–5.27	–5.23	–5.12	–5.15	–5.15
6	–5.88	–5.83	–5.41	–5.39	–5.30	–5.30	–4.92	–4.89	–4.87
Group X									
n	SH	OCH_3	OC_2H_5	SCH_3	SC_2H_5	NH_2	CH_3	C_2H_5	C_3H_7
2	–5.07	–5.03	–5.00	–4.98	–4.95	–4.97	–4.92	–4.89	–4.87
4	–5.04	–5.09	–5.11	–5.03	–4.98	–4.80	–4.82	–4.84	–4.75
6	–4.94	–4.78	–4.70	–4.74	–4.65	–4.63	–4.51	–4.45	–4.42

For the moderately polar groups –OH, –COOH, and $–CONH_2$, the values of μ are close to the potential of unmodified C_{60} (–5.19 eV). These substituents have a weak acceptor effect without disturbing the electronic structure of the fullerene. On the opposite end of a number are electron-releasing substituents — alkyl ($–CH_3$, $–C_2H_5$, $–C_3H_7$), the alkoxy- and thioalkyl group ($–OCH_3$, $–OC_2H_5$, $–SCH_3$, $–SC_2H_5$) and amino group ($–NH_2$). For them, μ increases sequentially with increasing length of the alkyl chain or degree of substitution. This reflects an increased donor effect and an increase in the electron density on the fullerene framework. Thus, the distribution of μ values makes it possible to divide the studied functional groups into three main classes according to the nature of electronic influence:

1) strong acceptors ($–NO_2$, –CN, –COCl, –F, –Cl, –Br);

2) temperate polar groups (–OH, –COOH, $–CONH_2$);

3) donors (alkyl, alkoxy, thioalkyl, amino groups).

This classification reflects the general electronic structure of fullerene derivatives and forms the basis for subsequent analysis of their reactivity. Since μ is directly related to the thermodynamic characteristics of the reduction processes, a further comparison of the obtained values with the energies of the superoxide ion (ΔE) capture reaction makes it possible to establish patterns between the electronic structure and the antioxidant activity of fullerenes. For all the studied series of fullerene derivatives $C_{60}X_n$ ($n = 2, 4, 6$), a clear relationship was revealed between the energy of the superoxide ion deactivation reaction (ΔE) and the electronic chemical potential μ calculated using the conceptual density functional theory (Figs. 4 and 5). The red dashed line in these figures at a value of $\mu = 5.19$ eV shows the numerical value for pure unmodified fullerene C_{60}.

According to the data in Figure 4, it can be seen that, in general, with a decrease in the chemical potential (with an increase in the ability of the fullerene structure to accept electrons), antioxidant activity increases. The dependence is far from linear, as indicated by the low correlation coefficient ($R^2 = 0.5543$). But the following trend is observed. Practically all the structures studied, which have an μ value that is more negative than that of pure fullerene (to the left of the red dashed line), have increased antioxidant activity with respect to the superoxide ion compared to pure fullerene. This can be explained by the fact that the deactivation of the superoxide ion according to the reaction scheme (5) occurs by the electron transfer mechanism, and the fullerene structure acts as an electron acceptor. More negative values of the chemical potential give the structure more acceptor properties.

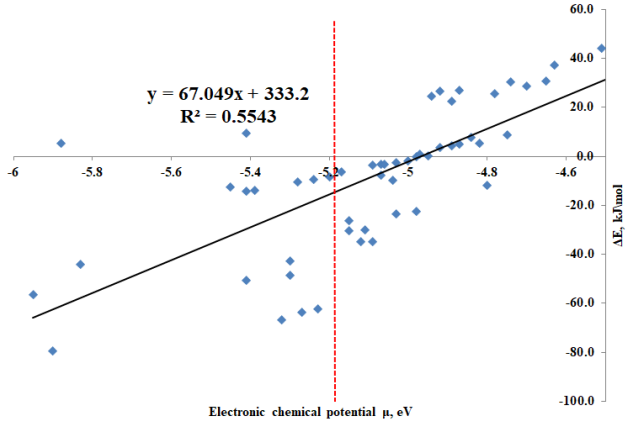

Figure 4. Dependence of the antioxidant activity of fullerene structures $C_{60}X_n$ with respect to the superoxide ion (ΔE) on the electronic chemical potential μ without differentiation by series of derivatives

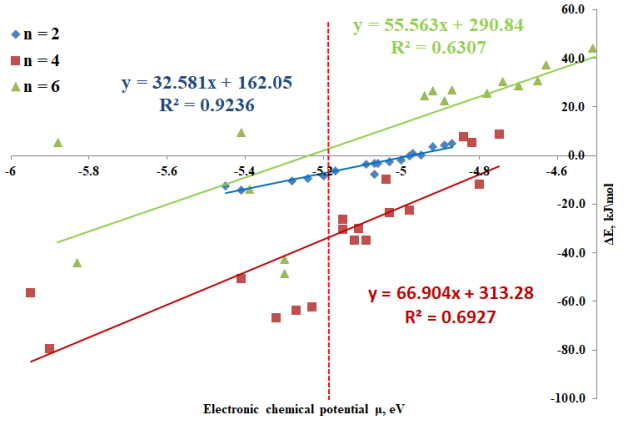

Figure 5. Dependence of the antioxidant activity of fullerene structures $C_{60}X_n$ with respect to the superoxide ion (ΔE) on the electronic chemical potential μ with differentiation by three series of derivatives: n = 2, n = 4, n = 6

A clearer picture is observed if we differentiate the values in Figure 4 by three series of derivatives (n = 2, n = 4 and n = 6). The most linear dependence is inherent in $C_{60}X_2$. Such a small number of groups, even being in close proximity to each other with neighboring carbon atoms of the fullerene framework, do not significantly distort the linearity and additivity of antioxidant properties (R^2 = 0.9236). The more groups are fixed on fullerene, the greater the deviations from linearity (n = 4, R^2 = 0.6927; n = 6, R^2 = 0.6307). But in general, the trend originally outlined in Figure 4 is also evident here separately in three series of derivatives: with a decrease in chemical potential, antioxidant activity increases.

4 Conclusions

A comprehensive quantum-chemical study of 54 functionalized $C_{60}X_n$ (n = 2, 4, 6) derivatives was performed using the hybrid PBE0 functional with dispersion correction. In this work, the properties of modified fullerenes, such as hydrophilicity, electronic chemical potential as a measure of the structure's ability to transfer electron density, and the oxidizing capacity of modified fullerenes towards the active form of oxygen, the superoxide ion, were modeled.

Electronic nature and number of substituents systematically determine the hydrophilicity, electronic properties, and antioxidant activity of the fullerene framework. Hydrophilicity increases with the introduction of electron-withdrawing substituents (–NO_2, –CN, –COCl, –F, –Cl, –Br), while alkyl and thioalkyl groups act as strong hydrophobizers. Optimal antioxidant activity is achieved for tetra-substituted derivatives (n = 4), where the π-system remains sufficiently delocalized, and the electron-accepting effect of substituents is maximal. The reaction energy (ΔE) for the deactivation of the superoxide ion O_2^- correlates inversely with the electronic chemical potential μ, indicating that the lowering of μ enhances electron affinity and antioxidant reactivity. Moderately polar groups (–OH, –$CONH_2$, –COOH) exhibit balanced solubility and redox behavior, making them promising candidates for biomedical fullerene derivatives with tunable antioxidant efficiency.

Overall, the results establish quantitative structure–property relationships connecting hydrophilicity, electronic potential, and thermodynamic reactivity, offering a rational framework for the molecular design of fullerene-based antioxidants.

Supporting Information

The Supporting Information is available free at https://ejc.buketov.edu.kz/ejc/article/view/567/392

Funding

This research was carried out as part of the University's Development Program for 2021–2030 as part of the strategic academic leadership program "Priority 2030", the project "Modified fullerenes in medicine and nanotechnology: quantum chemical modeling of structural, electronic and antioxidant properties".

*Author Information**

**The authors' names are presented in the following order: First Name, Middle Name and Last Name*

Andrey Valerievich Ryabykh (*corresponding author*) — Candidate of Chemical Sciences, Associate Professor, Department of Physical and Inorganic Chemistry, Altai State University, Lenin Avenue, 61, 656049, Barnaul, Russia; e-mail: ryabykh@chem.asu.ru; https://orcid.org/0000-0003-3699-3932

Olga Andreevna Maslova — Candidate of Physico-Mathematical Sciences, Associate Professor, Department of Physical and Inorganic Chemistry, Altai State University, Lenin Avenue, 61, 656049, Barnaul, Russia; e-mail: maslova@chem.asu.ru; https://orcid.org/0000-0003-3862-3687

Sergey Alexandrovich Beznosyuk — Doctor of Physico-Mathematical Sciences, Head of the Department of Physical and Inorganic Chemistry, Altai State University, Lenin Avenue, 61, 656049, Barnaul, Russia; e-mail: bsa1953@mail.ru; https://orcid.org/0000-0002-4945-7197

Roman Ivanovich Kravchuk — Assistant, Department of Physical and Inorganic Chemistry, Altai State University, Lenin Avenue, 61, 656049, Barnaul, Russia; e-mail: kravchuk_r@mail.asu.ru; https://orcid.org/0009-0004-2153-5271

Artem Sergeevich Polyntsev — 4th Year Undergraduate Student, Department of Physical and Inorganic Chemistry, Altai State University, Lenin Avenue, 61, 656049, Barnaul, Russia; e-mail: polyntsev.chem@mail.ru; https://orcid.org/0009-0000-7617-1584

Dmitriy Stanislavovich Spodarev — 4th Year Student, Department of Physical and Inorganic Chemistry, Altai State University, Lenin Avenue, 61, 656049, Barnaul, Russia; e-mail: 031204dmitriy@gmail.com; https://orcid.org/0009-0006-0474-5634

Svetlana Vadimovna Spodareva — 4th Year Student, Department of Physical and Inorganic Chemistry, Altai State University, Lenin Avenue, 61, 656049, Barnaul, Russia; e-mail: svetlanaspodareva@gmail.com; https://orcid.org/0009-0006-4226-7864

Author Contributions

The manuscript was written through contributions of all authors. All authors have given approval to the final version of the manuscript. CRediT: **Andrey Valerievich Ryabykh** conceptualization, data curation, investigation, methodology, validation, visualization, writing-review & editing; **Olga Andreevna Maslova** conceptualization, data curation, writing-review & editing; **Sergey Alexandrovich Beznosyuk** methodology, validation, supervision, writing-review & editing; **Roman Ivanovich Kravchuk** visualization, data analysis & writing-original draft; **Artem Sergeevich Polyntsev** analysis of results, data processing & visualization; **Dmitriy Stanislavovich Spodarev** analysis of results, data processing & visualization; **Svetlana Vadimovna Spodareva** analysis of results, data processing & visualization.

Conflicts of Interest

The authors declare no conflict of interest.

References

1 Sam, M., & Akbari, S. (2024). An overview of functionalized fullerenes and their applications in industry. *Journal of NanoScience Technology*, 13, 1–11.

2 Bhakta, P., & Barthunia, B. (2020). Fullerene and its applications: A review. *Journal of Indian academy of oral medicine and radiology*, 32(2), 159–163. https://doi.org/10.4103/jiaomr.jiaomr_191_19

3 Jafvert, C.T., & Kulkarni, P.P. (2008). Buckminsterfullerene's (C60) Octanol−Water Partition Coefficient (K_{ow}) and Aqueous Solubility. *Environ. Sci. Technol*., 42, 5945–5950. https://doi.org/10.1021/es702809a.

4 Kop, T.J., Bjelaković, M.S., Živković, L., Žekić, A., & Milić, D.R. (2022). Stable colloidal dispersions of fullerene C60, curcumin and C60-curcumin in water as potential antioxidants. *Colloids and Surfaces A: Physicochemical and Engineering Aspects*, 648, 129379. https://doi.org/10.1016/j.colsurfa.2022.129379

5 Zhen Hu, Wenchao Guan, Wei Wang, Lizhen Huang, Xiangying Tang, Hong Xu, Zhou Zhu, Xingzi Xie, & Haiping Xing. (2008). Synthesis of amphiphilic amino acid C60 derivatives and their protective effect on hydrogen peroxide-induced apoptosis in rat pheochromocytoma cells. *Carbon*, 46 (1), 99–109. https://doi.org/10.1016/j.carbon.2007.10.041

6 Volkov, V.A., Yamskova, O.V., Shepel', N.E., Romanova, V.S., Kurilov, D.V., Tregubov, A.V., ... & Kustov, L.M. (2019). Antioxidant Properties of Amino Acid Derivatives of Fullerene C60. *Russian Journal of Physical Chemistry A*, *93*(11), 2152–2157. https://doi.org/10.1134/S0036024419110335.

7 Kulkarni, S., Chaudhari, S.B., Chikkamath, S.S., Kurale, R.S., Thopate, T.S., Praveenkumar, S., Ghotekar, S., Patil, P. & Kumar, D. (2025). Potential applications of fullerenes in drug delivery and medical advances. *Inorganic Chemistry Communications*, *173*, 113829. https://doi.org/10.1016/j.inoche.2024.113829

8 Bogdanova, Yu.G., Tepanov, A.A., Ioutsi, V.A., Romanova, V.S., Bogdanov, G.N., Kotel'nikova, R.A., Mishchenko, D.V., Rybkin, A.Yu., & Kotel'nikov, A.I. (2012). Effect of lipophilicity of C60 fullerene derivatives on their ability to inhibit peroxide oxidation of lipids in aqueous medium. *Moscow University Chemistry Bulletin*, 67(4), 154–158. https://doi.org/10.3103/s0027131412040025

9 Semenov, K.N., Charykov, N.A., & Keskinov, V.N. (2011). Fullerenol synthesis and identification. Properties of the fullerenol water solutions. *Journal of Chemical & Engineering Data*, 56(2), 230–239. https://doi.org/10.1021/je100755v

10 Sabirov, D.S., Garipova, R.R., & Bulgakov, R.G. (2013). Density functional theory study on the decay of fullerenyl radicals RC_{60}•, ROC_{60}•, and $ROOC_{60}$• (R= tert-butyl and cumyl) and polarizability of the formed fullerene dimers. *The Journal of Physical Chemistry A*, 117(49), 13176–13183. https://doi.org/10.1021/jp409845q

11 Sabirov, D.S., Khursan, S.L., & Bulgakov, R.G. (2008). Ozone addition to C60 and C70 fullerenes: A DFT study. *Journal of Molecular Graphics and Modelling*, 27(2), 124–130. https://doi.org/10.1016/j.jmgm.2008.03.006

12 Zheng, G., Irle, S., & Morokuma, K. (2005). Performance of the DFTB method in comparison to DFT and semiempirical methods for geometries and energies of C_{20}–C_{86} fullerene isomers. *Chemical Physics Letters*, 412(1–3), 210–216. https://doi.org/10.1016/j.cplett.2005.06.105

13 Shao, N., Gao, Y., & Zeng, X. C. (2007). Search for lowest-energy fullerenes 2: C38 to C80 and C112 to C120. *The Journal of Physical Chemistry C*, 111(48), 17671–17677. https://doi.org/10.1021/jp0701082

14 Charykov, N.A., Keskinov, V.A., & Petrov, A.V. (2021). Addukty legkikh fullerenov i aminokislot: sintez, identifikatsiya i kvantovo-mekhanicheskoye modelirovaniye ikh fiziko-khimicheskikh svoystv [Adducts of light fullerenes and amino acids: synthesis, identification, and quantum mechanical modeling of their physicochemical properties]. *Zhurnal fizicheskoi khimii — Journal of Physical Chemistry*, 95(12), 1787–1803. https://doi.org/10.31857/S0044453721120049 [in Russian].

15 A de Leon, A, Jalbout, A.F. & Basiuk, V.A. (2008). Fullerene–amino acid interactions. A theoretical study. *Chemical Physics Letters*, 452 (4–6), 306–314. https://doi.org/10.1016/j.cplett.2007.12.065

16 Clare, B. W., & Kepert, D. L. (2003). Early stages in the addition to C_{60} to form $C_{60}X_n$, X = H, F, Cl, Br, CH_3, C_4H_9. *Journal of Molecular Structure: THEOCHEM*, 621(3), 211–231. https://doi.org/10.1016/S0166-1280(02)00551-1

17 Neese, F. (2022). Software update: The ORCA program system—Version 5.0. *Wiley Interdisciplinary Reviews: Computational Molecular Science*, *12*(5), e1606. https://doi.org/10.1002/wcms.1606

18 Adamo, C., & Barone, V. (1999). Toward reliable density functional methods without adjustable parameters: The PBE0 model. *The Journal of Chemical Physics*, *110*(13), 6158–6170. https://doi.org/10.1063/1.478522

19 Caldeweyher, E., Ehlert, S., Hansen, A., Neugebauer, H., Spicher, S., Bannwarth, C., & Grimme, S. (2019). A generally applicable atomic-charge dependent London dispersion correction. *The Journal of chemical physics*, *150*(15). https://doi.org/10.1063/1.5090222

20 Weigend, F., & Ahlrichs, R. (2005). Balanced basis sets of split valence, triple zeta valence and quadruple zeta valence quality for H to Rn: Design and assessment of accuracy. *Physical Chemistry Chemical Physics*, 7(18), 3297–3305. https://doi.org/10.1039/B508541A

21 Rappoport, D., & Furche, F. (2010). Property-optimized Gaussian basis sets for molecular response calculations. *The Journal of chemical physics*, *133*(13). https://doi.org/10.1063/1.3484283

22 Ryabykh, A.V., Maslova, O.A., & Beznosyuk, S.A. (2023). Mechanisms of Docking of Superoxide Ions in the Catalytic Cycle of Manganese and Iron Superoxide Dismutases. *Eurasian Journal of Chemistry*, *111*(3), 104–113. https://doi.org/10.31489/2959-0663/3-23-4

23 Marenich, A.V., Cramer, C.J., & Truhlar, D.G. (2009). Universal solvation model based on solute electron density and on a continuum model of the solvent defined by the bulk dielectric constant and atomic surface tensions. *The Journal of Physical Chemistry B, 113*(18), 6378–6396. https://doi.org/https://doi.org/10.1021/jp810292n

24 Jafvert, C.T., & Kulkarni, P.P. (2008). Buckminsterfullerene's (C_{60}) octanol-water partition coefficient (K_{ow}) and aqueous solubility. *Environmental science & technology*, *42*(16), 5945–5950. https://doi.org/10.1021/es702809a

25 Kongsted, J., Söderhjelm, P., & Ryde, U. (2009). How accurate are continuum solvation models for drug-like molecules? *Journal of Computer-Aided Molecular Design*, *23*(7), 395–409. https://doi.org/10.1007/s10822-009-9271-6

26 Chakraborty, D., & Chattaraj, P.K. (2021). Conceptual density functional theory based electronic structure principles. *Chemical Science*, *12*(18), 6264–6279. https://doi.org/10.1039/D0SC07017C

How to Cite: Fomin, V.N., Ainabayev, A.A., Aldabergenova, S.K., Kaikenov, D.A., & Turovets, M.A. (2026). Classification Analysis of Bituminous Coals Using a Combination of GC-MS and Chemometric Methods. *Eurasian Journal of Chemistry, 31, 2(122), 65–76.* https://doi.org/10.31489/2959-0663/2-26-6

Article

Received: 15 January 2026 | Revised: 30 April 2026 | Accepted: 5 May 2026 | Published online: 6 May 2026

UDC 543.06:519.23

https://doi.org/10.31489/2959-0663/2-26-6

Vitaliy N. Fomin, Assanali A. Ainabayev, Saule K. Aldabergenova, Dauletkhan A. Kaikenov, Milana A. Turovets*

Karaganda National Research University named after Academician Ye.A. Buketov, Karaganda, Kazakhstan
*(*Corresponding author's e-mail: turovec26.07@mail.ru)*

Classification Analysis of Bituminous Coals Using a Combination of GC-MS and Chemometric Methods

A comprehensive approach to the analysis of organic matter in bituminous coals from Kazakhstani deposits was developed, based on a combination of liquid extraction, gas chromatography with mass spectrometric detection (GC-MS), and chemometric data processing. A triple extraction system of dichloromethane–chloroform–tetrachloromethane (1:1:1) was proposed for sample preparation, providing representative extraction of aliphatic, aromatic and heteroatomic components without additional extract concentration. Chromatographic profiles of 120 coal extracts from four sources in Central and Northern Kazakhstan were analyzed. Optimization of the chromatographic separation conditions was carried out using probabilistic-deterministic design of experiment, which made it possible to establish robust relationships between the instrument parameters (column heating rate, carrier gas pressure) and the chromatogram characteristics. Chemometric data processing using principal component analysis (PCA), hierarchical cluster analysis (HCA), and k-means method revealed reproducible grouping of samples based on chromatographic profile similarity. Compact clusters corresponding to conventionally designated coal sources were formed in the principal component space, which is confirmed by the clustering results. The obtained results demonstrate the applicability of GC-MS and the chemometric approach for coal classification analysis and provide the foundation for the creation of a database of chromatographic fingerprints of the organic phase of coals.

Keywords: chemometrics, gas chromatography, PCA, hierarchical cluster analysis, k-means, coal classification, PDDoE, Kazakhstani deposits

Introduction

Since its inception, gas chromatography has become the primary method for studying volatile organic compounds in coal and its degradation products [1–3]. The wide variety of components in coal extracts and pyrolysis products makes traditional chromatogram interpretation an extremely labor-intensive process, which has driven the active implementation of chemometric methods and machine learning for GC-MS data processing.

In the 1990s, gas chromatographic and combined methods became the primary tools for analyzing pyrolysis products and coal extracts [3–5]. By the late 1990s, three main approaches to coal classification analysis had emerged: extraction analysis of soluble compounds, pyrolysis gas chromatography for thermal degradation products, and direct comparison of chromatograms from different coals. At that time, an analytical approach was commonly used where each peak was considered separately and processing was performed manually.

In the 2000s, gas chromatography evolved from merely a component identification method into a universal tool for molecular analysis of coals and their processing products [6–10]. A study [6] described an elemental gas chromatographic analysis methodology that increased result reproducibility for solid fuels several-fold. The first application of two-dimensional GC×GC-MS to slow pyrolysis tars from lignite showed that multidimensional gas chromatography could separate the most complex product matrices by classes — aromatic, aliphatic, and oxygen-containing [7]. Systematization of the entire spectrum of chromatographic approaches, including GC-MS, LC-MS, and TLC-MS, demonstrated that GC-MS remains the optimal method for the analysis of volatile and semi-volatile organic compounds [8, 9].

During 2010–2020, GC×GC-MS methods actively developed, enabling analysis of thousands of compounds in a single run [10–13]. One research direction in coal science involves studying the solubility of coal organic matter and the fractional composition of extracts using various solvents [12, 14–19]. CS2 and

tetrahydrofuran extract aromatic and heterocyclic compounds effectively; toluene and pyridine extract alkanes and fatty alcohol fractions [12, 15]. *n*-Hexane predominantly isolates alkane and aromatic fractions, while methanol extracts oxygen-containing compounds. Thus, studies of coal extracts with various solvents have shown that gas chromatography and GC-MS effectively separate dozens and hundreds of volatile and semi-volatile organic compounds in complex matrices. However, with increasing data volumes, the need arose for processing using intelligent tools such as chemometrics and machine learning [20–23].

The transition from classical data processing methods to handling large datasets became a necessity. In mixtures containing numerous components, visual interpretation becomes uninformative [24–27]. The use of chemometric methods such as principal component analysis (PCA), hierarchical cluster analysis (HCA), partial least squares (PLS), and linear discriminant analysis (LDA) enabled a shift from disparate chromatograms to quantitative assessment of relationships between samples and compound classes.

PCA allows combining interrelated variables (peak areas of various compound classes) into several principal components, revealing main trends in complex data [14, 25]. Analysis of extracts from three brown coals using GC-MS and GC×GC-Q-TOF-MS showed that PCA allows of characterization of over 85 % of data variance [28].

Hierarchical clustering methods proved particularly effective in the processing of GC×GC-MS datasets [29, 30]. HCA paired with PCA were used to classify 190 compounds in lignite and subbituminous coal extracts [18]. It was found that extracts from one coal type form stable clusters regardless of solvent, confirming internal consistency of molecular composition.

Partial least squares (PLS) methods found application in quantitative analysis of compound class content based on peak intensities [31]. When applying PLS-R to determine aromatic compounds in coal extracts based on GC-MS signals, the coefficient of determination reached 0.98 [32].

Machine learning (ML) algorithms and neural networks (NN) have recently been actively applied for automatic classification of coals and their processing products [33–35]. Using a combination of HS-GC-IMS (gas chromatography with ion mobility spectrometry) and Random Forest and Support Vector Machine algorithms for identifying coal geographical origin, classification accuracy exceeded 99 %, demonstrating ML advantages [33].

Use of chemometric data processing methods can be more effective with careful physical separation of variables intended for future use as predictors. An effective method for tuning physicochemical analysis instruments involves mathematical experimental design. Probabilistic-deterministic design of experiment was previously successfully applied to optimize gas chromatograph settings for analyzing coal tar hydrogenation products [36], similar in volatile substance composition to extracts. The combination of instrument setting optimization using probabilistic-deterministic experimental design with subsequent chemometric analysis of results has been successfully applied in several LIBS studies, including [37–40].

Thus, a combination of existing chemometric methods opens new possibilities for analyzing extracts and pyrolysis products: accelerated analysis, reduced subjectivity, improved reproducibility, and creation of "coal fingerprint" databases. The combination of GC-MS analysis with chemometric processing significantly enhances capabilities, allowing identification of key variables among hundreds of peaks, improving qualitative analysis, and enabling sample classification by rank, geochemical group, and technological application.

It should also be noted that the literature lacks examples of applying such comprehensive methods to coals from Kazakhstan deposits. This opens directions for relevant research contributing to understanding of geochemistry and technologically important properties of domestic coals. Thus, the main goal of this research is a development of an efficient method for classification analysis of coal with combination of GS-MS and chemometrics.

Experimental

Coal samples were purchased from four different commercial sources rather than collected directly from deposits. For convenience, the samples were labeled based on vendor-provided origin information (RA — "Rapid", KA — "Karazhyra", SH — "Shubarkol", EK — "Ekibastuz"). These labels should be considered as nominal identifiers, and not as the confirmed deposit names, since this information could not be independently verified.

Two-stage grinding was performed for material homogenization. At the first stage, a jaw crusher was used, providing coarse grinding and simultaneous mixing of portions weighing approximately 1 kg. Thirty randomly selected coal samples from each source were used. This approach reduces heterogeneity and eliminates systematic differences between samples. After the coarse crushing, the material was quartered and ad-

ditionally ground in a mortar mill in 20-gram batches for 20 minutes until a fine powder with particle size of approximately 20–50 μm was obtained. The resulting powder was thoroughly mixed and dried at room temperature to constant weight.

To clarify the provenance of the coal samples, ash content was determined in accordance with GOST 11022-95, and ash composition by major components was analyzed by LIBS on sodium tetraborate glass fusion discs, following the procedure described in the literature [37]. Ash content measurements were performed three times. Confidence intervals were calculated using the Student's t-coefficient for two degrees of freedom at a 95 % confidence level. Elemental composition was determined on a composite sample, with the confidence interval derived from the calibration curve.

A triple mixture of dichloromethane, chloroform, and tetrachloromethane (all solvents purity is reagent grade, "Komponent-Reaktiv" manufacturer, Russia) in a 1:1:1 molar ratio was selected for extraction. This combination integrates solvent capacity toward aliphatic, aromatic, and heteroatomic components of coal organic matter, ensuring representative extract recovery. The mixture was prepared immediately before use. Extraction was performed by adding 5.00 mL of solvent to 1.00 g of coal and mixing on an orbital thermostated shaker at 120 rpm for 60 minutes at 20 °C. The resulting solution was filtered under atmospheric pressure through paper filter, and the filtrate was used directly for GC-MS.

Probabilistic-deterministic design of experiment was applied for optimization of chromatographic separation conditions based on the previous work with the similar samples [36]. The analysis was performed using the following instrumental parameters: stationary phase — Rxi-5ms capillary column with a length of 30 m, an inner diameter of 0.25 mm, and absorbent thickness of 0.25 μm; injector temperature — 250 °C; temperature program — 60–250 °C. Helium was used as a carrier gas, injection volume — 0.2 μl in split mode (1:1). The heating rate and carrier gas pressure were varied in accordance with a four-factor experimental design incorporating three variation levels, after which the corresponding chromatograms were obtained. Two factor positions within the experimental design matrix were intentionally left vacant. Structural configuration of the PDDoE design, mathematical treatment of the experimental results, and computations based on the derived empirical equations were performed using the software package "PDDoE" [41].

An Agilent 7890A gas chromatograph (USA, manufacturing year — 2008) with an Agilent 5975C mass-selective detector (USA, manufacturing year — 2008) were used for data collection. Mathematical processing of the method application results, as well as calculations based on the obtained empirical equations, were performed using the previously developed "VDPE" program [41] and a more flexible pipeline of scripts. Scripts were developed with "R" programming language in "R" development framework with RStudio IDE [42]. The applicability of the scripts was validated on small data set (singular chromatograms). Developed scripts are applicable to the processing of data from analysis of similar samples (see *Supporting Information*).

Results and Discussion

The previous application of probabilistic-deterministic design of experiment [36] ensures optimization of gas chromatography conditions with a minimum number of experiments and yields robust relationships suitable for extrapolation to other systems. Optimal conditions for the column heating rate and gas pressure levels were calculated and selected based on response surface analysis. The generalized empirical equations for retention time (1) and resolution (2) derived from the PDDoE analysis take the following forms:

$$\overline{t_R} = 81.26 \times \Delta T^{-0.7631} \times \frac{1}{0.03421 + 0.0004116 \times P} / 27.3804 \text{, } R = 0.9917, t_R = 146.9447 \quad (1)$$

$$R_S = (0.083 + 0.2346 / P) \times (0.1364 + 0.08223 / \Delta T) / 0.1577 \text{, } R = 0.8003, t_R = 5.4526 \quad (2)$$

Based on the obtained equation, the optimal values of carrier gas pressure and column heating rate were selected to ensure a balance between chromatographic resolution and total analysis duration. Given the substantial number of measurements in the present study — 120 samples in total (four coal types, 30 extracts each) — minimizing individual run time was a practical necessity.

Overall device settings provide a balance between analysis time and separation quality:

– column type — Rtx-100DHA;
– column length — 30 m;
– column diameter — 0.25 mm;
– column adsorbent thickness — 0.5 μm;

– injector temperature — 280 °C;
– column temperature — 60–300 °C;
– column heating rate — 8 °C/min;
– ion source temperature — 230 °C;
– quadrupole condenser temperature — 150 °C; EI+ = 70 eV;
– carrier gas — helium grade A;
– column gas pressure — 12 psi;
– sample volume — 0.2 μL;
– injection mode — splitless;
– mass spectrum recording mode — scan;
– library — NIST 08;
– analysis time — 32 min.

The chosen parameters (column heating rate — 8 °C/min, column gas pressure — 12 psi) therefore represent a compromise solution: maximizing peak resolution while avoiding unnecessary prolongation of each chromatographic cycle.

Extract components were identified using GS-MSD DataAnalysis software by comparing acquired mass spectra with the NIST 08 library data. The accuracy of the data for subsequent use in the calculations was ensured by 30 individual measurements on each of four samples.

Examples of extract chromatograms for each coal source are presented in Figures 1, 2.

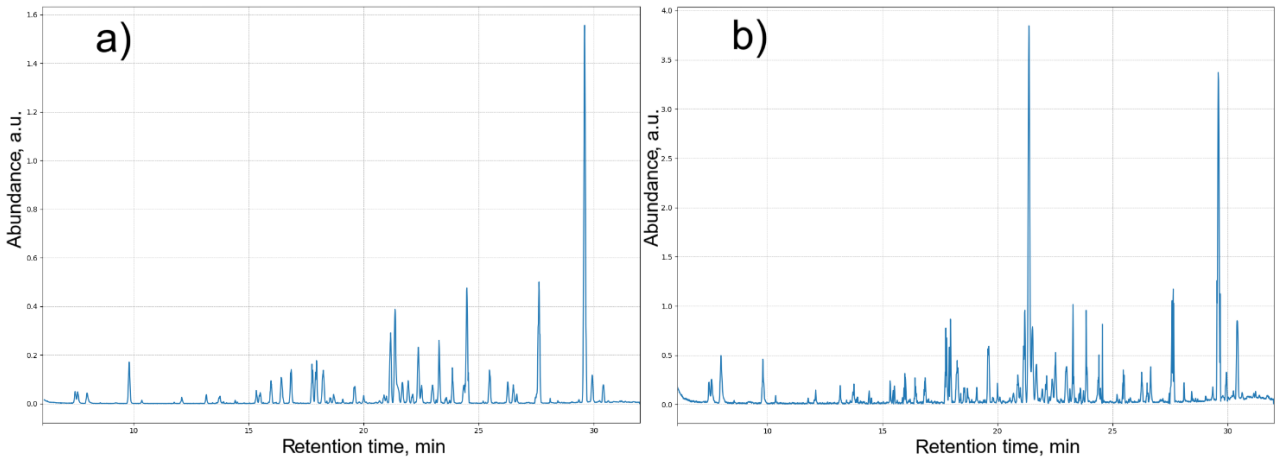

Figure 1. Chromatogram of the coal extract samples: *a* — "KA" sample (KA_1), *b* — "RA" sample (RA_1)

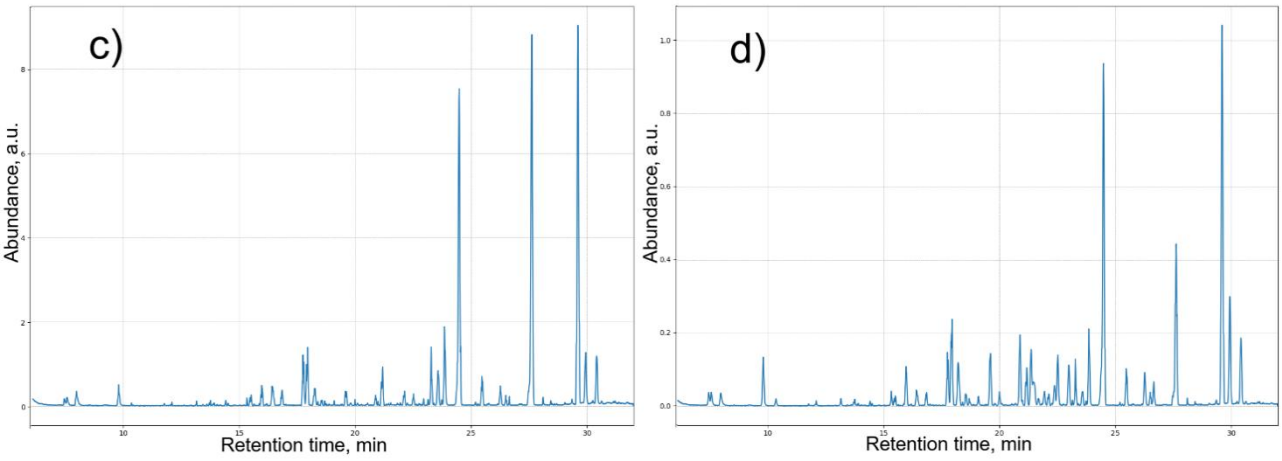

Figure 2. Chromatogram of the coal extract samples: *c* — "SH" sample (SH_1), *d* — "EK" sample (EK_1)

Additional data on the composition and ash content of the coals are presented in Table 1. Overall, the analytical results are consistent with published data on Central Kazakhstan coals [43, 44]; however, they are

not considered sufficient to draw conclusions regarding sample provenance. The use of normalized mineral composition data in combination with chromatographic data through data fusion approaches appears promising, though its applicability is constrained by the labour intensity of data collection.

Table 1

Mineral composition of the studied coals

Sample name	Ash content, %	SiO_2, %	Al_2O_3, %	CaO, %	MgO, %	Fe_2O_3, %	TiO_2, %
KA	22.31±0.12	55.11±3.56	28.48±2.41	2.62±0.025	1.89±0.01	4.51±0.08	2.61±0.05
EK	40.93±0.14	61.1±3.97	23.51±1.99	4.76±0.045	1.01±0.005	4.97±0.09	1.05±0.02
SH	14.82±0.07	56.32±3.64	22.45±1.89	2.11±0.02	1.61±0.008	8.27±0.15	0.87±0.01
RA	24.27±0.17	62.54±4.02	24.77±2.03	3.17±0.036	1.21±0.007	6.08±0.11	0.53±0.01

Scripts were developed in R programming environment for the chromatograms data extraction needed for the calculations. A key feature of used data extraction method is peak alignment of identical components by retention time and assignment of zero areas when a peak is absent in one or more chromatograms. This avoids NA and/or NaN values during further processing.

The script performs line-by-line reading of source files, sample name extraction, recognition of tabular blocks, conversion of text structure to tables, and compilation of a final matrix into a format suitable for further chemometric processing (PCA, clustering, etc.). Chromatograms of 120 coal extract samples obtained from four deposits in central and northern Kazakhstan were used to build the model.

During chemometric processing, all relative peak areas (Area Pct) are treated as a feature vector for each sample. Centering and scaling eliminate the unequal contribution of peaks depending on absolute area.

Principal component analysis transforms the original feature space into new orthogonal axes (PC1, PC2, PC3, etc.), each describing a decreasing proportion of total data variance. This reduces sample data dimensionality from approximately 40–45 original variables (peak areas) to several principal components describing almost all dataset variance.

An interactive scores and loadings plot (See *Supporting Information*) allows rotation of the point cloud to examine spatial clusters and sample relative positions, and to track the directional influence of original variables — chemical components of the mixture — on classification in the space of the first three principal components. Coincident or proximate points correspond to similar chromatographic profiles. Distinguishable point groups indicate differences in extract composition. Adjacent samples (coal samples from one deposit) form compact clusters.

In the space of the first three principal components, compact clusters are observed corresponding to samples attributed to the same source. Notably, one sample group distinctly separates from the others along the first principal component (PC1), indicating systematic differences in extractable organic fraction composition compared to other samples. The remaining samples form several closely spaced but distinct clusters, the separation of which is primarily evident along PC2 and PC3.

Loading vectors plotted on the graph reflect the contribution of individual chromatographic peaks to principal component formation. Vector direction and length indicate variables most strongly influencing sample separation in PC1-PC3 space. Thus, differences between clusters are determined by the cumulative contribution of several organic phase components rather than single marker compounds, emphasizing the complex nature of coal extract chromatographic "fingerprints."

The projection of the obtained three-dimensional model onto a plane is presented in Figure 3.

Loading vectors are labeled with the retention time of the corresponding peak:

20.88 — Nonadecane (93 %);
21.16 — 1,2-Benzenedicarboxylic acid, butyl 2-methylpropyl ester (94 %);
10.36 — Dodecane (72 %);
16.42 — Carbonic acid, pentadecyl 2,2,2-trichloroethyl ester (64 %);
15.49 — 1,8-Naphthyridin-2-amine, 5,7-dimethyl- (64 %);
16.47 — Naphthalene, 1,6,7-trimethyl- (94 %);
23.27 — Heneicosane (87 %);
17.93 — Naphthalene, 1,6-dimethyl-4-(1-methylethyl)- (98 %);
7.46 — Benzene, 1,2-diethyl- (90 %);

19.09 — Phenanthrene (80 %);
27.49 — Pentacosane (93 %);
29.59 — Terephthalic acid, di(4-octyl) ester (81 %);
20.00 — Nonadecane (78 %);
24.48 — Phenanthrene, 1-methyl-7-(1-methylethyl)- (99 %).

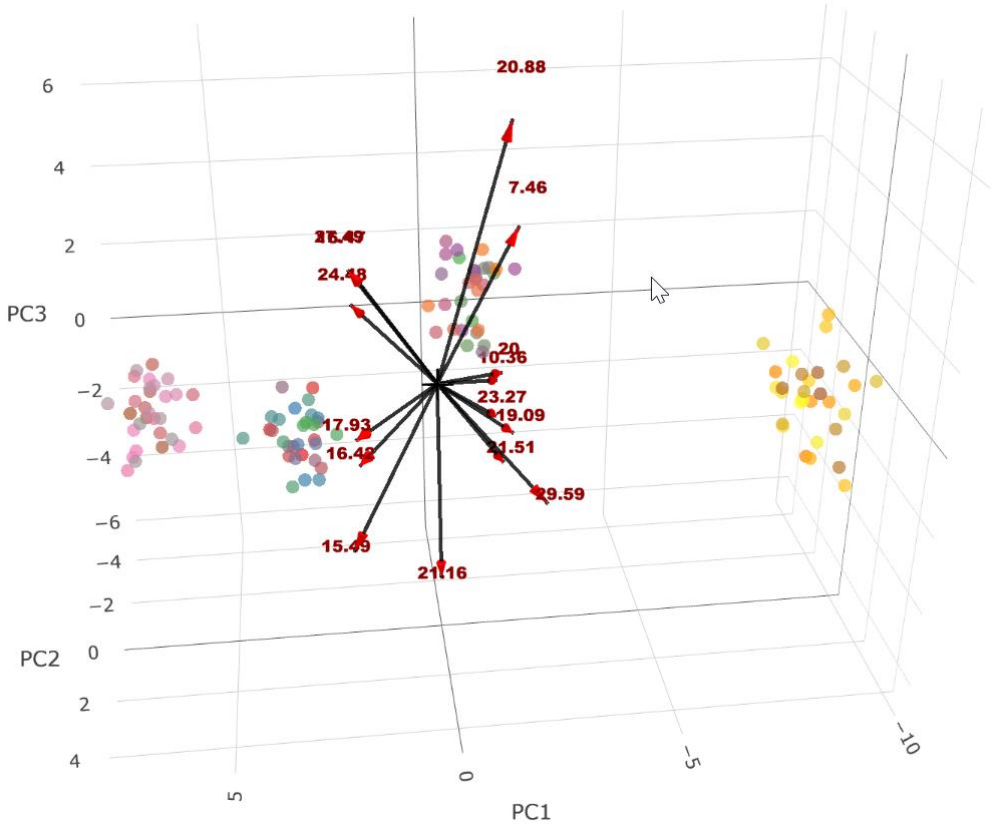

PC1 axis depicts the coordinates of the 1st principal component,
PC2 axis depicts the coordinates of 2nd principal component,
PC3 axis depicts the coordinates of 3rd principal component

Figure 3. PCA of GC data results: scores and loadings

There are existing clustering methods that work with native variables without dimensionality reduction. One such method is hierarchical clustering of chromatographic profiles. Hierarchical clustering of the obtained chromatographic data enables visual representation of the degree of similarity between samples based on the all registered peaks. In some cases, this approach proves to be even more informative than PCA, as it preserves the metric structure of the original data and allows identification of sample groups with similar profiles without preliminary dimensionality reduction, as shown in Figure 4.

Hierarchical clustering was performed using the Euclidean distance metric and Ward's minimum variance linkage method (Ward.D2). Prior to clustering, the data were autoscaled to prevent domination of variables with larger numerical ranges.

The clustering of coal extract chromatographic profiles revealed a clear multilevel structure of sample similarity. At the top level of the dendrogram, all samples separate into two main groups, indicating fundamental differences in organic extract composition. One of these groups is formed predominantly by samples from one deposit, while the second combines samples from three other sources.

With further clustering depth, each main group subdivides into more compact subgroups, resulting in four stable clusters. These clusters are characterized by high intragroup similarity of chromatographic profiles and are distinctly different from each other based on the total set of registered peaks.

The obtained cluster structure indicates that differences between samples are systematic in nature and determined by peculiarities in the composition of extractable organic matter, rather than random variations in analytical measurements.

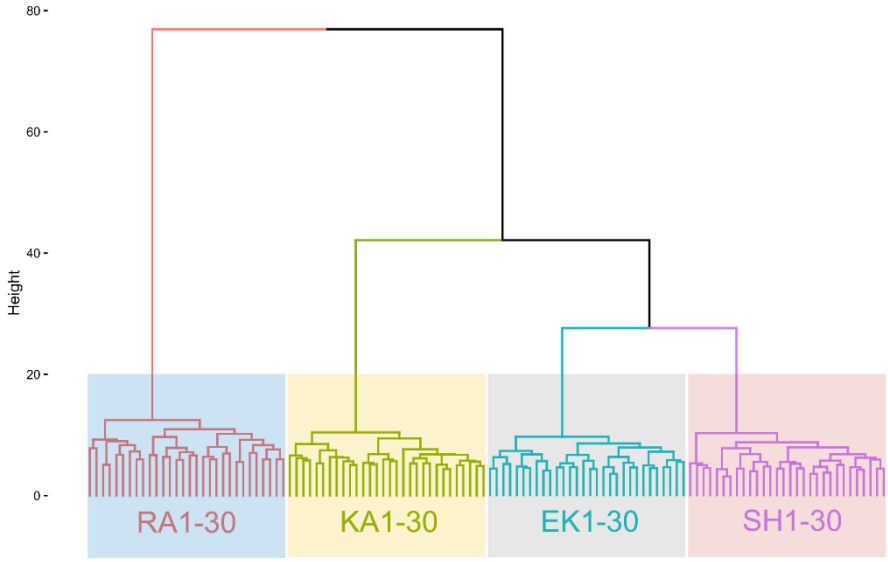

Figure 4. Hierarchical clustering of coal samples (RA1-30 — "Rapid" coal sample, 30 repetitions; KA1-30 — "Karazhyra" coal sample, 30 repetitions; EK1-30 — "Ekibastuz" coal sample, 30 repetitions; SH — "Shubarkol" coal sample, 30 repetitions)

Hierarchical clustering was performed directly on normalized chromatographic data without preliminary dimensionality reduction, which allowed assessment of the natural similarity structure of samples.

To verify the stability of the identified grouping, k-means clustering was additionally applied. The optimal number of clusters for the k-means method was determined using the elbow method, based on analysis of the dependence of within-cluster sum of squares on the number of clusters.

Analysis of the corresponding graph (Fig. 5) shows that the transition from three to four clusters leads to notable improvement in clustering quality, whereas further increase in cluster number yields only marginal gains. Therefore, $k = 4$ was chosen as a compromise between model complexity and its descriptive capacity.

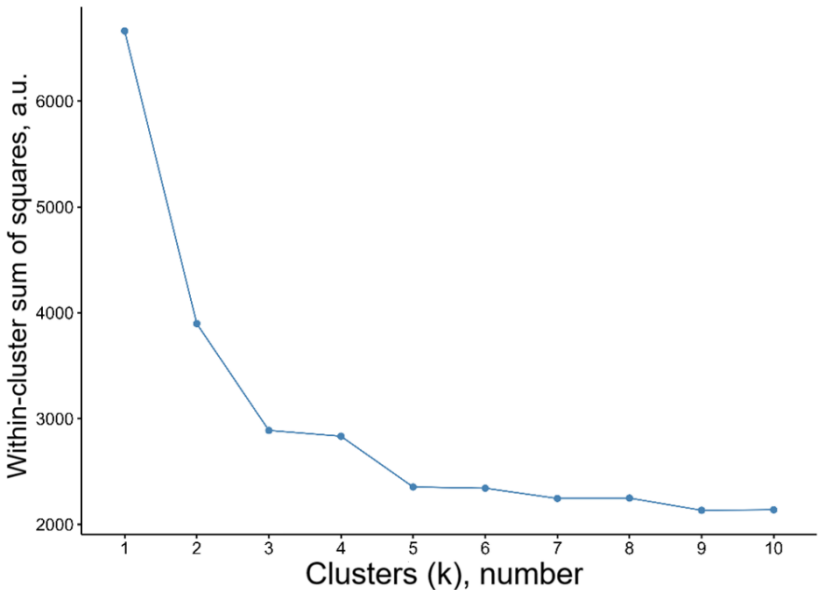

Figure 5. The elbow method — determination of the optimal cluster number

Theoretically, the *k*-means algorithm is based on minimizing the total squared distance between points and cluster centers (so-called centroids). The process iteratively recalculates center positions until the distance between them and the points belonging to the group becomes minimal. Thus, each sample is assigned to the cluster whose centroid is closest to it in multidimensional feature space. In the case of this work, the normalized percentage peak areas from GC-MS identified by retention times were used.

Despite its simplicity, the method reliably identifies main patterns: samples with similar chromatographic profiles group together, while distinct ones form separate clusters. The resulting picture clearly shows the internal data structure: which samples are similar, which differ, and to what extent (Fig. 6). The outcome demonstrates that 4 clusters was defined as "optimal", meaning the method classified the entire set of chromatograms into 4 groups.

Unlike PCA, where data is projected onto generalized variance axes, *k*-means works directly in the original space of normalized features, making cluster interpretation more straightforward and sometimes more understandable for practical analysis of coal extracts.

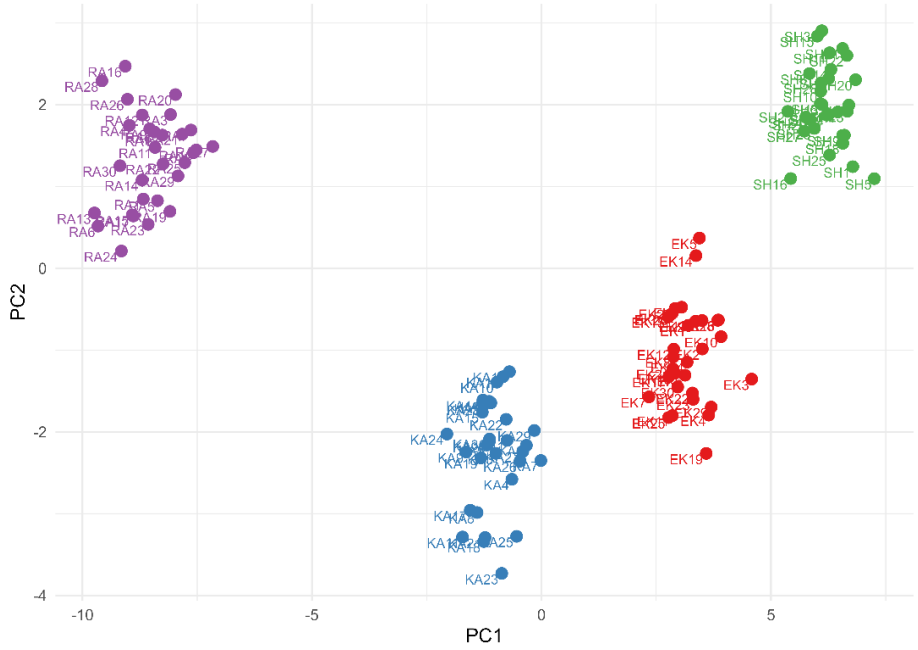

PC1 axis depicts the coordinates of the 1st principal component,
PC2 axis depicts the coordinates of 2nd principal component

Figure 6. *k*-means clustering

Thus, unsupervised clustering results confirm that coal extracts possess stable and reproducible features suitable for automatic classification. Methods like *k*-means can be used as a preliminary stage of chemometric analysis for initial sample grouping, selection of representative standards, and verification of models based on PCA, PLS, or neural network approaches. This makes them a valuable tool in constructing coal classification schemes by origin and other potential unifying characteristics.

Conclusions

In the present work, the applicability of a comprehensive analytical approach was evaluated, including sample preparation, gas chromatographic analysis of extracts, and subsequent chemometric data processing, for identifying similarities and differences between bituminous coal samples. Primary attention was given to verifying whether the combination of experimental and computational procedures yields a reproducible and interpretable data structure suitable for further classification and analysis.

Application of principal component analysis showed that the main differences between coal extract samples can be described by a limited number of principal components reflecting the cumulative contribution of multiple chromatographic peaks. In the space of the first three principal components, compact clusters of samples with similar chromatographic profiles form, indicating the presence of stable differences in extractable organic fraction composition.

Hierarchical clustering, performed directly on normalized chromatographic data without preliminary dimensionality reduction, revealed a multilevel structure of sample similarity. At the top level of the dendrogram, samples separate into two main groups, one of which predominantly corresponds to one coal source, while the second combines samples from three other sources. With further clustering depth, four stable clusters form, characterized by high intragroup profile similarity.

Additional *k*-means clustering confirmed the stability of the identified grouping. Analysis of the dependence of within-cluster sum of squares on the number of clusters showed that selecting four clusters results in an optimal compromise between model complexity and its descriptive capacity. The consistency of PCA, HCA, and k-means results, which can be seen by clear identification of four groups by each used method, indicates the systematic nature of differences between samples and the absence of dominant influence from random analytical variations.

The obtained results demonstrate that chromatographic profiles of bituminous coal extracts contain sufficient information for automatic sample grouping without preliminary assignment of deposit affiliation. The advantage of the developed method is that it requires no additional data on the qualitative and quantitative composition of coals, as classification is performed purely based on extract chromatograms. This allows for effective reduction of both analysis time and cost.

The considered approach can be used as a method for primary coal characterization, batch homogeneity control, and formation of "chromatographic fingerprint" databases. In the future, the identified patterns can be compared with technologically significant coal characteristics, such as volatile matter yield, flame length, spontaneous ignition propensity, or thermal degradation features, which opens prospects for expanding the methodology toward predictive models.

Supporting Information

The Supporting Information (Interactive 3D visualization of the results of using PCA; an Excel file with data extracted from chromatograms; a pipeline of R scripts for extracting and processing chromatogram data) is available free at https://github.com/Vtah/SuplimentaryEJoCh2026_2

Funding

This research is funded by the Science Committee of the Ministry of Science and Higher Education of the Republic of Kazakhstan (Grant No. BR24993009).

*Author Information**

**The authors' names are presented in the following order: First Name, Middle Name and Last Name*

Vitaliy Nikolayevich Fomin — Candidate of Chemical Sciences, Head of LEP "Physical-chemical methods of investigation", Karaganda National Research University named after Academician Ye.A. Buketov, Universitetskaya street, 28, 100024, Karaganda, Kazakhstan; e-mail: vitfomin@mail.ru; https://orcid.org/0000-0002-2182-2885

Assanali Anuarovich Ainabayev — Candidate of Chemical Sciences, Senior Researcher of the LEP "Physical-chemical methods of investigation", Karaganda National Research University named after Academician Ye.A. Buketov, Universitetskaya street, 28, 100024, Karaganda, Kazakhstan; e-mail: aliopel_82t@mail.ru; https://orcid.org/0000-0002-3443-446X

Saule Kidirbayevna Aldabergenova — Candidate of Chemical Sciences, Associated Professor, Department of Inorganic and Technical Chemistry, Karaganda National Research University named after Academician Ye.A. Buketov, Universitetskaya street, 28, 100024, Karaganda, Kazakhstan; e-mail: aldsau@mail.ru; https://orcid.org/0000-0002-4262-911X

Dauletkhan Asanovich Kaikenov — PhD, Lead Researcher of the LEP "Physical-chemical methods of investigation", Karaganda National Research University named after Academician Ye.A. Buketov, Universitetskaya street, 28, 100024, Karaganda, Kazakhstan; e-mail: krg.daykai@mail.ru; https://orcid.org/0000-0003-4621-7603

Milana Alexandrovna Turovets (*corresponding author*) — Master of Technical Sciences, 2nd year PhD student, Engineer, LEP "Physical-chemical methods of investigation", Karaganda National Research University named after Academician Ye.A. Buketov, Universitetskaya street, 28, 100024, Karaganda, Kazakhstan; e-mail: turovec26.07@mail.ru; https://orcid.org/0000-0002-0493-6426

Author Contributions

The manuscript was written through contributions of all authors. All authors have given approval to the final version of the manuscript. CRediT: **Vitaliy Nikolayevich Fomin** conceptualization, methodology, vis-

ualization, supervision; **Assanali Anuarovich Ainabayev** data curation, investigation, formal analysis; **Saule Kidirbayevna Aldabergenova** investigation, methodology, validation; **Dauletkhan Asanovich Kaikenov** data curation, formal analysis, visualization; **Milana Alexandrovna Turovets** project administration, methodology, writing-review & editing;

Conflicts of Interest

The authors declare no conflict of interest.

References

1 Alexander, G., & Hazai, I. (1981). Chromatographic fingerprinting of coal extracts. *Journal of Chromatography*, 217, 19–38. https://doi.org/10.1016/S0021-9673(00)88059-0

2 Bartle, K.D., Mills, D.G., Mulligan, M.J., Amaechina, I.O., & Taylor, N. (1984). Molecular mass calibration in size-exclusion chromatography of coal derivatives. *Fuel*, *63*(11), 1556–1560. https://doi.org/10.1016/0016-2361(84)90226-6

3 Blanco, C., Prado, J.G., Guillén, M.D., Borrego, A.G., & Iglesias, M.J. (1991). Capillary gas-chromatographic and combined gas-chromatography mass-spectrometric study of the volatile fraction of a coal-tar pitch using OV-1701 stationary phase. *Journal of Chromatography*, *539*(1), 157–167. https://doi.org/10.1016/S0021-9673(01)95369-5

4 Assis, L., & Lanças, F. (1999). High-resolution gas chromatography and high-resolution gas chromatography/mass spectrometry study of the volatile fraction obtained from high-inertinite Brazilian coal by supercritical fluid extraction. *Journal of Microcolumn Separations*, *11*(7), 501–512. https://doi.org/10.1002/(SICI)1520-667X(1999)11:7<501::AID-MCS2>3.0.CO;2-V

5 Takanohashi, T., Yoshida, T., Iino, M., Katoh, K., & Nishioka, M. (2000). An inverse liquid chromatography study of the interaction of organic compounds with Argonne premium coals. *Energy & Fuels*, *14*(3), 720–726. https://doi.org/10.1021/ef990261y

6 Platonov, V.V., Proskuryakov, V.A., Korotaeva, K.V., & Yur'ev, E.M. (2002). Development and optimization of the procedure of gas-chromatographic elemental analysis of high-carbon solid fossil fuels. *Russian Journal of Applied Chemistry*, *75*(5), 834–839. https://doi.org/10.1023/A:1020387318686

7 Rathsack, P., & Otto, M. (2014). Classification of chemical compound classes in slow pyrolysis liquids from brown coal using comprehensive gas-chromatography mass-spectrometry. *Fuel*, *116*, 841–849. https://doi.org/10.1016/j.fuel.2013.05.100

8 Zubkova, V., & Witkiewicz, Z. (2016). Chromatographic analysis of chemical compositions of coals and changes in them during technological processing. *Critical Reviews in Environmental Science and Technology*, *46*(7), 701–755. https://doi.org/10.1080/10643389.2016.1154779

9 Zuber, J., Ecker, D., Otto, M., & Wüst, E. (2016). Gas chromatography/atmospheric pressure chemical ionization-Fourier transform ion cyclotron resonance mass spectrometry of pyrolysis oil from German brown coal. *International Journal of Analytical Chemistry*, 2016, Article 5960916. https://doi.org/10.1155/2016/5960916

10 Li, G., Li, Z., Ma, C., Zhang, L., Cheng, J., & Hou, Y. (2019). Molecular characteristics of the soluble components from three low-rank coals based on the analyses using GC/MS and GC/Q-TOF MS. *Fuel*, 254, Article 115671. https://doi.org/10.1016/j.fuel.2019.06.010

11 Li, W., Zhang, D., Hou, Y., Qiao, E., & Cui, S. (2019). Analysis of light weight fractions of coal-based crude oil by gas chromatography combined with mass spectroscopy and flame ionization detection. *Fuel*, 241, 392–401. https://doi.org/10.1016/j.fuel.2019.04.108

12 Wang, X., Zhu, Z., & Li, X. (2024). Analysis of the Organic Chemical Fractions of Three Coal Extracts. *Applied Sciences*, *14*(19), 8933. https://doi.org/10.3390/app14198933

13 Wang, X., & He, X. (2022). Cluster Analysis of Soluble Organic Fractions in Two Low-Rank Coals. *Applied Sciences*, *12*(22), 11562. https://doi.org/10.3390/app122211562

14 McGregor, L., Gauchotte, E., Habets, F., & Goovaerts, P. (2012). Multivariate statistical methods for the environmental forensic classification of coal tars from former manufactured gas plants. *Environmental Science & Technology*, *46*(7), 3744–3752. https://doi.org/10.1021/es203708w

15 Zhang, X., Wei, X., Li, G., Wang, Y., Zhang, L., & Zong, Z. (2020). Structural characteristics of soluble organic matter in four low-rank coals. *Fuel*, 267, Article 117230. https://doi.org/10.1016/j.fuel.2020.117230

16 Fan, X., Yu, H., Liu, Z., Yu, J., Zhou, Q., & Wei, X. (2018). Molecular characteristics of Shenfu coal characterized by mass spectrometers with three ion sources. *ChemistrySelect*, *3*(37), 10383–10387. https://doi.org/10.1002/slct.201802238

17 Xu, H., Zhang, L., Wei, X., Fan, X., & Zong, Z. (2024). Exploring the molecular characteristics of organic matter in low-rank coals using GCxGC/TOF-MS plus data mining. *Journal of Analytical and Applied Pyrolysis*, 181, Article 106605. https://doi.org/10.1016/j.jaap.2024.106605

18 Hamilton, J.F., Webb, P.J., Lewis, A.C., & Reviejo, M.M. (2007). Comprehensive two-dimensional gas chromatography coupled to time-of-flight mass spectrometry of coal liquids produced during a coal liquefaction process. *Energy & Fuels*, *21*(1), 286–294. https://doi.org/10.1021/ef060366i

19 Zhang, X., Li, G., Wei, X., Zhang, L., & Zong, Z. (2019). Cluster analysis of molecular characteristics for soluble organic matter in coals. *Chinese Journal of Analytical Chemistry*, *47*(1), 99–105. https://doi.org/10.19756/j.issn.0253-3820.181585

20 Zeng, Z., Hugel, H.M., Marriott, P.J., & Schoenmakers, P.J. (2014). Interpretation of comprehensive two-dimensional gas chromatography data using advanced chemometrics. *TrAC Trends in Analytical Chemistry*, 53, 150–166. https://doi.org/10.1016/j.trac.2013.08.009

21 Li, G., Li, Z., Jiang, H., Mo, W., Hu, H., & Zhang, L. (2019). Insight into molecular information of Huolinguole lignite obtained by Fourier transform ion cyclotron resonance mass spectrometry and statistical methods. *Rapid Communications in Mass Spectrometry*, *33*(13), 1107–1113. https://doi.org/10.1002/rcm.8448

22 Huang, J., Li, G., Xu, H., Li, Z., Qin, Z., Fan, X., & Wei, X. (2024). Molecular characteristics of eight lignites based on the big data obtained from Orbitrap mass spectrometry. *Journal of the Energy Institute*, 114, Article 101569. https://doi.org/10.1016/j.joei.2024.101569

23 Li, G., Qin, Z., Li, Z., Xu, H., & Wei, X. (2024). Combination of chemometrics and mass spectrometric methods for the data mining of molecular structure information of coal and biomass. *Fuel*, 361, Article 130714. https://doi.org/10.1016/j.fuel.2023.130714

24 Roy, A., Varma, A. K., Sar, T. K., Biswas, S., & Gupta, S. (2021). Insights from principal component analysis applied to Py-GCMS study of Indian coals and their solvent extracted clean coal products. *International Journal of Coal Science & Technology*, *8*(6), 1504–1514. https://doi.org/10.21203/rs.3.rs-127356/v1

25 Li, Y., Li, G., Xu, H., Li, Z., Fan, X., Qin, Z., & Wei, X. (2024). Accurate classification of the molecular characteristics of soluble portions from various lignites: Joint analysis of thermal dissolution experiments and data mining methods. *Journal of Analytical and Applied Pyrolysis*, 180, Article 106536. https://doi.org/10.1016/j.jaap.2024.106536

26 Fan, H.-H., Li, J., Song, L., & Cui, Y. (2025). Comprehensive quantitative analysis of coal-based liquids by Mask R-CNN-assisted two-dimensional gas chromatography. *Separations*, *12*(2), Article 22. https://doi.org/10.3390/separations12020022

27 Li, B., Li, G., Jiang, H., Mo, W., Hu, H., & Zhang, L. (2019). Insight into molecular information of Huolinguole lignite obtained by Fourier transform ion cyclotron resonance mass spectrometry and statistical methods. *Rapid Communications in Mass Spectrometry*, *33*(13), 1107–1113. https://doi.org/10.1002/rcm.8448

28 Khare, P., Baruah, B.P., & Rao, P.G. (2011). Application of chemometrics to study the kinetics of coal pyrolysis: A novel approach. *Fuel*, *90*(11), 3299–3305. https://doi.org/10.1016/j.fuel.2011.05.017

29 Roy, A., Varma, A.K., Rao, K.S., Prasad, M., & Reddy, B.S. (2019). Py-GCMS studies of Indian coals and their solvent extracted products. *Fuel*, 256, Article 115981. https://doi.org/10.1016/j.fuel.2019.115981

30 Yin, H., Yang, Y., Liu, X., Li, J., & Zhang, X. (2021). Application of chemometrics for coal pyrolysis products by online py-GCxGC-MS. *ACS Omega*, *6*(5), 3763–3770. https://doi.org/10.1021/acsomega.0c05359

31 Lu, W., Li, H., Wang, X., Zhang, Y., & Chen, J. (2024). Discrimination of coal geographical origins through HS-GC-IMS assisted with machine learning algorithms in larceny case. *Journal of Chromatography A*, 1735, Article 465330. https://doi.org/10.1016/j.chroma.2024.465330

32 Zhang, L., Li, G., Wei, X., Fan, X., & Zong, Z. (2022). Characterization of nitrogen-containing compounds in coal tar and its subfractions by comprehensive two-dimensional GC x GC-TOF and ESI FT-ICR mass spectrometry based on new separation method. *Fuel Processing Technology*, 227, Article 107213. https://doi.org/10.1016/j.fuproc.2022.107213

33 Fan, H.-H., Li, J., Song, L., & Cui, Y. (2025). Comprehensive quantitative analysis of coal-based liquids by Mask R-CNN-assisted two-dimensional gas chromatography. *Separations*, *12*(2), Article 22. https://doi.org/10.3390/separations12020022

34 Wu, Z., Rodgers, R.P., & Marshall, A.G. (2003). Resolution of 10,000 compositionally distinct components in polar coal extracts by negative-ion electrospray ionization Fourier transform ion cyclotron resonance mass spectrometry. *Energy & Fuels*, *17*(4), 946–953. https://doi.org/10.1021/ef030026m

35 Li, Z., Li, G., Xu, H., Qin, Z., Fan, X., & Wei, X. (2025). Classification of soluble proportions derived from coals and their correlation with coal type: Conjoint analyses of extraction, thermal dissolution and machine learning. *Journal of the Energy Institute*, 119, Article 102010. https://doi.org/10.1016/j.joei.2025.102010

36 Fomin, V.N., Aynabaev, A.A., Kaykenov, D.A., Sadyrbekov, D.T., Bakhytkyzy, I., & Aldabergenova, S.K. (2021). Optimization of coal tar gas chromatography conditions using probabilistic-deterministic design of experiment. *Bulletin of the Karaganda University. Chemistry Series*, *4*(104), 39–46. https://doi.org/10.31489/2021Ch4/39-46

37 Turovets, M.A., Fomin, V.N., Kelesbek, N.K., Ainabayev, A.A., & Sadyrbekov, D.T. (2024). Chemometric approach for the determination of vanadium by the LIBS method. *Eurasian Journal of Chemistry*, *29*(4), 61–70. https://doi.org/10.31489/2959-0663/4-24-10

38 Fomin, V.N., Aldabergenova, S.K., Kelesbek, N.K., Ainabayev, A.A., Sadyrbekov, D.T., Kaykenov, D.A., Borsynbayev, A.S., Azhibay, N.T., & Turovets, M.A. (2024). Method of classification and quantitative analysis of vein quartz using LIBS and chemometric techniques. *Bulletin of the L.N. Gumilyov Eurasian National University. Chemistry. Geography. Ecology Series*, *2*(147), 48–60. https://doi.org/10.32523/2616-6771-2024-147-2-48-60

39 Fomin, V.N., Aldabergenova, S.K., Rustembekov, K.T., Omarov, K.B., Rozhkovoy, I.E., Dik, A.V., & Saulebekov, D.M. (2021). Optimization of the parameters of a laser induced breakdown spectrometer (LIBS) using probabilistic-deterministic design of experiment. Industrial Laboratory. *Diagnostics of Materials*, *87*(5), 14–19. https://doi.org/10.26896/1028-6861-2021-87-5-14-19

40 Fomin, V., Turovets, M., Kelesbek, N., Ainabayev, A., Sadyrbekov, D., Kaykenov, D., Borsynbayev, A., Azhibay, N., & Aldabergenova, S. (2025). LIBS of low-alloyed lead systems: Chemometric data processing and quantitative analysis. *Analytica*, *6*(4), Article 55. https://doi.org/10.3390/analytica6040055

41 Fomin, V.N. (2018). *Veroiatnostno-determinirovannoe planirovanie eksperimenta (VDPE)* [Probabilistically-deterministic design of experiments (PDDE)] (Certificate of Authorship of the Republic of Kazakhstan No. 26 dated 01.10.2018) [Computer software]. Kazpatent. https://copyright.kazpatent.kz/?!.iD=kux

42 Fomin, V. (2025). Software implementation of probabilistic-deterministic design of a chemical experiment on R. *Bulletin of the L.N. Gumilyov Eurasian National University. Chemistry. Geography. Ecology Series, 2*(151), 130–142. https://doi.org/10.32523/2616-6771-2025-151-2-130-142

43 Buldakov, Y.M., Egizekov, M.G., Kulenova, N.A., Reymer, Y.A., & Skorikov, S.P. (2018). Tovarnyy ugol' i produkty yego szhiganiya — perspektivy razvitiya novykh proizvodstv [Commercial coal and its combustion products: prospects for new industry development]. *Novosti nauki Kazahstana — News of Kazakhstan Science*, *1*(135), 99–116. https://vestnik.nauka.kz/storage/docs/2018/03/9-%D0 %91 %D1 %83 %D0 %BB%D0 %B4 %D0 %B0 %D0 %BA%D0 %BE%D0 %B2.pdf [in Russian]

44 Ermagambet, B.T., Kasenov, B.K., Nurgaliyev, N.U., Kazankapova, M.K., Kasenova, Zh.M., & Kuanyshbekov, E.E. (2020). Chemical Composition and Electrophysical Characteristics of the Ash of Bogatyr Coal. *Solid Fuel Chemistry*, *54*(2), 99–104. https://doi.org/10.3103/s0361521920020020

How to Cite: Gulomjonov, Kh.A., Ashurov, N.Sh., Atakhanov, A.A., & Berdiyorov, G.R. (2026). Effect of HF Concentration on the Structural, Morphological, and Electrical Properties of $Ti_3C_2T_x$ MXene Prepared by Microwave-Assisted Etching. *Eurasian Journal of Chemistry, 31, 2(122), 77–90*. https://doi.org/10.31489/2959-0663/2-26-9

INORGANIC CHEMISTRY

Article

Received: 4 March 2026 | Revised: 18 May 2026 |
Accepted: 1 June 2026 | Published online: 2 June 2026

UDC 620.3:544.23

https://doi.org/10.31489/2959-0663/2-26-9

Khumoyunmirzo A. Gulomjonov[1*], Nurbek Sh. Ashurov[1], Abdumutolib A. Atakhanov[1], Golibjon R. Berdiyorov[2]

[1]*Institute of Polymer Chemistry and Physics, Tashkent, Uzbekistan;*
[2]*Hamad Bin Khalifa University, Doha, Qatar*
*(*Corresponding author's e-mail: khumoyungulomjonov@gmail.com)*

Effect of HF Concentration on the Structural, Morphological, and Electrical Properties of $Ti_3C_2T_x$ MXene Prepared by Microwave-Assisted Etching

Two-dimensional MXenes have emerged as a versatile class of materials for energy storage, electronics, and catalysis owing to their high electrical conductivity, tunable surface chemistry, and layered structure; however, the controlled synthesis of $Ti_3C_2T_x$ MXene with well-defined morphology and stable surface chemistry remains a major challenge, as etching conditions strongly influence structural integrity, degree of exfoliation, and functional performance. In this study, the morphological, structural, and functional evolution of $Ti_3C_2T_x$ MXene materials was systematically investigated by applying hydrofluoric acid (HF) etching at varying concentrations (6 %, 12 %, 24 %, 36 %, and 48 %) using microwave-assisted method. The impact of etching intensity on Al removal, layer delamination, and surface functionalization was examined through a multitechnique characterization approach including scanning electron microscopy (SEM), X-ray diffraction (XRD), Fourier transform infrared spectroscopy (FTIR), and energy-dispersive X-ray spectroscopy (EDS). The results reveal that an HF concentration of 24 % achieves efficient Al extraction while preserving the Ti–C framework, yielding well-exfoliated and structurally stable MXene sheets. Lower HF concentrations (6 % and 12 %) lead to incomplete etching and limited exfoliation, whereas higher concentrations (36 % and 48 %) cause over-etching and pronounced structural degradation. These findings underscore the critical role of etching conditions in tuning MXene morphology and functional properties. The ability to balance surface termination control and structural integrity via gradient etching is particularly relevant for the use of $Ti_3C_2T_x$ MXenes as conductive electrodes and interfacial layers in photovoltaic and other energy-conversion devices.

Keywords: $Ti_3C_2T_x$ MXene, MAX phase, gradient HF etching, etching concentration, surface terminations, exfoliation, morphology, structural integrity

Introduction

Two-dimensional (2D) transition metal carbides and nitrides, collectively known as MXenes, have rapidly emerged as an exciting class of nanomaterials due to their unique combination of metallic conductivity, hydrophilic surfaces, mechanical robustness, and versatile surface chemistries [1–3]. Since their discovery in 2011 via selective etching of the "A" layer from MAX phases ($M_{n+1}AX_n$), MXenes such as $Ti_3C_2T_x$ have attracted extensive research interest for applications including energy storage, catalysis, electromagnetic interference (EMI) shielding, sensing, and environmental remediation [4–6].

The conventional synthesis of MXenes involves chemical etching of the parent MAX phase using hydrofluoric acid (HF) or in situ generated HF from fluoride salts [7–10]. This process removes the "A" element (typically Aluminum), resulting in multilayered $Ti_3C_2T_x$ with surface terminations like –F, –OH, and –O, collectively denoted as T_x groups. These terminal groups strongly influence MXene's electrochemical, optical, and interfacial properties [11–14].

Theoretical and experimental studies have demonstrated that different surface terminations lead to distinct electronic, ionic, and optical behaviors in $Ti_3C_2T_x$ [15–21], significantly impacting their potential for energy storage, water purification, and membrane design. For instance, $Ti_3C_2T_x$ membranes with optimized surface terminations exhibit excellent ion-sieving and antibacterial capabilities, highlighting the key role of surface chemistry in functional performance [22–27].

The concentration of HF used during etching is a crucial parameter affecting MXene quality. Low HF concentrations often result in incomplete etching and poor delamination, whereas high HF concentrations promote over-etching, structural defects, and excessive fluorination, which degrade conductivity and mechanical integrity [28–30]. Excessive fluorination adversely affects selective ion intercalation and electrochemical behaviour, while oxygen terminations improve ion mobility and device performance [31–33].

To overcome the limitations of HF-based synthesis, alternative strategies such as in situ HF generation (e.g., LiF+HCl), molten salt etching, and electrochemical methods have been developed, allowing better control over surface terminations and morphology [34–36]. Moreover, hybrid structures combining MXenes with graphene or silver nanoparticles have been proposed to enhance membrane stability and electronic conductivity [37], demonstrating that post-synthesis modifications can synergistically improve properties when etching is well controlled. Furthermore, environmentally friendly approaches to MXene synthesis, particularly those based on microwave irradiation, are currently being actively developed [38, 39]. Microwave-assisted synthesis is reported to enhance reaction kinetics through rapid and uniform heating, thereby reducing processing time and improving etching efficiency compared to conventional methods [38–41]. These characteristics make microwave irradiation particularly suitable for controlled MXene synthesis. This technology offers several advantages, including cost-effectiveness, operational simplicity, rapid and uniform heating, high reaction rates, and improved control over morphology [40, 41]. In addition, microwave irradiation can promote selective and localized heating at the solid–liquid interface, which facilitates more effective disruption of Al layers and accelerates their removal from the Ti_3AlC_2 structure, contributing to improved etching uniformity and structural evolution of $Ti_3C_2T_x$ [42].

Recent advances in the MXene field have increasingly focused on engineering both the atomic surface terminations and multiscale architectures of $Ti_3C_2T_x$ and related systems to enhance their functional performance. In energy-storage applications, post-treatments such as atomic surface reduction have been shown to greatly improve capacitance and rate capability by optimizing termination chemistry and defect density [43, 44]. At the same time, the design of hierarchical MXene macrostructures including porous films, foams, and composite frameworks has enabled outstanding (EMI) shielding performance with high conductivity and mechanical robustness [45, 46]. Water-treatment and membrane technologies have also progressed rapidly, with MXene laminates and MXene–polymer hybrids demonstrating high desalination flux, ion-sieving selectivity, and antibacterial activity due to controlled interlayer spacing and surface surface terminations [47]. In the sensing field, $Ti_3C_2T_x$ based gas sensors have achieved high room-temperature sensitivity and selectivity by tuning defects, terminations, and hybridization with oxides or other 2D materials [48]. These developments are driven by rational synthesis control etching pathway, termination tuning, and structural design positioning MXenes as a versatile platform for next-generation supercapacitors, batteries, nanofluidic devices, sensors, and environmental remediation systems [49, 50].

Latest studies underscore that even after extensive exploration of MXenes, surface functionalization remains a pivotal lever for unlocking new application spaces and improving performance. By introducing tailored functional groups, ligands or dopants on the MXene surface, researchers have been able to modulate electronic work-function, wettability, interlayer spacing and defect states thereby improving properties for catalysis, sensing, biomedicine and energy storage [51–53]. For example, controlled termination engineering on $Ti_3C_2T_x$ enables precise tuning of the work function and charge-transfer kinetics, opening pathways to high-efficiency sensors and heterostructure devices [54]. In biomedicine and wearable electronics, surface-functionalized MXene platforms promise enhanced biocompatibility, selective binding and long-term stability in complex physiological environments something unmodified MXene surfaces alone struggle to deliver [55]. In electro-catalysis, the introduction of specific functional moieties on the MXene basal plane or edges improves active-site exposure and stabilises the material under harsh conditions, thus expanding MXene utility beyond its initial energy-storage niche [56]. Collectively, these advances reveal that surface functionalization isn't just a fine-tuning step, but a core strategy for diversifying MXene applications and achieving next-generation performance across domains.

The aim of this work was to systematically investigate the effect of hydrofluoric acid (HF) concentration on the morphological, structural, and functional evolution of $Ti_3C_2T_x$ MXene using a microwave-

assisted gradient etching approach. Unlike traditional HF etching, which relies solely on thermal conditions, this strategy accelerates reaction kinetics and allows for more precise control over the selective removal of aluminum from Ti_3AlC_2. The novelty of this work lies in the systematic investigation of HF concentration under microwave-assisted conditions, enabling the identification of a processing window where efficient Al removal, structural integrity, and controlled surface functionalization are simultaneously achieved. This study demonstrates that microwave irradiation facilitates the development of the characteristic accordion-like MXene morphology at 24 % HF, which suggests that microwave-assisted etching may enable efficient morphology formation at comparatively moderate HF concentrations. It establishes a quantitative structure–property correlation, linking shifts in the (002) reflection and increases in the c lattice parameter and interlayer spacing to the reaction yield and electrical conductivity of MXene and it identifies a practical processing window where efficient aluminum removal occurs while maintaining the integrity of the Ti–C framework, as higher HF concentrations lead to over-etching and structural degradation. These findings provide a rational basis for tailoring the morphology and functional properties of $Ti_3C_2T_x$ MXenes through controlled etching conditions. In the present work, a direct experimental comparison with conventional non-microwave HF etching was not performed; however, the role of microwave irradiation is discussed based on literature reports and the observed formation of accordion-like $Ti_3C_2T_x$ morphology at 24 % HF.

Experimental

Chemicals and Materials

MAX phase (Ti_3AlC_2, powder, 98 wt%) was purchased from Shandong Fan Tai Fine Chemical Biotechnology Co., Ltd., China. Hydrofluoric acid (HF, 48 wt %) was purchased from Sigma-Aldrich Chemical Co. Ltd. (Tianjin, China). Filtration and delamination processes employed cellulose acetate membranes with a pore size of 0.22 μm (GVS). All reagents were of analytical grade and used without further purification. Deionized water was employed throughout all experiments unless otherwise stated.

Synthesis of $Ti_3C_2T_x$ (MXene)

$Ti_3C_2T_x$ was synthesized by selective chemical etching of the Al layer from the Ti_3AlC_2 using a published method with a slight modification [57]. Briefly, 1 g of Ti_3AlC_2 powder was added to 10 mL of hydrofluoric acid solutions of varying concentrations (6 %, 12 %, 24 %, 36 %, and 48 %). The mixtures were placed into a Microwave Digester (BMD-12H, China) and treatment with microwave radiation at 2450 MHz for 30 minutes. Following the microwave treatment, the suspensions were centrifuged at 3500 rpm for 10 minutes, and the black powder was separated. The sediments were washed repeatedly with deionized (until pH ≈ 6-7) to remove residual HF. To obtain delaminated MXene powders, the washed sediments were mildly sonicated for 30 minutes. The final $Ti_3C_2T_x$ powders were collected by vacuum drying at 60 °C for 12 hours. MXene samples synthesized using 6 %, 12 %, 24 %, 36 %, and 48 % HF solution were labeled as MX-6, MX-12, MX-24, MX-36 and MX-48, respectively.

Although it is not possible to calculate an accurate reaction yield because it isn't possible to define an exact stoichiometry for the samples obtained, a yield was calculated by the following formula, that usually is used in literature for these materials [58]:

$$\text{Yield}(\%)=\left(\frac{\text{MXene mass}}{\text{MAX phase mass}}\right)\times 100.$$

Characterization Methods

FTIR

The FTIR spectrometer "Inventio-S" (Bruker) was used and FTIR spectra were recorded in 400–4000 cm^{-1} wavenumber range with a resolution of 2 cm^{-1} and 32 scans at a temperature of 25 °C. All samples were finely ground, dried at 60 °C for 12 h, and pressed into KBr pellets (1 wt%) before analysis. Software of OPUS was applied to determine the peaks at specific points.

Wide-Angle X-Ray Diffraction

XRD studies were carried out using XRD Miniflex 600 (Rigaku, Japan) with monochromatic CuKα radiation isolated by a nickel filter with a wavelength of 1.5418 Å at 40 kV and the current strength of 15 mA. The spectrum was recorded in the interval $2\theta = 5°–40°$. The air-dried MXene powders were gently ground, mounted on zero-background glass slides, and analyzed under identical sample thickness and humidity conditions. The data processing of experimental diffraction patterns, peak deconvolution, describing the peaks

used by Miller indices, peak shape, and the basis for the amorphous contribution were conducted using the software "SmartLab Studio II" and data base PDF-2 (2020 Powder diffraction file, ICDD).

Scanning Electron Microscopy (SEM)

Scanning electron microscopy studies were performed using SEM equipment Jeol-210 (Japan). Magnification of the device ×10–300000, voltage 200–300 V, maximum scanning area ($x \div y \div z$) is 120÷120÷65 μm. SEM images were obtained at an accelerating voltage of 10 kV and a working distance of 10.6 mm.

Conductivity

The electrical conductivity of MXene and MAX phases samples was evaluated from measured sheet resistance using the Ossila four-point probe system (Osilla, UK), combined with thickness measurements to calculate conductivity. Four-point probe measurements were performed following the procedures described in [59].

Statistical Analysis

All experimental data were collected in triplicates and data expressed as average ± standard deviation. Data were compared using a one-way ANOVA with post-Bonferroni test using GraphPad Prism 5.04 (GraphPad Software Inc.)

Results and Discussion

$Ti_3C_2T_x$ MXene was synthesized through selective chemical etching of the aluminum layers in the parent MAX phase Ti_3AlC_2 using hydrofluoric acid (HF) at various concentrations. This etching process occurs due to the preferential reactivity of aluminum with HF, resulting in the formation of soluble AlF_3 species and the release of hydrogen gas (H_2), while the titanium-carbon framework remains largely intact. Consequently, the layered structure of Ti_3C_2 is preserved, and surface terminations such as –F, –OH, and –O are introduced, resulting in $Ti_3C_2T_x$ (Fig. 1).

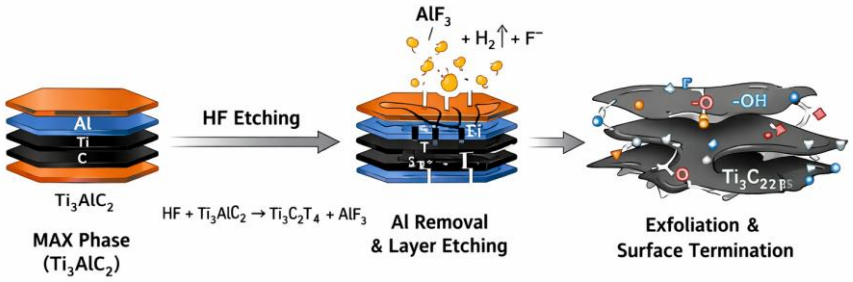

Figure 1. Schematic representation of MXene preparation via selective chemical etching process

In the FTIR spectrum of pristine, non-etched Ti_3AlC_2 (Fig. 2, curve 1), the weak absorption bands are observed, indicating the absence of significant surface functionalization. A broad, low-intensity band in the 3443–3439 cm^{-1} region corresponds to O–H stretching vibrations. The bands at 2854 and 2925 cm^{-1} arise from C–H stretching vibrations, likely associated with trace organic residues remaining from the synthesis process, while the weak band near 1640 cm^{-1} is assigned to the bending vibration of adsorbed water molecules, attributed to their hydrophilic nature [60]. In the low wavenumber region (500–800 cm^{-1}), characteristic vibrations of Ti–C and Ti–Al bonds dominate, which are typical of Ti-based MAX phases and confirm that the layered Ti_3AlC_2 structure is preserved with negligible surface terminations.

For the sample MX-6 (Fig. 2, curve 2), a noticeable broadening and increase in intensity of the O–H stretching band at ~3440 cm^{-1} is observed, indicating the initial formation of hydroxyl groups on the MXene surface. At the same time, weak new features appearing in the 550–650 cm^{-1} region indicate the onset of Ti–O bond formation. When the HF concentration is increased to 12 % and 24 %, the intensity of the O–H stretching band increases significantly, reflecting a higher density of hydroxyl terminations. In addition, absorption bands in the 1200–1400 cm^{-1} region, assigned to C–F stretching vibrations, indicate the progressive incorporation of fluorine terminations. Notably, for the sample MX-24 (Fig. 2, curve 4), a balanced intensity of O–H and C–F groups is observed, together with clear Ti–O/Ti–F vibrations in the low-wavenumber region [61]. This behaviour indicates that the Al layers were effectively removed while the Ti–C backbone of the structure remained intact. With further increase of the HF concentration to 36 % and 48 %, an intense O–H stretching band is also observed; however, the comparison of absolute intensities between different KBr

tablets is semi-quantitative due to different water sorption. The enhanced intensity of the band near 1640 cm^{-1} is attributed to a higher degree of water molecule intercalation between the MXene layers. However, the appearance of distinct Ti–F vibrations in the 550–650 cm^{-1} region for these samples indicates excessive fluorine coverage of the surface. This observation is consistent with the structural degradation and over-etching effects revealed by SEM and XRD analyses.

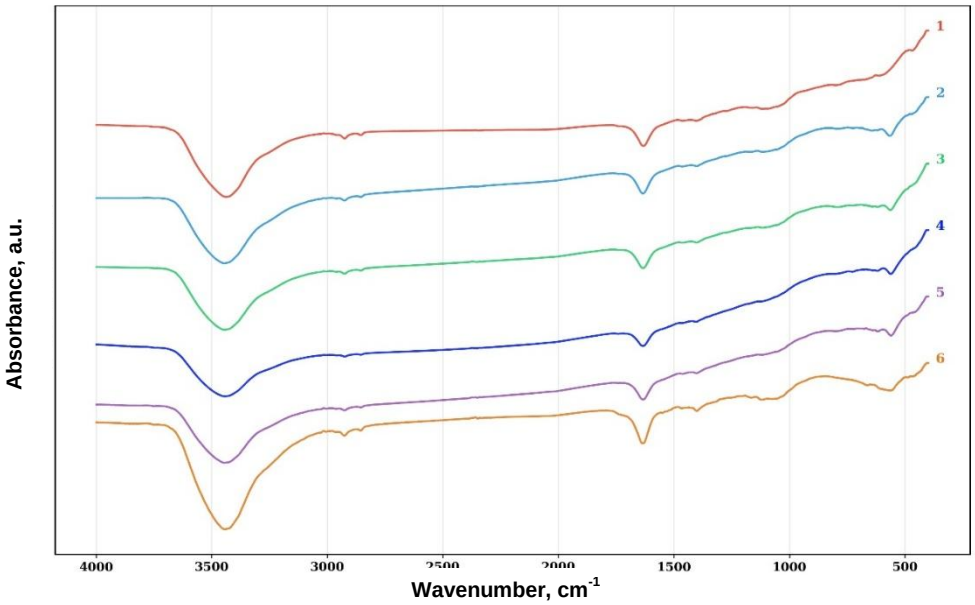

Figure 2. FTIR spectra of MAX phase (*1*) and MXene samples:
MX-6 (*2*), MX-12 (*3*), MX-24 (*4*), MX-36 (*5*), MX-48 (*6*)

Overall, the FTIR analysis indicates that HF concentration influences the evolution of surface-related functional groups on $Ti_3C_2T_x$ MXene. Since FTIR provides qualitative information on vibrational features, the observed band intensities are discussed as relative trends rather than precise quantitative measurements. While incomplete functionalization is observed at low concentrations, an optimal ratio of –OH, –F, and =O groups is achieved at an intermediate concentration (24 %). Higher HF concentrations, however, lead to excessive fluorination, which may compromise the structural stability of the material.

The structural changes occurring during HF etching of Ti_3AlC_2 and the subsequent formation of $Ti_3C_2T_x$ MXene were investigated using XRD (Fig. 3*a*). The neat Ti_3AlC_2 sample exhibits sharp and intense diffraction peaks characteristic of the MAX phase, confirming its high crystallinity and well-ordered layered structure. The (002) peak observed at a low angle (~9.49°) corresponds to the regular stacking of Ti–C layers separated by Al atomic layers, including characteristic peaks around 2θ = 19.2° (004), 29.5° (103/006), 36.4° (104), 39.2° (105), and 42.3° (106) [62].

After HF etching, significant changes are observed in the diffraction patterns of all $Ti_3C_2T_x$ samples. For the sample MX-6, the (002) peak shifts to a lower 2θ value, indicating an increase in interlayer spacing, which is commonly attributed to partial Al removal and is often accompanied by the formation of surface functional groups. The persistence of a few residual MAX-phase peaks, such as the (104) reflection at ~39°, indicates that etching was not fully complete and exfoliation of the MAX phase is limited. When the HF concentration is increased to 12 %, Al-related peaks further weaken and the (002) peak becomes more pronounced at ~9.26°. This indicates more effective Al removal and partial opening of the layered structure; however, traces of the MAX phase are still present, confirming that the etching process is not yet complete. At low HF concentrations (6 % and 12 %), the etching reaction proceeds slowly and incompletely. SEM and XRD results indicate that a significant fraction of the Al layers remains within the structure, which limits interlayer expansion and suppresses effective layer separation. The persistence of MAX-phase reflections in XRD patterns and the relatively compact layered morphology observed by SEM confirm that insufficient etching hinders the formation of well-separated MXene sheets (Fig. 4*b*, *c*). In this regime, the Ti_3AlC_2 structure is only partially transformed, resulting in limited layer separation and structurally heterogeneous products.

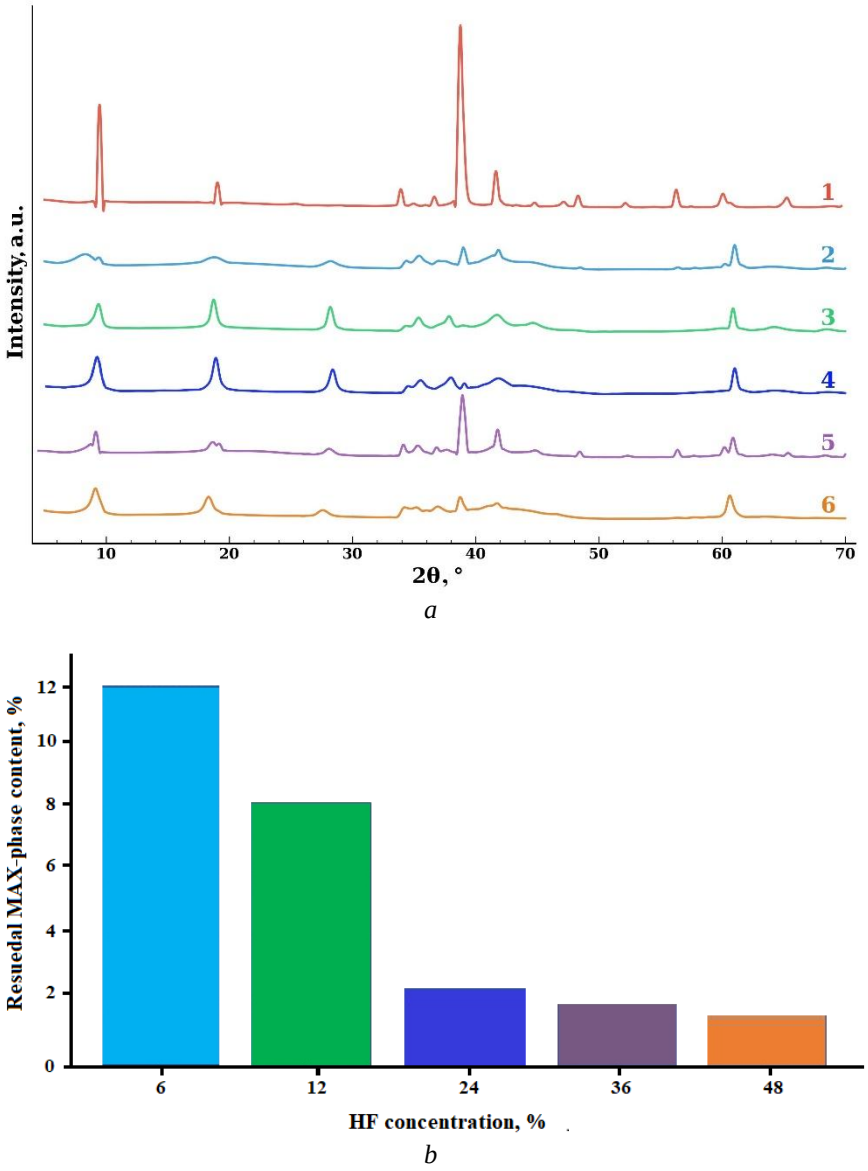

Figure 3. XRD patterns (*a*) of MAX-phase (*1*) and MXene samples: MX-6 (*2*), MX-12 (*3*), MX-24 (*4*), MX-36 (*5*), MX-48 (*6*); Residual MAX-phase content of etched samples at different HF concentration, determined from XRD analysis (*b*)

The most obvious structural transformation is observed in the sample MX-24. The XRD pattern shows a strong and well-defined (002) MXene peak at ~9.21°, indicating successful conversion from Ti_3AlC_2 MAX phase, while the characteristic MAX-phase reflections, such as (104) at ~39° and (105) at ~41°, have nearly vanished. The observed shift of the (002) peak, which is often the result of delamination or intercalation, may also be related to the etching process. It is possible that functional groups such as –F, –OH, and =O formed during etching can increase the interlayer spacing [63]. Increasing the HF concentration to an intermediate level (24 %) results in efficient and selective Al removal. The disappearance (or significant weakening) of the (104) peak of the MAX phase and a pronounced shift of the (002) reflection to smaller angles confirm successful etching and expansion of the interlayer space. The disappearance (or strong attenuation) of the MAX-phase (104) peak and the pronounced shift of the (002) reflection to lower angles in XRD patterns indicate successful etching and interlayer expansion. SEM observations reveal a typical accordion-like multilayer morphology, characteristic of well-formed MXene (Fig. 4*d*). At this concentration, the Ti–C framework remains structurally stable, while the surface becomes functionalized by –F, –OH, and –O groups originating from the etching medium and subsequent washing steps. This balance between Al removal and framework preservation results in structurally intact, multilayer $Ti_3C_2T_x$ with expanded interlayer spacing.

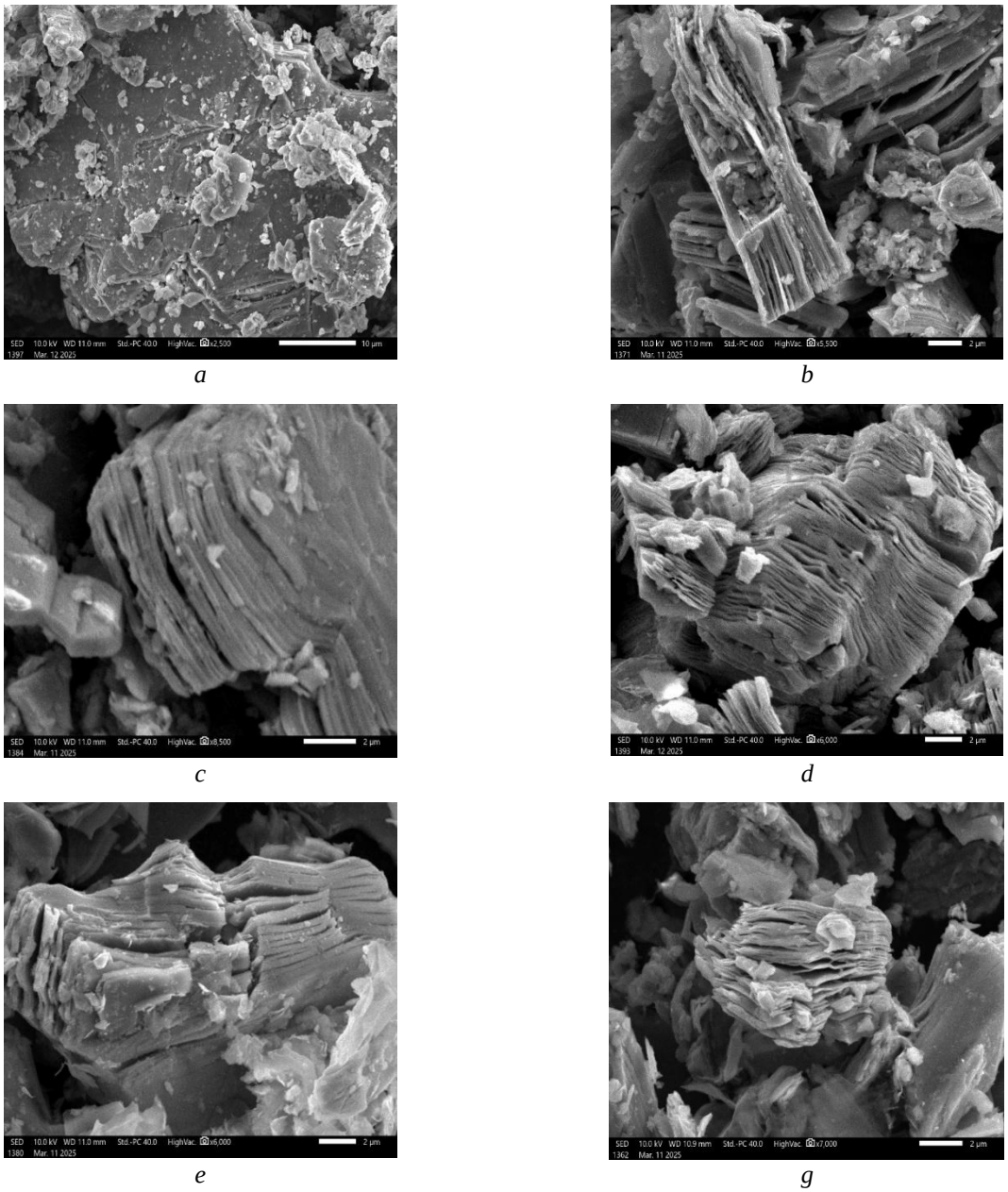

Figure 4. SEM images of MAX (*a*) and MXene samples: *b*) MX-6; *c*) MX-12; *d*) MX-24; *e*) MX-36; *g*) MX-48

XRD patterns of MX-36 and MX-48 show peak broadening and a decrease in intensity. These features indicate structural disorder, defect formation, and partial degradation of the Ti–C framework. Although weaker MXene peaks, such as (004) and (006), remain detectable, the intensity reduction indicates a significant loss of long-range structural order. At higher HF concentrations (36 % and 48 %), the etching becomes overly aggressive. Although Al is completely removed, excessive chemical attack leads to partial degradation of the Ti_3C_2 layers, generation of structural defects, and possible thinning or fragmentation of the sheets. This over-etching is reflected in the deterioration of the layered morphology in SEM images (Fig. 4*e*, *f*) and the broadening or weakening of characteristic MXene diffraction peaks in XRD patterns. In addition, stronger fluorination at high HF concentrations increases the density of –F terminations, which may adversely affect electrical conductivity and mechanical integrity [64].

As the HF concentration increased from 6 to 48 %, the (002) reflection gradually shifted to lower angles (from 9.30° to 9.07°), indicating an increase in the c lattice parameter from 18.85 to 21.08 Å and an expansion of the interlayer spacing from 9.7 to 13.0 Å (Tab. 1).

Table 1

Structural parameters, yield and conductivity of samples

Sample	*a*, Å	*c*, Å	2θ, °	Interlayer spacing, Å	Yield, %	Conductivity, S m^{-1}
MX-6	3.08	18.85	9.30	9.7	65	14400
MX-12	3.08	19.55	9.26	10.2	68	16500
MX-24	3.07	20.51	9.21	12.2	72	19200
MX-36	3.06	21.02	9.17	12.6	70	22300
MX-48	3.08	21.08	9.07	13.0	67	23800

The evolution of the low-angle (002) reflection can be interpreted in three complementary aspects. First, the progressive attenuation/disappearance of characteristic MAX reflections (e.g., around ~39–41°) evidences the gradual conversion of Ti_3AlC_2 to $Ti_3C_2T_x$ as the HF concentration increases. Second, the shift of the (002) reflection towards lower 2θ values together with the increase of the c lattice parameter (Tab. 1) indicates interlayer expansion, which can arise from Al removal and the introduction of surface species and interlayer water during washing. Third, at high HF concentrations (36–48 %), the pronounced broadening and intensity loss of the (002) and higher-order peaks suggest increased structural disorder and defect generation, consistent with over-etching effects observed by SEM. Importantly, in this work no dedicated intercalation chemistry (e.g., Li^+-intercalation [65]) was applied; therefore, the observed basal-spacing changes associated with interlayer expansion are attributed primarily to etching-induced structural evolution and surface functionalization rather than deliberate intercalation-driven delamination.

This structural evolution was accompanied by a steady increase in MXene yield (from 65 % to 72 %) and electrical conductivity of the corresponding films from 1.44×10^4 to 2.38×10^4 S m^{-1} with increasing HF concentration (Tab. 1), which corresponds to 144–238 S cm^{-1}. It should be noted that the conductivity of $Ti_3C_2T_x$ films reported in the literature [34, 66] spans a broad range depending on the etching route, oxidation state, flake size distribution, film density, and post-treatments (e.g., pressing, annealing, surface reduction). In this work, the films were prepared without additional densification, high-temperature annealing, or chemical reduction, therefore the obtained values are expected to fall into a moderate conductivity regime. Importantly, the consistent increase in conductivity correlates with the structural evolution revealed by XRD (increasing c parameter and interlayer spacing), indicating that more efficient Al removal and improved delamination reduce the interflake contact resistance and promote better stacking/alignment of conductive flakes in the film. At the highest HF concentrations (36–48 %), the conductivity continues to increase; however, SEM and XRD indicate the onset of structural degradation/over-etching, which suggests that further optimization should balance conductivity gains against the preservation of sheet integrity.

Figure 3*b* illustrate the effect of HF concentration on the phase purity; increasing the HF concentration leads to a significant decrease in the residual Ti_3AlC_2 content: approximately 12 % at MX-6, 8 % at MX-12, 2 % at MX-24, 1.5 % at MX-36 and a minimum of 1 % at MX-48.

Overall, the XRD results demonstrate that HF concentration plays a critical role in controlling the etching efficiency and structural integrity of MXene. Low HF concentrations lead to incomplete Al removal, whereas excessive HF results in structural degradation. Among the investigated conditions, HF concentrations in the range of 24 % are considered optimal for producing well-exfoliated and structurally stable MXene. These findings are in good agreement with the SEM, FTIR, and EDS analyses.

The smooth and dense surface, along with the absence of layer separation or significant structural defects, can be attributed to the strong interlayer bonding characteristic of the MAX phase (Fig. 4*a*). EDS results provided a semi-quantitative estimation of the elemental composition, showing Ti, Al, and C as the dominant elements with approximate values of 73.75 wt%, 18.20 wt%, and 8.04 wt%, respectively (Figure 5*a*), which are in reasonable agreement with the expected composition of the Ti_3AlC_2 MAX phase [67]. Importantly, fluorine (F) and oxygen (O) were not detected in this sample, indicating the absence of surface terminationsprior to etching. This confirms that the Ti_3AlC_2 phase has a chemically inert and stable surface.

After etching the MAX phase with 6 % HF, initial changes on the material surface were observed (Fig. 4*b*). SEM images revealed shallow pits and small voids, indicating the onset of the etching process. Interlayer expansion was still very limited, and the overall structural integrity remained largely intact. EDS analysis suggests an apparent decrease in the Ti signal to approximately 68.70 wt%, along with a marked decrease in the Al signal. (Fig. 5) The apparent increase in the carbon signal to approximately 13.96 wt% may be related to the relative enrichment of the Ti–C framework following Al removal. Additionally, the

detected fluorine (~11.31 wt%) and oxygen (~6.03 wt%) signals in the EDS spectrum suggest the formation of fluorine- and oxygen-containing surface species through interaction with HF. These groups likely play an important role in enhancing the hydrophilicity and chemical reactivity of the MXene surface [68]. Minor Ti loss and partial exfoliation were not clearly visible in the SEM images, and these phenomena were primarily confirmed through elemental analysis.

At 12 % HF, the etching process became more pronounced. It was observed the partial separation of layers and loosely packed lamellar structures, suggesting further Al removal and partial formation of MXene (Fig.4*c*). Full delamination had not yet occurred, as the layers remained partially aggregated. EDS analysis suggests an apparent increase in the Ti signal to approximately 73.65 wt%, which may reflect the exposure of additional Ti_3C_2 layers after Al removal. Meanwhile, the C content slightly decreased to 11.14 wt%, possibly due to partial surface restructuring or degradation. The detected F (~10.15 wt%) and O (~4.76 wt%) signals remained noticeable, suggesting continued surface functionalization. This sample represents a transitional stage between partial etching and optimal exfoliation.

The sample M-24 exhibited the most favourable structural and chemical characteristics. SEM images revealed the characteristic "accordion-like" morphology of MXenes, with significantly expanded interlayer spacing. A similar "accordion-like" morphology of MXenes was also observed in Ref. [69] when the MAX phase was etched using a 30 % HF solution. In our case, the development of this morphology at an HF concentration of 24 % can be attributed to the use of microwave irradiation, which enhances the reaction kinetics and allows efficient etching at a comparatively lower etchant concentration [41].

This morphology is particularly beneficial for applications requiring a high surface area, such as energy storage or catalysis. Although some regions still showed partial interlayer cohesion, the overall structure was well exfoliated. EDS analysis showed an apparent high Ti signal (~76.74 wt%) among the samples, supporting the preservation of the Ti–C framework (Fig. 5). The detected F (~8.55 wt%) and O (~4.47 wt%) signals suggest relatively balanced surface functionalization. This sample represents the optimal balance between effective Al removal, structural stability, and surface functionalization.

At 36 % HF concentration, significant changes in morphology and chemistry were observed. Partial collapse of lamellar structures, excessive widening of interlayer gaps, and local distortions were observed (Fig. 4*e*). Although expanded layers remained, mechanical integrity began to deteriorate. EDS analysis suggests that the Ti signal remained relatively high (~76.94 wt%), while the apparent C signal decreased to approximately 7.03 wt%, which may indicate partial degradation of the carbon framework. The F signal increased to approximately 9.61 wt%, while the O signal appeared very low (~0.03 wt%); however, these values should be interpreted with caution due to the limited accuracy of EDS for light elements.

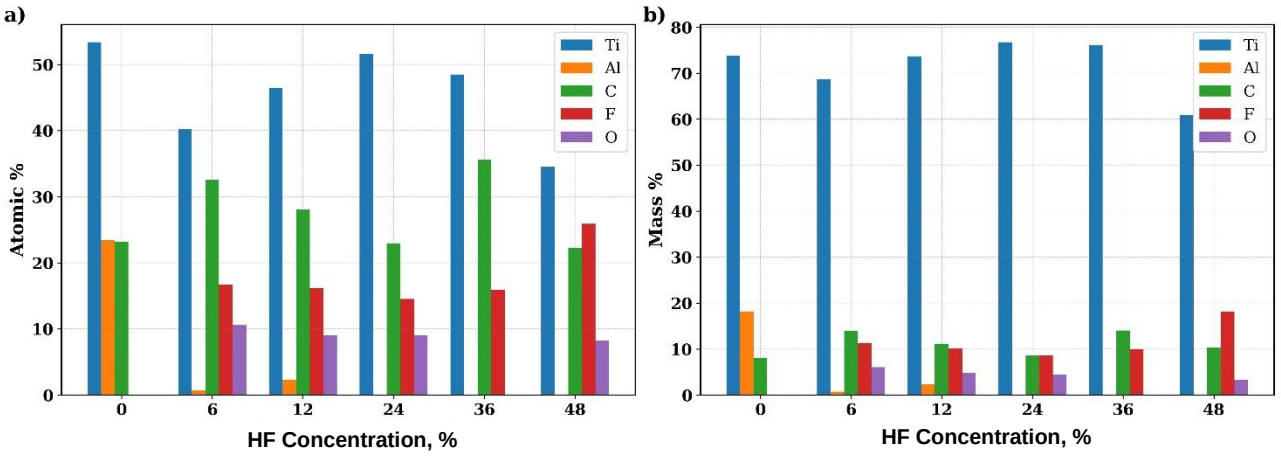

Figure 5. (*a*) Atomic percentage of Ti, Al, C, F and O in MAX phase Ti_3AlC_2 and $Ti_3C_2T_x$ samples etched at different HF concentrations obtained from EDS analysis; (*b*) Mass percentage of corresponding elements as a function of HF concentration

With 48 % HF, the sample showed severe alterations in both morphology, elemental composition and size. SEM images revealed well-separated, thin, and smooth lamellar sheets, indicating high exfoliation. EDS results suggest substantial compositional changes: the Ti signal decreased to approximately 60.93 wt%, while the F (~18.15 wt%) and O (~8.27 wt%) signals increased markedly, suggesting over-functionalization

(Fig. 5). Excessive etching led to surface passivation, which could significantly impair the electrochemical properties of the material.

The SEM observations are consistent with the XRD-derived structural evolution and the electrical conductivity trend. At low HF concentrations (6–12 %), the limited layer separation and the presence of residual MAX reflections indicate incomplete etching, which likely results in heterogeneous stacking and higher interflake contact resistance in films. At intermediate HF concentration (24 %), the formation of a well-developed accordion-like architecture indicates effective Al extraction and opening of interlayer galleries, while XRD still shows comparatively preserved structural order and EDS suggests relatively balanced F/O signals. This condition provides the best overall balance between phase conversion, structural integrity, and controlled surface functionalization, which is reflected in the highest yield (72 %) among the studied conditions and a notable conductivity increase relative to MX-6 and MX-12. In contrast, at higher HF concentrations (36–48 %), SEM and XRD evidence increasing disorder/fragmentation (peak broadening and morphology deterioration), suggesting over-etching that may compromise mechanical integrity despite higher conductivity. Therefore, MX-24 is identified as the most practical synthesis condition when both structural preservation and functional performance are considered. Although the highest electrical conductivity is observed for the 48 % HF sample, this condition is associated with increased structural disorder and over-etching effects. In contrast, the 24 % HF sample provides the best overall balance between structural integrity, controlled surface functionalization, morphology, yield, and electrical performance.

FTIR and EDS results indicate the formation of surface-containing species (e.g., oxygen- and fluorine-containing groups) after HF treatment; however, these methods do not provide a complete chemical-state assignment of the $Ti_3C_2T_x$ surface. FTIR reflects vibrational features that can overlap, and EDS is semi-quantitative and does not distinguish bonding configurations. The apparent discrepancy between EDS and FTIR results can be attributed to the limited sensitivity of EDS for detecting low concentrations of light elements and the fact that FTIR detects vibrational features of surface functional groups rather than bulk composition. Therefore, the discussion of –F/–OH/–O terminations in this work is presented as qualitative evidence of termination evolution with etching conditions, while more definitive chemical-state identification would require complementary XPS analysis.

In summary, SEM and EDS analyses demonstrate the critical effect of HF concentration on the morphological, yield and conductivity of $Ti_3C_2T_x$ MXene. 24 % HF provided the optimal balance, ensuring effective Al removal, controlled surface functionalization, and high structural integrity. Lower concentrations (6 % and 12 %) were insufficient for full exfoliation, while higher concentrations (36 % and 48 %) resulted in over-functionalization and structural degradation. These findings highlight the importance of carefully optimizing etching conditions for MXene applications in energy storage, catalysis, and sensing.

Conclusions

$Ti_3C_2T_x$ (MXene) was successfully synthesized from Ti_3AlC_2 (MAX phase) by selective etching in hydrofluoric acid (HF) solutions with different concentrations (6 %, 12 %, 24 %, 36 %, and 48 %) using a microwave-assisted approach. The obtained samples were comprehensively characterized by FTIR, XRD, SEM, and EDS techniques.

FTIR spectra indicated the presence of various surface-related species on the MXene layers. Samples etched at lower HF concentrations (6 % and 12 %) exhibited relatively more visible O–H vibrational features, whereas those treated at higher HF concentrations (36 % and 48 %) were dominated by bands associated with F- and O-containing groups, highlighting the strong influence of etching conditions on the surface chemistry of MXene. XRD analysis revealed a systematic shift and broadening of the characteristic (002) reflection near $2\theta \approx 9.5°$, indicating an increase in the interlayer spacing and partial structural disordering. This effect became more pronounced for the MX-24, MX-36, and MX-48 samples, confirming progressive etching and structural transformation of the MAX phase.

SEM observations showed that increasing HF concentration led to a more pronounced separation of the layered structure. At higher HF concentrations (36–48 %), stronger etching led to more pronounced interlayer opening; however, this was accompanied by peak broadening, structural disorder, and partial degradation of the Ti–C framework, indicating over-etching rather than improved structural quality. EDS analysis further demonstrated a significant decrease in aluminum content with increasing HF concentration, accompanied by an increase in fluorine and oxygen contents, which is consistent with progressive surface functionalization of $Ti_3C_2T_x$.

Overall, this work not only provides a systematic assessment of the effect of HF concentration on the formation of $Ti_3C_2T_x$ MXene, but also highlights the effectiveness of microwave-assisted etching in overcoming kinetic limitations of the selective etching process. The identified processing window and the established structure–property correlations offer practical guidelines for tailoring $Ti_3C_2T_x$ MXenes for conductive film and interfacial layer applications.

Funding

This research was supported by the Basic Fundamental Program of the Academy of Sciences of the Republic of Uzbekistan, and the Project "Biomass-based composite fibers for non-woven fabric with electromagnetic interference shielding" supported by the Korea International Cooperation Agency (KOICA).

*Author Information**

**The authors' names are presented in the following order: First Name, Middle Name and Last Name*

Khumoyunmirzo Adkhamjon o'gli Gulomjonov (*corresponding author*) — Junior Researcher, Institute of Polymer Chemistry and Physics, Abdulla Kadiri Street, 7-b, 100128, Tashkent, Uzbekistan; e-mail: khumoyungulomjonov@gmail.com; https://orcid.org/0009-0005-0330-0097

Nurbek Shodievich Ashurov — Candidate of Physical and Mathematical Sciences, Senior Researcher, Institute of Polymer Chemistry and Physics, Abdulla Kadiri street, 7-b, 100128, Tashkent, Uzbekistan; e-mail: ansss72@mail.ru; https://orcid.org/0000-0001-5246-434X

Abdumutolib Abdupatto o'g'li Atakhanov — Doctor of Technical Sciences, Professor, Director of Institute of Polymer Chemistry and Physics, Abdulla Kadiri Street, 7-b, 100128, Tashkent, Uzbekistan; e-mail: a-atakhanov@yandex.com; https://orcid.org/0000-0002-4975-3658

Golibjon Rakhmatullaevich Berdiyorov — Senior Scientist, Energy Center, Qatar Environment and Energy Research Institute, Hamad Bin Khalifa University, P.O Box 5825, Doha, Qatar; e-mail: gberdiyorov@hbku.edu.qa; https://orcid.org/0000-0003-4483-4800

Author Contributions

The manuscript was written through contributions of all authors. All authors have given approval to the final version of the manuscript. CRediT: **Khumoyunmirzo Adkhamjon o'gli Gulomjonov** writing — original draft; **Nurbek Shodievich Ashurov** writing — original draft, conceptualization; **Abdumutolib Abdupatto o'g'li Atakhanov** conceptualization, supervision; **Golibjon Rakhmatullaevich Berdiyorov** writing — original draft, formal analysis, investigation, methodology.

Conflicts of Interest

The authors declare no conflict of interest.

References

1 Naguib, M., Kurtoglu, M., Presser, V., Lu, J., Niu, J., Heon, M., Hultman, L., Gogotsi, Y., & Barsoum, M. (2011). Two-dimensional nanocrystals produced by exfoliation of $Ti_3C_2T_x$. *Advanced Materials,* 23, 4207. https://doi.org/10.1002/adma.201190147

2 Anasori, B., Lukatskaya, M.R., & Gogotsi, Y. (2017). 2D metal carbides and nitrides (MXenes) for energy storage. *Nature Reviews Materials,* 2, 16098. https://doi.org/10.1038/natrevmats.2016.98

3 Vahid Mohammadi, A., Rosen, J., & Gogotsi, Y. (2021). The world of two-dimensional carbides and nitrides (MXenes). *Science*, 372(6547). https://doi.org/10.1126/science.abf1581

4 Lei, J.C., Zhang, X., & Zhou, Z. (2015). Recent advances in MXene: preparation, properties, and applications. *Frontiers of Physics*, 10, 276–286. https://doi.org/10.1007/s11467-015-0493-x

5 Alhabeb, M., Maleski, K., Anasori, B., Lelyukh, P., Clark, L., Sin, S., & Gogotsi, Y. (2017). Guidelines for synthesis and processing of 2D titanium carbide ($Ti_3C_2T_x$) MXene. *Chemistry of Materials,* 29, 7633–7644. https://doi.org/10.1021/acs.chemmater.7b02847

6 Krishnaiah, P., Awan, H., Walvekar, R., & Manickam, S. (2022). MXene-based composites and their applications. In: MXene Materials. *Springer,* 4, 53–86. https://doi.org/10.1007/978-3-031-05006-0_4

7 Mashtalir, O., Naguib, M., Mochalin, V.N., Dall'Agnese, Y., Heon, M., Barsoum, M.W., & Gogotsi, Y. (2013). Intercalation and delamination of layered carbides and carbonitrides. *Nature Communications*, 4, 1716. https://doi.org/10.1038/ncomms2664

8 Nouseen, S., & Pumera, M. (2025). Electrochemical etching of MXenes: mechanism, challenges and future outlooks. *Journal of Materials Chemistry A*, 13, 34055–34084. https://doi.org/10.1039/D5TA04176G

9 Rahman, U.U., Humayun, M., Ghani, U., Usman, M., Ullah, H., Khan, A., El-Metwaly, N., & Khan, A. (2022). MXenes as emerging materials: synthesis, properties, and applications. *Molecules*, 27, 4909. https://doi.org/10.3390/molecules27154909

10 Peng, Y.Y., Akuzum, B., Kurra, N., Zhao, M., Alhabeb, M., Anasori, B., & Gogotsi, Y. (2016). All-MXene solid-state microsupercapacitors for on-chip energy storage. *Energy & Environmental Science*, 9, 2847–2854. https://doi.org/10.1039/C6EE01717G

11 Khazaei, M., Arai, M., Sasaki, T., Chung, C.Y., Estili, M., Sakka, Y., & Kawazoe, Y. (2013). Novel electronic and magnetic properties of two-dimensional transition metal carbides and nitrides. *Advanced Functional Materials*, 23, 2185–2192. https://doi.org/10.1002/adfm.201202502

12 Khanal, R., & Irle, S. (2023). Effect of surface functional groups on MXene conductivity. *Journal of Chemical Physics*, 158, 124703. https://doi.org/10.1063/5.0141589

13 Rafique, M., Tahir, M., & Anwar, S. (2024). MXenes for energy storage applications. In *MXene Materials*. CRC Press. https://doi.org/10.1201/9781003465768

14 Mozafari, M., & Soroush, M. (2021). Surface functionalization of MXenes. *Materials Advances*, 2, 7277–7291. https://doi.org/10.1039/D1MA00625H

15 Yang, G., Yao, X., Li, Y., Hu, Y., Chen, X., Li, J., Chen, J., & Jiang, J. (2023). $Ti_3C_2T_x$ MXene Nanosheet-Based Hybrid Films for Enhanced Wave Absorption-Dominated Electromagnetic Interference Shielding. *ACS Applied Nano Materials*, 6(20), 19378–19391. https://doi.org/10.1021/acsanm.3c03932

16 Berdiyorov, G. (2015). Effect of lithium and sodium ion adsorption on electronic transport properties of Ti_3C_2 MXene. *Applied Surface Science*, 359, 153–158. https://doi.org/10.1016/j.apsusc.2015.10.050

17 Berdiyorov, G., & Mahmoud, K. (2017). Effect of surface termination on ion intercalation selectivity of bilayer $Ti_3C_2T_x$ MXene. *Applied Surface Science*, 416, 980–986. https://doi.org/10.1016/j.apsusc.2017.04.195

18 Berdiyorov, G. R. (2016). Optical properties of functionalized $Ti_3C_2T_2$ (T = F, O, OH) MXene: First-principles calculations. *AIP Advances*, 6(5). https://doi.org/10.1063/1.4948799

19 Rasool, K., Pandey, R., Rasheed, P.A., Berdiyorov, G., & Mahmoud, K. (2019). MXenes for environmental and water treatment applications. In: *MXenes.* Springer. https://doi.org/10.1007/978-3-030-19026-2_22

20 Rasool, K., Mahmoud, K., Johnson, D.J., Helal, M.I., Berdiyorov, G., & Gogotsi, Y. (2017). Efficient antibacterial membrane based on $Ti_3C_2T_x$ MXene nanosheets. *Scientific Reports*. 7:1598. https://doi.org/10.1038/s41598-017-01714-3

21 Liu, L., Zschiesche, H., Antonietti, M., Daffos, B., Tarakina, N., Gibilaro, M., Chamelot, P., Massot, L., Duployer, B., Taberna, P.L., & Simon, P. (2023). Tuning the surface chemistry of MXene to improve energy storage: example of nitrification by salt melt. *Advanced Energy Materials*, 13, 2202709. https://doi.org/10.1002/aenm.202202709

22 Fagerli, F., Wang, Z., Grande, T., Kaland, H., Selbach, S.M., Wagner, N., & Wiik, K. (2022). Removing fluoride terminations from multilayered V_2CT_x MXene by gas hydrolyzation. *ACS Omega*, 7, 24656–24665. https://doi.org/10.1021/acsomega.2c02441

23 Lei, J., Yu, F., Xie, H., & Ma, J. (2023). $Ti_3C_2T_x$ MXene/carbon nanofiber multifunction electrode for electrodeionization with antifouling activity. *Chemical Science*, *14*(13), 3610–3621. https://doi.org/10.1039/d2sc06946f

24 Huang, L., Ding, L., & Wang, H. (2021). MXene-based membranes for separation applications. *Small Science*, 1, 2100013. https://doi.org/10.1002/smsc.202100013

25 Carey, M., & Barsoum, M.W. (2021). MXene polymer nanocomposites: a review. Materials Today Advances, 9, 100120. https://doi.org/10.1016/j.mtadv.2020.100120

26 Abbasi, F., Hajilary, N., & Rezakazemi, M. (2022). Antibacterial properties of MXene-based nanomaterials: a review. *Materials Express*, 12, 34–48. https://doi.org/10.1166/mex.2022.2138

27 Naguib, M., Unocic, R.R., Armstrong, B.L., & Nanda, J. (2015). Large-scale delamination of multilayer transition metal carbides and carbonitrides (MXenes). *Dalton Transactions*, 44, 9353–9358. https://doi.org/10.1039/C5DT01247C

28 Gentile, A., Marchionna, S., Balordi, M., Pagot, G., Ferrara, C., Noto, V., & Ruffo, R. (2022). Critical analysis of MXene production with in situ HF forming agents for sustainable manufacturing. *ChemElectroChem*, 9, e202200891. https://doi.org/10.1002/celc.202200891

29 Wang, Y., Xu, Y., Hu, M., Ling, H., & Zhu, X. (2020). MXenes: focus on optical and electronic properties and corresponding applications. *Nanophotonics*, 9, 1–24. https://doi.org/10.1515/nanoph-2019-0556

30 Ahmed, Z., Rehman, F.U., Ali, U., Ali, A., Iqbal, M., & Thebo, K.H. (2021). Recent advances in MXene-based separation membranes. *ChemBioEng Reviews*, 8, 1–12. https://doi.org/10.1002/cben.202000026

31 Thangavelu, H., Huang, C., Chabanais, F., Palisaitis, J., & Persson, P. (2025). A review on MXene terminations. *Advanced Functional Materials*, 36, 25015604. https://doi.org/10.1002/adfm.202515604

32 Kumar, S., Park, H., Kumar, M., & Seo, Y. (2023). Long-term stability studies and applications of $Ti_3C_2T_x$ MXene. *International Journal of Energy Research*, 2023, 5275439. https://doi.org/10.1155/2023/5275439

33 Lee, A., Shekhirev, M., Anayee, M., & Gogotsi, Y. (2024). Multi-year study of environmental stability of $Ti_3C_2T_x$ MXene films. *Graphene and 2D Materials*, 9, 1–9. https://doi.org/10.1007/s41127-024-00076-8

34 Jun, B.M., Kim, S., Heo, J., Park, C.M., Her, N.G., Jang, M., Huang, H., Han, J., & Yoon, Y. (2019). Review of MXenes as new nanomaterials for energy storage/delivery and selected environmental applications. *Nano Research*, 12, 471–487. https://doi.org/10.1007/s12274-018-2225-3

35 Kouao, D.S., & Siuzdak, K. (2025). Electrochemical synthesis of MXenes: a promising leap beyond hydrothermal MAX phase etching. *2D Materials*, 13, 012001. https://doi.org/10.1088/2053-1583/ae2a4d

36 Kruger, D., Garcia, H., & Primo, A. (2024). Molten salt derived MXenes: synthesis and applications. *Advanced Science*, 11, 2307106. https://doi.org/10.1002/advs.202307106

37 Berdiyorov, G., Madjet, M., & Mahmoud, K. (2021). First-principles density functional theory calculations of bilayer $Ti_3C_2T_x$ MXene/graphene and AgNP heterostructure membranes. *Membranes*, 11, 543. https://doi.org/10.3390/membranes11070543

38 Mahabari, K., Mohili, R.D., Patel, M., Jadhav, A.H., Lee, K., & Chaudhari, N.K. (2024). HF-free microwave-assisted synthesis of MXene as an electrocatalyst for hydrogen evolution in alkaline media. *Nanoscale Advances*, 6, 5388–5397. https://doi.org/10.1039/D4NA00250D

39 Feng, Y., Zhang, M., Yan, H., Zhang, Y., Guo, R., & Wang, H. (2022). Microwave-assisted efficient exfoliation of MXene and its composite for high-performance supercapacitors. *Ceramics International*, 48, 9518–9526. https://doi.org/10.1016/j.ceramint.2021.12.149

40 Mashangva, T.T., Vishwakarma, N., Singh, P.P., Prasher, S., Dhiman, R., Kumar, M., & Sharma, A. (2026). Synergistic enhancement of electrochemical properties in domestic microwave-assisted $Ti_3C_2T_x$ MXene composite with V_2O_5 nanoparticles for supercapacitor applications. *Journal of Energy Storage*, 150, 120387. https://doi.org/10.1016/j.est.2026.120387

41 Bagri, U., Jan, S., Sharma, A., & Singh, P.P. (2025). Enhanced photocatalytic degradation of ciprofloxacin from pharmaceutical wastewater using microwave-synthesized lanthanum/MXene nanocomposites. *Topics in Catalysis*. https://doi.org/10.1007/s11244-025-02214-9

42 Numan, A., Rafique, S., Khalid, M., Zaharin, H., Radwan, A., Mokri, N., Oh, P.C., & Rashmi, W. (2022). Microwave-assisted rapid MAX phase etching and delamination: A paradigm shift in MXene synthesis. *Materials Chemistry and Physics*, 288, 126429. https://doi.org/10.1016/j.matchemphys.2022.126429

43 Saha, A., Shpigel, N., Leifer, N., Taragin, S., Sharabani, T., Aviv, H., Perelshtein, I., Nessim, G., Noked, M., & Gogotsi, Y. (2021). Enhancing the energy storage capabilities of $Ti_3C_2T_x$ MXene electrodes by atomic surface reduction. *Advanced Functional Materials*, 31, 2106294. https://doi.org/10.1002/adfm.202106294

44 Liu, S., Zhou, Y., Zhou, J., Tang, H., Gao, F., Zhao, D., Ren, J., Wu, Y., Wang, Z., Luo, Y., Liu, X., & Zhang, Y. (2022). $Ti_3C_2T_x$ MXene-based flexible materials for electrochemical energy storage and solar energy conversion. *Nanophotonics*, 11, 3139–3164. https://doi.org/10.1515/nanoph-2022-0228

45 Liu, Y., Wang, Y., Wu, N., Han, M., Liu, W., Liu, J., & Zeng, Z. (2023). Diverse structural design strategies of MXene-based macrostructures for high-performance electromagnetic interference shielding. *Nano-Micro Letters*, 15, 203. https://doi.org/10.1007/s40820-023-01203-5

46 Hwang, H., Yang, S., Yuk, S., Lee, K.S., Byun, S., & Lee, D. (2023). $Ti_3C_2T_x$ MXene as a growth template for amorphous RuO_x in carbon nanofiber-based flexible electrodes for enhanced pseudocapacitive energy storage. *NPG Asia Materials*, 15, 76. https://doi.org/10.1038/s41427-023-00476-x

47 Jose, S., Price, J., Lopez, J., Perez-Perez, E., & Menezes, P. (2025). Advances in MXene materials: fabrication, properties, and applications. *Materials*, 18, 4894. https://doi.org/10.3390/ma18214894

48 Cai, Z., & Kim, H. (2025). Recent advances in MXene gas sensors: synthesis, composites, and mechanisms. *npj 2D Materials and Applications*, 9, 58. https://doi.org/10.1038/s41699-025-00586-w

49 Said, Z., Sohail, M., Tabassum, H., Sajid, I., Ali, H., Jamil, F., Mishra, Y.K., & Pandey, A. (2025). MXenes at the forefront: advances in energy storage and nanofluidic applications. *Advanced Composites and Hybrid Materials*, 8, 1404. https://doi.org/10.1007/s42114-025-01404-z

50 Silva, L., Fileti, E.E., & Colherinhas, G. (2025). Exploring MXene materials in energy storage devices: a review of supercapacitor applications. *ACS Materials Au*, 5, 1–18. https://doi.org/10.1021/acsmaterialsau.5c00102

51 Jawad, N., Darwesh, T., Abbas, A., Yahya, A.A., Hilal, A., Rashid, K., Abood, T., Al-Juboori, R., Meskher, H., & Al-Saadi, S. (2025). MXene synthesis, surface functionalization, and membrane integration for photocatalytic removal of heavy metals from wastewater. *Materials Today Sustainability*, 32, 101208. https://doi.org/10.1016/j.mtsust.2025.101208

52 Han, Y., Hu, J., Liu, X., & Liu, F. (2025). Progress in Surface and Interface Modification Strategies of MXene Materials for Energy Storage Applications. *Materials*, *18*(15), 3576. https://doi.org/10.3390/ma18153576

53 Li, H., Liu, L., Yuan, T., Zhang, J., Wang, T., Hou, J., & Chen, J. (2024). Advances in MXene surface functionalization strategies for CO_2 reduction. *Nanoscale*, *16*(24), 11480–11495. https://doi.org/10.1039/d4nr01517g

54 Koh, S.W., Rekhi, L., Arramel, A., Birowosuto, M.D., Trinh, T., Ge, J., Yu, W., Wee, A.T.S., & Li, C.H. (2024). Tuning the work function of MXene via surface functionalization. *ACS Applied Materials & Interfaces*, 16, 11234–11244. https://doi.org/10.1021/acsami.3c11857

55 Ganesan, S., Ethiraj, K., Kumar, K., & Palaniappan, A. (2022). Biomedical applications of MXenes. In: *MXene Materials*. Springer. https://doi.org/10.1007/978-3-031-05006-0_11

56 Bhattacharjee, Y., Mielke, L., Al-Hussein, M., Singh, S., Schaefer, K., Rodriguez-Barea, B., Li, Q., Ghosh, A.K., Erbe, A., Herrmann, C., Vaynzof, Y., Fery, A., & Schlicke, H. (2025). Molecular cross-linking of MXenes: tunable interfaces and chemiresistive sensing. *Advanced Functional Materials*, 35, 2501884. https://doi.org/10.1002/adfm.202518884

57 Shuck, C.E., Sarycheva, A., Anayee, M., Levitt, A., Zhu, Y., Uzun, S., Balitskiy, V., Zahorodna, V., & Gogotsi, Y. (2020). Scalable synthesis of $Ti_3C_2T_x$ MXene. *Advanced Engineering Materials*, 22, 1901241. https://doi.org/10.1002/adem.201901241

58 Gentile, A., Marchionna, S., Balordi, M., Pagot, G., Ferrara, Ch., Di Noto, V., & Ruffo, R. (2022). Critical Analysis of MXene Production with In-Situ HF Forming Agents for Sustainable Manufacturing. *ChemElectroChem*, *9*(23). https://doi.org/10.1002/celc.202200891

59 Lee, A., Shekhirev, M., Anayee, M. & Gogotsi, Y. (2024). Multi-year study of environmental stability of $Ti_3C_2T_x$ MXene films. *Graphene and 2D Materials*, 9, 77–85. https://doi.org/10.1007/s41127-024-00076-8

60 Kiran, N.U., Deore, A., More, M., Raye, D., Rout, C.S., Mane, P., Chakraborty, B., Besra, L., & Chatterjee, S. (2022). Comparative study of cold electron emission from 2D $Ti_3C_2T_x$ MXene nanosheets with respect to its precursor Ti_3SiC_2 MAX phase. *ACS Applied Electronic Materials*, *4*(6), 2656–2666. https://doi.org/10.1021/acsaelm.2c00128

61 Solangi, M.Y., Hanan, A., Aftab, U., Soomro, I.A., & Ibupoto, Z.H. (2025). Novel titanium carbide ($Ti_3C_2T_x$) MXene electrocatalyst for HER application. *NUST Journal of Engineering Sciences*, *18*(1). https://journals.nust.edu.pk/index.php/njes/issue/view/35

62 Fu, S., Zhou, Q., Jin, C., Gao, Z., Niu, M., Wan, D., & Bao, Y. (2025). Interface protection mechanism of Ti_3AlC_2 ceramics under CMAS corrosion condition. *International Journal of Applied Ceramic Technology*, 22, e15134. https://doi.org/10.1111/ijac.15134

63 Bagheri, S., Lipatov, A., Vorobeva, N.S., & Sinitskii, A. (2023). Interlayer Incorporation of A-Elements into MXenes Via Selective Etching of A′ from $M_{n+1}A'_{1-x}A''_xC_n$ MAX Phases. *ACS Nano*, 17, 18747–18757. https://doi.org/10.1021/acsnano.3c02198

64 Ahmed, E.M., Ali, A.S., Hieba, E.M., Shaban, Z.S., Fathy, M.S., Amer, A.M., Ishmael, A.M., Bakr, A., Rashdan, H.R.M., & Elzwawy, A. (2025). Exploring the potential of MXenes in advanced energy, environmental, and biomedical applications. *RSC Advances*, 15, 44812–44863. https://doi.org/10.1039/D5RA04498G

65 Mashtalir, O., Naguib, M., Mochalin, V.N., Dall'Agnese, Y., Heon, M., Barsoum, M.W., & Gogotsi, Y. (2013). Intercalation and Delamination of Layered Carbides (MXenes). *Nature Communication*, 4, 1716. https://doi.org/10.1038/ncomms2715

66 Lipatov, A., Goad, A., Loes, M.J., Vorobeva, N.S., Abourahma, J., Gogotsi, Y., & Sinitski, A. (2021). High electrical conductivity and breakdown current density of individual monolayer $Ti_3C_2T_x$·MXene flakes. *Matter*, *4*(4), 1413–1427. https://doi.org/10.1016/j.matt.2021.01.021

67 Magnuson, M. & Mattesini, M. (2017). Chemical bonding and electronic-structure in MAX phases as viewed by X-ray spectroscopy and density functional theory. *Thin Solid Films*, 621, 108–130. https://doi.org/10.1016/j.tsf.2016.11.005

68 Long, Y., Tao, Y., Shang, T., Yang, H., Sun, Z., Chen, W. & Yang, Q. (2022). Roles of Metal Ions in MXene Synthesis, Processing and Applications: A Perspective. *Advanced Science*, 9, 2200296. https://doi.org/10.1002/advs.202200296

69 Alhabeb, M., Maleski, K., Anasori, B., Lelyukh, P., Clark, L., Sin, S., & and Gogotsi, Y. (2017). Guidelines for Synthesis and Processing of Two-Dimensional Titanium Carbide ($Ti_3C_2T_x$·MXene). *Chemistry of Materials*, 29, 7633−7644. https://doi.org/10.1021/acs.chemmater.7b02847

How to Cite: Dondulkar, A.O., Muley, M., Purohit, R.A., Yenorkar, N.Y., Akojwar, N.S., & Prasad, S.K. (2026). Simultaneous RP-HPLC Quantification and Characterization of Apigenin-Naringenin Co-Loaded ZnO Nanoparticles for Topical Delivery. *Eurasian Journal of Chemistry, 31, 2(122), 91–101*. https://doi.org/10.31489/2959-0663/2-26-3

Article

Received: 27 February 2026 | Revised: 28 April 2026 | Accepted: 29 April 2026 | Published online: 30 April 2026

UDC 546.47-31 : 543.544.5.068.7

https://doi.org/10.31489/2959-0663/2-26-3

Ayusha O. Dondulkar, Mandar Muley, Raksha A. Purohit, Nikhil Y. Yenorkar, Natasha S. Akojwar, Satyendra K. Prasad*

Department of Pharmaceutical Sciences, Rashtrasant Tukadoji Maharaj Nagpur University, Nagpur, Maharashtra, India
*(*Corresponding author's e-mail: skprasad.itbhu@gmail.com, skprasad.rs.phe@itbhu.ac.in)*

Simultaneous RP-HPLC Quantification and Characterization of Apigenin-Naringenin Co-Loaded ZnO Nanoparticles for Topical Delivery

Apigenin and Naringenin has proven beneficial prospects owing to an anti-inflammatory, antioxidant and wound healing effects. But having poor water solubility and low bioavailability hinders their application. Therefore, we developed a dual drug-loaded zinc oxide nanoparticle and validated a sensitive and selective liquid chromatography method for simultaneous determination. The nanoparticles were synthesized through chemical precipitation method followed by drug loading. They were evaluated for particle size, surface potential and FTIR, while morphology was determined by scanning electron microscopy. RP-HPLC method utilizing a C18 column as stationary phase and methanol/0.1 % orthophosphoric acid (75:25 v/v) as eluent at a flow rate of 1.0 mL/min with detection at 272 nm. Method was validated as per to ICH Q2(R1) guidelines and having linearity (5–25 µg/mL), accuracy, precision, specificity and robustness. The entrapment efficiencies of Apigenin and Naringenin were 88.6 ± 2.1 % and 85.2 ±1.8 %, respectively. The average size by dynamic-light scattering was 202.67 ± 3.2 nm and zeta potential were –30.51 ± 0.6 mV. Electron-microscopy confirmed mixture of mildly aggregated spherical and rod-shaped particles, size less than 200 nm. The validated analytical method and the nanoparticle system would together serve as a propitious groundwork, for combinatorial delivery of Apigenin and Naringenin.

Keywords: HPLC, polyphenols, simultaneous method, nanoparticles, apigenin, naringenin, isocratic, validation

1 Introduction

Polyphenols have garnered increasing attention in the treatment of various human diseases due to their safety profiles, wide accessibility, and cost-effectiveness [1]. Among them, natural flavonoids Apigenin and Naringenin have been shown to have potential therapeutic efficacy in the treatment of various pathological conditions, including diabetic wounds. Apigenin (4′,5,7-trihydroxyflavone), widely found in parsley, chamomile and celery, has anti-inflammatory, antioxidant, anti-diabetic, wound-healing potential. Another example is Naringenin (4′,5,7-trihydroxyflavanone), predominantly found in citrus fruits displays anti-inflammatory, antioxidant, and anti-microbial properties; as well as an inhibitory action on enzymes involved in releasing pro-inflammatory cytokines contributing to enhanced wound repair and tissue regeneration [2].

Apigenin and Naringenin have complementary pharmacological activities thereby making them suitable candidate to be co-delivered together in complex conditions as seen in diabetic wounds characterised by chronic inflammation, oxidative stress and impaired healing. However, water-insoluble, poorly available and rapidly metabolized limiting both compounds their therapeutic efficacies in clinical practice [3]. To overcome these challenges and harness their synergistic effects, we have established zinc oxide nanoparticles (ZnO NP) co-loaded formulation which not only provides stability for the drugs but also promotes controlled release mechanism and targets wound repair mechanisms under diabetic conditions. ZnO NPs are well established for their intrinsic antibacterial, anti-inflammatory, and skin healing properties that make them an ideal carrier system. Our formulation consists of adsorption of Apigenin and Naringenin over ZnO NPs resulting in a nano-sized system potentiated for better penetration and action at the wound site [4]. Currently, individual analytical methods are available for the quantification of Apigenin and Naringenin but a validated method is not reported simultaneously estimating them from nanoparticles-based delivery system. The pharmaceutical applications of dual-drug nanocarrier systems are increasing, especially for the management of complex disorders such as diabetic wounds; hence an established high throughput and non-destructive approach to support formulation development becomes imperative [5]. Simultaneous RP-HPLC methods are mainly

essential because it improves the analytical throughput that leads to reducing simplified analysis time and reduced use of solvent compared to single drug estimation. It also enables precise examination of drug encapsulation, release kinetics and stability within the nanoparticle, which are vital for verifying therapeutic efficacy and batch-to-batch consistency. Furthermore, this methodology supports regulatory compliance by generating confirmed routine data for quality control purposes [6].

Considering these factors, our study focused on the development and validation of a robust, rapid, and accurate RP-HPLC method for the simultaneous quantification of Apigenin and Naringenin from co-loaded ZnO nanoparticles. The technique utilizes the isosbestic point, the wavelength at which both compounds show equal and maximum absorbance, to guarantee precise and consistent detection.

2 Experimental

2.1 Materials

Apigenin and Naringenin (purity >98 %) were purchased from Ottokemi and sigma Aldrich respectively, and used without further purification. Zinc precursor, such as zinc acetate dihydrate, was obtained from SRL chemicals. Methanol, acetonitrile, and water used for chromatographic analysis were of HPLC grade and sourced from merc. All other chemicals and reagents were of analytical grade. Dialysis membranes and 0.45 μm syringe filters were used during the nanoparticle purification process. All glassware was appropriately cleaned and dried before use.

2.2 Preparation and Characterization of Dual Drug-Loaded ZnO Nanoparticles

Zinc oxide (ZnO) nanoparticles were synthesized from zinc acetate using a simple wet chemical precipitation method. In this approach, zinc acetate dihydrate is initially dissolved in distilled water to form a clear solution, typically with a concentration between 0.1 M and 0.5 M. A separate solution of sodium hydroxide (NaOH) is then prepared, often with a slightly higher molarity (e.g., 0.2 M to 1 M), and added dropwise to the zinc acetate solution under continuous stirring. This leads to a white precipitate of zinc hydroxide ($Zn(OH)_2$), that gradually transforms into ZnO nanoparticles with progression in the reaction. Precipitation is done at pH 10–12 to have maximum precipitation. The reaction mixture had been stirred for a few hours at room temperature or mild heating (60–80 °C) to ensure complete conversion of $Zn(OH)_2$ to ZnO. Finally, the product is separated by centrifuge or filtration after aging, and then repeatedly washed with doubly distilled water and ethanol to remove impurities and then dried. The crystallinity was improved further by calcining the powder that has previously been dried using a temperature of 300–500 °C for 4 hours. This method is preferred due to its simplicity, low-cost and tunability of the nanoparticle size and morphology by varying concentration, pH, and temperature [7].

Apigenin and Naringenin were co-loaded on the nanoparticles. Each drug solution (1 mg/ml) was dissolved in ethanol and 5 mg of ZnO nanoparticles were taken in distilled water. Following that, the nanoparticle suspension was stirred for 800 rpm for 12 h; centrifuged under a speed of 8000 RPM for 20 min; then washed with distilled water to remove unbound drugs and reagents before dialyzed to eliminate other impurities. The pure formulation obtained after drying the suspension at 50 °C overnight, is stored in air tight containers for future use.

2.3 Characterization of Drug-Loaded ZnO Nanoparticles

The physicochemical characterization of the synthesized dual drug loaded ZnO nanoparticles is very important for stability, drug loading and biological performance. Attenuated Total reflectance (ATR) Infrared Spectroscopy (FTIR) with Shimadzu, was carried out in order to study any probable interaction between Apigenin, Naringenin, and ZnO nanoparticles. The FTIR spectra of ZnO nanoparticles loaded with the drugs were measured within the wavelength range of 4000–400 cm^{-1} through ATR-FTIR spectrophotometry, and the resulting peaks were correlated with their respective characteristic peaks from the literature. The particle size, polydispersity index (PDI), and zeta potential of these complexes were measured via Horiba scientific nanoparticle analyzer (SZ–100V2). The size distribution and homogeneity of the ZnO nanoparticles provide further insights into their proposed drug delivery mechanism. The surface morphology of the nanoparticles was observed by scanning electron microscopy (SEM). RP-HPLC method was used for the estimation of Apigenin and Naringenin entrapment efficiency in ZnO nanoparticles. This was done by centrifugation of the nanoparticle suspension and measuring the amount of free (unentrapped) drug in solution [8, 9]. All measurements were performed in triplicate (n = 3) using the same nanoparticle batch to evaluate analytical repeat-

ability. Batch-to-batch reproducibility of independent nanoparticle syntheses was not investigated in this study. Entrapment efficiency was calculated as follows:

$$\text{Entrapment Efficiency (\%)} = [(\text{Total drug} - \text{Free drug}) / \text{Total drug}] \times 100,$$

where Total drug is the initial amount of drug used for loading, Free drug is the amount of unentrapped drug present in the supernatant.

2.4 Instrumentation and Chromatographic Conditions

The RP-HPLC system employed for the chromatographic separation was Agilent 1100 (Agilent Technologies, Waldbronn, Germany) interfaced with Chemstation 10.01 software and a UV–Vis detector. We used Thermo C18 column with a dimension of 4.6 mm × 250 mm, particle size of 5.0 μm, at room temperature for separation of Apigenin and Naringenin. The mobile phase was a 75:25 mixture of methanol and 0.1 % OPA which was filtered and degassed before use. Flow rate was maintained at 1.0 mL/min, injection volume; 20 μL, detection at wave length of absorption of Apigenin and Naringenin (272 nm) which possess maximal absorbance and overlapping each other (isosbestic point). The full run time per sample was close. The column temperature was kept at 25 °C with a sample size of 20 μL.

2.5 Preparation of Standard and Sample Solutions

Stock standard solutions were prepared by dissolving 5 mg of each API in 10 mL of methanol giving STOCK-I with a final concentration of 500 μg/mL for both Apigenin and Naringenin. To validate the methodology, calibration range was set by serial dilution using working standard solutions. Quantities of drug-loaded ZnO nanoparticles were sonicated in methanol to achieve sample extraction for analysis. The resulting solution was filtered with 0.45 μm syringe filter and then injected in the system.

2.6 Method Validation

The developed RP-HPLC method used for simultaneous estimation of Apigenin and Naringenin from dual drug-loaded ZnO nanoparticles was validated as per International Council for Harmonisation (ICH Q2 (R1)) guidelines for analytical method validation. The method was validated as per ICH guidelines for linearity, accuracy, precision, LOD and LOQ, specificity, robustness and system suitability to ensure consistent analytical performance of the method.

The linearity was performed in the concentration range of 5–25 μg /mL by preparing the standard solutions of Apigenin and Naringenin at five different concentrations. The specified concentration range was selected considering the concentrations of Apigenin and Naringenin after the extraction process using nanoparticles, and was proven suitable for the best signal response, linearity, and sensitivity. Concentration levels: each concentration level was injected in triplicate, and calibration curves were constructed by plotting peak area against drug concentration. Linearity along with coefficients of Correlation (R^2) for both the drugs were carried out in the tested range.

The accuracy of the method was confirmed by recovery studies with three different levels: 80 %, 100 %, and 120 % of the target concentration. The quantities of Apigenin and Naringenin standards were spiked with the blank ZnO nanoparticle matrix, and their percent recovery was calculated by comparing the measured amounts to the quantity actually added. From there the mean recovery values of both drugs were verified.

The precision of the method was tested at two different levels namely intra-day (repeatability) and inter-day (intermediate precision). To determine the intra-day accuracy, same three concentrations (low, medium and high) were analysed $n = 3$ time in a day with similar condition. To evaluate inter-day precision, each sample was analysed on three different days by a single analyst on the same instrument to measure both within and between day variation.

Sensitivity for each drug was determined by calculating the Limit of Detection (LOD) and Limit of Quantification (LOQ) based on standard deviation of response (σ), and slope (S) of calibration curve utilizing the following equations:

$$\text{LOD} = 3.3\ (\times\sigma/S) \text{ and } \text{LOQ} = 10\ (\times\sigma/S).$$

The specificity was verified with the system suitability and also by analyzing blank nanoparticles of ZnO (drug-free) to see any interfering peak at Apigenin and Naringenin retention times. The method should be able to separate the analytes from other formulation excipients and nanoparticle components which will validate its specificity for simultaneous quantification of drugs.

Robustness was evaluated by making deliberate minor variations in chromatographic conditions, including flow rate ±0.1 mL/min, mobile phase composition ±2 %, and detection wavelength (±2 nm). These

variations did not significantly affect the retention times, peak areas, or resolution of the analytes, indicating the method's robustness and reliability under small operational deviations [10].

The ruggedness of the developed RP-HPLC method was assessed to determine its reproducibility under variable conditions such as different analysts and instruments. The study was conducted by performing replicate analyses of Apigenin and Naringenin standard solutions (15 µg/mL) on two different days, by two different analysts using two separate instruments of the same model [11].

Specificity was evaluated by analyzing blank ZnO nanoparticles (without drug) to confirm the absence of interference at the retention times of Apigenin and Naringenin. System suitability parameters were assessed before analysis to ensure consistent chromatographic performance. Parameters such as retention time, theoretical plate count, peak symmetry (tailing factor), and resolution between Apigenin and Naringenin peaks were evaluated. The results met the acceptance criteria, with resolution >2.0, theoretical plates >2000, and tailing factors <1.5, confirming the suitability of the system for routine analysis [12].

2.7 Data Analysis

The data were analysed statistically using Microsoft Excel (USA) to calculate the least squares (R^2), standard deviation, mean, relative standard deviation, and the equation of the calibration curve.

3 Results and Discussion

3.1 Optimization of Chromatographic Parameters

Various chromatographic parameters, such as the flow rate of mobile phase, the pH of the mobile phase, temperature and ratio between components of mobile phase were optimized by extensive analysis. After several trials, the optimized conditions were found as follows:

– flow rate of the mobile phase: 1.0 ml/min;
– column temperature: 25 °C;
– ratio of methanol and 0.1 % OPA (75:25);
– sample size: 20 µl;
– maximum pressure: 400 BAR;
– discharge rate: 0.001 to 5 ml.

Initially, different mobile phase compositions at various ratios resulted in poor resolution and the peak symmetry. For the simultaneous estimation of Apigenin and Naringenin, the isosbestic wavelength was set to 272 nm as shown in Figure 1 ensuring reliable and consistent quantification.

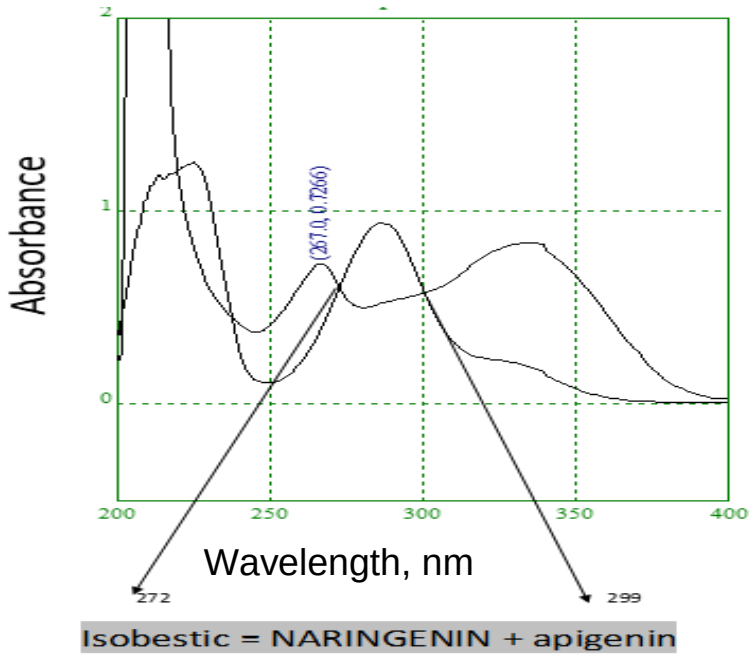

Figure 1. Absorption maxima showing isobestic point

The optimal retention times for Naringenin and Apigenin were 6.152 min and 7.539 min, respectively, with resolution of 4.24 as shown in Figure 2. The method exhibited good theoretical plate numbers and acceptable tailing factors, confirming efficient operation of the system. The chosen optimal parameters are applicable for the analysis of flavonoids [13].

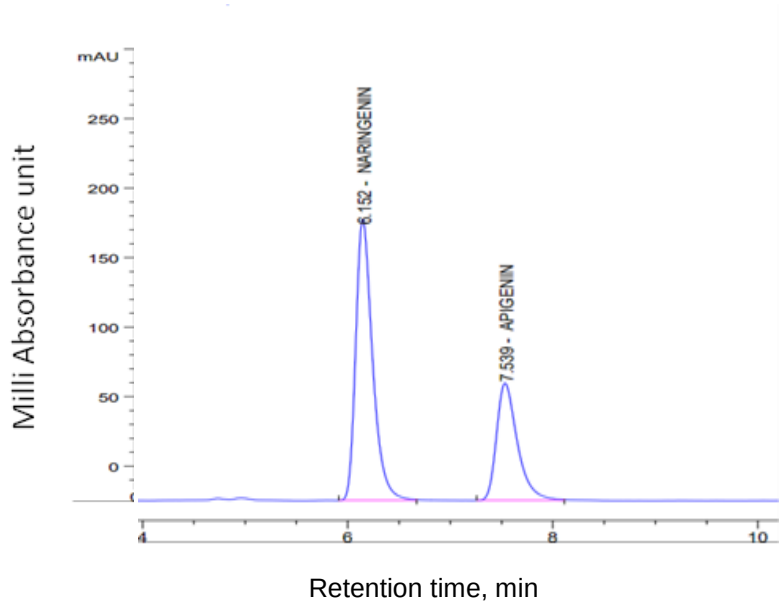

Figure 2. HPLC chromatogram for simultaneous estimation of Apigenin and Naringenin

3.2 Method Validation

For RP-HPLC method validation, the ICH guideline Q2(R1) was followed.

3.2.1 System Suitability Test

The mixture of Apigenin and Naringenin solution was injected into the HPLC column six times to assess the system suitability of the developed method. The analyzing concentration of both drugs in the mixture was 5µg/ml each. The average resolution of both drugs was 4.24, which indicates complete separation of the peaks. The RSD value for all parameters was less than 2 %, fulfilling both ICH and USP guidelines, confirming that the developed method is highly suitable and effective.

3.2.2 Linearity, Range, and Sensitivity

Five different concentrations of Apigenin (5–25 µg/ml) and Naringenin (5–25 µg/ml) were analysed separately. Each standard solution of six different concentrations was injected in three replicates and chromatographed. The AUCs of the different concentrations of both compounds were plotted against their respective concentrations in MS-Excel as shown in Figures 2 and 3. The calibration curve equations were as follows:

$$\text{Apigenin: } y = 83.811x - 26.353 \ (R^2 = 0.9984);$$

$$\text{Naringenin: } Y = y = 165.75x + 50.715 \ (R^2 = 0.9999).$$

The linear calibration curves showed excellent R^2 correlation coefficients (Apigenin $R^2 = 0.9984$ and Naringenin $R^2 = 0.9999$), indicating a direct linear proportionality between the concentration and the peak area. The limits of detection (LOD) and quantification (LOQ) for both drugs were calculated and found to be LOD for Apigenin 0.36 µg/ml and LOQ for Apigenin 1.0929 µg/ml, whereas LOD for Naringenin 0.2363 µg/ml and LOQ for Naringenin 0.7163 µg/ml. The values of LOD and LOQ obtained show that the method has adequate sensitivity for quantification purposes. The selected concentration range was adequate for practical purposes and falls within the expected range in the formulation of nanoparticles [14].

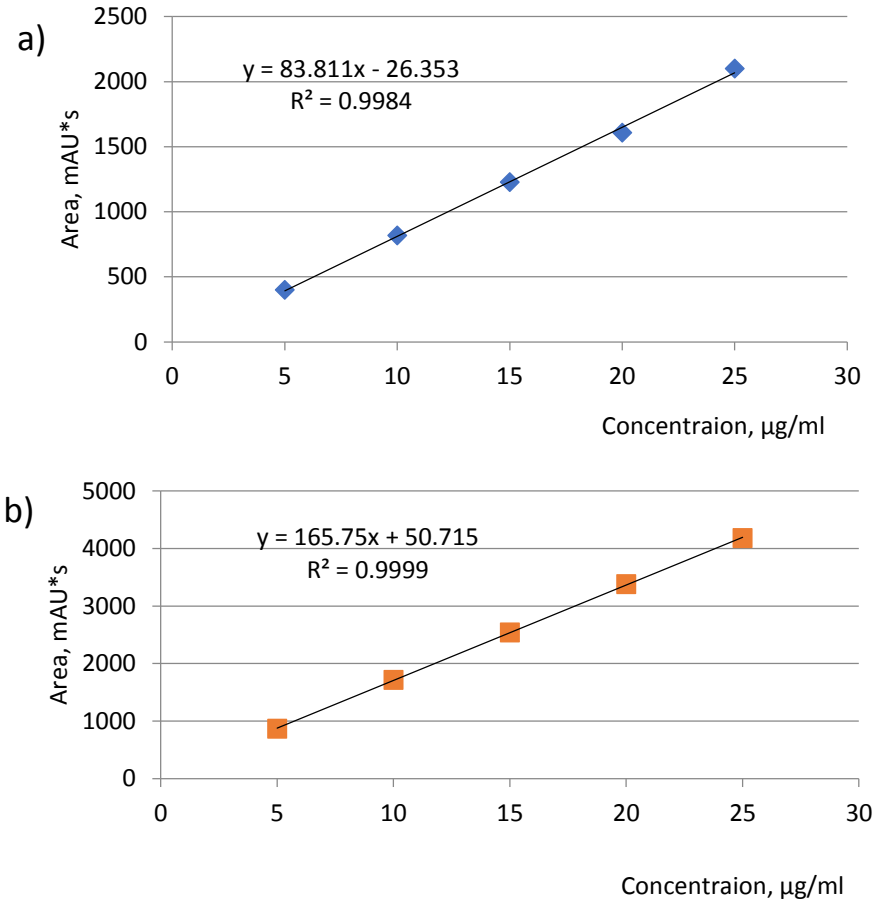

Figure 3. Linearity curve for *a*) Apigenin and *b*) Naringenin

3.2.3 Accuracy (Recovery Studies)

The accuracy of the developed RP-HPLC method was assessed through standard recovery experiments at three concentration levels: 80 %, 100 %, and 120 % of the target concentration. Known amounts of Apigenin and Naringenin were spiked into a blank ZnO nanoparticle matrix, and the recovered amounts were determined using the validated method. The recovery of Apigenin and Naringenin was found to be in between 98 % to 102 % which proved the reliability of the proposed method. The results are acceptable according to ICH standards and therefore can be used for the determination of analytes in the presence of matrix elements as presented in Table 1.

Table 1

Recovery study results of Apigenin and Naringenin values are mean of three replicates (*n* = 3)

Spike Level, %	Drug	Amount Added, µg/mL	Amount Recovered, µg/mL	Recovery, %	RSD, %
80 %	Apigenin	4.0	3.97	99.42	0.18
	Naringenin	4.0	3.96	99.03	0.36
100 %	Apigenin	5.0	4.99	99.36	0.63
	Naringenin	5.0	5.01	100.25	0.39
120 %	Apigenin	6.0	5.96	101.58	0.58
	Naringenin	6.0	6.03	101.58	0.05

3.2.4 Precision

Method precision was evaluated in terms of intra-day (repeatability) and inter-day (intermediate precision) by analyzing three different concentration levels (low, medium, and high) of both analytes (e.g., 5, 15, and 25 µg/mL). Intra-day precision was assessed by analyzing three replicates at each concentration within the same day, while inter-day precision was determined by repeating the procedure on three consecutive days

under identical conditions. The %RSD values for both intra-day and inter-day precision studies were below 2 %, indicating high reproducibility of the method. The low variability confirms that the method provides consistent results under the same and varying analytical conditions, fulfilling standard validation requirements, summarized in Table 2.

Table 2

Intraday and interday precision results for Apigenin and Naringenin values are mean of three replicates (*n* = 3)

Drug	Concentration, µg/mL	Intra-Day RSD, %	Inter-Day RSD, %
Apigenin	5	0.36	0.33
	15	0.13	0.07
	25	0.17	0.12
Naringenin	5	0.05	0.11
	15	0.15	1.11
	25	0.07	0.01

3.2.5 Robustness

The robustness of the implemented RP-HPLC technique was assessed by introducing little changes in essential chromatographic parameters systematically to ascertain that the process is still reliable, for regular quality control testing. Modifications were limited to minor adjustments of the flow rate (±0.1 mL/min), the mobile phase composition (±2 % methanol from optimal) and the detection wavelength (±2 nm from the most sensitive 272 nm). The variations were tested on a standard solution of Apigenin and Naringenin at the mid-level concentration (15 µg/mL). The newly developed technique was completely insensitive to small intentional changes in the experimental conditions like flow rate, mobile phase composition, and wavelength of detection. There was no noticeable change in any of the above-mentioned parameters, which indicated that the technique was quite robust [15]. Table 3 summarizes the results of the robustness study.

Table 3

Values shown are for 15 µg/mL of each drug. Resolution is reported only for Apigenin-Naringenin pair. values are mean of three replicates (*n* = 3)

Parameter	Conditions	Drug	Peak Area	Resolution	Plate Count	RSD, %
Flow rate	0.9 mL/min	Apigenin	1252.92	6.05	20703	0.26
		Naringenin	2563.95		23563	0.11
	1.1 mL/min	Apigenin	999.15	5.07	20043	0.05
		Naringenin	2062.21		22785	0.17
Mobile phase ratio	74:26 (Methanol:0.1 % OPA)	Apigenin	1092.0	5.88	21360	0.04
		Naringenin	2307.5		17899	0.05
	76:24 (Methanol:0.1 % OPA)	Apigenin	1112.28	5.33	23523	0.12
		Naringenin	2297.18		20712	0.04
Detection wavelength	271 nm	Apigenin	1037.8	5.60	24048	0.34
		Naringenin	2229.6		21232	0.06
	273 nm	Apigenin	1113.30	5.52	24024	0.30
		Naringenin	2156.44		21375	0.10

3.2.6 Ruggedness

Peak area, retention time (*Rt*), resolution (*R*) and percentage relative standard deviation (*RSD*, %) of results were evaluated. The *RSD* values under all the conditions are less than 2 % which indicates that the method is rugged and also able to give reproducible results when a different laboratory person work on these matrices. These results verify the robustness of the approach for routine implementation.

3.2.7 Specificity

Contrary to formulation, the chromatograms had no co-eluting peaks or interfering signals near the corresponding retention times attesting that presence of excipients and nanoparticle matrix did not affect drug detection. No interference peaks were observed at the retention times of Apigenin and Naringenin, indicating

that the method was specific. The possibility of quantification of both substances in the presence of nanoparticle constituents indicates that the method is suitable for complex formulations.

3.2.8 Characterization of Drug-Loaded ZnO Nanoparticles

The physicochemical properties of the dual drug-loaded ZnO nanoparticles illustrated the successful formulation and stability. FTIR spectra of the drug-loaded ZnO nanoparticles shown in Figure 4*a*, revealed some distinctive peaks associated with both ZnO and drug-loaded particles. First, the broad peak observed near 3400 cm^{-1} is associated with O–H stretching modes, which shows that there are some phenolic groups (apigenin and naringenin) and hydroxyl groups on the surface of ZnO nanoparticles. Second, peaks near 1600–1650 cm^{-1} are related to aromatic C=C or C=O stretching modes of flavonoid compound structure. Finally, the peak near 500–600 cm^{-1} corresponds to Zn-O stretching. Compared with reported spectra of the individual components, slight shifts and changes in intensity were observed, suggesting successful drug loading through physical adsorption or weak intermolecular interactions rather than formation of new covalent bonds.

Upon drying, the nanoparticles were found to form a tan-coloured fine powder and were consistently able to disperse in an aqueous medium after mild sonication. The DLS results as depicted in Figure 4*b*, indicated that the average hydrodynamic diameter of the ZnO nanoparticles was 202.67 ± 3.2 nm, while the polydispersity index was 0.301, implying that the particle sizes were relatively close, thus suitable for topical applications. In addition, the zeta potential value of –30.51 ± 0.6 mV suggests high colloidal stability, thanks to electrostatic repulsions (Fig. 4*c*). Based on the SEM images (Fig. 5), the ZnO nanoparticles appeared spherical and rod-shaped, with some particles agglomerated, which is common among ZnO nanoparticles due to their high surface energy.

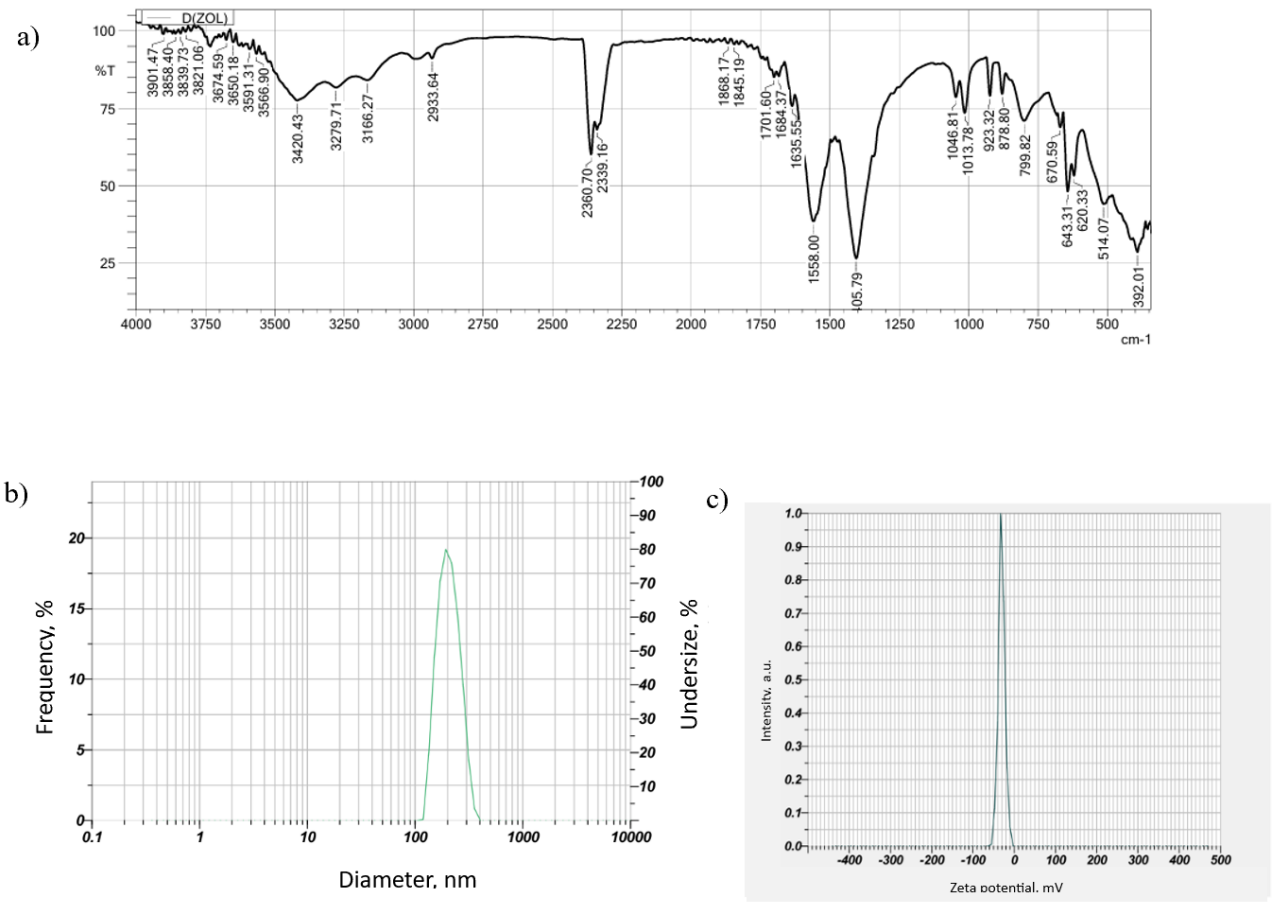

Figure 4. *a* — FTIR spectra of the apigenin-naringenin coloaded ZnO nanoparticles;
b — particle size distribution and *c* — zeta potential distribution of the apigenin-naringenin coloaded ZnO nanoparticles

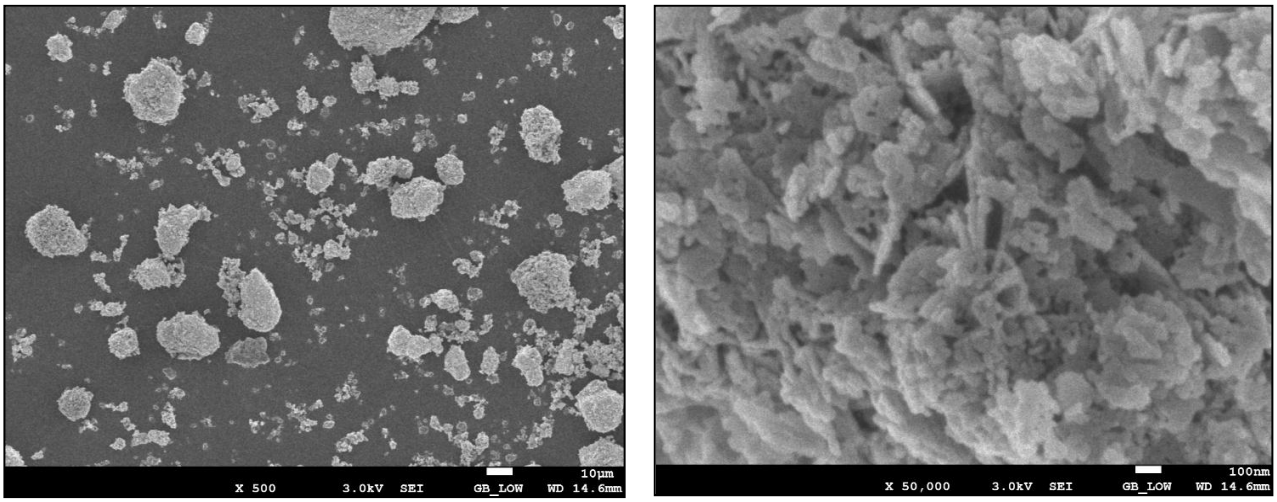

Figure 5. Scanning electron micrograms showing the morphology of Apigenin-naringenin coloaded ZnO nanoparticles

3.2.9 Drug Entrapment Efficiency

Validated RP-HPLC method confirmed the entrapment efficiency of Apigenin and Naringenin in the ZnO nanoparticles. It was found that this method allows for the distinction of both drugs without interference from components present on the nanoparticle (Fig. 6). Apigenin and Naringenin entrapment efficiency results with both phytochemicals showing a high level of entrapment; apigenin had an average of 88.6 ± 2.1 % entrapment efficiency, naringenin also showed an 85.2 ± 1.8 %. These numbers reveal an efficient encapsulation of the drugs within the ZnO nanoparticle matrix and a probably high drug-ZnO surface interaction [7].

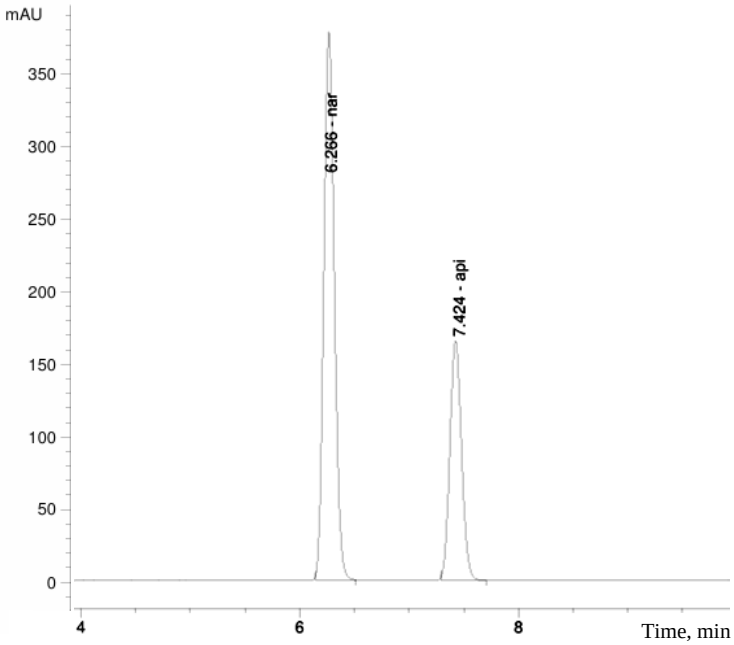

Figure 6. HPLC chromatogram for the drug entrapment study of Apigenin-naringenin coloaded ZnO nanoparticles

4 Conclusions

The synthesized nanocrystalline ZnO NPs had nanosize dimension, good colloidal stability, and spherical shaped morphology. The high entrapment efficiency of Apigenin and Naringenin shows good encapsulation within the ZnO host matrix. A simple, rapid High-Performance Liquid Chromatography with Reversed Phase (RP-HPLC) method was successfully developed and validated for simultaneous estimation of

Apigenin and Naringenin from co-loaded ZnO nanoparticles. This method had a linear concentration dependence, was specific, sensitive and repeatable, and therefore could be used in routine quality analysis or *in vitro* studies.

In conclusion, the ZnO nanoparticle formulation was successful in loading two drugs and when used with a quantitative analytical method described here. It may be further optimized for sufficient delivery polyphenolic compounds to perform a sustained effect making it suitable for therapeutic applications including wound healing.

Funding

The authors wish to sincerely acknowledge the financial assistance provided by DST-PURSE, Government of India. This work is supported by PAIR network of SAKSHAM funded by ANRF (Anusandhan National Research Foundation), India, through grant ANRF/PAIR/ 2025/000018/PAIR, administered and mentored by IIT Indore.

*Author Information**

**The authors' names are presented in the following order: First Name, Middle Name and Last Name*

Ayusha Omprakash Dondulkar — Researcher, Department of Pharmaceutical Sciences, Rashtrasant Tukadoji Maharaj Nagpur University, 440033, Nagpur, Maharashtra, India; e-mail: ayushadondulkar155@gmail.com, https://orcid.org/0000-0002-3544-4248

Mandar Mahendra Muley — NMPB Research Fellow, Department of Pharmaceutical Sciences, Rashtrasant Tukadoji Maharaj Nagpur University, 440033, Nagpur, Maharashtra, India; e-mail: mandar.niper2019@gmail.com, https://orcid.org/0009-0001-2115-5621

Raksha Anand Purohit — Researcher, Department of Pharmaceutical Sciences, Rashtrasant Tukadoji Maharaj Nagpur University, 440033, Nagpur, Maharashtra, India; e-mail: rapurohit03@gmail.com, https://orcid.org/0009-0005-0707-0575

Nikhil Yadavrao Yenorkar — PhD Scholar, Department of Pharmaceutical Sciences, Rashtrasant Tukadoji Maharaj Nagpur University, 440033, Nagpur, Maharashtra, India; e-mail: nikhilyenorkar23@gmail.com, https://orcid.org/0000-0003-0660-5652

Natasha Sudhir Akojwar — PhD Research Scholar, Department of Pharmaceutical Sciences, Rashtrasant Tukadoji Maharaj Nagpur University, 440033, Nagpur, Maharashtra, India; e-mail: natashaakojwar@gmail.com, https://orcid.org/0009-0000-3010-3754

Satyendra Kuldip Prasad — Assistant Professor, Department of Pharmaceutical Sciences, Rashtrasant Tukadoji Maharaj Nagpur University, 440033, Nagpur, Maharashtra, India; e-mail: skprasad.rs.phe@itbhu.ac.in, https://orcid.org/0000-0002-4762-9733

Authors Contributions

The manuscript was written through contributions of all authors. All authors have given approval to the final version of the manuscript. CRediT: **Ayusha Omprakash Dondulkar** conceptualization, data creation, investigation, methodology, validation writing original draft; **Mandar Mahendra Muley** data creation, **Raksha Anand Purohit** Writing review and editing; **Nikhil Yadavrao Yenorkar** Visualization and editing; **Natasha Sudhir Akojwar** Review and editing; **Satyendra Kuldeep Prasad** conceptualization, review, supervision and communication.

Acknowledgement

Authors would like to acknowledge the fellowship awarded by Mahatma Jyotiba Phuley Research Fellowship, Government of Maharashtra, India to Ms. Ayusha O. Dondulkar (Letter No.: Fellowship2022_973 dated 13/12/2022).

Conflicts of Interest

The authors declare no conflict of interest.

Data Availability Statement

All data supporting the findings of this study are available within the article or its supplementary materials.

References

1 Ghasemi, J., Shamsabadi, S., Mahzoon, E., Nazer, Y., Rahimi, V.B., & Askari, V.R. (2024). A Mechanistic Insight into the Effects of Marine Sources as Functional Foods Against Metabolic Syndrome: A Review Article. *Letters in Drug Design & Discovery*, *21*(19), 4668–4682. https://doi.org/10.2174/0115701808344500250115114637

2 Li, J., Mao, B., Tang, X., Zhang, Q., Zhao, J., Zhang, H., & Cui, S. (2023). Protective effects of naringenin and apigenin in ameliorating skin damage via mediating the Nrf2 and NF-κB pathways in mice. *Foods*, *12*(11), 2120. https://doi.org/10.3390/foods12112120

3 Yoon, J.H., Kim, M.Y., & Cho, J.Y. (2023). Apigenin: A therapeutic agent for treatment of skin inflammatory diseases and cancer. *International Journal of Molecular Sciences*, *24*(2), 1498. https://doi.org/10.3390/ijms24021498

4 Xie, J., Li, H., Zhang, T., Song, B., Wang, X., & Gu, Z. (2023). Recent advances in ZnO nanomaterial-mediated biological applications and action mechanisms. *Nanomaterials*, *13*(9), 1500. https://doi.org/10.3390/nano13091500

5 Gouda, A., Sakr, O.S., Nasr, M., & Sammour, O.A. (2024). Developing a rapid analytical method for simultaneous determination of apigenin and gallic acid: validation and application in a nanoliposomal formulation. *Drug Development and Industrial Pharmacy*, *50*(3), 274–283. https://doi.org/10.1080/03639045.2024.2318386

6 Bhia, M., Motallebi, M., Abadi, B., Zarepour, A., Pereira-Silva, M., Saremnejad, F., ... & Shakibaei, M. (2021). Naringenin nano-delivery systems and their therapeutic applications. *Pharmaceutics*, *13*(2), 291. https://doi.org/10.3390/pharmaceutics13020291

7 Manyasree, D., Kiranmayi, P., & Venkata, R.K. (2018). Characterization and antibacterial activity of ZnO nanoparticles synthesized by co-precipitation method. *International Journal of Applied Pharmaceutics*, *10*(6), 224–228. http://dx.doi.org/10.22159/ijap.2018v10i6.29376

8 Mandal, A.K., Katuwal, S., Tettey, F., Gupta, A., Bhattarai, S., Jaisi, S., Bhandari, D.P., Shah, A.K., Bhattarai, N., & Parajuli, N. (2022). Current Research on Zinc Oxide Nanoparticles: Synthesis, Characterization, and Biomedical Applications. *Nanomaterials*, *12*(17), 3066. https://doi.org/10.3390/nano12173066

9 Rajabi, H.R., Naghiha, R., Kheirizadeh, M., Sadatfaraji, H., Mirzaei, A., & Alvand, Z.M. (2017). Microwave assisted extraction as an efficient approach for biosynthesis of zinc oxide nanoparticles: synthesis, characterization, and biological properties. *Materials Science and Engineering: C*, *78*, 1109–1118. https://doi.org/10.1016/j.msec.2017.03.090

10 Chaudhari, V.S., Borkar, R.M., Murty, U.S., & Banerjee, S. (2020). Analytical method development and validation of reverse-phase high-performance liquid chromatography (RP-HPLC) method for simultaneous quantifications of quercetin and piperine in dual-drug loaded nanostructured lipid carriers. *Journal of Pharmaceutical and Biomedical Analysis*, *186*, 113325. https://doi.org/10.1016/j.jpba.2020.113325

11 Bhutia, G.T., Kumar DE.A., & Bera, T. (2022). Validation, stability studies, and simultaneous estimation of co-encapsulated curcumin, epigallocatechin gallate nanoformulation by RP-HPLC method. *International Journal of Applied Pharmaceutics*, *14*, 186–195. https://dx.doi.org/10.22159/ijap.2022v14i6.45818

12 Khismatrao, A., Bhairy, S., & Hirlekar, R. (2018). Development and validation of RP-HPLC method for simultaneous estimation of curcumin and piperine. *International Journal of Applied Pharmaceutics*, *10*(5), 43. https://doi.org/10.22159/ijap.2018v10i5.21140

13 Patil, C., Naik, P., Mallamma, T., & Goudanavar, P. (2025). Exploring the potential of a quick and simultaneous DoE-based stability indicating novel RP-HPLC method for the estimation of capecitabine and curcumin in biodegradable nanoparticles and human plasma. *Journal of Chromatography B*, 124731. https://doi.org/10.1016/j.jchromb.2025.124731

14 Khatak, S., Khatak, M., Ali, F., Rathi, A., Singh, R., Singh, G.N., & Dureja, H. (2018). Development and Validation of a RP-HPLC Method for Simultaneous Estimation of Antitubercular Drugs in Solid Lipid Nanoparticles. *Indian Journal of Pharmaceutical Sciences*, 80(6). https://doi.org/10.4172/pharmaceutical-sciences.1000449

15 Venishetty, V.K., Parikh, N., Sistla, R., Ahmed, F.J., & Diwan, P.V. (2011). Application of validated RP-HPLC method for simultaneous determination of docetaxel and ketoconazole in solid lipid nanoparticles. *Journal of Chromatographic Science*, *49*(2), 136–141. https://doi.org/10.1093/chrsci/49.2.136

How to Cite: Muradova, P.A., Litvishkov, Y.N., Baloglanov, E.E., Yolchuyeva, U.J., Akhundov, R.V., & Samedov, E.S. (2026). Microwave Aquathermolysis of Oil Shales: Enhancement of Light Hydrocarbon Yield and Modification of Gaseous Product Composition. *Eurasian Journal of Chemistry, 31, 2(122), 102–111*. https://doi.org/10.31489/2959-0663/2-26-5

CHEMICAL TECHNOLOGY

Article

Received: 27 January 2026 | Revised: 23 April 2026 |
Accepted: 27 April 2026 | Published online: 29 April 2026

UDC 553.982+662.75+621.382.3

https://doi.org/10.31489/2959-0663/2-26-5

Peri A. Muradova[1*], Yuriy N. Litvishkov[2], Elnur E. Baloglanov[3], Ulviyya J. Yolchuyeva[4, 5, 6], Ruslan V. Akhundov[3], Elmar S. Samedov[3]

[1]*Institute of Chemistry of the Ministry of Science and Education of the Republic of Azerbaijan, Baku, Azerbaijan;*
[2]*Azerbaijan National Academy of Sciences, Baku, Azerbaijan;*
[3]*Institute of Geology of the Ministry of Science and Education of the Republic of Azerbaijan, Baku, Azerbaijan;*
[4]*Institute of Petrochemical Processes named after Academician Y. Mammadaliyev of the Ministry of Science and Education of the Republic of Azerbaijan, Baku, Azerbaijan;*
[5]*Department of Chemical Engineering, School of Engineering and Applied Science, Khazar University, Baku, Azerbaijan;*
[6]*Azerbaijan University of Architecture and Construction, Baku, Azerbaijan*
*(*Corresponding author's e-mail: muradovaperi@rambler.ru)*

Microwave Aquathermolysis of Oil Shales: Enhancement of Light Hydrocarbon Yield and Modification of Gaseous Product Composition

The growing global demand for energy and the depletion of conventional light hydrocarbon resources necessitate the development of alternative and hard-to-recover feedstocks, among which oil shales represent a strategically important resource due to their vast reserves. In this study, the efficiency of conventional microwave thermolysis in an inert atmosphere is compared with an innovative microwave aquathermolysis approach employing activated steam for oil shale samples from three Azerbaijani deposits (Diyally, Guba, and Jangichay). The experiments were conducted under microwave irradiation (2.45 GHz, 600–800 W) at 300–400 °C with a treatment duration of 20 minutes, ensuring rapid and uniform heating. Microwave aquathermolysis was shown to enhance heat and mass transfer, promoting deeper degassing and partial kerogen conversion. Steam activation led to an increased yield of light hydrocarbons, a marked reduction of heavy resins and asphaltenes, and significant changes in gaseous product composition. Gas chromatographic and SARA analyses confirmed accelerated thermochemical reactions, suppression of secondary coking, steam-assisted conversion of carbon oxides, and partial hydrogenation of unsaturated compounds. Overall, the results indicate that microwave aquathermolysis is more efficient and energy-saving than conventional microwave thermolysis, demonstrating strong potential for processing Azerbaijani oil shales and other kerogen-rich unconventional resources.

Keywords: oil shale, microwave aquathermolysis, heat–mass transfer, enhanced light fraction yield, energy-efficient processing, microwave irradiation, kerogen conversion, steam activation, gaseous product modification

Introduction

The depletion of conventional oil reserves poses a challenge for the energy and chemical industries to identify alternative sources of hydrocarbon feedstock [1–10]. In this context, oil shales acquire particular importance, as their global reserves far exceed the combined resources of oil, natural gas, and coal [11–13].

The decline in conventional hydrocarbon production in Azerbaijan has also increased attention to heavy hydrocarbons, including oil shales, discovered in the eastern regions of the country and considered a secondary hydrocarbon resource [14, 15]. These shales belong to a stratigraphic sequence ranging from the Middle

Eocene to the Upper Miocene [16, 17]. Their thickness reaches 400–500 m, with individual layers measuring 10–20 m or more [18, 19].

Tectonic activity in the collision zone of the African and Arabian plates in Eastern Azerbaijan has led to the exposure of oil shales at the surface, both as natural outcrops and as mud volcano ejecta [17–19]. The distribution of mud volcanism provides favorable conditions for obtaining valuable information on the internal structure and geochemical–mineralogical characteristics of the volcanic system, as well as on the extent, composition, and distribution of oil shale layers in the subsurface, which can be traced over considerable distances at the surface [20–27].

Oil shales widespread on the land of Eastern Azerbaijan are characterized by a high organic matter content (up to 24 wt% total organic carbon — TOC) and low thermal maturity [17]. This necessitates the use of innovative methods for the production of synthetic hydrocarbons, employing technologies such as in–situ pyrolysis and surface processing [18].

Conventional processing methods based on convective heating (e.g., electric heating, heat carriers) require prolonged exposure, which induces secondary coking reactions, reduces liquid product yields, and promotes the formation of carbon oxides (CO and CO_2) [12, 28–31]. The low reactivity of kerogen and the high ash content of shales make the use of alternative energy-based methods reasonable, such as microwave irradiation, which provides rapid heating and uniform heat distribution [32]. In recent years, the conventional (dry) microwave thermolysis of oil shales has been extensively studied globally due to its ability to accelerate heating rates and alter the fractional yield of retorting products compared to traditional convective heating [33, 34]. Comprehensive reviews and three-dimensional numerical simulations have confirmed that microwave application effectively enhances hydrocarbon desorption and volumetric heating within the shale matrix [35, 36]. In this broader global context, previous studies have shown that microwave thermolysis of Azerbaijani shale samples is highly effective, confirming the promise of this approach [37]. However, conventional dry microwave processing still faces critical challenges, such as secondary coking and the limited hydrogen availability within the kerogen itself, which restricts the maximum achievable yield of light liquid hydrocarbons. Recently, independent studies exposing oil shales to high-temperature water vapor have shown promising results in improving micro-fracture evolution and permeability [38, 39]. By combining the rapid heating benefits of microwaves with the chemical reactivity of steam, in the present study, results are presented for a modified microwave aquathermolysis method, based on the treatment of samples with steam activated by microwave radiation, which enhances degassing intensity, increases the yield of light hydrocarbons, and reduces coking.

Experimental

For this study, oil shale samples were selected from the stratigraphic sequence ranging from the Middle Eocene to the Upper Miocene, obtained from three prospective deposits in Eastern Azerbaijan: Diyally (Middle Eocene), Guba (Middle–Upper Miocene), and Jangichay (Middle Eocene) [18, 40, 41]. The samples are characterized by high TOC contents: Diyally — 24 %, Guba — 20 %, Jangichay — 18 % (2). Petrographic and pyrolytic analyses showed that the organic matter in these shales is predominantly type II kerogen, formed in marine conditions from algal detritus, indicating a high potential for liquid hydrocarbon generation [2, 18].

The mineralogy of the rocks was analyzed via X-ray diffraction using a Rigaku Miniflex X-ray diffractometer (Rigaku, Japan). The measurements were performed to identify the crystalline phases and provide a semi-quantitative assessment of the inorganic matrix, which plays a vital role in the samples' interaction with microwave radiation. Table 1 presents the mineralogical composition of the studied oil shale samples.

Table 1

Semi-quantitative mineralogical composition of the studied oil shale samples (wt. %)

Sample	Clay minerals (illite, montmorillonite, kaolinite, chlorite)	Silicates (quartz, feldspar)	Carbonates (calcite, Mg-calcite)	Sulfur-bearing minerals (pyrite, jarozite)	Iron Oxides (hematite, rutile)
Diyally	33	44	12	2	9
Guba	45	40	8	1.8	5
Jangichay	43	34	8	15	0

Microwave irradiation experiments were conducted using a setup based on a Panasonic EM–G5593V laboratory microwave oven with a 23 L cavity. The magnetron output power ranged from 200 to 800 W at an operating frequency of 2450 MHz. Under the applied optimal microwave power settings (600–800 W), the sample temperature reached 500–600 °C over the 20-minute exposure period, which corresponds to an average actual heating rate of approximately 25–30 °C/min. Sample and steam line temperatures were monitored with a CEM DT–8858 infrared pyrometer (range 50–1300 °C), which recorded the surface temperature of the oil shale samples through the microwave-transparent quartz vessel. Shale samples with a particle size of 1–5 mm were placed in a 100 mL quartz reaction vessel, which is transparent to microwaves and equipped with inlet and gas outlet lines. To prevent oxidative reactions of desorbed products, the inlet line was saturated with steam delivered from a heated distillation water evaporator at a flow rate of 0.05–0.3 mol/min. To avoid local overheating of the samples, a water-shunting vessel with circulating cooling fluid was employed. The setup included a condensation and collection system for liquid thermolysis products. Gaseous compounds were collected in a coil trap cooled in a Dewar vessel filled with solid CO_2.

The liquid fraction of the desorbed hydrocarbons was separated using liquid adsorption chromatography (Saturates, Aromatics, Resins, Asphaltenes — SARA) with a column packed with KSK–grade silica gel, allowing the isolation of four compound groups: saturated hydrocarbons, aromatic compounds, resins, and asphaltenes [42]. The separation procedure followed ASTM D4124–09 standards.

Qualitative and quantitative analysis of the gaseous phase was performed using an LKhM-8MD gas chromatograph (column length 3.6 m, internal diameter 3 mm, stationary phase “Porapak QS”) under programmable thermostat heating from 30 to 650 °C at a rate of 3–5 °C/min.

All quantitative experiments, including the SARA fractionation and gas chromatographic analyses, were performed in triplicate (n = 3) to ensure reproducibility. The experimental data are presented as the mean values ± standard deviation (SD).

Results and Discussion

The study of the heating dynamics of oil shale samples under aquathermolysis conditions, with varying microwave power in the oven cavity, revealed differences in their heating rates (Fig. 1). This is likely associated with variations in dielectric losses, which are determined by the inorganic fraction of the shales, dominating over the organic matter (kerogen), and whose composition depends on their genesis [18]. As illustrated in Figure 1, while an applied power of 600 W is sufficient for all samples to surpass 400 °C (the onset of active thermolysis), the Diyally deposit sample required exposure at up to 800 W to reach the higher optimal temperature range of 450–500 °C. In contrast, samples from the Jangichay and Guba deposits more efficiently achieved these higher temperatures at only 600 W for the same duration.

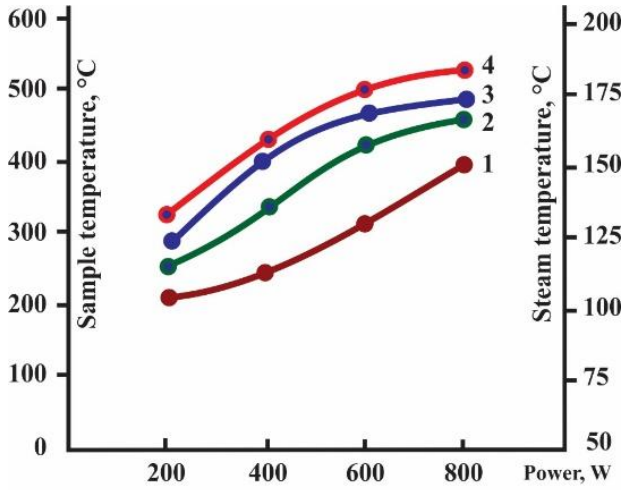

Figure 1. Temperature rise dynamics of the supplied steam (Y-axis, right) and oil shale samples (Y-axis, left) as a function of applied microwave power (X-axis) for the Diyally (2), Guba (3), and Jangichay (4) deposits. Exposure conditions: sample mass 50 g; duration 20 min; steam flow rate 0.2 mol/min; magnetron operating frequency 2450 MHz. The presented data points represent the mean values of three independent experiments (n = 3)

The selection of the 400–500 °C temperature range is fundamental for optimizing the yield of liquid products while minimizing secondary gasification. While some industrial processes targeting total gasification operate at 600 °C and above, such high temperatures promote the intensive secondary cracking of synthesized hydrocarbons and the undesirable decomposition of the inorganic carbonate matrix. In our microwave-assisted process, the presence of localized dielectric heating sites (e.g., pyrite and jarosite) ensures efficient kerogen transformation within the moderate 400–500 °C range, preserving the integrity of the liquid fractions.

The efficiency of microwave irradiation on heterogeneous materials, such as oil shales, is determined by their ability to absorb electromagnetic energy and convert it into heat [43]. Regardless of the electromagnetic radiation parameters, the measured result corresponds to the average power loss:

$$\Delta P_x = \frac{c \cdot m \cdot \Delta T}{0.24\tau} \text{ (J/s)},$$

where: 0.24 — the mechanical equivalent of heat; m — mass of the sample (g); c — specific heat capacity of the sample (kJ/kg·K); ΔT — measured temperature increase of the sample (K); τ — exposure time in the microwave oven (s).

Figure 2 shows that the dielectric losses of microwave radiation by oil shale samples from the three deposits are relatively high, facilitating the efficient attainment of the temperature required for microwave thermolysis. Power losses during aquathermolysis were found to exceed those in the absence of steam, likely due to the formation of adsorbed moisture layers on the shale surfaces, which enhance particle polarization [44].

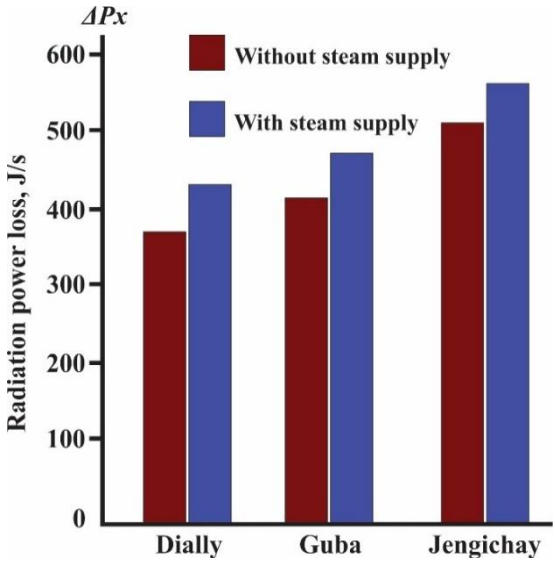

Figure 2. Comparative microwave power losses (ΔP_x, J/s) for different oil shale deposits under inert and steam-supplied conditions. Exposure conditions: sample mass 50 g; magnetron power 600 W; operating frequency 2450 MHz; exposure time 10 min; steam flow rate 0.3 mol/min. The presented data points represent the mean values of three independent experiments (n = 3)

After the exposure in the oven cavity, a relatively large variation in weight loss among the samples was observed. The maximum weight loss, due to degassing of organic matter and removal of volatile components, occurred for the Jangichay sample. It should also be noted that the highest ratio of desorbed liquid phase to gaseous phase, characteristic of this sample, is determined by the geochemical conditions of its formation (e.g., the kerogen composition, predominantly derived from marine lipid matter, relatively low influence of reducing conditions, and a certain degree of geothermal maturity) [18]. Considering this, from a practical standpoint, it is reasonable to conduct further microwave thermolysis experiments using the Jangichay deposit sample. While the overall multi-stage kinetic trends for the Diyally and Guba samples were broadly similar, plotting the data for all three deposits on a single graph would have severely cluttered the visualization. Therefore, the Jangichay shale was selected as the most representative optimal model to visually illustrate the comparative weight loss dynamics between inert thermolysis and aquathermolysis, as its mass-loss transitions are the most pronounced and visually distinct.

As evident from the aquathermolysis results of the Jangichay shale, weight loss during the desorption of hydrocarbon components, present both in the kerogen and adsorbed by the inorganic matrix of the sample [18], occurs in stages, as in an inert atmosphere (Fig. 3). Three main temperature regions of weight loss are observed. It is important to note that oil shale thermolysis is a complex process involving parallel and partially overlapping thermochemical transformations. Therefore, while dominant temperature intervals can be clearly identified for each sequence, precise and strict absolute boundaries between primary gas desorption, liquid phase evolution, and the coking stage cannot be rigidly defined.

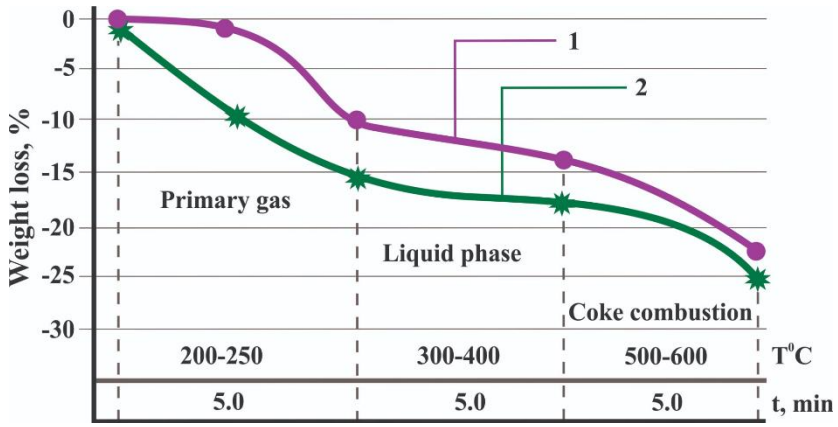

Figure 3. Comparison of the weight loss dynamics of a shale sample from the Jangichay deposit during microwave thermolysis in an inert atmosphere (1) and microwave aquathermolysis (2). Conditions: magnetron power 800 W, sample mass 50 g (fraction 3–5 mm), steam flow rate 0.5 mol/min. The presented data points represent the mean values of three independent experiments (n = 3)

In the first exposure region, during 5 minutes of irradiation at a temperature of ~200–250 °C, desorption of primary gaseous components occurs [15]. It was observed that under aquathermolysis conditions, with the activating effect of steam, desorption of gaseous components proceeds more intensively. Continued exposure of the samples for the next 5 minutes raises the temperature to ~300–400 °C, during which condensation of the heavier hydrocarbon components is observed in the trap. In the final stage of microwave treatment, the sample temperature rises to 600 °C and above. In this temperature range, desorption of gaseous products is again observed, associated with the combustion of coke-like residues formed during thermolysis.

Comparison of the weight-loss dynamics of the Jangichay shale sample during thermolysis in an inert nitrogen atmosphere and under aquathermolysis showed that weight change during the primary gas formation stage occurs more intensively under the influence of steam. In contrast, the intensity of weight loss associated with the release of the liquid fraction is slightly lower compared to the process conducted in an inert atmosphere.

The results of the SARA analysis of thermally desorbed high-molecular-weight hydrocarbon products (Tab. 2) show that under microwave aquathermolysis, the yield of saturated and aromatic hydrocarbons increases, while the content of high-molecular-weight resins and asphaltenes decreases. The observed decrease in resins and simultaneous increase in saturates are attributed to the hydrogen-assisted cracking (hydrocracking) of heavy organic macromolecules. The in-situ generated hydrogen, derived from steam activation, effectively stabilizes thermally generated organic radicals and promotes the scission of long-chain hydrocarbons into lighter, saturated fractions, thereby preventing secondary condensation into coke. It is important to clarify that “steam activation” under 2.45 GHz microwave irradiation does not imply the direct photolytic generation of free H• or OH• radicals, as the radiation is non-ionizing. Instead, activation occurs through intense dipole polarization and rotational excitation of the water molecules. When this rotationally excited steam interacts with micro-scale “hot spots”, generated by the strongly microwave-absorbing inorganic shale matrix, it vigorously drives localized hydrogen-generating pathways. The primary mechanism is the steam-carbon reaction ($C + H_2O \rightarrow CO + H_2$) occurring at these extreme-temperature solid-gas interfaces. The newly generated molecular hydrogen, potentially catalyzed by inherent shale minerals such as pyrite, stabilizes the thermally cracked organic radicals. This in situ generated hydrogen facilitates partial hydrogenation and completely suppresses secondary condensation and coking, as directly evidenced by the increased yield of saturated and aromatic fractions [45].

Table 2

Content of high-molecular-weight organic products in shale samples desorbed under microwave irradiation during thermolysis in an inert atmosphere and aquathermolysis. Magnetron power 800 W; sample mass 50 g; exposure time in the oven cavity 20 min; steam flow rate 0.5 mol/min

Sample	Content of organic products (% by mass)			
	Saturate	Aromatic	Resins	Asphaltenes
Microwave thermolysis in an inert atmosphere				
Diyally	2.2 ± 0.4	6.5 ± 0.4	8.6 ± 0.3	3.2 ± 0.4
Guba	3.2 ± 0.3	5.2 ± 0.4	8.7 ± 0.4	3.5 ± 0.5
Jangichay	2.7 ± 0.3	8.5 ± 0.5	8.8 ± 0.5	3.1 ± 0.4
Microwave aquathermolysis				
Diyally	3.4 ± 0.5	7.0 ± 0.4	7.4 ± 0.4	2.8 ± 0.5
Guba	3.8 ± 0.5	5.7 ± 0.4	7.2 ± 0.4	2.5 ± 0.5
Jangichay	3.6 ± 0.5	9.4 ± 0.4	6.9 ± 0.4	2.3 ± 0.5
Note: Data are presented as mean ± standard deviation (n = 3).				

Gas chromatographic analysis of the gas phase desorbed at the initial stage of microwave treatment (Tab. 3) also revealed significant differences in the thermolysis products under an inert atmosphere versus aquathermolysis. Treatment in a steam flow leads to an increase in carbon dioxide and hydrogen sulfide yields, accompanied by a simultaneous decrease in carbon monoxide content. Methane yield remains stable, while hydrogen concentration shows a slight increase.

Table 3

Content of gaseous products in shale samples desorbed under microwave irradiation at 800 W; sample amount — 50 g; exposure time in the oven cavity — 20 min; steam flow rate — 0.5 mol/min

Sample	Content of gaseous products (% by mass)				
	CO	CO_2	H_2S	CH_4	H_2
Microwave thermolysis in an inert atmosphere					
Diyally	0.8 ± 0.1	1.6 ± 0.2	1.8 ± 0.2	2.2 ± 0.2	1.7 ± 0.1
Guba	0.6 ± 0.1	0.8 ± 0.1	1.3 ± 0.2	2.5 ± 0.2	1.5 ± 0.1
Jangichay	0.5 ± 0.1	0.4 ± 0.1	0.7 ± 0.1	3.1 ± 0.3	2.3 ± 0.2
Microwave aquathermolysis					
Diyally	0.7 ± 0.1	1.8 ± 0.2	2.0 ± 0.2	2.2 ± 0.2	1.8 ± 0.1
Guba	0.4 ± 0.1	0.9 ± 0.1	1.4 ± 0.2	2.5 ± 0.2	1.6 ± 0.1
Jangichay	0.3 ± 0.1	0.6 ± 0.1	0.9 ± 0.1	3.1 ± 0.3	2.5 ± 0.2
Note: Data are presented as mean ± standard deviation (n = 3).					

Interestingly, the mineralogical composition data presented in Table 1 serves as a critical foundation for interpreting these gaseous yields. The presence of sulfur-bearing minerals in all studied samples, specifically pyrite in Diyally and Guba, and a significant amount of jarosite (15 %) in Jangichay, correlates with the detection of H_2S in the gaseous phase (Tab. 3). This suggests that H_2S originates from a multi-component mechanism: the hydrothermal decomposition of both sulfide (pyrite) and sulfate (jarosite) minerals, alongside the intensified thermal cracking of sulfur-containing organic macromolecules (organosulfur) within the kerogen structure [46]. Furthermore, while Table 1 identifies the presence of carbonates in the shale matrix, their thermal decomposition typically requires temperatures well above 700 °C. Therefore, the significant amounts of CO_2 generated at our operating temperatures (400–500 °C) are primarily driven by the decarboxylation of the organic matter itself, rather than inorganic matrix decomposition.

The observed changes in the composition of gaseous products can be explained by the combined effect of activated steam on the progression of thermochemical processes. Steam activated by microwave irradiation intensifies the oxidative conversion of organic oxygen-containing functional groups and heavy fractions, manifested by an increased CO_2 yield. Simultaneously, the steam-mediated conversion of carbon monoxide (the water-gas shift reaction) shifts the equilibrium toward the formation of carbon dioxide and hydrogen [47]. The slight increase in hydrogen concentration (by 0.1-0.2 %) confirms the in-situ generation of hy-

drogen at the activated solid-gas interfaces, where it facilitates partial hydrogenation and suppresses secondary coking [48].

The contribution of the water-gas shift (WGS) reaction ($CO + H_2O \rightarrow CO_2 + H_2$) can be qualitatively differentiated from the oxidative conversion of coke residues by analyzing the stoichiometry of the carbon oxide changes. In our experiments (Tab. 3), the decrease in CO concentration (0.1-0.2 % by mass) aligns with the simultaneous increase in H_2, confirming the activity of the WGS pathway. However, the total increase in CO_2 yield often exceeds the stoichiometric equivalent of CO consumed, particularly in the Diyally and Jangichay samples. This indicates that the oxidative conversion of oxygen-containing organic functional groups and coke residues remains a primary source of CO_2 under microwave aquathermolysis conditions.

To evaluate the energy efficiency of the proposed method, the specific energy consumption (SEC) was calculated. The total energy input during the 20-minute exposure at 800 W was 0.267 kWh. The specific energy consumption per unit mass of the shale sample was determined using the relation:

$$SEC_{shale} = \frac{P \cdot \tau}{m} = \frac{0.8\ \text{kW} \cdot (20/60)\text{h}}{0.05\ \text{kg}}.$$

This calculation directly justifies the energy density required to reach the target thermolysis temperatures within the microwave cavity, providing a quantitative basis for comparing the efficiency of the different processing regimes. For a 50 g shale sample, the specific energy consumption per mass of raw material (SEC shale) is 5.34 kWh/kg. However, the true efficiency is reflected in the energy required to produce a unit of the desired light hydrocarbon fraction (saturates and aromatics). As shown in Table 4, microwave aquathermolysis reduces the energy/product ratio for light fractions by approximately 14–16 % compared to inert thermolysis, confirming its superior energy efficiency.

Table 4

Energy efficiency and specific energy consumption (SEC) for the Jangichay shale sample

Parameter	Microwave thermolysis (Inert)	Microwave aquathermolysis
Total Energy Input (kWh)	0.267	0.267
Specific Energy (SEC shale), kWh/kg shale	5.34	5.34
Light Product Yield (Saturates + Aromatics), wt%	11.2	13.0
Energy/Product Ratio (SEC product), kWh/kg light product	47.7	41.1

Conclusions

The study demonstrated that microwave aquathermolysis is an effective approach for the thermochemical conversion of the organic fraction in oil shales. Treatment with steam activated by microwave irradiation provides rapid sample heating, enhances heat and mass transfer, and increases the degree of hydrocarbon desorption at 400–600 °C. Thermal analysis confirmed the staged nature of the process and a higher rate of gaseous and liquid product release compared to microwave thermolysis in an inert atmosphere.

Quantitative analysis confirmed the method's effectiveness: SARA data showed a consistent increase in the content of saturated and aromatic hydrocarbons (e.g., up to 1.2 % for saturates), accompanied by a noticeable decrease in resins and asphaltenes (e.g., up to 1.9 % for resins). In the gas phase, an increase in hydrogen and hydrogen sulfide yields up to 0.2 % was observed, while methane yield remained stable and carbon monoxide content decreased to 0.3 %.

Thus, microwave aquathermolysis provides a high degree of conversion of the organic fraction in shales, reduces the intensity of coking, and increases the yield of light hydrocarbon fractions in a short time, confirming its superior energy efficiency with a 14–16 % reduction in energy/product ratio compared to inert thermolysis.

*Author Information**

**The authors' names are presented in the following order: First Name, Middle Name and Last Name*

Peri Aghaguseyn Muradova — PhD (Chemistry), Associate Professor, Senior Researcher, Institute of Catalysis and Inorganic Chemistry named after Academician M. Nagiyev of the Ministry of Science and Ed-

ucation of the Republic of Azerbaijan, H. Javid ave., 113, AZ1143, Baku, Azerbaijan; e-mail: muradovaperi@rambler.ru; https://orcid.org/0009-0009-2803-9509

Yuriy Nikolayevich Litvishkov — Corresponding Member of the Azerbaijan National Academy of Sciences, Professor; e-mail: yuriylit@rambler.ru; https://orcid.org/0000-0003-0662-1257

Elnur Eyvaz Baloglanov — Researcher of Department of Mud Volcanism, Institute of Geology and Geophysics of the Ministry of Science and Education of the Republic of Azerbaijan, H. Javid ave., 119, AZ1073, Baku, Azerbaijan; e-mail: b.elnur2016@gmail.com; https://orcid.org/0009-0004-3620-0052

Ulviyya Jeyhun Yolchuyeva — PhD (Chemistry), Associate Professor, Head of Laboratory, Institute of Petrochemical Processes named after Academician Y. Mammadaliyev of the Ministry of Science and Education of the Republic of Azerbaijan, Khojali ave. 30, Baku, AZ1025, Azerbaijan; Department of Chemical Engineering, School of Engineering and Applied Science, Khazar University, Mahsati Str., 41, AZ1096, Baku, Azerbaijan; Azerbaijan University of Architecture and Construction, Ayna Sultanova Str. 5, AZ1073, Baku, Azerbaijan; e-mail: u.jeyhunzade@gmail.com; https://orcid.org/0000-0003-4419-1016

Ruslan Vagif Akhundov — Researcher of Department of Mud Volcanism, Institute of Geology and Geophysics of the Ministry of Science and Education of the Republic of Azerbaijan, H. Javid ave., 119, AZ1073, Baku, Azerbaijan; e-mail: ruslanaxundoff@gmail.com; https://orcid.org/0009-0003-6447-1952

Elmar Surkhay Samedov — Engineer of Department of Mud Volcanism, Institute of Geology and Geophysics of the Ministry of Science and Education of the Republic of Azerbaijan, H. Javid ave., 119, AZ1073, Baku, Azerbaijan; e-mail: samedovelmar@gmail.com; https://orcid.org/0009-0002-6835-0229

Author Contributions

The manuscript was written through contributions of all authors. All authors have given approval to the final version of the manuscript. CRediT: **Peri Aghaguseyn Muradova** — conceptualization, methodology, supervision, investigation, writing — original draft, writing — review & editing; **Yuriy Nikolayevich Litvishkov** — conceptualization, data curation, formal analysis, validation, writing — review & editing; **Elnur Eyvaz Baloglanov**, **Ruslan Vagif Akhundov** and **Elmar Surkhay Samedov** — investigation, data curation, visualization, resources, writing — review & editing; **Ulviyya Jeyhun Yolchuyeva** — methodology, investigation, data curation, visualization, writing — original draft.

Acknowledgments

Authors thank the Institute of Chemistry of the Ministry of Science and Education of the Republic of Azerbaijan and the Institute of Geology of the Ministry of Science and Education of the Republic of Azerbaijan for providing institutional support, access to facilities, and assistance essential for carrying out this work and conducting the analytical investigations.

Conflicts of Interest

The authors declare no conflict of interest.

References

1 Abbasov, O.R., Aliyev, A.A., & Baloglanov, E.E. (2024, April 14–19). *A comparative mineralogical and geochemical studies of Eocene and Maikop oil shales in Eastern Azerbaijan: Stratigraphic controls on formation of oil and gas hydrocarbons in the South Caspian basin* [Conference presentation abstract]. EGU General Assembly 2024, Vienna, Austria. https://doi.org/10.5194/egusphere-egu24-925

2 Abbasov, O.R. (2022). Eocene–Miocene oil shales in Azerbaijan: Stratigraphic controls on formation, distribution and hydrocarbon generation. *Stratigraphy and Sedimentology of Oil-Gas Basins*, 1, 39–55. https://doi.org/10.35714/ggistrat20220100004

3 Nurlybayeva, A., Yermekova, A., Taubayeva, R., Sarova, N., Sapiyeva, A., Mateeva, S., Matniyazova, G., Bulekbayeva, K., Jetpisbayeva, G., & Tamabekova, M. (2025). Modern methods of obtaining synthetic oil from unconventional hydrocarbon raw materials: Technologies, catalysts, and development prospects. *Polymers*, *17*(6), Article 776. https://doi.org/10.3390/polym17060776

4 Jafarova, R.A., Yolchuyeva, U.J., Abbasov, O.R., Aliyeva, A.F., Baloglanov, E.E., Mehdiyeva, N.A., & Gasimova, F.I. (2025). Phototransformation processes of oil sands bitumen under the influence of ultraviolet radiation. *Coke and Chemistry*, 68, 45–51. https://doi.org/10.3103/S1068364X25600022

5 Dutta, S. (2023). Sustainable synthesis of drop-in chemicals from biomass via chemical catalysis: Scopes, challenges, and the way forward. *Energy & Fuels, 37*(4), 2648–2666. https://doi.org/10.1021/acs.energyfuels.2c03891

6 Prischepa, O.M., Xu, R., Martynov, A., Ibatullin, A., Krykova, T., & Sinitsa, N. (2024). Potential of high-carbon Domanik (Upper Devonian) shale deposits: Timan–Pechora oil and gas province assessment. *International Journal of Engineering, 37*(8), 1639–1657. https://doi.org/10.5829/ije.2024.37.08b.16

7 Prischepa, O.M., & Xu, R. (2025). Criteria for oil and gas bearing potential of Jurassic continental sediments of the central part of the Junggarian sedimentary basin. *International Journal of Engineering, 38*(1), 223–235. https://doi.org/10.5829/ije.2025.38.01a.20

8 Nefedov, Y.V., Gao, H., Gribanov, M.A., Vostrikov, N.N., Yashmolkin, A.M., Yandulov, P.V., Loginov, A.V., Gribanov, D.A., & Karimov, V.M. (2024). Analysis of oil and gas controlling factors of Lower Silurian and Upper Ordovician sediments of the Wufeng–Longmaxi Formation in the Sichuan Basin. *International Journal of Engineering, 37*(10), 2066–2079. https://doi.org/10.5829/ije.2024.37.10a.17

9 Khuduzade, A.I., Abbasov, O.R., Guliyev, I.S., Yolchuyeva, U.J., Baloglanov, E.E., Jafarova, R.A., Akhundov, R.R., Aliyeva, N.M. & Bashirov, O.K. (2026). Geochemical-paleontological study of Mesozoic source rocks, Eurasian–Gondwana junction, Azerbaijan. Episodes. https://doi.org/10.18814/epiiugs/2026/026002

10 Abbasov, O.R., Khuduzade, A.I., Guliyev, I.S., Yolchuyeva, U.J., Baloglanov, E.E., Jafarova, R.A., Akhundov, R.R., Samadov, E.S., & Bashirov, O.K. (2026, May 3–8). Mesozoic source rock systems at the junction between Eurasia and Gondwana: Tethyan vs Boreal controls in the Southeastern Caucasus, Northeastern Azerbaijan [Conference presentation abstract]. EGU General Assembly 2026, Vienna, Austria. https://doi.org/10.5194/egusphere-egu26-14353

11 Sabanov, S., Qureshi, A.R., Dauitbay, Z., & Kurmangazy, G. (2023). A method for the modified estimation of oil shale mineable reserves for shale oil projects: A case study. *Energies, 16*(16), Article 5853. https://doi.org/10.3390/en16165853

12 Zhao, D., Zhang, Q., Ren, C., Zhang, Z., Zhang, J., Hu, F., Zhou, X., Tan, X., & Guo, Y. (2023). A bibliometric comparative study on global oil shale research: Hotspots, trends and regional focus. *Oil Shale, 40*(1), 1–24. https://doi.org/10.3176/oil.2023.1.01

13 Liu, X., Yi, R., Zhao, D., Luo, W., Huang, L., Su, J., & Zhu, J. (2025). Research progress on the pyrolysis characteristics of oil shale in laboratory experiments. *Processes, 13*(9), Article 2787. https://doi.org/10.3390/pr13092787

14 Yolchuyeva, U.J., Abbasov, O.R., Jafarova, R.A., Hajiyeva, G.A., Rahimov, R.A., Mehdiyeva, N.A., & Baloglanov, E.E. (2025). A study of asphaltene solubility and aggregation due to sulfur heteroatoms: Molecular dynamics simulation. *Journal of Molecular Modeling*, 31, Article 133. https://doi.org/10.1007/s00894-025-06358-z

15 Yolchuyeva, U.J., Abbasov, V.M., Abbasov, O.R., Abdullayev, Y., Jafarova, R.A., Mammadov, A.M., Rahimov, R.A., Hajiyeva, G.A., & Autschbach, J. (2026). N-Octylaminopropan-2-ol surfactant for crude-oil asphaltene dispersion: Integrated experimental and modeling insights. *Fuel*, 404(Part B), Article 136286. https://doi.org/10.1016/j.fuel.2025.136286

16 Aliyev, A.A., & Abbasov, O.R. (2020). Distribution patterns, organic geochemistry and mineralogy of oil shales in Azerbaijan. *Gornyi Zhurnal*, 8, 13–18. https://doi.org/10.17580/gzh.2020.08.02

17 Aliyev, A.A., Abbasov, O.R., Ibadzade, A.J., & Mammadova, A.N. (2018). Genesis and organic geochemical characteristics of oil shale in Eastern Azerbaijan. *SOCAR Proceedings*, 3, 4–15. https://doi.org/10.5510/OGP20180300356

18 Abbasov, O., Baloglanov, E.E., Yolchuyeva, U.J., Khuduzade, A.I., & Akhundov, R.V. (2025). Factors controlling the formation and oil-generating potential of the Middle Eocene shales of Eastern Azerbaijan. *Boletín de la Sociedad Geológica Mexicana, 77*(1), Article A020724. https://doi.org/10.18268/BSGM2023v77n1a020724

19 Aliyev, A.A., Abbasov, O.R., Aghayev, A.M., Khuduzade, A.I., & Hasanov, E.H. (2022). Mineralogy, geochemistry and paleoweathering characteristics of Paleogene–Miocene oil shales in Azerbaijan. *SOCAR Proceedings*, 1, 24–36. https://doi.org/10.5510/OGP20220100625

20 Aliyev, A., Huseynov, D., Abbasov, O., Rashidov, T., & Kangarli, I. (2024). Mud volcanoes of Azerbaijan: The unique natural objects of the geoheritage. *Geoheritage*, 16, Article 20. https://doi.org/10.1007/s12371-024-00931-3

21 Baldermann, A., Abbasov, O.R., Bayramova, A., Abdullayev, E., & Dietzel, M. (2020). New insights into fluid–rock interaction mechanisms at mud volcanoes. *Chemical Geology*, 537, Article 119479. https://doi.org/10.1016/j.chemgeo.2020.119479

22 Baloglanov, E., Yolchuyeva, U., Akhundov, R., Samedov, E., & Mustafayev, K. (2025). Mineralogical and geochemical proxies of Miocene sediments of Eastern Azerbaijan. *Visnyk of V.N. Karazin Kharkiv National University. Series Geology, Geography, Ecology*, 62, 11–24. https://doi.org/10.26565/2410-7360-2025-62-01

23 Baloglanov, E. (2023). Geochemical proxies of the gryphon breccia of mud volcanoes in East Azerbaijan. *Visnyk of V.N. Karazin Kharkiv National University. Series Geology, Geography, Ecology*, 59, 8–17. https://doi.org/10.26565/2410-7360-2023-59-01

24 Bayramova, A., Abbasov, O.R., Aliyev, A.A., Baloglanov, E.E., Stamm, F.M., Dietzel, M., & Baldermann, A. (2023). Tracing water–rock–gas reactions in shallow productive mud chambers of active mud volcanoes in the Caspian Sea region (Azerbaijan). *Minerals, 13*(5), Article 696. https://doi.org/10.3390/min13050696

25 Liu, J., Treude, T., Abbasov, O.R., Baloglanov, E.E., Aliyev, A.A., Harris, C.M., Leavitt, W.D., & Young, E.D. (2024). Clumped isotope evidence for microbial alteration of thermogenic methane in terrestrial mud volcanoes. *Geology*, 52(1), 22–26. https://doi.org/10.1130/G51667.1

26 Odonne, F., Imbert, P., Dupuis, M., Aliyev, A.A., Abbasov, O.R., Baloglanov, E.E., Vendeville, B.C., Gabalda, G., Remy, D., Bichaud, V., Juste, R., Pain, M., Blouin, A., Dofal, A., & Gertauda, M. (2020). Mud volcano growth by radial expansion: Examples from onshore Azerbaijan. *Marine and Petroleum Geology*, 112, Article 104051. https://doi.org/10.1016/j.marpetgeo.2019.104051

27 Odonne, F., Imbert, P., Remy, D., Gabalda, G., Aliyev, A.A., Abbasov, O.R., Baloglanov, E.E., Bichaud, V., Juste, R., Dupuis, M., & Bonvalot, S. (2021). Surface structure, activity and microgravimetry modeling delineate contrasted mud chamber types below flat and conical mud volcanoes from Azerbaijan. *Marine and Petroleum Geology*, 134, Article 105315. https://doi.org/10.1016/j.marpetgeo.2021.105315

28 Jerzak, W., Acha, E., & Li, B. (2024). Comprehensive review of biomass pyrolysis: Conventional and advanced technologies, reactor designs, product compositions and yields, and techno-economic analysis. *Energies*, *17*(20), Article 5082. https://doi.org/10.3390/en17205082

29 Yang, C., Shang, H., Li, J., Fan, X., Sun, J., & Duan, A. (2023). A review on the microwave-assisted pyrolysis of waste plastics. *Processes*, *11*(5), Article 1487. https://doi.org/10.3390/pr11051487

30 Karkach, B., Tahiri, M., Haibi, A., Bouya, M., & Kifani-Sahban, F. (2023). Review on fast pyrolysis of biomass for biofuel production from date palm. *Applied Sciences*, *13*(18), Article 10463. https://doi.org/10.3390/app131810463

31 Krylov, K.A., Bazhin, V.Y., Sharikov, F.Y., Matylsky, B.E., & Dydin, V.M. (2026). Thermophysical Treatment of Petroleum Coke-Based Electrode Paste as a New Promising Approach to Integrating the Oil Refining and Metallurgical Industries for Carbon-Graphite Electrode Production. *International Journal of Engineering*, *39*(2), 341–350. https://doi.org/10.5829/ije.2026.39.02b.0535

32 Muradova, P.A., Zulfugarova, S.M., Graser, E., Strekov, A.S., & Litvishkov, Y.N. (2018). Microwaves-induced thermolysis of petroleum under contact with heterogenous catalysts. *Chemie Ingenieur Technik*, *90*(3), 393–397. https://doi.org/10.1002/cite.201700010

33 Al-Harahsheh, A., Al-Ayed, O., Al-Harahsheh, M., & Abu-El-Halawah, R. (2010). Heating rate effect on fractional yield and composition of oil retorted from El-Lajjun oil shale. *Journal of Analytical and Applied Pyrolysis*, *89*(2), 239–243. https://doi.org/10.1016/j.jaap.2010.08.009

34 Ben Chanaa, M., Lalleman, M. & Mohlisse, A. (1994). Pyrolysis of Timahdit oil shales under microwave field influence. *Fuel*, *73*(10), 1643–1649. https://doi.org/10.1016/0016-2361(94)90145-7

35 Taheri-Shakib, J., & Kantzas, A. (2021). A comprehensive review of microwave application on oil shale: Prospects for shale oil production. *Fuel*, 305, Article 121519. https://doi.org/10.1016/j.fuel.2021.121519

36 Zhu, J., Yi, L., Yang, Z., & Duan, M. (2021). Three-dimensional numerical simulation on the thermal response of oil shale subjected to microwave heating. *Chemical Engineering Journal*, 407, Article 127197. https://doi.org/10.1016/j.cej.2020.127197

37 Muradova, P.A., Litvishkov, Y.N., & Abbasov, O.R. (2024). Thermogravimetric study of oil shales of some deposits in Eastern Azerbaijan by the method of microwave impact. *ANAS Transactions, Earth Sciences*, 2, 160–167. https://doi.org/10.33677/ggianas20240200134

38 Wang, L., Yang, D., & Kang, Z. (2021). Evolution of permeability and mesostructure of oil shale exposed to high-temperature water vapor. *Fuel*, 290, Article 119786. https://doi.org/10.1016/j.fuel.2020.119786

39 Huang, X., Kang, Z., Zhao, J., Wang, G., Zhang, H., & Yang, D. (2023). Experimental investigation on micro-fracture evolution and fracture permeability of oil shale heated by water vapor. *Energy*, 277, Article 127677. https://doi.org/10.1016/j.energy.2023.127677

40 Aliyev, A., Abbasov, O., & Agayev, A. (2019). Mineralogy and geochemistry of oil shale in Azerbaijan: Classification, palaeoweathering and maturity features. *Visnyk of V.N. Karazin Kharkiv National University. Series Geology, Geography, Ecology*, 50, 11–26. https://doi.org/10.26565/2410-7360-2019-50-01

41 Aliyev, A.A., & Abbasov, O.R. (2019). Nature of the provenance and tectonic setting of oil shale (Middle Eocene) in the Greater Caucasus southeastern plunge. *Geodynamics*, *1*(26), 43–59. https://doi.org/10.23939/jgd2019.01.043

42 Srinivasan, P., Endara Arguello, E. M., & Atwah, I. (2024). Evaluating the reliability of solid phase extraction techniques for hydrocarbon analysis by GC–MS. *Journal of Chromatography A*, 1737, Article 465435. https://doi.org/10.1016/j.chroma.2024.465435

43 Pan, Y., Lou, X., Wang, Y., Yang, S., Li, Z., Zhang, X., Yan, Y., & Xin, H. (2023). A review on the application of microwave absorbents in oil shale. *Industrial & Engineering Chemistry Research*, *62*(46), 19402–19426. https://doi.org/10.1021/acs.iecr.3c01683

44 Nottenburg, R., Rajeshwar, K., Freeman, M., & Dubow, J. (1979). Effect of pore water and adsorbed moisture on the dielectric properties of Green River oil shale. *Thermochimica Acta*, *31*(1), 39–46. https://doi.org/10.1016/0040-6031(79)80005-2

45 Fedyaeva, O.N., Antipenko, V.R., & Vostrikov, A.A. (2017). Peculiarities of composition of hydrocarbon and heteroatomic substances obtained during conversion of Kashpir oil shale in supercritical water. *Russian Journal of Physical Chemistry B*, 11, 1246–1254. https://doi.org/10.1134/S1990793117080036

46 Kutuzov, I., Xiao, Q., Cai, C., & Amrani, A. (2023). Formation of volatile organic sulfur compounds by low thermal maturation of source rocks: A geochemical proxy for natural gas. *Marine and Petroleum Geology*, 158, Article 106531. https://doi.org/10.1016/j.marpetgeo.2023.106531

47 Qiu, M., Xiang, C., Wen, Y., Hong, W., Liu, R., Chen, D., & Chen, D. (2025). H_2 production from pyrolysis-steam reforming of municipal solid waste and biomass: A comparative study when using the self-derived char-based catalysts. *Catalysts*, 15(6), Article 531. https://doi.org/10.3390/catal15060531

48 Meng, W., Wang, H., Yu, C., Liu, Y., & Wang, W. (2026). Mechanistic analysis of in situ hydrogen production during heavy oil gasification based on numerical simulations. *Processes*, 14(6), Article 1026. https://doi.org/10.3390/pr14061026

How to Cite: Vassilets, Ye.P., Zhakina, A.Kh., Arnt, O.V., Zhakin, A.M., & Muldakhmetov, Z. (2026). Synthesis and Study of the Properties of a Composite Material Based on Sulfohumic Acid and Multi-Walled Carbon Nanotubes. *Eurasian Journal of Chemistry, 31, 2(122), 112–124.* https://doi.org/10.31489/2959-0663/2-26-8

Article

Received: 27 February 2026 | Revised: 14 May 2026 | Accepted: 18 May 2026 | Published online: 25 May 2026

UDC 547.639.7

https://doi.org/10.31489/2959-0663/2-26-8

Yevgeniy P. Vassilets[1, 2], Alma Kh. Zhakina[1*], Oxana V. Arnt[1], Almat M. Zhakin[1], Zainulla Muldakhmetov[1]

[1]*LLP "Institute of Organic Synthesis and Coal Chemistry of the Republic of Kazakhstan", Karaganda, Kazakhstan;*
[2]*Karaganda Industrial University, Temirtau, Kazakhstan*
*(*Corresponding author's e-mail: alzhakina@mail.ru)*

Synthesis and Study of the Properties of a Composite Material Based on Sulfohumic Acid and Multi-Walled Carbon Nanotubes

A composite sorption material based on sulfohumic acid (SHA) and multi-walled carbon nanotubes (MWCNTs) was synthesized. The composite was obtained via ultrasonic-enhanced coprecipitation, which ensures the efficient incorporation of nanotubes into the sulfohumic matrix. The structural and physicochemical properties of the initial SHA and the SHA:MWCNTs composite were studied using elemental analysis, conductometric titration, infrared spectroscopy, thermogravimetric analysis, and electron microscopy. The introduction of MWCNTs was shown to alter the surface morphology, increase roughness, and form a more developed porous structure. Thermogravimetric analysis indicates increased thermal stability of the composite material. The sorption properties of the synthesized composite with respect to Cu^{2+} ions from aqueous solutions were also studied. It was established that the SHA:MWCNTs composite possesses higher sorption capacity compared to the original SHA. Analysis of sorption isotherms revealed that the process is predominantly described by the Langmuir model, while satisfactory agreement with the Freundlich model indicates the energetic heterogeneity of the sorbent surface. These results demonstrate the potential of the SHA:MWCNTs composite as an effective sorption material for removing heavy metal ions from aqueous solutions.

Keywords: natural polymer, composite, sulfohumic acid, multi-walled carbon nanotubes, modification, ultrasound, sorbent, sorption

Introduction

Water pollution with heavy metals remains a serious global problem. Researchers are devoting considerable attention to the development of effective sorption materials for the extraction of heavy metal ions from aqueous solutions [1–4]. One promising area is the creation of composite sorbents incorporating carbon nanomaterials with a developed surface area and unique physicochemical properties [5–7].

Among the various types of carbon nanomaterials, multi-walled carbon nanotubes (MWCNTs) are of particular interest. These structures are cylindrical nanomaterials formed by several concentric graphene layers. MWCNTs are characterized by a high specific surface area, significant mechanical strength, chemical and thermal stability, and a developed π-bond electron system. Due to these properties, carbon nanotubes can effectively participate in the adsorption of various organic and inorganic compounds [8–11].

However, the use of native carbon nanotubes in sorption systems has several limitations. The surface of unmodified nanotubes contains a relatively small number of functional groups capable of interacting with metal ions. Furthermore, nanotubes are prone to aggregation due to strong van der Waals interactions between graphene layers, which leads to a decrease in the available specific surface area and a reduction in sorption efficiency [12–14].

To improve the sorption properties of carbon nanotubes, methods of chemical modification and the formation of composite materials combining nanostructured carbon with functionally active organic compounds are widely used [9, 15, 16]. One of the most promising areas is the creation of hybrid systems based on carbon nanotubes and natural organic substances, in particular humic compounds [17, 18].

Humic acids (HA) are natural, high-molecular-weight organic substances with a complex structure, formed during the humification of organic residues. Their macromolecules include condensed aromatic fragments linked by aliphatic chains of varying degrees of branching. The structure of humic acids contains a wide range of functional groups, the most common of which are carboxyl (–COOH), phenolic hydroxyl

(–OH), carbonyl, and quinone groups. The presence of these functional centers determines the pronounced physicochemical properties of humic substances, including ion-exchange capacity, sorption activity, hydrophilicity, and the ability to complex with metal ions [19–25].

Due to the combination of hydrophobic aromatic fragments and hydrophilic functional groups, humic acids are capable of adsorbing on various surfaces and exhibiting the properties of natural surfactants. Moreover, their sorption properties can be significantly improved through chemical modification aimed at increasing the number of functional groups and ionogenic centers in the macromolecule structure [23–25].

One effective method for modifying humic acids is sulfonation, which results in the formation of sulfohumic acids. The introduction of sulfo groups ($–SO_3H$) into the structure of the humic matrix increases the content of ionogenic centers and enhances the cation-exchange capacity of the material. The resulting sulfated derivatives are characterized by more pronounced surface-active and sorption properties and can be considered promising organic ion-exchange materials. Given the low solubility of sulfohumic acids, their synthesis is of practical interest for the creation of solid-phase sorbents [26–30].

Despite the significant sorption potential of humic and sulfohumic acids, their use in individual form has certain limitations. The main disadvantages include relatively low mechanical strength, a tendency to partially dissolve in alkaline environments, and difficulties in separating the sorbent from aqueous solutions after the sorption process. Therefore, a relevant area of research is the development of composite materials in which humic substances are immobilized on the surface of various inorganic or carbon matrices [31].

In such composite systems, carbon nanotubes act as a structural framework with a high specific surface area and a developed porous structure. Humic components, in turn, provide the functional groups involved in the binding of metal ions. Interactions between humic molecules and the nanotube surface can occur through π–π interactions between the aromatic fragments of the humic structures and the graphene layers of the nanotubes, as well as through hydrogen bonds and electrostatic interactions [17, 32–34].

The creation of composite materials based on sulfohumic acid and multi-walled carbon nanotubes is of particular interest, as this combination combines the advantages of both components. Carbon nanotubes provide a high specific surface area, structural stability, and mechanical strength to the composite, while sulfohumic acid forms a layer of polyfunctional organic groups on the nanotube surface that can effectively interact with metal ions.

The presence of carboxyl, phenolic, and sulfonic functional groups in the composite structure creates a developed system of active sites capable of binding copper cations through complexation, ion exchange, and electrostatic interactions. The carbon nanostructure also increases the accessibility of active sites and prevents the aggregation of organic components, which can lead to increased efficiency of sorption processes.

The proposed composite differs from previously described sorbents based on humic acids and carbon nanotubes in that the humic matrix undergoes preliminary chemical functionalization by sulfonation, resulting in the formation of sulfated humic acid (SHA) with an increased density of oxygen-containing functional groups, including sulfone groups ($–SO_3H$). The sulfonation stage leads to targeted chemical modification of the humic matrix, accompanied by changes in the distribution of active sites, acid-base characteristics, and complexing properties of the material. This fundamentally distinguishes the developed composite from previously described sorbents.

The role of MWCNTs in the developed composite is not limited to mechanical filling alone. MWCNTs form a developed structural framework that promotes a more uniform distribution of SHA, reduces the degree of aggregation of sulfohumic macromolecules, and forms a hierarchically organized sorption structure with increased accessibility of active sites.

Thus, the scientific novelty of this work lies in the development of a new type of functionalized composite based on SHA and MWCNTs, which utilizes the synergistic effect of chemical functionalization and nanostructured reinforcement. This ensures a change in the structural and chemical organization of the sorbent and increased accessibility of functional groups compared to previously described humic nanocomposites.

Experimental

Materials and Methods

Natural polymers — humic acids (HA), isolated from oxidized coal waste from the Shubarkol deposit (Karaganda, Kazakhstan), were used as feedstock for the synthesis of composite materials [17]. Chemical modification of HA by sulfonation allowed the synthesis of their sulfonated derivatives — sulfohumic acids (SHA).

Multi-walled carbon nanotubes (MWCNTs) from Sigma Aldrich (USA, 412988-2G) were used as a composite modifier. They have the following characteristics: as-produced cathode deposit > 75 % MWCNTs basis, OD×L 7–15 nm × 0.5–10 μm. Concentrated sulfuric acid was used as the sulfonating agent. Distilled water was used to prepare solutions. Analytical-grade NaOH (0.1 M) and HCl (0.1 M) solutions were used to adjust the pH.

The functional composition of the composite materials was studied using infrared spectroscopy (FTIR). Spectra were recorded in the 400–4000 cm^{-1} range using an *FSM-1201* spectrometer (Infraspec Company, St. Petersburg, Russia). Samples were prepared using the standard potassium bromide (KBr) pressing method. The resulting spectral data were processed and approximated using *Fityk 1.3.1* software, which allowed for the isolation and identification of characteristic absorption bands corresponding to the functional groups of the composites.

The quantitative content of oxygen-containing functional groups in the composite materials was determined conductometrically using an *Anion-4100* laboratory conductometer (Infraspak-Analit, Novosibirsk, Russia). The progress of the sulfonation reaction was monitored by monitoring the functional composition of the resulting products. The total content of oxygen-containing functional groups, including carboxyl, phenolic, and sulfo groups ($\Sigma COOH+OH+SO_3H$), was determined by conductometric titration. The total concentration of functional groups was calculated based on the volume of titrant consumed to the equivalence point, taking into account its molar concentration and the mass of the test sample. The amount of introduced sulfo groups was calculated as the difference between the total content of oxygen-containing functional groups in the sulfonated product and the initial sulfohumic acid. The obtained values are expressed as mg-eq/g. Each determination was performed in three parallel experiments, after which the average values were calculated. The relative standard deviation of the results did not exceed 3–5 %.

The surface morphology of the composite materials was characterized using a *MIRA 3* scanning electron microscopy system (Tescan Orsay Holding, Brno-Kohoutovice, Czech Republic), equipped with detectors recording various signals. The resulting SEM images were used to analyze the surface morphological features.

The thermal stability of the composites was studied using differential thermal analysis (DTA) combined with thermogravimetric analysis on a *STA 6000* (Perkin Elmer, USA) synchronous thermal analyzer. Measurements were performed in the temperature range from room temperature to 900 °C under a nitrogen atmosphere, at a heating rate of 10 °C/min.

Experimental Procedure

Sulfonation of Humic Acids

A two-necked flask was charged with 100 ml of H_2SO_4 solution of varying concentrations (25, 52, and 96 %) at a 1:1 ratio of the initial components, HA:H_2SO_4. The reaction mixture was cooled to –2 °C, after which 10 g of humic acid was gradually added with continuous stirring over 40 minutes. Stirring was continued for 3 hours at room temperature (23 °C). The reaction mixture was then heated in a water bath to boiling point and maintained at this temperature for 3 hours. Upon completion of the reaction, the mixture was cooled, 500 ml of distilled water was added, and stirring was continued for another 2 hours at room temperature. The solid phase was separated from the liquid by centrifugation, after which the precipitate was thoroughly washed with copious amounts of distilled water.

Synthesis of Composite Materials Based on Humic Acids and MWCNTs

Composite materials based on sulfohumic acids (SHA) and multi-walled carbon nanotubes (MWCNTs) were synthesized via ultrasound-enhanced coprecipitation. First, a 0.25 g sample of MWCNTs was dispersed in 50 ml of distilled water. Dispersion was performed using an *IL 100-6/2* ultrasonic unit equipped with an ultrasonic generator with a magnetostrictive transducer operating at a frequency of 22 kHz and a cylindrical waveguide. The resulting MWCNTs dispersion was slowly introduced into an aqueous solution of sulfohumic acid containing 2 g of SHA with constant stirring. During mixing, the pH of the reaction system was maintained at approximately 9. After the components were completely added, the resulting suspension was further ultrasonicated for 15, 30, and 60 min to enhance interfacial interactions between the components. The reaction mixture was then stirred at 60 °C for 6 hours, which facilitated the formation of the composite structure. Upon completion, the system was acidified with an HCl solution to a pH of 2.0–2.5, resulting in the precipitation of the composite material. The resulting precipitate was separated by filtration, washed with distilled water until neutral (pH 7.0), and dried at 60 °C to constant weight. The yield of the resulting composite materials was 50–60 %.

Study of the Adsorption Properties of Composites

Sorption experiments were conducted in static mode. A 1.0 g sample of the composite was placed in a flat-bottomed flask with a ground-glass stopper, after which 100 ml of aqueous copper sulfate solutions with initial concentrations ranging from 10 to 150 mmol/L were added to each flask. The resulting systems were stirred for 24 hours on a *PE-6410* laboratory shaker (St. Petersburg, Russia) until sorption equilibrium was reached. Afterward, the sorbent was separated from the solution by filtration. The residual concentration of Cu^{2+} ions in the filtrate was determined using iCAP6500 inductively coupled plasma atomic emission spectrometry (*SPECTRO ARCOS EOP SPECTRO* Analytical instruments GmbH, Germany).

The sorption capacity of the composite with respect to the Cu^{2+} ion was calculated based on the difference in their concentrations in the solution before and after sorption:

$$A = \frac{(C_0 - C_{eq}) \cdot V}{m},$$

where A — the sorption capacity of the composite (mmol/g); C_0 — the initial concentration of Cu^{2+} ions in the solution before sorption (mmol/L); C_{eq} — the equilibrium concentration of Cu^{2+} ions in the solution after sorption (mmol/L); V — the volume of the analyzed solution (L); m — the mass of the composite (g).

The elemental composition of the resulting composite materials was determined by elemental analysis (C, H, O) using an *Elementar Unicube* automated analyzer (Elementar Analysensysteme GmbH, Germany). At least three parallel measurements were performed for each sample, from which the average mass fractions of the corresponding elements were calculated.

Results and Discussion

Humic acids were sulfonated using concentrated sulfuric acid at varying concentrations. The progress of the sulfonation reaction was monitored by monitoring the functional composition of the resulting products. The results are presented in Table 1.

Table 1

Sulfonation of humic acids

Sample	H_2SO_4 concentration, %	∑COOH+OH+SO_3H, mg-eq/g	Yield, %
HA	–	4.5±0.2	80
SHA	25	4.9±0.2	75
SHA	52	5.8±0.2	70
SHA	96	6.5±0.2	66

The study results showed that increasing the sulfuric acid concentration in the reaction system leads to an increase in the total amount of oxygen-containing functional groups in the product. Thus, when using 25 % H_2SO_4, the total content of oxygen-containing functional groups reached 4.9 mg-eq/g, and the yield of SHA was 75 %. Increasing the acid concentration to 52 % resulted in a further increase in oxygen-containing functional groups to 5.8 mg-eq/g. The highest content of oxygen-containing functional groups was achieved using 96 % H_2SO_4, where the total content of oxygen-containing functional groups increased to 6.5 mg-eq/g. However, this was accompanied by a decrease in product yield to 66 %, which is likely due to partial destruction of the humic matrix under high acidity conditions.

Thus, it has been established that increasing the sulfuric acid concentration in the reaction system promotes an increase in the content of oxygen-containing functional groups in the humic acid structure. The sulfonation process occurs via the mechanism of electrophilic aromatic substitution in the aromatic fragments of the humic macromolecule. In concentrated sulfuric acid, an active sulfonating agent (HSO_3^+) is formed, which acts as an electrophile and attacks the aromatic rings of the humic acid. This results in the formation of an intermediate σ-complex, followed by proton detachment and reduction of the aromatic system, forming a sulfo group (–SO_3H) in the macromolecule structure (Scheme 1).

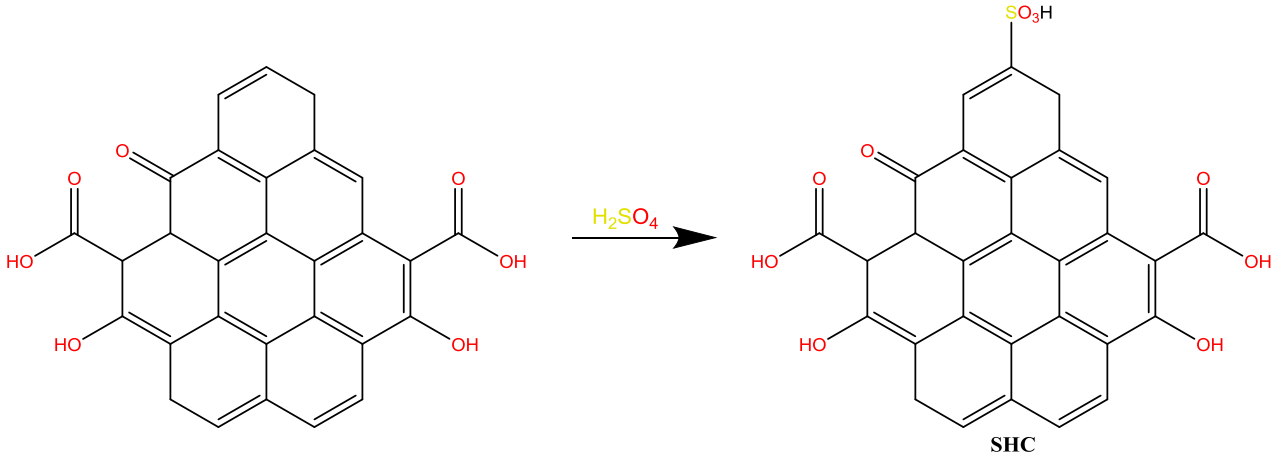

Scheme 1. Sulfonation process in the aromatic fragments of the humic macromolecule

To obtain a composite material based on the synthesized SHC, it was further modified with multi-walled carbon nanotubes (MWCNTs) from Sigma-Aldrich (USA, 412988-2G). The formation of a composite material based on SHA and MWCNTs occurs through a complex of non-covalent interactions between the functional groups of the sulfohumin matrix and the surface of the carbon nanostructures. SHA contains aromatic fragments and oxygen-containing functional groups (–COOH, –OH, >C=O), as well as sulfonic groups (–SO_3H), capable of participating in intermolecular interactions.

The primary mechanism for SHC attachment to the MWCNTs surface is π–π stacking between the aromatic structures of the sulfohumin matrix and the graphene-like layers of the nanotubes. Additionally, the composite is stabilized due to the formation of hydrogen bonds and electrostatic interactions between the functional groups of the SHA and defective oxygen-containing centers on the surface of the MWCNTs (Scheme 2).

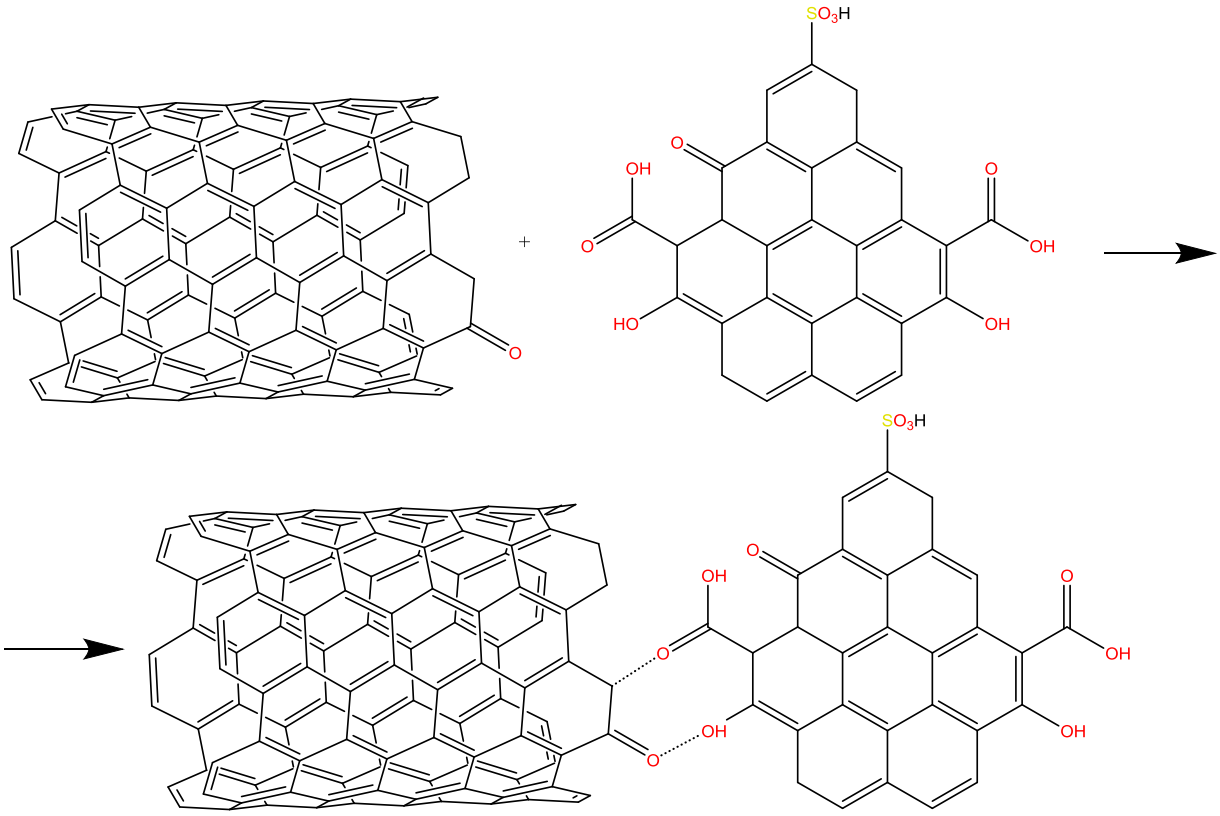

Scheme 2. SHC attachment to the multi-walled carbon nanotubes (MWCNTs) surface

The structural and functional characteristics of the synthesized composite material were confirmed by elemental analysis, conductometric titration, infrared spectroscopy (IR), thermogravimetric analysis (TGA), and electron microscopy.

Table 2

Elemental composition and functional characteristics of SHA and composite

Sample	C, mass. %	H, mass. %	O, mass. %	S, mass. %	Σ(COOH+OH+SO_3H), mg-eq/g	Yield, %
SHA	57.3±0.2	4.5±0.1	36.2±0.2	2.0±0.2	6.5±0.2	66
SHA:MWCNTs	61.5±0.2	4.1±0.1	32.6±0.2	1.8±0.2	5.6±0.2	75

Table 2 presents the results of elemental analysis, the total content of oxygen-containing functional groups Σ(COOH+OH+SO_3H), and the yields of the initial SHA and the synthesized composite material, allowing us to evaluate changes in the material's functional composition during the modification process.

According to the elemental analysis data, the initial SHA contains 57.3 wt.% carbon, 4.5 wt.% hydrogen, 36.2 wt.% oxygen, and 2.0 wt.% sulfur. The high oxygen content is due to the presence of oxygen-containing functional groups, primarily carboxyl and phenolic ones, the total content of which is Σ(COOH+OH) = 6.5 mmol/g. The yield of the product in the production of sulfohumic acid is 66 %.

The introduction of multiwalled carbon nanotubes leads to a change in the elemental composition of the composite. For the SHA:MWCNTs sample, an increase in the carbon mass fraction to 61.5 % and a simultaneous decrease in the oxygen content to 32.6 % are observed, which is due to the introduction of a carbon nanofiller characterized by a high carbon content. The hydrogen content decreases to 4.1 %, and the sulfur content to 1.8 %.

The total content of oxygen-containing functional groups Σ(COOH+OH) for the composite is 5.6 mmol/g. This slight decrease in this value compared to the original SHA is due to the dilution of the humic matrix with carbon nanotubes. At the same time, the yield of the composite material increases to 75 %.

The obtained results indicate the formation of a composite structure in which the humic matrix, containing oxygen-containing functional groups, is combined with a carbon nanofiller. This combination can contribute to the improvement of the physicochemical and sorption properties of the synthesized material.

The composition of the SHA and the composite based on it was confirmed by IR spectroscopy (Fig. 1).

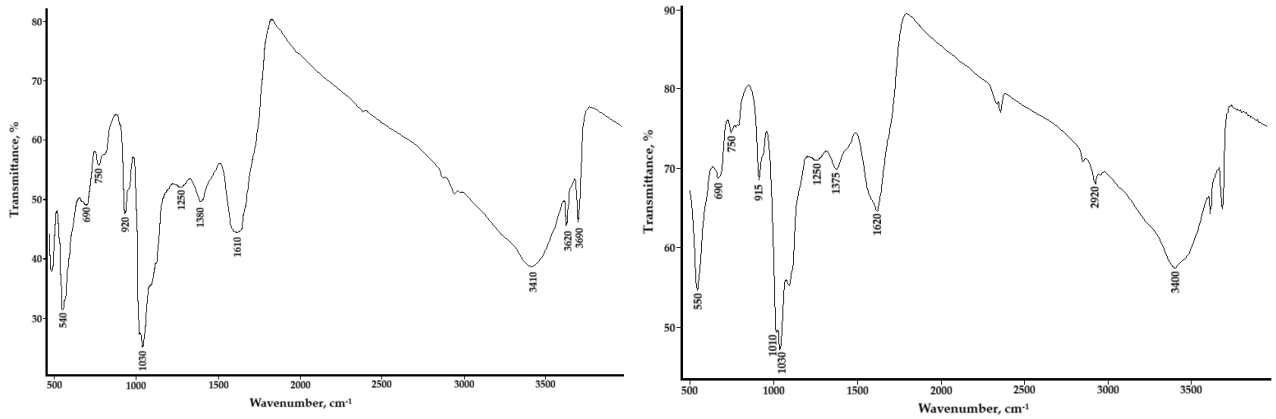

a *b*

Figure 1. IR spectra of SHA (*a*) and SHA:MWCNTs composite (*b*)

The IR spectrum of SHA exhibits a broad, intense absorption band in the 3200–3400 cm^{-1} region, corresponding to the stretching vibrations of the hydroxyl groups –OH associated with the phenolic and carboxyl fragments of the sulfohumin structure. The bands in the 2920–2850 cm^{-1} region are attributed to the stretching vibrations of the aliphatic fragments $–CH_2$ and $–CH_3$. The absorption band near 1610 cm^{-1} is primarily due to the stretching vibrations of the aromatic C=C bonds in the condensed aromatic fragments of the sulfohumin matrix, with possible overlap with the asymmetric vibrations of the carboxylate groups $–COO^-$. The absorption band at 1380 cm^{-1} corresponds to the symmetric stretching vibrations of the $–COO^-$ carboxylate groups and may be partially related to the deformation vibrations of the $–CH_3$ aliphatic groups.

The presence of sulfonic acid groups is confirmed by absorption bands at 1220–1250 cm^{-1} and 1030–1040 cm^{-1}, corresponding to the asymmetric and symmetric stretching vibrations of the S=O bonds of the $–SO_3H$ functional group. In this region, overlapping bands due to the vibrations of the C–O and S–O bonds of the oxygen-containing functional groups of the sulfohumic matrix is possible.

The spectrum of the SHA:MWCNTs composite retains the main characteristic bands of SHA, but exhibits changes in their intensity and slight shifts in the absorption maxima. In particular, a decrease in the band intensity in the 3200–3400 cm^{-1} region is noted, which may indicate a redistribution of the hydrogen bond system due to the interaction of the functional groups of the SHA with the surface of the carbon nanotubes. The change in the band intensity in the 1600 cm^{-1} region is due to the contribution of the sp^2-hybridized graphite-like structure of the MWCNTs. However, the absorption bands of the carboxyl and sulfonic acid groups are retained, indicating the preservation of the active functional centers of the sulfohumic matrix.

Thus, analysis of the IR spectra confirms the formation of a composite material in which MWCNTs are integrated into the sulfohumic matrix primarily through hydrogen bonds and π–π interactions, while maintaining the main functional groups.

Figure 2 shows the TG of the initial SHA and the SHA:MWCNTs composite in the temperature range from room temperature to 1000 °C.

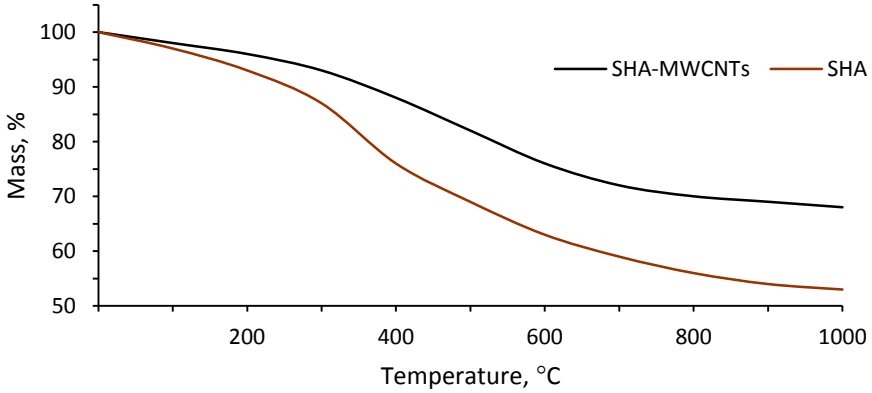

Figure 2. Thermogravimetric curves of samples SHA and SHA:MWCNTs

In the initial temperature range (up to 150–200 °C), both samples exhibit minor weight loss due to the removal of physically adsorbed water and volatile compounds retained within the material structure. In the temperature range of approximately 200–450 °C, a more intense weight loss is observed due to the thermal decomposition of oxygen-containing functional groups (carboxyl, phenolic, and sulfonic groups), as well as partial destruction of the organic sulfohumic acid matrix. For the original SHA, this process is more intense, resulting in a sharper weight loss compared to the composite.

In the range of 450–700 °C, the degradation of aromatic and aliphatic fragments of the organic structure of sulfohumic acid continues. In this temperature range, the contribution of decomposition processes is significantly greater for the original SHA, whereas for the SHA : MWCNTs composite, the weight loss is more gradual. With a further increase in temperature to 1000 °C, the residual mass of the composite (approximately 69 %) remains significantly higher than that of the initial SHA (up to 53 %). This higher residual mass is due to the presence of thermally stable multiwalled carbon nanotubes (MWCNTs), which exhibit high thermal stability.

Thus, the results of thermogravimetric analysis indicate that modification of sulfohumic acid with MWCNTs leads to increased thermal stability of the composite.

Figure 3 shows scanning electron micrographs of the surface of the initial SHA and the SHA : MWCNTs composite. The images were taken at a magnification of ×20,000, an accelerating voltage of 5 kV, and a working distance of 5 mm; the scale bar is 5 μm. Scanning electron microscopy revealed significant differences in the surface morphology of the SHA and the SHA : MWCNTs composite.

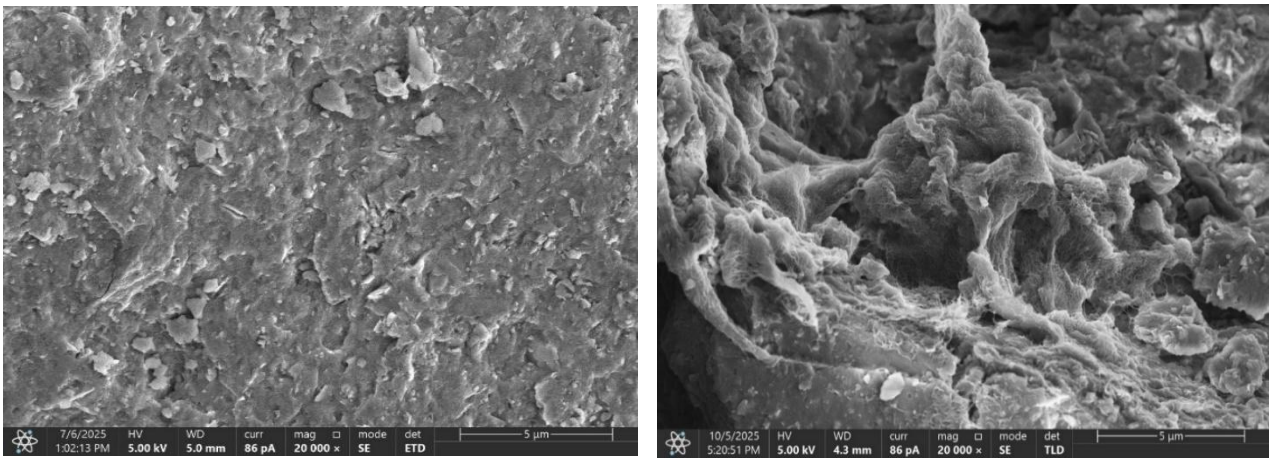

a *b*

Figure 3. Surface morphology of SHA (*a*) and SHA:MWCNTs (*b*)

The surface of the SHA (Fig. 3*a*) is characterized by pronounced morphological heterogeneity and an amorphous structure with developed roughness. The particles form dense, irregularly shaped aggregates with an uneven relief. Fragments of various shapes and sizes are observed on the surface, forming a microstructure represented by individual lamellar formations. This morphology is characteristic of humic substances and is due to the tendency of macromolecular fragments to aggregate and form associated structures. The presence of a rough microrelief can contribute to an increase in the number of accessible active sites, including functional groups (–SO_3H, –COOH, and –OH), which play an important role in sorption interactions with metal ions.

Unlike the original SHA, the surface of the SHA : MWCNTs composite (Fig. 3*b*) is characterized by a more developed and structurally organized morphology. The composite structure clearly displays elongated filiform structures corresponding to MWCNTs, distributed throughout the sulfohumic matrix. The nanotubes are partially incorporated into the sulfohumic phase, forming areas of intertwined fragments and forming a unique spatial framework. This distribution indicates the effective fixation of MWCNTs on the surface of the SHA. The introduction of MWCNTs significantly modifies the surface texture, resulting in increased roughness, the formation of additional interparticle voids, and the development of a more pronounced porous structure. This morphology indicates partial decompression of the original sulfohumic matrix and the formation of a more open spatial structure in the composite. The presence of carbon nanotubes prevents dense aggregation of humic macromolecules and promotes the formation of a spatially developed network structure.

Thus, modification of SHA with multi-walled carbon nanotubes results in the formation of a heterogeneous composite microstructure with a more developed surface area and an increased number of accessible active sites. The formation of such a structure can contribute to improved sorption properties of the material, making the SHA : MWCNTs composite a promising sorbent for the extraction of metal ions and organic compounds from aqueous solutions.

In this study, Cu^{2+} ions were chosen as a model ion due to their high environmental significance and widespread occurrence in industrial wastewater, as well as their pronounced ability to complex with oxygen-containing functional groups of humic substances. Furthermore, Cu^{2+} is often used as a model ion in studies of the sorption mechanisms of functionalized carbon-containing and humic materials, allowing for a reliable comparison of the obtained results with literature data. The study was limited to the Cu^{2+} model system for a more detailed analysis of the mechanisms of interaction between metal ions and the functional groups of the composite. Figure 4 shows the dependence of sorption capacity Q (mmol/g) on the equilibrium sorbate concentration C (mmol/L) for sulfohumic acid (SHA) and the SHA : MWCNTs composite.

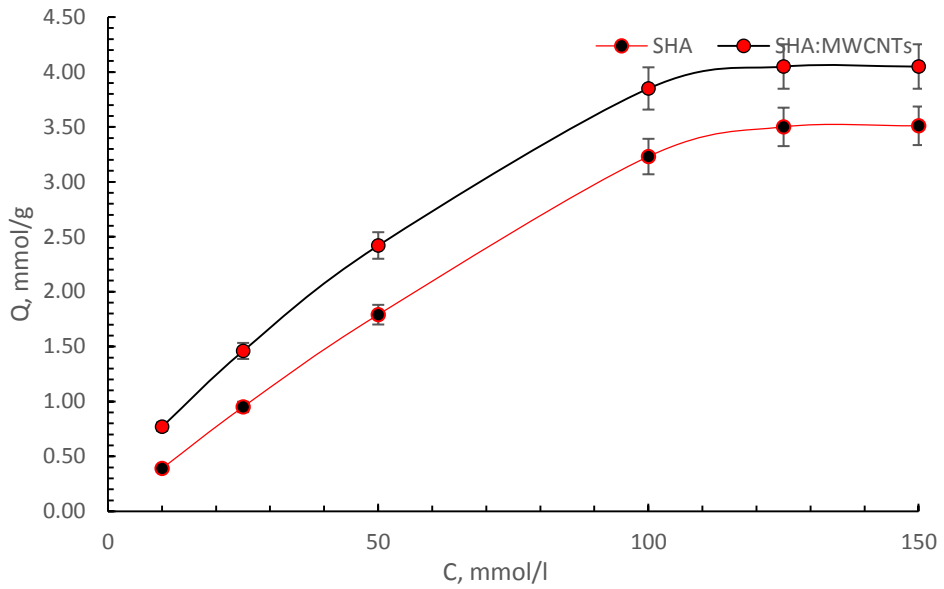

Figure 4. Sorption isotherms of Cu^{2+} ions in SHA and SHA : MWCNTs

With increasing sorbate concentration in the solution, a monotonic increase in sorption capacity is observed for both samples. At low concentrations (10–50 mmol/L), sorption capacity increases most rapidly, indicating the presence of a significant number of accessible active sites on the sorbent surface. As the solution concentration increases, the increase in sorption capacity gradually slows, and at concentrations of approximately 120–150 mmol/L, the curves reach a plateau, indicating gradual saturation of the sorption sites and the attainment of the maximum sorption capacity. The SHA : MWCNTs composite exhibits higher sorption capacity values compared to the original SHA across the entire concentration range studied. The maximum sorption capacity for the composite is approximately 4.0 mmol/g, while for SHA it is 3.5 mmol/g. The increase in sorption capacity from 3.5 to 4.0 mmol/g may seem modest when considering only absolute values. However, it should be noted that for humic sorbents, even a relatively small increase in sorption capacity is significant, since it is achieved without the use of expensive methods of deep chemical functionalization, aggressive reagents, or complex multi-stage synthesis procedures. The increase in sorption capacity is accompanied by an improvement in the structural organization of the composite, increased accessibility of functional groups, and a decrease in the degree of aggregation of the sulfohumic matrix due to the introduction of MWCNTs, which contributes to more efficient interaction of the sorbent's active centers with metal ions.

Table 3 shows the coefficients of the linear approximation of the equation $y = kx + b$, as well as the calculated parameters of the Langmuir and Freundlich isotherms for sulfohumic acid (SHA) and the SHA : MWCNTs composite.

Table 3

Parameters of the Cu^{2+} sorption isotherms on SHA and SHA : MWCNTs calculated using the Langmuir and Freundlich models

Langmuir isotherm parameters					
Sample	*k*	*b*	Maximum specific adsorption A_∞, mmol/g	Adsorption equilibrium constant K_L, L/mmol	*r*
SHA	0.2038	6.7031	4.9058	0.0304	0.9808
SHA : MWCNTs	0.1688	5.0822	5.9238	0.0322	0.9915
Freundlich isotherm parameters					
Sample	*k*	*b*	K_F	*n*	*r*
SHA	0.5651	–0.5297	1.9923	1.7695	0.9815
SHA : MWCNTs	0.5648	–0.4315	1.7527	1.7706	0.9881

High correlation coefficients for the Langmuir model ($r = 0.9808$ for SHA and $r = 0.9915$ for SHA : MWCNTs) demonstrate good agreement with the experimental data of this model and indicate a predominantly monomolecular nature of sorption on a limited number of active sites on the sorbent surface.

The calculated values of the maximum sorption capacity A_∞ indicate that the SHA : MWCNTs composite has a higher sorption capacity (5.9238 mmol/g) compared to the original SHA (4.9058 mmol/g). The increase in the maximum sorption capacity is due to the introduction of multi-walled carbon nanotubes, which contribute to an increase in the specific surface area of the composite and the formation of additional active sorption sites. The adsorption equilibrium constant K_L for SHA is 0.0304 L/mmol, while for the SHA : MWCNTs composite it is 0.0332 L/mmol. The obtained values characterize the affinity of the sorbate for the surface of the studied materials and confirm the effective interaction of the sorbents with the adsorbed molecules.

The correlation coefficients obtained by approximating the experimental data with the Freundlich equation ($r = 0.9815$ for SHA and $r = 0.9881$ for SHA : MWCNTs) also indicate a good fit to this model. This indicates a certain heterogeneity in the sorption surface of the studied materials, caused by the presence of various functional groups and structural defects.

The Freundlich constant K_F, which characterizes the sorption capacity of the material, is 1.9673 for SHA, while for the SHA : MWCNTs composite it is 1.7527. The parameter n, which reflects the intensity of the sorption process, has values of 1.7695 for SHA and 1.7706 for SHA : MWCNTs. Values of $n > 1$ indicate favorable sorption and indicate high affinity of the sorbate for the sorbent surface.

Comparison of isotherm parameters shows that the sorption process on the surface of SHA and the SHA : MWCNTs composite can be satisfactorily described by both the Langmuir and Freundlich models, as evidenced by high correlation coefficients ($r = 0.9815$–0.9881). However, slightly higher r values obtained for the Langmuir equation indicate a better fit of the experimental data with this model. This indicates that sorption predominantly occurs via the mechanism of monomolecular filling of active sites on the sorbent surface.

At the same time, the satisfactory description of the experimental data by the Freundlich model indicates the presence of energetic heterogeneity on the sorbent surface due to the presence of various functional groups (–COOH, –OH, and $–SO_3H$), as well as structural heterogeneities in the composite material.

Thus, an analysis of the parameters of both models shows that sorption predominantly occurs via the mechanism of monomolecular filling of active sites (the Langmuir model). However, the sorbent surface is characterized by a certain amount of energetic heterogeneity, which is also reflected in the satisfactory description of the process by the Freundlich model. Modification of sulfohumic acid with multiwalled carbon nanotubes leads to an increase in the ultimate sorption capacity and improved sorption characteristics of the composite material.

To assess the reusability of the synthesized SHA : MWCNTs composite, we further studied its regeneration after adsorption of Zn^{2+} ions from a model solution. Regeneration was performed by acid hydrolysis using a 0.1 N HCl solution at 50–60 °C for 30 min. After treatment, the composite was separated by filtration and washed with distilled water until Cl^- ions were completely removed. Regeneration was performed after each adsorption cycle. The Zn^{2+} concentration in the solution was determined by atomic emission spectrometry, and the amount of adsorbed ions was calculated from the difference in concentrations before and after sorption, normalized to the mass of the sorbent.

It was found that after the first regeneration cycle, the composite retained approximately 60 % of its initial adsorption capacity, while after the second cycle, this value decreased to 40 % of the initial value. The obtained results indicate a gradual decrease in the material's sorption activity with repeated regeneration, which is likely due to partial changes in the composite’s structure and functional groups under acid hydrolysis conditions.

Thus, the conducted studies confirm the feasibility of regeneration and reuse of the SHA : MWCNTs composite. However, it was found that with an increasing number of regeneration cycles, a decrease in the material’s sorption activity is observed. Under the studied conditions, acceptable adsorption efficiency is maintained with no more than two regeneration cycles.

Conclusions

As a result of the study, a composite material based on SHA and MWCNTs was synthesized. The composite was obtained by ultrasonic-enhanced co-precipitation, which ensured the effective incorporation of carbon nanotubes into the structure of the sulfohumic matrix. A comprehensive study of the synthesized

composite using elemental analysis, conductometric titration, infrared spectroscopy, thermogravimetric analysis, and electron microscopy confirmed changes in the structural and functional characteristics of the material after modification. It was found that the introduction of MWCNTs leads to the formation of a more developed and disordered surface morphology, increased roughness, and the formation of additional interparticle voids, which contributes to the increased availability of active sorption sites. The results of thermogravimetric analysis showed that modification of SHA with carbon nanotubes leads to increased thermal stability of the composite material. A study of the sorption properties showed that the SHA : MWCNTs composite is characterized by higher sorption capacity compared to the original SHA. The maximum sorption capacity increases from 4.9058 mmol/g for SHA to 5.9238 mmol/g for the composite. Analysis of the sorption isotherms showed that the adsorption process is predominantly described by the Langmuir model, indicating a monomolecular occupation of the active sites on the sorbent surface. At the same time, satisfactory agreement between the experimental data and the Freundlich model indicates the presence of energetic heterogeneity on the surface due to the presence of various functional groups and structural features of the composite material.

Thus, the use of ultrasonic-enhanced coprecipitation enables the efficient formation of composite materials based on SHA and MWCNTs with improved structural, thermal, and sorption properties. The obtained results demonstrate the potential of the SHA : MWCNTs composite as an effective sorbent for the extraction of metal ions from aqueous solutions.

Funding

This research is funded by the Committee of Science of the Ministry of Science and Higher Education of the Republic of Kazakhstan (Grant No. BR24992921) “Development of innovative technologies for obtaining new organic substances and composite materials from waste from coal mining and coal chemical enterprises in Kazakhstan”.

*Author Information**

**The authors' names are presented in the following order: First Name, Middle Name and Last Name*

Yevgeniy Petrovich Vassilets — Master of Pedagogical Sciences, Researcher, Laboratory of Polymer Chemistry, LLP “Institute of Organic Synthesis and Coal Chemistry of the Republic of Kazakhstan”, Alikhanov str. 1, 100012, Karaganda, Kazakhstan; 1st year PhD Student, Department of Chemical Technology and Ecology, Faculty of Metallurgy and Mechanical Engineering, Karaganda Industrial University, Republic ave. 30, 101400, Temirtau, Kazakhstan; e-mail: vassilets88@mail.ru; https://orcid.org/0000-0003-2242-486X

Alma Khassenovna Zhakina (*corresponding author*) — Candidate of Chemical Sciences, Assoc. Professor, Head of the Laboratory of Polymer Chemistry, LLP “Institute of Organic Synthesis and Coal Chemistry of the Republic of Kazakhstan”, Alikhanov str. 1, 100012, Karaganda, Kazakhstan; e-mail: alzhakina@mail.ru; https://orcid.org/0000-0001-5724-2279

Oxana Vasilievna Arnt — Master of Technical Sciences, Researcher, Laboratory of Polymer Chemistry, LLP “Institute of Organic Synthesis and Coal Chemistry of the Republic of Kazakhstan”, Alikhanov str. 1, 100012, Karaganda, Kazakhstan; e-mail: oxana230590@mail.ru; https://orcid.org/0000-0002-8996-4572

Almat Maulenuly Zhakin — Master of Technical Sciences, Junior Researcher, Laboratory of Polymer Chemistry, LLP “Institute of Organic Synthesis and Coal Chemistry of the Republic of Kazakhstan”, Alikhanov str. 1, 100012, Karaganda, Kazakhstan; e-mail: zhakin-almat@mail.ru; https://orcid.org/0000-0002-5940-7097

Zainulla Muldakhmetov — Academician of the National Academy of Sciences of the Republic of Kazakhstan, Doctor of Chemical Sciences, Director, LLP “Institute of Organic Synthesis and Coal Chemistry of the Republic of Kazakhstan”, Alikhanov str. 1, 100012, Karaganda, Kazakhstan; e-mail: iosu@mail.ru; https://orcid.org/0000-0001-9497-2545

Author Contributions

The manuscript was written through contributions of all authors. All authors have given approval to the final version of the manuscript. CRediT: **Yevgeniy Petrovich Vassilets** formal analysis, investigation, visu-

alization; **Alma Khassenovna Zhakina** conceptualization, data curation, methodology, project administration, resources, software, writing — original draft, writing — review & editing; **Oxana Vasilievna Arnt** formal analysis, investigation, visualization; **Almat Maulenuly Zhakin** formal analysis, investigation; **Zainulla Muldakhmetov** conceptualization, data curation, methodology, project administration, resources, software, writing — original draft, writing — review & editing;

Conflicts of Interest

The authors declare no conflict of interest.

References

1 Ciobanu, R., Bucatariu, F., Mihai, M., & Teodosiu, C. (2024). Silica-Based Composite Sorbents for Heavy Metal Ions Removal from Aqueous Solutions. *Polymers*, *16*(21), 3048. https://doi.org/10.3390/polym16213048

2 Islam, R., Smith, N., Jang, B., & Guo, L. (2026). The Comparison of Fresh and Dry Duckweed (Lemna minor L.) on Metal (Cr^{6+}, Cd^{2+}, and Zn^{2+}) Removal from Wastewater. *Plants*, *15*(5), 848. https://doi.org/10.3390/plants15050848

3 Stanković, K., Telečki, I., Smiljanić, D., Bajuk-Bogdanović, D., Potočnik, J., Veselinović, L., & Kumrić, K. (2026). Chitosan/Cellulose Functional Composite Hydrogel as Adsorbent for the Removal of Cu(II) from Aqueous Solutions in Dynamic Adsorption System. *Polysaccharides*, *7*(1), 30. https://doi.org/10.3390/polysaccharides7010030

4 Morozova, A.G., Lonzinger, T.M., Skotnikov, V.A., Mikhailov, G.G., Kapelyushin, Y., Khandaker, M.U., Alqahtani, A., Bradley, D.A., Sayyed, M.I., Tishkevich, D.I., Vinnik, D.A., & Trukhanov, A.V. (2022). Insights into Sorption–Mineralization Mechanism for Sustainable Granular Composite of MgO-CaO-Al_2O_3-SiO_2-CO_2 Based on Nanosized Adsorption Centers and Its Effect on Aqueous Cu(II) Removal. *Nanomaterials*, *12*(1), 116. https://doi.org/10.3390/nano12010116

5 Baby, R., Saifullah, B. & Hussein, M.Z. (2019). Carbon Nanomaterials for the Treatment of Heavy Metal-Contaminated Water and Environmental Remediation. *Nanoscale Res Lett*, *14*, 341. https://doi.org/10.1186/s11671-019-3167-8

6 Sakthivel, U., & Gopi Kumar, S. (2025). A Review on Heavy Metal Adsorption Using Nanocomposites for Wastewater Treatment. In S.B. Singh, M. Gopalarathnam, N. Roy. (Eds), Proceedings of the 3rd International Conference on Advances in Concrete, Structural, and Geotechnical Engineering-Volume 3. ACSGE 2024. (pp 317–325). Springer Proceedings in Materials, Springer, Singapore. https://doi.org/10.1007/978-981-96-0755-6_26

7 Kumari, S., Kaur, M., & Dhania, G. (2023). Carbon Nanomaterials for Wastewater Treatment. In: Malik, J.A., Sadiq Mohamed, M.J. (eds) Modern Nanotechnology. *Springer, Cham.,* 255-277. https://doi.org/10.1007/978-3-031-31111-6_11

8 Wang, H., Sun, X., Wang, Y., Hong Wang, Xu Sun, Yizhuo Wang, Li K., Wang, J., Dai, X., Chen, B., Chong, D., Zhang, L. & Yan J. (2023). Acid enhanced zipping effect to densify MWCNT packing for multifunctional MWCNT films with ultra-high electrical conductivity. *Nat Commun*, *14*, 380. https://doi.org/10.1038/s41467-023-36082-2

9 Sabzehmeidani, M. M., Mahnaee, S., Ghaedi, M., Heidari, H., & Roy, V.A.L. (2021). Carbon based materials: a review of adsorbents for inorganic and organic compounds. *Mater. Adv.*, 2, 598. https://doi.org/10.1039/D0MA00087F

10 Adegoke, K.A., Okon-Akan, O.A., Adebusuyi, T.A., Adewuyi, O.I., Oluwatosin Adu, P., Bamisaye, A., Adegoke, O.R., Opeyemi Babarinde, C., & Bello, O.S. (2025). Adsorptive removal of gaseous contaminants using biomass-based adsorbents. *RSC Adv.*, *15*, 13960. https://doi.org/10.1039/D4RA08572H

11 Oladipo, M., Ogunsola, S., & Oladoye, P. (2025). Covalent and non-covalent carbon nanotube functionalization: A review for the case of assessment criteria, and practical implementation in wastewater treatment. *Chemosphere*, *385*, 144549. https://doi.org/10.1016/j.chemosphere.2025.144549

12 Suthar, V., Sharma, P., & Murthy, C.N. (2024). Advances in Functionalized Polymer Nanocomposites: From Synthesis to Applications (Woodhead Publishing Series in Composites Science and Engineering). 339–378. https://doi.org/10.1016/B978-0-443-18860-2.00021-9

13 Temirgaliyeva, T.S., Nazhipkyzy, M., Nurgain, A., Turganbay, Dinistanova, B., & Mansurov, Z.A. (2020). Synthesis of Multiwall Carbon Nanotubes by the Cvd Method and their Functionalization. *J Eng Phys Thermophy*, *93*, 91–94 https://doi.org/10.1007/s10891-020-02094-8

14 Brito, C.L., Ferreira, E.I., & La-Scalea, M.A. (2020). Multi-walled carbon nanotube functionalization and the dispersing agents study applied for the glassy carbon electrode modification and voltammetric reduction of nitrofurazone. *J Solid State Electrochem*, *24*, 1969–1980 https://doi.org/10.1007/s10008-020-04621-2

15 Parameshwarappa, S., Chinnagiri, K.T., Chinnagiri, R.T., & Thippandegowdru, R.M. (2026). Sulfathiazole-Azo-Aniline Dye as Electrode Modifier for Carbon Paste Electrode: Synthesis and Electrochemical Evaluation for the Simultaneous Determination of Dopamine, Uric Acid, and Tyrosine. *Top Catal*. https://doi.org/10.1007/s11244-026-02271-8

16 Gao, L., Zhang, J., Liu, Q., Xu, H., Wan, M., & Guan, X. (2026). Study on the synergistic modification of Chinese fir wood cell walls by carbon dots and polyethylene glycol. *Wood Sci Technol*, *60*, 40 https://doi.org/10.1007/s00226-026-01753-y

17 Zhakina, A.K., Vassilets, Y.P., Arnt, O.V., Kudryavtseva Ye.V., Zhivotova T.S., Gazaliev A.M., & Muldakhmetov Z.M. (2020). Synthesis and Properties of a Nanocomposite Material Based on a Product of Coal Waste Processing. *Solid Fuel Chem.*, *54*, 274–279. https://doi.org/10.3103/S0361521920050109

18 Tian, X., Yang, K., Xu, Y., Lu, H., & Lin, D. (2013). Effect of Humic Acids on the Physicochemical Property and Cd(II) Sorption of Multiwalled Carbon Nanotubes. In J. Xu, J. Wu, Y. He (Eds.). *Functions of Natural Organic Matter in Changing Environment* (pp. 751–755). Springer, Dordrecht. https://doi.org/10.1007/978-94-007-5634-2_136

19 Gvozdeva, Y., Peneva, P., & Katsarov, P. (2025). Biomedical Applications of Humic Substances: From Natural Biopolymers to Therapeutic Agents. *Antioxidants, 14*(9), 1139. https://doi.org/10.3390/antiox14091139

20 Ioannidis, I., Vakarou, G., Sarrou, I., & Pashalidis, I. (2026). Uranium Adsorption at Increased and Ultra-Trace Levels by Humic Acid-Coated Alumina: Thermodynamic and Kinetic Studies. *Applied Sciences, 16*(4), 1829. https://doi.org/10.3390/app16041829

21 Beza, P., Anastopoulos, I., Arkas, M., Bompotis, T., Giannakopoulos, K., Ioannidis, I., & Pashalidis, I. (2025). The Impact of Humic Acid Coating on the Adsorption of Radionuclides (U-232) by Fe_3O_4 Particles. *Coatings, 15*(12), 1399. https://doi.org/10.3390/coatings15121399

22 Helal, A.A., Ahmed, I.M., Gamal, R., Abo-El-Enein, S.A., & Helal, A.A. (2022). Sorption of uranium(VI) from aqueous solution using nanomagnetite particles; with and without humic acid coating. *J. Radioanal. Nucl. Chem., 331*, 3005–3014. https://doi.org/10.1007/s10967-022-08352-8

23 He, Z., Wang, D., Shi, L., Xie, H., Xiong, Y., & Zhang, D. (2025). Effects of Humic Acids, Freeze–Thaw and Oxidative Aging on the Adsorption of Cd(II) by the Derived Cuttlebones: Performance and Mechanism. *Sustainability, 17*(21), 9628. https://doi.org/10.3390/su17219628

24 Bolin, L., Zhongwu, L., Jia, C., Changsheng, J., Weicheng, C., & Bo, P. (2025). Humic-like components in dissolved organic matter inhibit cadmium sequestration by sediment. *Journal of Environmental Sciences, 150*, 645–656. https://doi.org/10.1016/j.jes.2024.03.055

25 Yang, Y., Wang, B., Guo, X., Zou, C., & Tan, X. (2019). Investigating adsorption performance of heavy metals onto humic acid from sludge using Fourier-transform infrared combined with two-dimensional correlation spectroscopy. *Environ Sci Pollut Res, 26*, 9842–9850. https://doi.org/10.1007/s11356-019-04445-2

26 Cozzolino, A., Conte, P., & Piccolo, A. (2001). Conformational changes of humic substances induced by some hydroxy-, keto-, and sulfonic acids. *Soil Biology and Biochemistry*, 33, 563–571. https://doi.org/10.1016/S0038-0717(00)00196-6

27 Khil'ko, S. (2011). Mekhanokhemicheskoe sulfirovanie khuminovich kislot [Mechanochemical Sulfonation of Humic Acids]. *Nauchnyye trudy Donetskogo natsionalnogo tekhnicheskogo universiteta. Seriia: Khimiia i khimicheskaia tekhnologiia — Scientific works of Donetsk National Technical University. Series: chemistry and Chemical Technology 17*(187), 103–111 [in Russian]. https://ea.donntu.edu.ua/bitstream/123456789/3425/1/Hil%27ko.pdf

28 Zhang, A., Shen, Y., Lv, P., & Li, M. (2018). Preparation of sulfonated humic acid aquasorb and its performance. *New Chemical Materials, 46*(9), 256–259. https://caod.oriprobe.com/articles/55261331/Preparation_of_sulfonated_humic_acid_aquasorb_and_.htm

29 Hou, K., Xu, X., Xiang, Y., Kun Hou, Xinshuai Xu, Yong Xiang, Chen, X., Lam, S. S., Naushad, M., Sonne C., & Ge, S. (2023). Rapid uptake of gold ions by sulfonated humic acid modified phenolic resin with high adsorption capacity and selectivity. *Adv Compos Hybrid Mater., 6*, 77. https://doi.org/10.1007/s42114-023-00647-y

30 Yudov, M.V., Zhilin, D.M., Pankova, A.P., Rusanov, A.G., Perminova, I.V., Petrosyan, V.S., & Matorin, D.N. (n.d.). Synthesis, metal-binding properties and detoxifying ability of sulphonated humic acids. Chapter 24. *Use of Humic Substances to Remediate Polluted Environments: From Theory to Practice*, 485–498. https://doi.org/10.1007/1-4020-3252-8

31 Osman, A.I., El-Monaem, E.M.A., Elgarahy, A.M., Aniagor, C.O., Hosny, M., Farghali, M., Rashad, E., Ejimofor, M.I., López-Maldonado, E.A., Ihara, I., Yap, P-S., Rooney D.W., & Eltaweil, Ab.S. (2023). Methods to prepare biosorbents and magnetic sorbents for water treatment: a review. *Environ Chem Lett., 21*, 2337–2398. https://doi.org/10.1007/s10311-023-01603-4

32 Dong, M., Guo, J., Wang, Y., Gai, X., Xiong, X., Zeng, J., Wang, Y., & Wu, Y. (2022). Humic acid non-covalent functionalized multi-walled carbon nanotubes composite membrane and its application for the removal of organic dyes. *J. Env. Chem. Eng., 10*, 2, 107320. https://doi.org/10.1016/j.jece.2022.107320

33 Chappell, M.A., George, A.J., Dontsova, K.M., Porter, B.E., Price, C.L., Zhou, P., Morikawa, E., Kennedy, A.J., & Steevens, J.A. (2009). Surfactive stabilization of multi-walled carbon nanotube dispersions with dissolved humic substances. *Environmental Pollution, 157*, 4, 1081–1087. https://doi.org/10.1016/j.envpol.2008.09.039

34 Akkulova, Z.G., Amirkhanova A.K., Zhakina A.Kh., Kudaibergen G.K., Vassilets E.P., & Sadykova O.V. (2015). Surface morphology and sorption characteristics of humates and sulphohumate nanocomposites with natural and synthetic polymers and carbon nanotubes. *Chemical Journal of Kazakhstan, 4*, 184–188.